FBMC-OQAM Transceivers for Wireless and Optical Fiber Communications

François Rottenberg

ICTEAM Institute, Université catholique de Louvain

OPERA Department, Université libre de Bruxelles

Thèse présentée en vue de l'obtention du grade de

Docteur en sciences de l'ingénieur et technologie

March 2018

Ph.D. Committee

Prof. Jérôme Louveaux, *supervisor*, Université catholique de Louvain, Belgium
Prof. François Horlin, *supervisor*, Université libre de Bruxelles, Belgium
Prof. Luc Vandendorpe, Université catholique de Louvain, Belgium
Prof. Philippe De Doncker, Université libre de Bruxelles, Belgium
Dr. Claude Desset, IMEC, Belgium
Dr. Xavier Mestre, Centre Tecnològic Telecomunicacions Catalunya, Spain
Prof. Christophe Craeye, *president*, Université catholique de Louvain, Belgium

Acknowledgements

First and foremost, I would like to thank my two supervisors, Jérôme Louveaux and François Horlin. From the beginning of my master thesis, four and a half years ago, to this day, Jérôme has been consistently supporting me, being extremely available for constructive discussions and brainstorming sessions. He gave me the opportunity to participate to the ICT-EMPhAtiC European project during the first six months of my PhD. The meetings and general assemblies of the project allowed me to meet, talk and interact with many researchers very active in my field. I was lucky to have François Horlin as another great mentor. I could benefit from his very deep experience in signal processing, more oriented towards implementation concerns. He introduced me to a new research environment at ULB, which led to numerous and prolific discussions. I can say that Jérôme and François allowed me to enter a truly international research context and to build a strong scientific network. During the last four years, I have been actively involved in the publication of conference and journal articles with about 20 different co-authors coming from institutions located in Japan, Spain, Greece, Finland, France, Germany and Belgium.

I am especially grateful to Xavier Mestre, who accepted to be part of my jury. Xavier welcomed me during three research stays at CTTC in Castelldefels. Xavier is not only an outstanding scientist capable to combine advanced engineering and purely mathematical tools in an exquisite manner, leading to efficient and practical solutions; he is also an incredibly humble, kind and generous person. I can truly say that I could not dream of a better host. Xavier gave me the push I needed to launch my scientific career. I cannot count the number of hours we spent discussing together, where he patiently explained to me the basics of random matrix theory or complex analysis. I would also like to thank all the people that I met at CTTC, who immediately accepted me and made me feel at home: Marc, David, Marius, Javier, Carles, Biljiana, Jordi and all the others.

I would also like to thank the other members of my PhD committee. I am convinced that the quality of this thesis was greatly improved by their constructive feedback. In particular, the courses of Luc Vandendorpe were a source of constant inspiration for my work. The more practical expertise of Claude Desset was very useful to make the different case studies investigated in this thesis more concrete. Philippe De Doncker gave me precious advice to better specify the underlying assumptions of the channel models used in this thesis. Finally, I thank Christophe Craeye for accepting to chair this PhD committee.

I would like to deeply thank Trung-Hien Nguyen, with whom I could enjoy very regular discussions at ULB. He allowed me to enter the optics community, much more oriented towards implementation and industry than the wireless and signal processing communities. If my papers were accepted in optics journals, it is mainly thanks to the careful reviewing and sometimes rewriting performed by Hien, who had the great ability to make my words sound understandable for people in optics. My thanks also go to Simon-Pierre Gorza from ULB who gave me very instructive explanations on the underlying physics of optical fiber propagation.

My gratitude also goes to Pham Tien Dat who invited for a research stay of two months in NICT in Japan. I could see and learn a completely different methodology and I could perform experimental validation of my previous works which were mostly theoretical. I would also like to thank my colleagues at NICT who welcomed me with an hospitality faithful to the Japanese culture and with whom I could enjoy playing football and badminton under the Japanese sun: Kanno, Yamamoto, Philippe, Benjamin, Georg, Rayana and Simon.

My special thanks go to my UCL office mates, Pierre-Yves, Valerio and Vincent, and Benoit, Simon and Stéphanie for our countless discussions on the state of the world, our attempts to grow mushrooms using the coffee (Alice's) waste, the compulsory coffee breaks, the dolphin songs, their careful proofreading of my articles and proposals, the kicker games... I extend my thanks to Damien, Céline, Maxime, Chunlei, Guillaume, Adriana, Mohieddine, Hussein, Gaëtan, Steaven, Amir, Thomas, Georgios, Jean, David, Souley, Esther, François, Cédric, Pascaline, Kaori, Sébastien, Christel and all the people that worked in the ELEN department during my thesis. I would also like to thank my ULB colleagues: Tania, Mathieu, Jean-François and Thomas. I also thank Laurent Jacques for the organization of the ISPS seminars that helped us to share our research and to find common points of interest. I thank Claude Oestges for giving me precious contacts and for his detailed explanations to my questions on channel models. I thank François Quitin for his careful coaching and tips to prepare interviews. I also thank the Fonds pour la Formation à la Recherche dans l'Industrie et dans l'Agriculture of the FNRS for funding my research and my research stays in Spain, Japan, Germany, UK, US, China, France...

Finally, I would like to thank with all my heart all the people outside my work environment that were always there to support me. A PhD is a long journey, stressful and not always easy. With all my heart, I thank my friends, my parents, my brother and Valérie for their constant encouragement and assistance.

ABSTRACT

How to communicate ? Human beings use the voice or gestures to give shape to their ideas. In digital communications, a modulation scheme is used to give shape to bits of information, *i.e.*, to convert zeros and ones into an analog waveform. The question of an ideal modulation scheme is discussed in this thesis and we study the one that seems the most promising to us.

The orthogonal frequency division multiplexing (OFDM) modulation is the most popular multicarrier modulation scheme nowadays. The main advantage of OFDM is its simplicity. However, due to the rectangular pulse shaping of the Fast Fourier transform filters, OFDM systems exhibit very high frequency leakage and poor stopband attenuation. In the light of these limitations, the offset-QAM-based filterbank multicarrier (FBMC-OQAM) modulation has recently received increasing attention. Rather than using a rectangular pulse, FBMC-OQAM uses a pulse shape which is more spread out in time, which results in a much better frequency localization. This in turn translates into higher spectral efficiency and much more flexibility for spectrum allocation.

The main objective of this thesis is to investigate the applicability of the FBMC-OQAM modulation for next generations of communication systems. More specifically, we focus on two main directions. The first direction studies advanced equalization algorithms for multiple-antenna wireless systems characterized by highly frequency and/or time selective channels. The second direction studies two main linear impairments in optical fiber systems, namely, phase noise and chromatic dispersion.

TABLE OF CONTENTS

Nomenclature

Symbols

$2M$	Number of subcarriers.
$2N_s$	Number of real-valued multicarrier symbols.
$\mathbf{A}_{m,l}$	Single-tap pre-equalizer at subcarrier m and multicarrier symbol l.
x	A scalar (lowercase and non-boldface).
$\mathbf{x}$	A column vector (lowercase and boldface).
$\mathbf{X}$	A matrix (uppercase and boldface).
$\mathbf{A}_m$	Single-tap pre-equalizer at subcarrier m and time-invariant.
$\mathbf{B}_{m,l}$	Single-tap equalizer at subcarrier m and multicarrier symbol l.
b	Tap index.
$O(x)$	Denotes a quantity that decays to zero at least at the same rate as x.
$\mathbf{B}_m$	Single-tap equalizer at subcarrier m and time-invariant.
$\mathbf{C}[b,n]$	Time-variant channel impulse response at time instant n and corresponding to delay b.

$\mathbf{C}[b]$	Time-invariant channel impulse response corresponding to delay b.
$\mathbf{C}_{\mathrm{BS}}$	Spatial correlation matrix between the BS antennas.
$\mathbf{d}_{m,l}$	Real-valued multicarrier symbols (SFB inputs) at subcarrier m and multicarrier symbol l.
D	Dispersion coefficient [ps/nm/km].
δ_{TF}	Lattice density.
δ_n	Kronecker delta (also written $\delta[n]$).
$\delta_{m,n}$	2D Kronecker delta.
$\Delta\nu$	Combined laser linewidth of transmit and receive lasers.
$\delta(t)$	Dirac delta.
$\hat{\mathbf{d}}_{m,l}$	Estimates of $\mathbf{d}_{m,l}$ after AFB processing, equalization and real operator at subcarrier m and multicarrier symbol l.
$\mathrm{diag}(.)$	When applied to a vector, returns a diagonal matrix whose k-th diagonal entry is equal to the k-th entry of the argument vector. When applied to a square matrix, returns the same matrix with off-diagonal elements set to zero.
E_s	Symbol energy.
η	Pulse-related quantity.
$\mathbb{E}(.)$	Expectation.
$g[n]$	Discrete receive prototype filter.
$g(t)$	Analog receive prototype filter.

$\mathbf{H}_{m,l}$	Time-variant channel frequency response evaluated at subcarrier m and multicarrier symbol l.
$\mathbf{H}_m$	Time-invariant channel frequency response evaluated at subcarrier m.
$\mathbf{H}(\omega)$	Time-invariant channel frequency response.
$\mathbf{H}(\omega, t)$	Time-variant channel frequency response.
$\jmath$	Imaginary unit.
K	Number of users.
κ	Overlapping factor.
$\otimes$	Kronecker product.
L	Fiber length.
l	Time index, expressed in multicarrier symbol periods.
m	Subcarrier index.
N	Number of base station antennas.
n	Time index, expressed in sampling periods.
N_0	Noise variance.
N_R	Number of receive signals.
N_T	Number of transmit signals.
$\tilde{N}_s$	Notation introduced for the sake of clarity, $\tilde{N}_s = \frac{2N_s+2\kappa-1}{2}$.
$(.)^*$	Conjugate operator.
$(.)^T$	Transpose operator.
$(.)^H$	Hermitian transpose operator.

$\Im(.)$	Imaginary operator.
$\Re(.)$	Real operator.
$p[n]$	Discrete transmit prototype filter.
$p(t)$	Analog transmit prototype filter.
$P_d(m)$	Distortion power at subcarrier m.
ϕ_l	PN at multicarrier symbol l.
$\phi[n]$	PN at sampling time n.
$g_{m,l}[n]$	OQAM modulated prototype pulse $g[n]$ translated in time and frequency, $g_{m,l}[n] = \jmath^{m+l} g[n-lM] e^{\jmath \frac{2\pi}{2M}(n-\frac{2M\kappa-1}{2})}$.
$p_{m,l}[n]$	OQAM modulated prototype pulse $p[n]$ translated in time and frequency, $p_{m,l}[n] = \jmath^{m+l} p[n-lM] e^{\jmath \frac{2\pi}{2M}(n-\frac{2M\kappa-1}{2})}$.
$\mathbf{r}[n]$	Discrete complex baseband equivalent of the received signal.
$\circledast$	Row-wise convolution.
S	Number of spatial streams.
σ_u^2	Variance of the intrinsic interference.
T	Multicarrier symbol period.
T_{CP}	Cyclic prefix duration.
tr[.]	Trace operator.
T_s	Sampling period, $T_s = T/2M$.
$\mathbf{u}_{m,l}$	Intrinsic interference at subcarrier m and multicarrier symbol l.
var (.)	Variance.

$\mathbf{w}[n]$	Noise samples.
$\mathbf{w}_{m,l}$	Filtered noise samples at subcarrier m and multicarrier symbol l.
$\mathbf{x}_{m,l}$	Equalized symbols at subcarrier m and multicarrier symbol l.
$\mathbf{y}_{m,l}$	Output of AFB and SFB placed back-to-back at subcarrier m and multicarrier symbol l.
$\mathbf{z}_{m,l}$	Demodulated symbols (AFB outputs) at subcarrier m and multicarrier symbol l.

Acronyms / Abbreviations

AFB	analysis filterbank
AML	adaptive maximum likelihood
ASE	amplified spontaneous emission
ATT	attenuator
AWG	arbitrary waveform generator
BC	broadcast channel
BER	bit error rate
BS	base station
CD	chromatic dispersion
CDF	cumulative density function
CFO	carrier frequency offset
CP-OFDM	cyclic prefix-orthogonal frequency division multiplexing

CP	cyclic prefix
CPR	carrier phase recovery
DL	downlink
FBMC-OQAM	offset-QAM-based filterbank multicarrier
FBMC	filterbank multicarrier
FDMA	frequency division multiple access
FEC	forward error correction
FFT	fast Fourier transform
ICI	inter-carrier interference
IFFT	inverse fast Fourier transform
IFoF	intermediate frequency-over-fiber
ISI	inter-symbol interference
IUI	inter-user interference
LD	laser diode
LED	light emitting diode
LMMSE	linear minimum mean squared error
LNA	low-noise amplifier
LO	local oscillator
M-BPS	modified-blind phase search
MAC	multiple access channel
MAP	maximum *a posteriori*

MF	matched filtering
MIMO	multiple-input-multiple-output
ML	maximum likelihood
MMSE	minimum mean squared error
MSE	mean squared error
MSI	multi-stream interference
MU	multi-user
MZM	Mach-Zehnder modulator
NPR	near perfect reconstruction
OC	optical coupler
OFDM	orthogonal frequency division multiplexing
OLED	organic light emitting diode
OQAM	offset quadrature amplitude modulation
OSNR	optical signal-to-noise ratio
OS	oscilloscope
PA	power amplifier
PD	photodetector
PDP	power delay profile
PN	phase noise
PPN	polyphase network
PR	perfect reconstruction

PTP	point-to-point
QAM	quadrature amplitude modulation
RAU	remote antenna unit
RoF	radio-over-fiber
RRH	remote radio head
SDMA	space division multiple access
SER	symbol error rate
SFB	synthesis filterbank
SISO	single-input-single-output
SNDR	signal-to-noise-and-distortion ratio
SNR	signal-to-noise ratio
SSMF	standard single-mode fiber
STO	symbol timing offset
TDMA	time division multiple access
UL	uplink
VLC	visible light communication
WDM	wavelength division multiplexing
ZF	zero forcing

CHAPTER 1

INTRODUCTION

1.1 Motivations

The standards for the future generations of communication systems let us expect revolutionary changes in terms of data rate, latency, energy efficiency, massive connectivity and network reliability [1–4]. The network should not only provide very high data rates but also be highly flexible to accommodate a considerable amount of devices with very different specifications and corresponding to different applications, such as the Internet of Things, the Tactile Internet or vehicle-to-vehicle communications. These high requirements will only be met by introducing innovative technologies radically different from existing ones.

The orthogonal frequency division multiplexing (OFDM) modulation has been very popular up to now mainly because of its low implementation complexity. Thanks to the combination of the fast Fourier transform (FFT) and the introduction at the transmitter of redundant symbols known as the cyclic prefix (CP), the OFDM modulation allows for a very simple compensation of the channel impairments at the receiver [5]. However, the rectangular pulse shaping of the FFT filters induces significant spectral leakage, which results in the need for large guard bands at the edges of the spectrum in order to prevent out-of-band emissions. Furthermore, the CP induces an additional loss of spectral efficiency since it does not carry useful information.

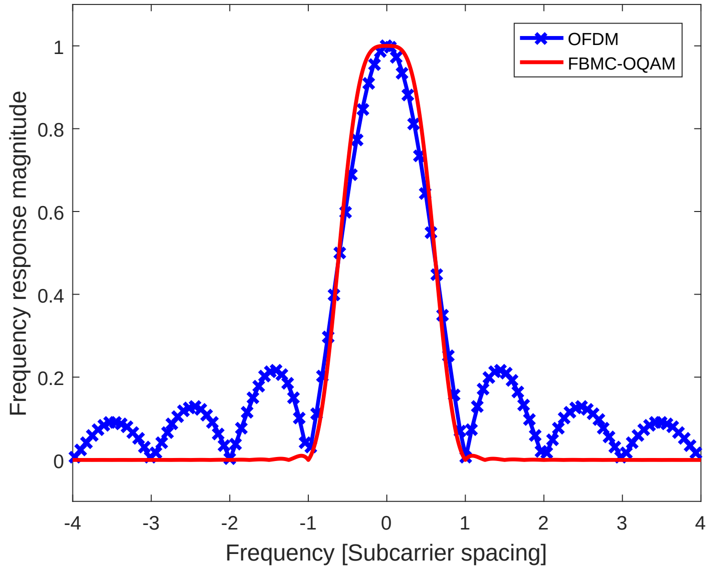

Figure 1.1 Comparison of the prototype filter frequency responses for OFDM and FBMC-OQAM modulations (Phydyas pulse with overlapping factor set to 4 [6]).

In the light of these limitations, the offset-QAM-based filterbank multicarrier (FBMC-OQAM) modulation has recently received a lot of attention as an attractive alternative to cyclic prefix-orthogonal frequency division multiplexing (CP-OFDM) systems [7]. As opposed to CP-OFDM, FBMC-OQAM uses a pulse shape which is more spread out in time, which results in a much better frequency localization of the prototype pulse, as shown in Fig. 1.1. This provides significant advantages. First, no CP is required to simplify the equalization process, leading to a larger spectral efficiency than CP-OFDM systems. Secondly, very small guard bands (of the order of one subcarrier) at the edges of the spectrum are sufficient to meet frequency emission masks, which again increases the system spectral efficiency [8]. Thirdly, it makes the system more robust to symbol timing offset (STO) and carrier frequency offset (CFO) [9]. Finally, it provides high flexibility for spectrum allocation with clear applications such as cognitive radios and the Internet of Things, which may require asynchronous transmission from multiple users which can be easily separated in the frequency domain [10].

The advantages of the FBMC-OQAM modulation come at the expense of an increase in the system implementation complexity. More specifically, this modulation generates a particular interference pattern, which may complicate the receiver design. Most of the MIMO algorithms originally devised for spatial multiplexing CP-OFDM systems can be straightforwardly applied to FBMC-OQAM systems if the channel is sufficiently slowly varying in time and frequency. However, the case of highly selective channels or the use of space time codes requires additional signal processing and results in more complex designs [11–13]. Furthermore, one should note that, to achieve higher spectral selectivity, the prototype pulse needs to be more spread out in the time domain, which induces more latency and might be detrimental for short burst transmissions. Pre-loading techniques and tail shortening algorithms have been designed to limit this effect [8, 14–16].

The main objective of this thesis is to investigate the applicability of the FBMC-OQAM modulation for next generations of communication systems. More specifically, we focus on two main directions.

The first direction studies advanced equalization algorithms for MIMO wireless systems. If the channel is slowly varying in time and frequency, single-tap equalization is sufficient to restore the FBMC-OQAM orthogonality. However, as the channel gets more selective in time and frequency, distortion will appear and the FBMC-OQAM system will suffer from so-called intrinsic interference caused by multi-stream interference (MSI), inter-carrier interference (ICI) and inter-symbol interference (ISI). This thesis precisely addresses the performance analysis and the design of compensation algorithms for various wireless MIMO scenarios characterized by highly frequency and/or time selective channels.

The second direction of this thesis studies two main linear impairments in optical fiber systems, namely, phase noise (PN) and chromatic dispersion (CD). It will be shown that these two impairments can be seen as special types of channel time and frequency selectivity respectively.

1.2 Outline and contributions

Chapter 2 first introduces the principle of the FBMC-OQAM modulation and the related state of the art, including a description of the main multicarrier modulations, their limitations and our motivation to go for the FBMC-OQAM modulation. A MIMO transmission model is introduced, including discussions on efficient implementations, channel equalization and estimation. Secondly, the different communication systems under study in this thesis are detailed.

The main content of this thesis is structured in three parts. **Part I** addresses channel equalization in MIMO FBMC-OQAM wireless systems. More specifically, Part I addresses various wireless MIMO scenarios characterized by highly frequency and/or time selective channels, *i.e.*, channels with large variations in the frequency and/or time domains. As the selectivity of channel increases, the FBMC-OQAM orthogonality is progressively destroyed and distortion appears after the demodulation process. The different works presented in Part I share a common approach of the channel selectivity based on a Taylor approximation of its variations and an asymptotic characterization of the residual error. These studies were performed in close collaboration with Dr. Xavier Mestre from the *Centre Tecnològic Telecomunicacions Catalunya* (Castelldefels, Spain). A main result of Part I is to show that, as opposed to a general claim in the literature, many low complexity solutions are possible to apply MIMO technologies to FBMC-OQAM systems, even in the case of highly selective channels. Part I is composed of the four following main contributions:

- **Chapter 3** investigates the design of optimized single-tap equalizers and pre-equalizers for a multi-user (MU)-multiple-input-multiple-output (MIMO) FBMC-OQAM scenario under highly frequency selective channel. The proposed single-tap (pre-)equalizers have a very low implementation complexity. As opposed to classical approaches that assume flat channel frequency selectivity at the subcarrier level, the base station (BS) does not make this assumption and takes into account the distortion caused by channel frequency selectivity. The equalizers and pre-equalizers are found by optimizing the mean squared error (MSE) of the symbol estimates under either a zero forcing (ZF) criterion or a minimum mean squared error (MMSE) criterion. It is shown that, as soon as the BS has more antennas than the number of users, the optimized (pre)-equalizers use those extra degrees of freedom to compensate for the distortion induced by channel frequency selectivity. From an asymptotic study at high signal-to-noise ratio (SNR), it is shown that the first order approximation of the distortion can even be completely removed if the BS has at least twice as many antennas as the number of users.

- In **Chapter 4**, the performance of an FBMC-OQAM uplink massive MIMO system is theoretically characterized in terms of the MSE of the decoded symbols. The study is performed for three types of single-tap equalizers, namely, a ZF, a linear minimum mean squared error (LMMSE) and a matched filtering (MF). Using random matrix theory, the output MSE of these equalizers is asymptotically characterized as the number of BS antennas N and the number of users K grow large, while keeping a finite ratio N/K. The obtained expressions allow to draw many conclusions. First, the MSE becomes uniform across the frequency band as a result of the channel hardening effect. Secondly, it is shown that a good synchronization of the users is crucial in a massive MIMO scenario. Finally, if the users are well synchronized, the different terms that compose the MSE, such as noise, inter-user interference (IUI) and the distortion caused by the channel frequency selectivity, become negligible for large values of the ratio N/K.

- While the impact of channel frequency selectivity has been very widely studied in the FBMC-OQAM literature, the impact of time selectivity of the channel has only received little attention. In **Chapter 5**, the effect of the two types of selectivity on a point-to-point (PTP) MIMO FBMC-OQAM system is characterized and a parallel equalization structure that can compensate for the doubly dispersive nature of the channel is proposed. A theoretical approximation of the remaining distortion after equalization is also given.

- **Chapter 6** proposes a very simple PTP MIMO equalizing structure for doubly selective channels based on a single-tap per-subcarrier equalizer. The equalizers are designed to minimize the MSE of the symbol estimates derived in Chapter 5 under a ZF constraint. This receiver exploits the degrees of freedom offered by the extra antennas at the receiver to compensate for the distortion induced by time and frequency selectivity. Chapter 6 can be seen as an extension of Chapter 3 to doubly selective channels.

Part II considers the compensation of linear impairments in FBMC-OQAM optical fiber systems. More specifically, two impairments, namely, PN and CD, are studied. These studies were conducted in close collaboration with Dr. Trung-Hien Nguyen from *Université libre de Bruxelles* (Brussels, Belgium). Part II is composed of the three following main contributions:

- **Chapter 7** addresses PN estimation and compensation. Several approaches have already been proposed in the FBMC-OQAM literature. However, most of them have a significant complexity and do not make use of all information at disposal such as previously decoded symbols. Here, we propose two new estimators, obtained by minimizing a maximum likelihood (ML) and a maximum *a posteriori* (MAP) criteria. They use an error model formulation which allows to easily use priors on the PN statistics. An analytical solution is found, which avoids the need for multiple phase tests.

- **Chapter 8** reports on several methods for the CD compensation. The typical approach to deal with channel frequency selectivity in FBMC-OQAM systems, and more generally multicarrier systems, is to increase the number of subcarriers. However, to avoid increasing the system sensitivity to phase noise, the number of subcarriers cannot always be made arbitrarily large. This implies that, for long optical fibers, more advanced CD compensation methods need to be investigated. Here, we show that several equalization structures, initially proposed for wireless FBMC-OQAM systems, can also be applied to optical FBMC-OQAM systems to compensate for the CD effect. The different algorithms are compared in terms of performance and complexity of implementation with state of the art solutions.

- **Chapter 9** investigates the joint compensation of CD and PN in FBMC-OQAM optical fiber systems. To deal with such impairments, the PN and CD compensation algorithms are working in the frequency domain, which allows for a simple and efficient implementation. We further discuss a methodology for the design of long haul FBMC-OQAM transmission systems in order to find the best trade-off between CD and PN compensation, and the complexity. It is shown that the number of subcarriers is a critical parameter in the optimization of the system design. This investigation can be extended to different values of the fiber length and laser linewidth, providing an efficient framework for system design.

Part III summarizes the experimental studies that were performed during the thesis. Only one contribution is presented in Chapter 10, which results from a collaboration with Dr. Pham Tien Dat from the *National Institute of Information and Communications Technology* (Tokyo, Japan). The others contributions to come are detailed in Section 11.2

containing the perspectives of this thesis. **Chapter 10** first proposes a frame design for MIMO FBMC-OQAM transmission systems including the description of the algorithms used for synchronization, channel estimation and equalization. The proposed design is scalable in the number of transmitted streams and flexible as multiple asynchronous users can be accommodated. The proposed system is experimentally validated for a 2x2 MIMO system over a seamless fiber–wireless link in the W-band. Satisfactory performance is confirmed for a data rate of up to 18 Gb/s in both downlink and uplink directions.

Finally, **Chapter 11** concludes the thesis with a summary of the main contributions and potential future directions.

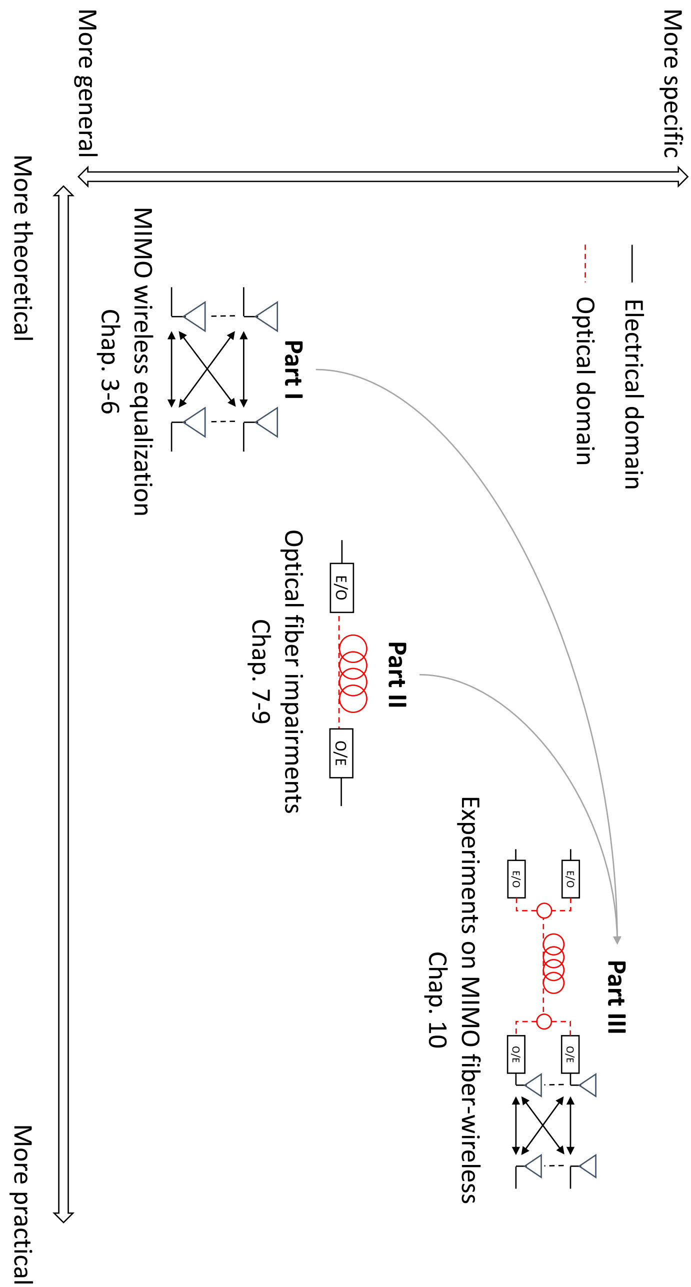
More general
More specific
More theoretical
More practical
Electrical domain
Optical domain
Part I
MIMO wireless equalization
Chap. 3-6
Part II
E/O
O/E
Optical fiber impairments
Chap. 7-9
Part III
E/O
E/O
O/E
O/E
Experiments on MIMO fiber-wireless
Chap. 10

CHAPTER 2

PRELIMINARIES

The goal of this chapter is to introduce some preliminaries on the principle of the FBMC-OQAM modulation and the communication systems under study in this thesis. This chapter is divided in two sections.

The first section gives a description of the FBMC-OQAM modulation. Before introducing the advantages of OQAM-based multicarrier systems, the Balian-Low theorem is recalled and its implications on conventional QAM-based multicarrier systems are detailed. The properties of several well-known multicarrier modulations are also discussed. To allow for a more physical intuition of time and frequency quantities, this discussion is given using a continuous-time formalism. After this discussion (and throughout the remainder of this thesis), we switch to a discrete-time formulation to introduce the MIMO FBMC-OQAM system model as it better represents how it is implemented in practice. More details are given on efficient FBMC-OQAM implementations and algorithms for channel equalization and estimation.

In the second section, the communication systems studied in this thesis are explained, including a discussion on the advantages of using FBMC-OQAM for each system and the related challenges.

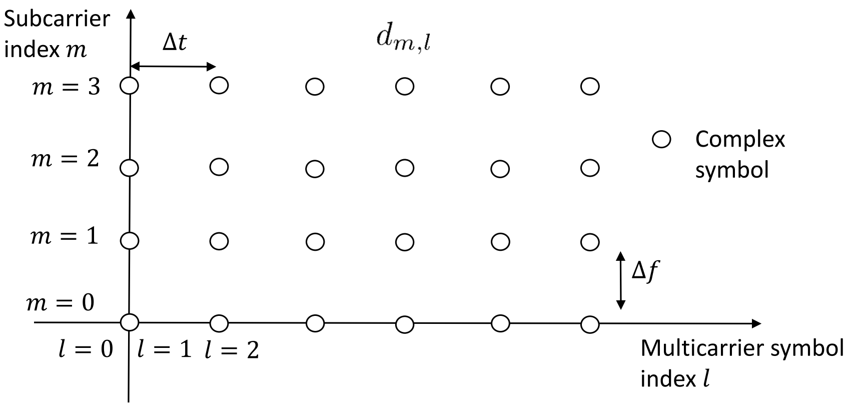

Figure 2.1 QAM time-frequency lattice.

2.1 FBMC-OQAM modulation

2.1.1 Limitations of QAM-based multicarrier systems

Let us first consider a conventional QAM-based multicarrier system. In such systems, the information symbols are first mapped to complex QAM symbols $d_{m,l}$, where m denotes the subcarrier index and l the multicarrier symbol index. The number of subcarriers is denoted by $2M$ and we denote the subcarrier spacing by Δf, expressed in [Hz] and the symbol spacing in time by Δt, expressed in [s]. Such a QAM time-frequency lattice is shown in Fig. 2.1. The transmit signal, denoted by $s_{\mathrm{QAM}}(t)$, is obtained by filtering of the symbols $d_{m,l}$ by a pulse shape $g(t)$ translated around multicarrier symbol l and modulated in frequency around subcarrier m, *i.e.*,

$$s_{\mathrm{QAM}}(t) = \sum_{m=0}^{2M-1} \sum_{l=0}^{+\infty} d_{m,l} g_{m,l}(t),$$

where $g_{m,l}(t) = g(t - l\Delta t)e^{\jmath 2\pi m \Delta f t}$. An important metric directly related to the system throughput is called the lattice density that we denote by δ_{TF}. It measures how many symbols are transmitted per unit of time and frequency and is given for the lattice in Fig. 2.1 by $\delta_{\mathrm{TF}} = \frac{1}{\Delta t \Delta f}$, expressed in complex symbol/s/Hz.

The limitations that we mentioned about such systems are related to the so-called Balian-Low theorem [17, 18].

Theorem 1. *Suppose $g(t)$ is a square-integrable function on the real line, and consider the so-called Gabor system*

$$g_{m,l}(t) = g(t - l\Delta t)e^{\jmath 2\pi m \Delta f t} \quad m, l \in \mathbb{Z}.$$

If $\delta_{\mathrm{TF}} = \Delta t \Delta f = 1$ and if $\{g_{m,l},\ m, l \in \mathbb{Z}\}$ is an orthonormal basis for the Hilbert space $L^2(\mathbb{R})$, then either

$$\left(\int_{-\infty}^{+\infty} t^2 |g(t)|^2 dt\right)\left(\int_{-\infty}^{+\infty} \omega^2 |G(\omega)|^2 d\omega\right) = \infty,$$

where $G(\omega)$ is the Fourier transform of $g(t)$.

In other words, the theorem states that is not possible to have a QAM-based multicarrier system that achieves at the same time the three following desirable properties:

1. A critically sampled lattice implying maximal spectral efficiency, *i.e.*, $\delta_{\mathrm{TF}} = 1$ complex symbol/s/Hz.

2. Orthogonality in the complex domain, *i.e.*,

$$\int_{-\infty}^{+\infty} g_{m,l}(t) g^*_{m_0,l_0}(t) dt = \delta_{m-m_0, l-l_0},$$

implying easy demodulation at the receiver as (in the ideal case where the received signal is equal to the transmit one)

$$\int_{-\infty}^{+\infty} s_{\mathrm{QAM}}(t) g^*_{m_0,l_0}(t) dt = d_{m,l}.$$

Table 2.1 Properties of various multicarrier modulation schemes

	Orthogonality	Maximal symbol density	Time-frequency localization
OFDM (no CP)	yes (ideal channel)	yes	no
CP-OFDM	yes	no	no
FMT	yes	no	yes
GFDM	no	no	yes
Filtered OFDM	depends	no	yes
FBMC-OQAM	real domain	yes	yes

3. Well localized prototype filter in time and frequency domains,

$$\left(\int_{-\infty}^{+\infty} t^2|g(t)|^2 dt\right)\left(\int_{-\infty}^{+\infty} \omega^2|G(\omega)|^2 d\omega\right) < \gamma,$$

for some constant γ, implying high flexibility for time-frequency resource allocation and high robustness to time and frequency selectivity of the channel.

In the end, one should choose which property to give up. In the following, we describe a few QAM-based multicarrier systems and specify which properties they satisfy, which are also summarized in Table 2.1.

Orthogonal frequency division multiplexing

For instance, the most well-known multicarrier modulation nowadays, OFDM, achieves complex orthogonality by using a rectangular pulse in time, which corresponds to a cardinal sine in frequency with very slowly decaying lobes, as can be seen in Fig. 2.3. This bad frequency localization has several consequences:

- A simple OFDM system would be very sensitive to channel frequency selectivity. To compensate for this effect, CP-OFDM systems are preferred. The principle of CP-OFDM is to add a CP at the beginning of each multicarrier symbol. If the CP is longer than the delay spread of the channel, it allows for easy channel equalization at the receiver [5]. However, the CP does not carry useful information and reduces

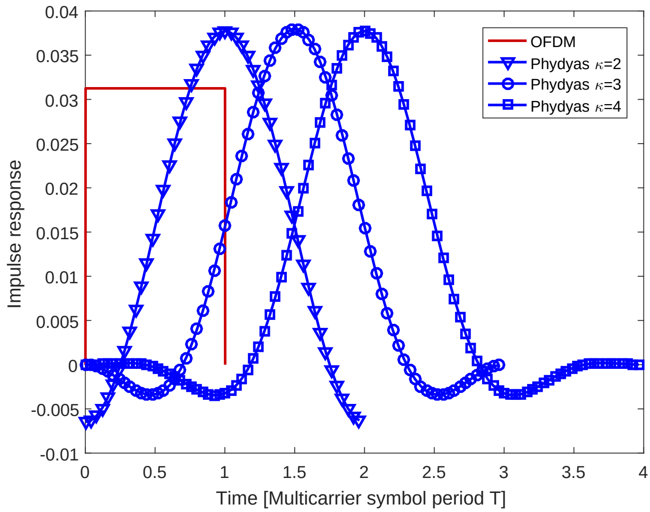

Figure 2.2 Time domain comparison of the prototype pulses of OFDM and FBMC-OQAM (Phydyas pulse [6]).

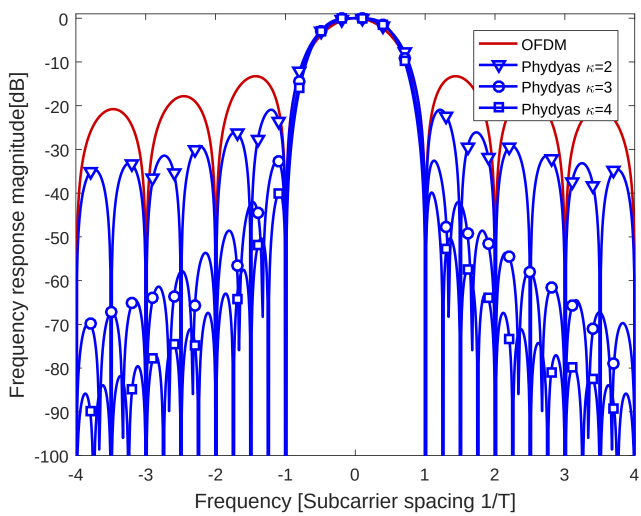

Figure 2.3 Frequency domain comparison of the prototype pulses of OFDM and FBMC-OQAM (Phydyas pulse [6]).

the system throughput. In fact, a CP-OFDM is not critically sampled because the multicarrier symbols are spaced further apart in time, *i.e.*, $\Delta f = 1/T$ and $\Delta t = T + T_{\text{CP}}$ leading to a density of $\delta_{\text{TF}} = \frac{1}{(T+T_{\text{CP}})\frac{1}{T}} < 1$.

- It induces high out-of-band emission. A CP-OFDM system requires very large guard bands at the edges of the spectrum to respect emission masks, resulting in a waste of the frequency resources.

- The system is not suited for asynchronous transmission of multiple users closely spaced in frequency.

These limitations are very detrimental for 5G scenarios where the modulation format should at the same time be highly flexible and achieve high spectral efficiency. In this sense, a good time-frequency localization of the pulse would be very desirable. This has motivated research for new waveforms that would better fit the 5G requirements. Actually, the research regarding waveform design has a long history and dates back to the sixties. This area of research has regained a lot of attention recently and a very large number of new waveforms has flourished, each one having its own specificity. For a review of the literature on orthogonal communication waveforms, we refer the interested reader to [19, Chap. 7]. A comprehensive survey on multicarrier modulations is proposed in [20], including modulations that are not constrained to be orthogonal. In the following we briefly describe some of the main ones.

Filtered multitone

The aim of the filtered multitone (FMT) modulation is to design a system, simultaneously achieving complex orthogonality and good time-frequency localization at the price of a lower spectral efficiency [21]. Several system designs exist. Usually, the subcarrier spacing is increased to space the subcarrier further apart and the prototype filter is designed to be highly frequency selective to avoid overlapping of adjacent subchannels. This generally results in an increased filter length in the time domain and hence an increased latency.

Generalized frequency division multiplexing

The generalized frequency division multiplexing (GFDM) modulation [22, 23] is a non-orthogonal scheme where the transmit signal is divided into multiple blocks. Each block is obtained by cyclic convolution of the QAM symbols with a well localized filter. It additionally uses a cyclic prefix to combat channel frequency selectivity. At the receiver side, successive interference cancellation is required to remove the interference between symbols [24].

Filtered OFDM

FMT and GFDM modulations provide an improved spectrum localization by using a finer filtering process at the sucbarrier level. However, this is often not required since resource allocation and adaptive coding and modulation schemes are commonly applied with a group of subcarriers or physical resource block [19, Chap. 7]. Many schemes have been proposed recently, aiming at performing an improved filtering process at the resource block level, namely, universal filtered multicarrier (UFMC) [25], resource block filtered-OFDM (RB-F-OFDM) [26] and filtered-OFDM (F-OFDM) [27]. This type of systems maintains a high compatibility with current OFDM systems, including simple channel equalization and straightforward application of OFDM multiple-antenna techniques. However, the additional filtering operations to suppress out-of-band emissions usually destroy the system orthogonality, especially for edge subcarriers, meaning that a trade-off should be made between implementation complexity, in-band interference and the guard band size between physical resource blocks.

2.1.2 Advantages of OQAM-based multicarrier systems

One could wonder if it is possible to circumvent the Balian-Low theorem to be able to simultaneously achieve a well localized pulse in time and frequency domains, orthogonality and critical lattice density. The answer

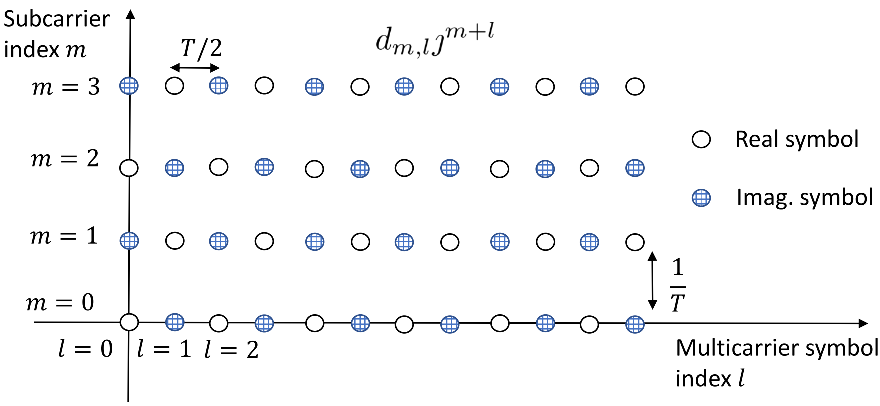

Figure 2.4 OQAM time-frequency lattice.

to this question is actually yes, it is possible and it is achieved by the FBMC-OQAM modulation, which was first proposed in the mid 1960s by Chang [28] and Saltzberg [29]. The basic principle of the FBMC-OQAM modulation is to use an OQAM lattice instead of the conventional QAM lattice. Such a lattice is represented in Fig. 2.4. The parameter T is defined as the multicarrier symbol period. In comparison with the QAM lattice of Fig. 2.1, one can make several comments:

- The purely real transmitted symbols $d_{m,l}$ are affected by a phase factor $\jmath^{m+l}$, making them alternatively purely real and imaginary[1]. For a QAM-based lattice, all symbols are complex. Secondly, the time and frequency spacing between symbols is $T/2$ and $1/T$ respectively, implying that the OQAM symbols are more closely spaced in time[2].

- The OQAM lattice density is $\delta_{\mathrm{TF}} = \frac{2}{T\frac{1}{T}} = 2$ real symbol/s/Hz. Since one complex symbol carries the same information as two real symbols,

[1]One could actually use a different OQAM phase factor than $\jmath^{m+l}$. Defining a arbitrary phase factor $e^{\jmath\theta_{m,l}}$, $\theta_{m,l}$ has just to be equal to $(\pi/2)(m+l) \mod \pi$ [30].

[2]There actually exists different OQAM lattice structure than the one detailed above, which is used in this thesis and in most of the FBMC-OQAM literature. The interested reader is referred to the review paper [20] for more details.

it achieves an equivalent density of one complex symbol/s/Hz and the system is said to be critically sampled.

The transmit signal for an FBMC-OQAM system is given by

$$s(t) = \sum_{m=0}^{2M-1} \sum_{l=0}^{+\infty} d_{m,l} p_{m,l}(t),$$

where the symbols $d_{m,l}$ are purely real and $p_{m,l}(t)$ is now defined as

$$p_{m,l}(t) = \jmath^{m+l} p(t - lT/2) e^{\jmath 2\pi m f \frac{t}{T}}.$$

Since the symbols $d_{m,l}$ are purely real, the orthogonality has to be only constrained in the real domain, *i.e.*,

$$\Re\left(\int_{-\infty}^{+\infty} p_{m,l}(t) p^*_{m_0,l_0}(t) dt\right) = \delta_{m-m_0,l-l_0}.$$

This relaxed orthogonality condition is what allows to circumvent the limitations imposed by the Balian-Low theorem. As shown in Fig. 2.2 and Fig. 2.3, FBMC-OQAM uses a filter which is more spread out in the time domain (of length κT where κ is the so-called overlapping factor), which results in a much better frequency localization and provides significant advantages:

- No CP is required to simplify the equalization process, leading to a larger spectral efficiency than CP-OFDM systems.

- Very small guard bands (of the order of one subcarrier) at the edges of the spectrum are sufficient to meet frequency emission masks.

- It provides high flexibility for spectrum allocation with clear applications such as cognitive radios or asynchronous transmission from multiple users who can be easily separated in the frequency domain.

The previous discussion motivates the choice made in this thesis to focus on the study of the FBMC-OQAM modulation as it is for us the most promising waveform candidate.

The advantages of FBMC-OQAM come at the expense of an increase in the system implementation complexity. More specifically, this modulation generates a particular interference pattern, which can easily be taken care of if the channel is mildly frequency selective and slowly changing over time but requires additional signal processing in more complex propagation environments. More details about this will be given in Section 2.1.5 and further in the thesis. Moreover, most of the MIMO algorithms originally devised for spatial multiplexing CP-OFDM systems can be straightforwardly applied to FBMC-OQAM systems if the channel is sufficiently slowly varying in time and frequency. However, the case of highly selective channels or the use of space time codes requires additional signal processing and results in more complex designs. For instance, the conventional Alamoutti scheme cannot be straightforwardly applied to MIMO FBMC-OQAM systems [11–13]. Furthermore, one should note that, to achieve higher spectral selectivity, the prototype pulse needs to be more spread out in the time domain, which induces more latency and might be detrimental for short burst transmissions. Many pre-loading techniques and tail shortening algorithms were designed to limit this effect [8, 14–16].

2.1.3 Discrete-time MIMO FBMC-OQAM transmission model

Let us consider the baseband equivalent of a MIMO FBMC-OQAM transmission chain, as depicted in Fig. 2.5. For a reminder on the notations and the definitions of the symbols used in this thesis, the reader is referred to the nomenclature section at the beginning ot this thesis.

The number of transmitted and received signals are denoted by N_T and N_R respectively. As will be further explained in Section 2.2, N_T and N_R might refer to the number of transmit and receive antennas in a wireless context or the number of transmitted streams in an optical

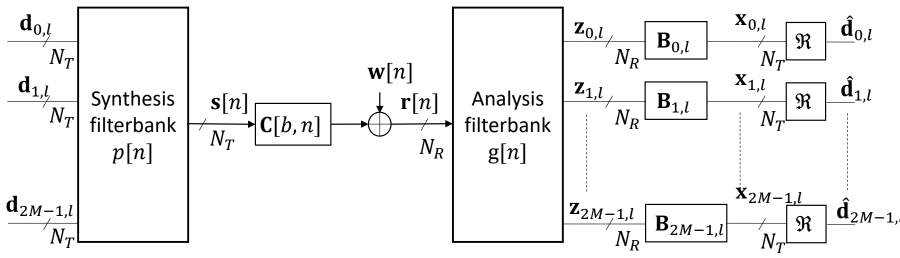

Figure 2.5 Baseband equivalent of a conventional MIMO FBMC-OQAM transmission chain.

fiber context. The symbols $\mathbf{d}_{m,l} \in \mathbb{R}^{S\times 1}$ denote the purely real symbols transmitted at subcarrier m and multicarrier symbol l and S denotes the number of spatial streams. In this section, we do not consider a pre-equalization or precoding scheme on the symbols $\mathbf{d}_{m,l}$ and S is set to N_T. However, depending on the scenarios considered in this thesis, other choices will be studied as well, as detailed more in depth in Section 2.2.

We consider the transmission of $2N_s$ multicarrier symbols. The transmit and receive prototype filters have an energy normalized to one. We make the classical assumption that the real-valued symbols $\mathbf{d}_{m,l}$ are independent, identically distributed bounded random variables with zero mean and variance[3] $E_s/2$. From now on, we switch to a discrete-time formulation since it better represents how the systems are implemented in practice. Throughout this thesis, the indexes l and n are time indexes that refer to the multicarrier symbol and sampling period of interest. The sampling period is given by $T_s = \frac{T}{2M}$. We define $\tilde{N}_s = \frac{2N_s+2\kappa-1}{2}$ so that the frame transmission duration is equal to $\tilde{N}_s T$, taking into account the tails of the frame. The transmitted signal is obtained after filtering of the OQAM symbols by the synthesis filterbank (SFB). More details on efficient implementations of the SFB and analysis filterbank (AFB) at the receiver will be given in Section 2.1.4.

[3]The factor $E_s/2$ comes from the fact that we consider the variance of the real PAM symbol so that one full complex symbol has a variance of E_s.

The discrete baseband equivalent of the transmitted signal, denoted by $\mathbf{s}[n] \in \mathbb{C}^{N_T \times 1}$, is given by

$$\begin{aligned} \mathbf{s}[n] &= \sum_{m=0}^{2M-1} \sum_{l=0}^{2N_s-1} \mathbf{d}_{m,l} \jmath^{m+l} p[n - lM] e^{\jmath \frac{2\pi}{2M} m (n - \frac{2M\kappa - 1}{2})} \\ &= \sum_{m=0}^{2M-1} \sum_{l=0}^{2N_s-1} \mathbf{d}_{m,l} p_{m,l}[n], \end{aligned} \tag{2.1}$$

where $n = 0, ..., 2M\tilde{N}_s - 1$ and $p_{m,l}[n] = \jmath^{m+l} p[n - lM] e^{\jmath \frac{2\pi}{2M} m (n - \frac{2M\kappa - 1}{2})}$. The pulse $p[n]$, defined for $n = 0, \ldots, 2M\kappa - 1$ is the so-called prototype filter at transmit side, which length is set to $2M\kappa$ with $\kappa > 1$ being the overlapping factor. One can note that, since the pulse length is longer than M, the symbols overlap in time. Furthermore, the delay of $\frac{2M\kappa - 1}{2} \frac{T}{2M}$ seconds is introduced for causality issues.

Ideal channel: Let us for now assume that the channel is ideal such that the received signal is equal to the transmitted signal, *i.e.*, $\mathbf{r}[n] = \mathbf{s}[n]$. We denote the receive prototype pulse by $g[n]$, defined for $n = 0, \ldots, 2M\kappa - 1$ and of length $2M\kappa$. As shown in [31], it might be interesting to choose a receive prototype filter different from the transmit one if the channel is not ideal. The samples $\mathbf{y}_{m_0,l_0} \in \mathbb{C}^{N_T \times 1}$ are defined as the complex demodulated symbols at subcarrier m_0 and multicarrier symbol l_0, if the symbols $\mathbf{d}_{m,l}$ are FBMC-OQAM modulated using a prototype pulse $p[n]$, demodulated using a prototype pulse $g[n]$ and for an ideal channel,

$$\mathbf{y}_{m_0,l_0} = \sum_{l=0}^{2N_s-1} \sum_{m=0}^{2M-1} \mathbf{d}_{m,l} \sum_{n=0}^{2M\tilde{N}_s-1} p_{m,l}[n] g^*_{m_0,l_0}[n], \tag{2.2}$$

where $g_{m,l}[n] = \jmath^{l+m} g[n - lM] e^{\jmath \frac{2\pi}{2M} m (n - \frac{2M\kappa - 1}{2})}$. In other words, the samples $\mathbf{y}_{m_0,l_0}$ would be the output of a SFB and an AFB placed back-to-back. Moreover, if the pulses $p[n]$ and $g[n]$ are designed to be bi-orthogonal

[31], meaning that they respect the so-called perfect reconstruction (PR) conditions, one will have

$$\Re\left\{\sum_{n=0}^{2M\tilde{N}_s-1} p_{m,l}[n]g^*_{m_0,l_0}[n]\right\} = \delta_{m-m_0,l-l_0}. \tag{2.3}$$

These conditions impose the orthogonality to be satisfied only in the real plane as opposed to QAM multicarrier modulations that require complex orthogonality and are limited by the Balian-Low theorem. For convenience, we define the so-called transmultiplexer response as

$$t_{m,m_0,l,l_0} = \sum_{n=0}^{2M\tilde{N}_s-1} p_{m,l}[n]g^*_{m_0,l_0}[n].$$

The PR conditions can rewritten more compactly as $\Re\{t_{m,m_0,l,l_0}\} = \delta_{m-m_0,l-l_0}$. If the PR conditions are met and in ideal propagation conditions, the vector $\mathbf{y}_{m_0,l_0}$ can be rewritten as

$$\mathbf{y}_{m_0,l_0} = \mathbf{d}_{m_0,l_0} + \jmath\mathbf{u}_{m_0,l_0},$$

with the following definition of $\mathbf{u}_{m_0,l_0}$

$$\mathbf{u}_{m_0,l_0} = \Im\left(\sum_{(m,l)\neq(m_0,l_0)} \mathbf{d}_{m,l}t_{m,m_0,l,l_0}\right).$$

The vector of symbols $\mathbf{u}_{m_0,l_0} \in \mathbb{R}^{N_T\times 1}$ is commonly referred to as the intrinsic interference [32, 33] and is composed of the purely imaginary contributions of the neighboring symbols. Table 2.2 shows the transmultiplexer response for the Phydyas filter ($\kappa = 4$) [6], *i.e.*, the contributions from neighboring symbols. Under the PR conditions, the transmitted symbols can be simply recovered by taking the real part, *i.e.*, $\mathbf{d}_{m_0,l_0} = \Re(\mathbf{y}_{m_0,l_0})$. The real conversion removes the purely imaginary intrinsic interference which affects the demodulated symbols. In prac-

Table 2.2 Transmultiplexer response - Phydyas filter ($\kappa = 4$)

t_{m,m_0,l,l_0}	l_0-4	l_0-3	l_0-2	l_0-1	l_0	l_0+1	l_0+2	l_0+3	l_0+4
m_0-1	$0.0054\jmath$	$-0.0429\jmath$	$-0.1250\jmath$	$0.2058\jmath$	$0.2393\jmath$	$-0.2058\jmath$	$-0.1250\jmath$	$0.0429\jmath$	$0.0054\jmath$
m_0	0	$-0.0668\jmath$	0.0002	$0.5644\jmath$	1	$0.5644\jmath$	0.0002	$-0.0668\jmath$	0
m_0+1	$0.0054\jmath$	$0.0429\jmath$	$-0.1250\jmath$	$-0.2058\jmath$	$0.2393\jmath$	$0.2058\jmath$	$-0.1250\jmath$	$-0.0429\jmath$	$0.0054\jmath$

tice, the transmission channel inevitably induces distortion. Therefore, to strictly respect the PR conditions is not essential and it is sufficient to guarantee that the cross-talk between subchannels is low enough relatively to residual interference. This means that the near perfect reconstruction (NPR) designs are sufficient and can be more efficient that PR designs by providing for instance a higher frequency selectivity of the prototype filter. Following this idea, the Phydyas NPR filter [6] will be used throughout this thesis. This is the origin of the non zero purely real terms in Table 2.2, which will not be removed after real conversion but are negligible in practice.

Time and frequency selective channel: We now consider the effect of a channel. In this thesis, we define the term "channel" in a general sense as the transfer function between the discrete baseband samples at the transmitter $\mathbf{s}[n]$ and the received baseband discrete samples at the receiver $\mathbf{r}[n]$. This definition includes not only the propagation channel but also the digital-to-analog and analog-to-digital conversions, the frequency up- and down-conversions, *etc*. We consider a linear channel model since we are mostly concerned by the effects of linear channel impairments. We denote by $\mathbf{C}[b,n] \in \mathbb{C}^{N_R \times N_T}$ the time-variant channel impulse response at time instant n and corresponding to delay b. This model allows to consider many different effects such as multipath fading, Doppler effect, CFO, STO, *etc*. The different types of channels that we considered in this thesis will be further developed in Section 2.2, depending on the considered communication system. Furthermore, the different chapters of this thesis address specific scenarios. The corresponding assumptions will be clearly detailed in each chapter. The received signal, denoted by $\mathbf{r}[n] \in \mathbb{C}^{N_R \times 1}$, is given by

$$\mathbf{r}[n] = \sum_{b=-\infty}^{+\infty} \mathbf{C}[b,n]\mathbf{s}[n-b] + \mathbf{w}[n], \tag{2.4}$$

where $\mathbf{w}[n] \in \mathbb{C}^{N_R \times 1}$ is made of additive noise samples, assumed to follow a circularly-symmetric white Gaussian distribution, with zero mean and variance N_0. The received signal is processed by the AFB using prototype pulse $g[n]$. The signal after demodulation, at subcarrier m_0 and multicarrier symbol l_0, denoted by $\mathbf{z}_{m_0,l_0} \in \mathbb{C}^{N_R \times 1}$, may be written as

$$\begin{aligned} \mathbf{z}_{m_0,l_0} &= \sum_{n=0}^{2M\tilde{N}_s-1} \mathbf{r}[n] g^*_{m_0,l_0}[n] + \mathbf{w}_{m_0,l_0} \\ &= \sum_{l=0}^{2N_s-1} \sum_{m=0}^{2M-1} \sum_{n=0}^{2M\tilde{N}_s-1} \sum_{b=-\infty}^{+\infty} \mathbf{C}[b,n]\mathbf{d}_{m,l} p_{m,l}[n-b] g^*_{m_0,l_0}[n] + \mathbf{w}_{m_0,l_0}, \end{aligned} \tag{2.5}$$

where $\mathbf{w}_{m_0,l_0}$ are the filtered noise samples. As it can be seen, the effect of the channel $\mathbf{C}[b,n]$ on $\mathbf{z}_{m_0,l_0}$ is a mixed function of the transmitted data, channel and pulses. Approximations can be used to simplify the expression of $\mathbf{z}_{m_0,l_0}$. In Section 2.1.5 reviewing channel equalization, we describe the conventional approximation made in most of the FBMC-OQAM literature, its underlying assumptions and its limitations. In the following of the thesis, we will propose several improved approximations.

2.1.4 Efficient implementation of the SFB and AFB

Implementing the SFB and the AFB by computing the double sums in (2.1) and (2.5) would be prohibitive in terms of complexity. Fortunately, it is possible to use much more efficient implementations. The most conventional implementation of the SFB (resp. AFB) relies on the combination of a polyphase network (PPN) and an inverse fast Fourier

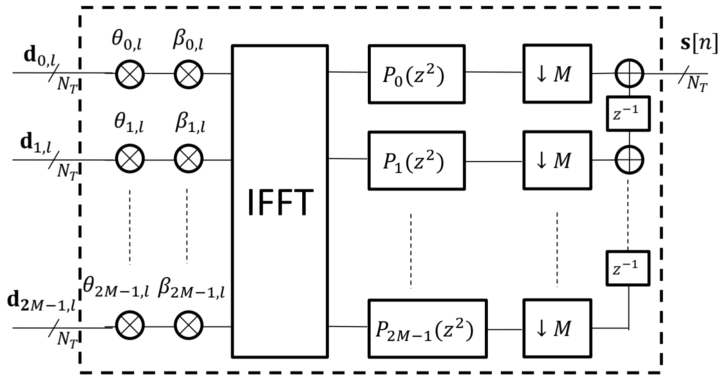

Figure 2.6 Efficient implementation of the SFB based on a polyphase network and an IFFT where $\theta_{m,l} = \jmath^{m+l}$, $\beta_{m,l} = e^{-\jmath \frac{2\pi}{2M} m \frac{2M\kappa-1}{2}}$ and $P_m(z^2)$ is the two times upsampled m-th polyphase component of the prototype filter $p[n]$.

transform (IFFT) (resp. FFT) [30, 34], as shown in Fig. 2.6 and 2.7. More details on the design and implementation of FBMC-OQAM systems are available in [35]. In particular, Section 8.3 of [35] details new realization structures with emphasis on the Fast-Convolution FilterBank (FC-FB), which provides an efficient implementation for realizing highly tunable multirate filterbank configurations [36, 37]. In this thesis, the conventional PPN implementation of FBMC-OQAM was used except for one work in Chapter 8 which uses the frequency-spreading-FBMC (FS-FBMC) [38, 39]. FS-FBMC can be seen as a special case of the FC-FB and will be detailed more in depth in Section 2.1.5.2.

2.1.5 Channel equalization

2.1.5.1 Conventional approximation of the demodulated symbols for mildly selective channels

Commonly, in most of the FBMC-OQAM literature [40], the channel is assumed to remain constant over the transmit and receive pulse dura-

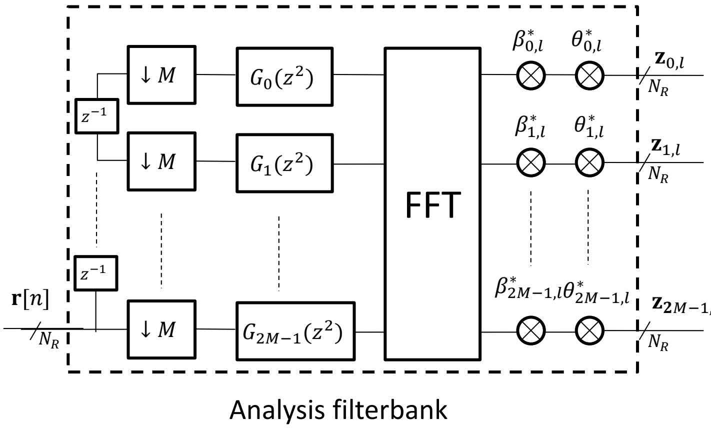

Figure 2.7 Efficient implementation of the AFB based on a polyphase network and an FFT where $\theta_{m,l} = \jmath^{m+l}$, $\beta_{m,l} = e^{-\jmath \frac{2\pi}{2M} m \frac{2M\kappa-1}{2}}$ and $G_m(z^2)$ is the two times upsampled m-th polyphase component of the prototype filter $g[n]$.

tions. Furthermore, the channel is typically assumed to be frequency flat at the subcarrier level. Under these conditions and if the pulses $p[n]$ and $g[n]$ are well localized in time and frequency, an approximation of $\mathbf{z}_{m_0,l_0}$, defined in (2.5), is given by

$$\mathbf{z}_{m_0,l_0} \approx \mathbf{H}_{m_0,l_0} \sum_{l=0}^{2N_s-1} \sum_{m=0}^{2M-1} \mathbf{d}_{m,l} \sum_{n=0}^{2M\tilde{N}_s-1} p_{m,l}[n] g^*_{m_0,l_0}[n] + \mathbf{w}_{m_0,l_0}, \quad (2.6)$$

where $\mathbf{H}_{m_0,l_0} = \sum_{b=-\infty}^{+\infty} \mathbf{C}[b, l_0 M + \frac{2M\kappa-1}{2}] e^{-\jmath \frac{2\pi}{2M} b m_0}$ is the time varying channel frequency response evaluated at the subcarrier and multicarrier symbol of interest. Throughout this thesis, we will refer to this approximation as a 0-th order approximation of $\mathbf{z}_{m_0,l_0}$. Using the definition of $\mathbf{y}_{m_0,l_0}$ in (2.2), the approximation (2.6) can be rewritten more compactly as

$$\mathbf{z}_{m_0,l_0} \approx \mathbf{H}_{m_0,l_0} \mathbf{y}_{m_0,l_0} + \mathbf{w}_{m_0,l_0}. \quad (2.7)$$

The accuracy of the 0-th order approximation critically depends on the channel variations in the time and frequency domains. As the channel

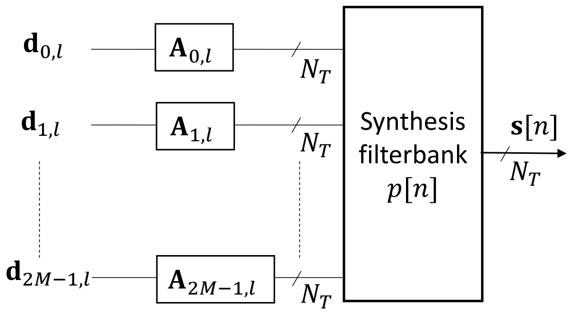

Figure 2.8 MIMO FBMC-OQAM system with pre-equalization.

gets more time and/or frequency selective, the approximation will deteriorate. Classically, as shown in Fig. 2.5, a per-subcarrier single-tap equalizer $\mathbf{B}_{m_0,l_0} \in \mathbb{C}^{S\times N_R}$ is applied, giving

$$\begin{aligned}\mathbf{x}_{m_0,l_0} &= \mathbf{B}_{m_0,l_0}\mathbf{z}_{m_0,l_0} + \mathbf{B}_{m_0,l_0}\mathbf{w}_{m_0,l_0} \\ &\approx \mathbf{B}_{m_0,l_0}\mathbf{H}_{m_0,l_0}\mathbf{y}_{m_0,l_0} + \mathbf{B}_{m_0,l_0}\mathbf{w}_{m_0,l_0}\end{aligned}$$

and the transmitted symbols $\mathbf{d}_{m_0,l_0}$ are estimated by taking the real part of $\mathbf{x}_{m_0,l_0}$, *i.e.*, $\hat{\mathbf{d}}_{m_0,l_0} = \Re(\mathbf{x}_{m_0,l_0})$. If $\mathbf{B}_{m_0,l_0}\mathbf{H}_{m_0,l_0} \approx \mathbf{I}_{N_T}$, if the channel is not too selective and if the additive noise power is not too large, one can expect to get $\hat{\mathbf{d}}_{m_0,l_0}$ close to $\mathbf{d}_{m_0,l_0}$.

There exist different criteria to design the single-tap equalization matrices $\mathbf{B}_{m_0,l_0}$. Most conventional designs are the LMMSE, ZF and MF equalizers, which rely on the general assumption that the channel is mildly selective in time and frequency (meaning that the approximation in (2.7) is made). The performance and design of the single equalizer $\mathbf{B}_{m_0,l_0}$ under multiple criteria will be studied in depth in Chapters 3, 4 and 6.

An alternative to compensate for the channel impairments is to use pre-equalization at the transmitter side. These algorithms usually require the receiver to feedback its channel estimate to make it available to the transmitter. Fig. 2.8 shows the block diagram of a MIMO FBMC-OQAM system with single-tap pre-equalization being performed on a subcarrier level. If we denote by $\mathbf{A}_{m,l} \in \mathbb{C}^{S\times N_T}$ the single-tap pre-equalizer at subcarrier m and multicarrier symbol l, the precoded signal can be rewritten as

$$\mathbf{s}[n] = \sum_{m=0}^{2M-1} \sum_{l=0}^{2N_s-1} \mathbf{A}_{m,l}\mathbf{d}_{m,l}p_{m,l}[n], \tag{2.8}$$

where we see that the symbols $\mathbf{d}_{m,l}$ are linearly precoded by matrix $\mathbf{A}_{m,l}$, prior to entering the SFB.

The main limitations of equalization by a single-tap equalizer $\mathbf{B}_{m,l}$ and/or pre-equalizer $\mathbf{A}_{m,l}$ is the sensitivity to channel variations in time and frequency. As soon as the channel becomes too selective in frequency and/or in time, the approximation in (2.7) becomes inaccurate and the equalization performance degrades due to the presence of distortion. This distortion is mainly composed of ICI, ISI and IUI. In these situations, more advanced equalization techniques are necessary to compensate for the channel impairments. We give below a review of the main equalization algorithms for frequency selective and doubly selective channels.

2.1.5.2 Frequency selective channels

Many works in the literature make the assumption of a quasi-static channel, which means that the channel is assumed not to change over the transmitted frame duration. When such assumption is made in this thesis (as in Chapter 3 and 4), we omit the l subscript in the notation of the equalizer, the pre-equalizer and the channel frequency response to emphasize that it does not vary over time, *i.e.*, $\mathbf{B}_{m,l} = \mathbf{B}_m$, $\mathbf{A}_{m,l} = \mathbf{A}_m$ and $\mathbf{H}_{m,l} = \mathbf{H}_m$. Similarly, the time-variant channel impulse response $\mathbf{C}[b,n]$ will be rewritten as $\mathbf{C}[b]$ and referred to as the time-invariant channel impulse response.

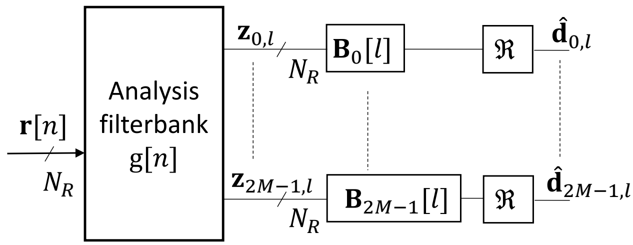

Figure 2.9 Multi-tap fractionally spaced per-subcarrier equalizer.

Multi-tap fractionally spaced per-subcarrier equalizer: one of the most common approach to compensate for the channel frequency selectivity is to use so-called multi-tap equalizers. This type of equalizer was first proposed in the SISO case [41–43] and later on in the MIMO case [44]. As shown in Fig. 2.9, the idea is simple: rather than using a single-tap (pre-)equalizer as previously detailed, a multi-tap filter is used which combine successive time samples at the AFB output of the subcarrier of interest. Even if the outputs of the adjacent subcarriers are not used, the fractional spacing $T/2$ of the equalizer allows for efficient mitigation of ISI and ICI, provided that the roll-off factor of the pulse is smaller than or equal to one, as it is commonly the case in FBMC-OQAM systems [6]. The estimated symbols at the receiver can be written as

$$\hat{\mathbf{d}}_{m_0,l_0} = \Re\left(\sum_{l=0}^{N_{\text{taps}}-1} \mathbf{B}_{m_0}[l]\mathbf{z}_{m_0,l_0-l+\zeta}\right), \tag{2.9}$$

where ζ is introduced in order to take into account the filtering delay and N_{taps} is the number of taps of the equalizer. Note that the equalizer adds a delay of $(N_{\text{taps}}-1)T/2$ seconds to the demodulation process. There are two main ways of computing the coefficients of the equalizer $\mathbf{B}_{m_0}[l]$. The MMSE equalizer [41], [43] optimizes the coefficients in order to minimize the MSE of the symbol estimate. This requires to evaluate, for each subcarrier, the equivalent channel made up of the convolution of the transmit filters, the channel and the receive filters, taking into account the interference of the two adjacent subcarriers. On the other hand, the principle of the frequency sampling technique is to choose certain values for the equalizer coefficients so that the equalizer frequency response is forced to pass through some target frequency points in the subchannel of interest [41], [42]. The target frequency points are chosen according to a ZF or MMSE criterion. If the channel is not too selective in frequency, one can expect the equalizer response to approximate well the optimal ZF or MMSE frequency response. This design allows for a simpler computation of the equalizer coefficients.

In [45], a two stage interference cancellation equalizer is proposed to enhance the multi-tap equalizer performance while in [46], a decision feedback equalizer is proposed. Moreover, [47, 48] proposes a MIMO multi-tap filtering solution at both transmit and receive sides, meaning that pre-equalization and equalization are performed at both sides of the communication link using a multi-tap filter. Channel equalization has also been analyzed in the MU MIMO context in several works. In [49], the authors extend the block diagonalization technique to FBMC systems. Through an iterative algorithm, the work of [50] alleviates the dimensionality constraint of [49] by allowing designs where the total number of receive antennas of the users exceeds the number of transmit antennas at the base station. In [51, 52], multi-tap pre-equalizers and equalizers are iteratively and jointly designed. We refer to [11] for a recent review paper on MIMO equalization.

Parallel multi-stage equalizer: the parallel equalization structure was initially proposed in [53] in the SISO case. The work was extended for the MIMO case in [54, 55] where a parallel multi-stage processing architecture is used at both sides of the communication link. As shown in Fig. 2.10 for the case $Q = 1$, this receiver uses $Q + 1$ AFB's working in parallel on the received signal. The q-th AFB is using the q-th derivative of the prototype pulse with respect to time. The demodulated symbols

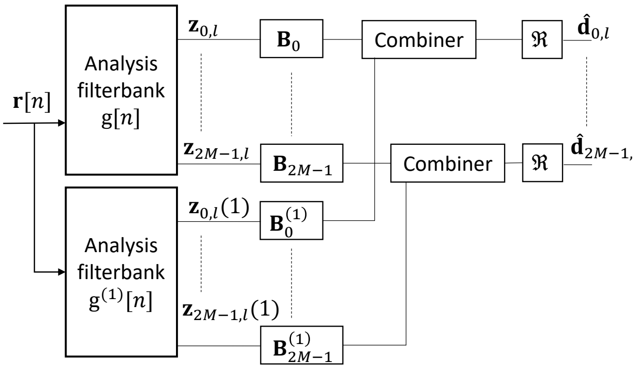

Figure 2.10 Parallel equalization at the receiver with $Q = 1$.

coming from the q-th parallel AFB, denoted by $\mathbf{z}_{m_0,l_0}(q)$, are then equalized by the q-th derivative of the equalizer with respect to frequency that we denote by $\mathbf{B}_m^{(q)}$. Finally, the outputs of each AFB are recombined in order to cancel the Q first orders of the distortion caused by the channel variations and the symbol is estimated as

$$\hat{\mathbf{d}}_{m_0,l_0} = \Re\left(\sum_{q=0}^{Q} \frac{\jmath^q}{(2M)^q} \mathbf{B}_{m_0}^{(q)} \mathbf{z}_{m_0,l_0}(q)\right). \tag{2.10}$$

Note that this processing does not require any additional delay as opposed to multi-tap equalizers. We will extend this equalization structure to the case of time selective channels in Chapter 5.

Frequency spreading receiver: several recent works have looked at an alternative scheme to implement FBMC systems, which is the so-called frequency-spreading FBMC (FS-FBMC) technique [38], [39]. It can be seen as a special case of the fast-convolution implementation of FBMC [36]. As shown in Fig. 2.11, in the FS-FBMC implementation of the receiver, an FFT of size $2M\kappa$ is first taken on the received signal. Then, the output bins of the FFT are equalized to compensate for the channel frequency selectivity before being recombined by the prototype pulse

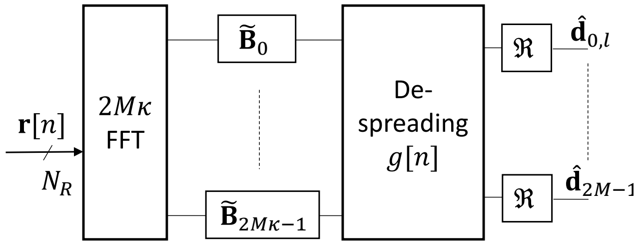

Figure 2.11 Frequency-spreading implementation of the receiver.

coefficients in the frequency domain ("de-spreading"). The complexity of FS-FBMC is larger than the classical structure relying on a PPN, due to the increased FFT size. However, the advantage of the approach comes from its simplicity of understanding and from the very efficient channel equalization being done in the frequency domain at the high resolution $1/2M\kappa$ and without additional delay.

Overlap and save algorithm: this method, widely applied in single-carrier and multi-carrier optical fiber communication systems [56], convolves the received signal before the AFB with an equalization filter. Classically, this time domain filtering operation is implemented in an efficient manner using the overlap and save algorithm. The algorithm first takes an FFT of block of size N_{FFT} on the received signal, the FFT outputs are then multiplied by the inverse of the CD frequency response and brought back to time domain by IFFT of size N_{FFT}. Finally, $K_{\mathrm{ov}}/2$ samples are discarded at the beginning and at the end of the block, which yields a block of $N_{\mathrm{FFT}} - K_{\mathrm{ov}}$ samples, assumed to be approximately free from CD. These samples are then fed to the AFB. Note that the parameters N_{FFT} and K_{ov} do not need to be related to the number of subcarriers $2M$ and that the overlap and save algorithm adds a delay of $N_{\mathrm{FFT}}T_s$ seconds to the demodulation chain.

2.1.5.3 Doubly selective channels

As detailed in Section 2.1.5.2, many works have proposed algorithms to compensate for the distortion induced by the frequency selectivity of the channel. On the contrary, the case of time selective channels, *i.e.*, the fact that the channel rapidly changes over time, has not been extensively studied in the FBMC literature. This issue is of crucial importance for the future of wireless communications. Two examples of applications are high speed trains and satellite communications. In [57–59], different multicarrier modulations schemes proposed for 5G systems, including CP-OFDM and FBMC-OQAM modulations, are compared under high speed scenarios. Their main result is that FBMC-OQAM provides more robustness to channel dispersion with respect to conventional CP-OFDM.

In [60, 61], the authors propose adaptive equalizers for doubly selective channels in MIMO FBMC-OQAM systems. The work of [62] addresses the same problem by designing a fractionally spaced per-subcarrier equalizer, taking into account the interference coming from neighboring subcarriers and adjacent symbols in time. In [63], the MSE of the received symbols for doubly selective channel is analyzed for SISO FBMC systems with classical single-tap equalization. From the channel estimation point of view, the authors in [64] propose a general framework for compressive estimation of doubly selective channels in multicarrier systems.

Other works study the effect of varying the prototype pulse shape to deal with doubly selective channels [65, 66].

2.1.6 Channel estimation

As explained in Section 2.1.3, the FBMC-OQAM modulation is impacted by intrinsic interference after demodulation. The presence of this interference complicates the channel estimation task. This has motivated numerous works. We give here below a short review of the main solutions devised in the literature. We refer the interested reader to [33, 67] for a more comprehensive review and to [68] for a recent review on the remaining challenges and solutions. The channel estimation algorithms can be divided into two main classes depending if they rely on the transmission of a preamble or scattered pilots.

Usually, the beginning of a transmitted frame is made of a known training sequence used for synchronization and channel estimation. The preamble should be properly designed to take into account the impact of intrinsic interference coming from neighboring symbols in time and frequency [33]. Commonly, the preamble section is "protected" from the unknown data symbols by guard symbols. Interference approximation methods were proposed to use the intrinsic interference as a way to improve the estimation accuracy [33, 40]. In [69], preambles are optimized under a least squares criterion and compared for CP-OFDM and FBMC-OQAM systems. In [10, 70], it is shown how a LMMSE channel estimator can be applied to FBMC-OQAM systems. Other works consider preamble-based channel estimation for highly selective channels [68, 71, 72]. The work of [10, 73] extended the study to the case of MIMO channels.

If the pilots are scattered in time and frequency, one should use a compensation method to avoid contamination of the pilot from the intrinsic interference coming from neighboring symbols. To counteract this effect, most of the existing algorithms properly fix the value of one or more neighboring symbols to ensure that the intrinsic interference at the pilot position is canceled. If only one neighboring symbol is used, this symbol is referred to as an auxiliary pilot (or help pilot) [32, 74]. Note that this scheme uses two OQAM symbols which corresponds to one complex QAM symbol. Hence, this scheme has the same overhead as the transmission of one complex pilot in an OFDM-like system. One of the drawback of the auxiliary pilot scheme is the fact that that the amplitude of the auxiliary pilot depends on the neighboring symbols and can be very high, which is detrimental regarding for instance peak-to-power average ratio. A generalization of this scheme which prevents power amplification is to use a coding scheme applied on several neighboring symbols [75, 76]. Most of the pilot-based channel estimators rely on the assumption of a channel sufficiently flat at the subcarrier level. In [77], the authors generalize the auxiliary pilot scheme to the case of highly frequency selective channels at the price of an increased pilot overhead. In [78–80], the authors extend the pilot scheme to MIMO systems.

During the writing process of this thesis, we did not include our works on channel estimation [10, 81, 82].

2.2 Communication sytems under study

The following sections detail the communications systems that are studied throughout this thesis and answer the following questions: what is the interest of using FBMC-OQAM in each case ? what are the challenges ? and what are the different scenarios that we addressed in this thesis ?

2.2.1 Wireless transceivers

The current fourth generation of wireless communication systems (4G) relies on the CP-OFDM modulation. As was explained in detail in Section 2.1, the FBMC-OQAM modulation has significant advantages compared to CP-OFDM modulations and it is now regarded as one of 5G waveform contenders. Indeed, FBMC-OQAM has a higher spectral efficiency due to the absence of CP and the low number of guard bands at the edges of the system spectrum. Furthermore, one of the main challenges investigated for future wireless communications systems is the ability to take care of the largely increasing number of devices. Allowing all devices to communicate simultaneously implies to choose a modulation format that can easily take care of the multiple access issue. The CP-OFDM requires time synchronization and a sufficiently large CP to work with multiple devices simultaneously, which will become very

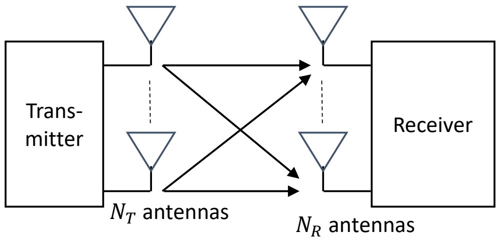

Figure 2.12 Point-to-point MIMO system.

difficult with the expected increase in the number of mobile devices as well as more complex cell infrastructures. On the other hand, thanks to the good frequency localization of its prototype pulse, FBMC-OQAM can very easily separate the users in frequency by using very small guard bands and no synchronization in time is required. In that regard, FBMC-OQAM offers much more flexibility and would much better fit the needs of future generations of wireless systems. Other applications where FBMC-OQAM is particularly useful are cognitive radios and unlicensed frequency bands where frequency resources should be shared and dynamically allocated. As explained earlier, the main disadvantages of FBMC-OQAM for wireless systems is the increased latency and the complex combination with space time codes.

The application of the FBMC-OQAM modulation to wireless systems has been extensively studied in the literature under different aspects such as channel estimation, equalization and synchronization. The related literature can be found in Section 2.1. In this thesis, Part I focuses on channel equalization for MIMO wireless systems under strong channel frequency and/or time selectivity. The different contributions are original as they propose new types of equalizers and consider scenarios not well studied in the literature. More specifically, we address three main types of MIMO scenarios, namely, PTP MIMO, MU-MIMO and massive MIMO.

In the **PTP MIMO** systems considered in Chapter 5 and 6, the antennas at the transmitter and receiver are co-localized, as shown in Fig. 2.12.

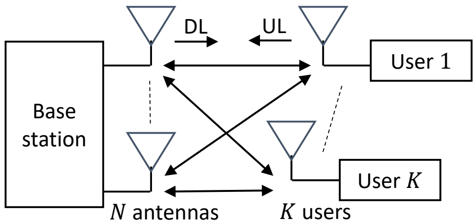

Figure 2.13 Multi-user-MIMO system.

The number of transmit and receive antennas are denoted by N_T and N_R respectively and we consider pure spatial multiplexing so that the number of spatial streams S is equal to N_T.[4]

In the **MU-MIMO** system considered in Chapter 3, we consider the presence of one BS equipped with N antennas and K single-antenna users, as shown in Fig. 2.13. The users are not able to cooperate. The users and the BS are assumed to use space division multiple access (SDMA), *i.e.*, they simultaneously communicate using the same time and frequency resources [83, Chap. 10]. Two transmission directions are considered, *i.e.*, downlink (DL) and uplink (UL). The number of spatial streams is equal to the number of users, *i.e.*, $S = K$.

The UL **massive MIMO** system considered in Chapter 4 can be seen as a MU-MIMO system where the number of BS antennas N and the number of users K grow large.

In this thesis, we consider a channel model which takes into account both the time and frequency selectivity of the channel. In most of the simulations performed in Part I, we will use the 3GPP and the ITU channel models [84] to characterize the power delay profile (PDP) of the discrete-time channel impulse response. As it is common, we neglect the inter-taps correlation that arises due to the analog filters at the transmitter and at the receiver. If the channel is considered to be time-varying, we will assume that the Doppler spectrum of each tap of the channel is characterized by a classical Jakes model.

[4]We will always assume that $N_R \geq N_T$.

2.2.2 Optical fiber transceivers

In order to satisfy the ever-increasing network capacity demand, multicarrier modulations have been recently proposed for optical fiber communication systems. Among multicarrier modulations, FBMC-OQAM is seen as a promising candidate to improve the spectral efficiency of optical fiber wavelength division multiplexing (WDM) communication systems [85–89]. As we already know, FBMC-OQAM does not require a CP while still allowing efficient channel equalization in the frequency domain. Furthermore, thanks to the very low spectral leakage of its prototype filter, it is sufficient to insert a very small guard band between unsynchronized optical lasers, which results in a higher spectral efficiency [89].

The propagation in optical fibers is characterized by various impairments [90]. In the Part II of this thesis, we will focus on the mitigation of two main linear impairments, namely, **CD** and **PN**. The presence of CD implies that the spectral components of the transmitted signal travel at different speeds in the fiber. The CD is assumed to have the following baseband frequency response

$$H\left(f\right) = e^{-\jmath \frac{\pi D \lambda^2 L}{c} f^2}, \tag{2.11}$$

where D is the dispersion coefficient [ps/nm/km], λ is the central wavelength, c is the speed of light and L is the fiber length [91]. As can be seen in (2.11), the distortion induced by CD is amplified as the fiber length and/or the system bandwidth increase. CD can actually be seen as a special case of channel frequency selectivity as it induces phase variations in the frequency domain.

On the other hand, PN does not originate from the optical fiber itself but from the phase mismatch between the lasers at the transmitter and the receiver. PN can be seen as a special case of time selectivity causing a phase rotation of the received samples. We model the PN as a Wiener

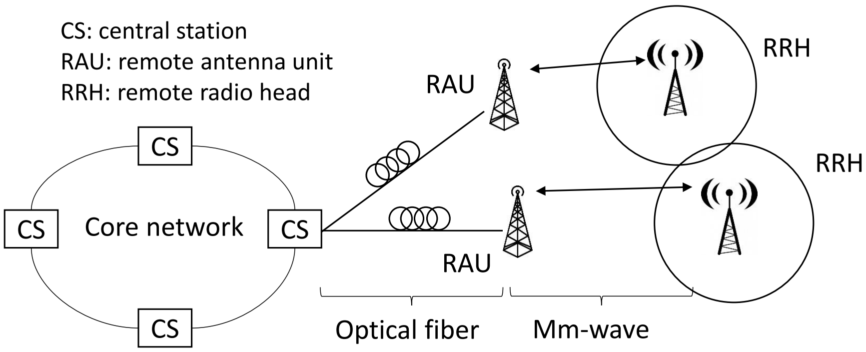

Figure 2.14 Radio-over-fiber system.

process, *i.e.*,

$$\phi[n+1] = \phi[n] + \nu[n], \tag{2.12}$$

where $\nu[n]$ is an independent real Gaussian random variable with zero mean and variance $\sigma_\nu^2 = 2\pi\Delta\nu\frac{T}{2M}$ [92]. The parameter $\Delta\nu$ refers to the combined laser linewidth. The baseband received signal, impacted by CD, PN and additive noise, can be written as

$$r\left[n\right] = \left(\int_{-1/2T_s}^{1/2T_s} S\left(f\right) H\left(f\right) e^{\jmath 2\pi f T_s n} df\right) e^{\jmath\phi[n]} + w[n], \tag{2.13}$$

where $S(f)$ is the Fourier transform of the transmitted signal. To focus on the CD and PN effects, only one polarization mode and a standard single-mode fiber (SSMF) will be considered in Part II, implying that $N_T = N_R = S = 1$.

2.2.3 Radio-over-fiber transceivers

The fifth generation of mobile communication systems is expected to offer a huge increase in the network capacity. In these networks, radio-over-fiber (RoF) systems would be very useful for mobile fronthaul deployment to simplify the access to remote antenna sites [93–95]. As shown in Fig. 2.14, the RoF system allows to connect a remote radio head (RRH) to the core network through a remote antenna unit (RAU) by the combination of an optical fiber and a radio link. The conversion from the optical domain to the electrical domain in the DL (and vice versa in the UL) at the RAU is efficiently performed in the analog domain without additional signal processing. Seamless fiber–wireless systems in high-frequency bands based on RoF technology are also very attractive for flexible and resilient broadband access networks where the use of optical fibers is not possible. RoF and fiber–wireless systems using CP-OFDM have already been studied in many works [96, 97]. However, the rectangular pulse shaping of the FFT filters induces high spectral leakage. This results in the need of large guard bands at the edges of the system band to prevent out-of-band emission. Furthermore, the CP, which is introduced in order to simplify the equalization of the channel at the receiver, induces an additional loss of spectral efficiency.

In the light of these limitations, the FBMC-OQAM modulation has been considered in some works for RoF and seamless fiber–wireless systems. The authors in [98] proposed and demonstrated a centralized pre-equalization algorithm to compensate for the channel impairments. In [99], full-duplex quasi-gapless carrier aggregation is demonstrated, taking advantage of the very high spectral containment of FBMC. In [100], a simultaneous transmission of OFDM and FBMC signals is experimentally demonstrated. In [101, 102], the authors respectively propose a 2x2 and a 4x4 MIMO FBMC-OQAM transmission over a radio-over-multicore fiber system and wireless links in the 2-GHz band.

In Chapter 10, we will report on a MIMO FBMC RoF experiment where the RAU and the RRH are equipped with a same number of antennas and using pure spatial multiplexing so that $N_T = N_R = S$.

Part I

Channel equalization for MIMO wireless systems

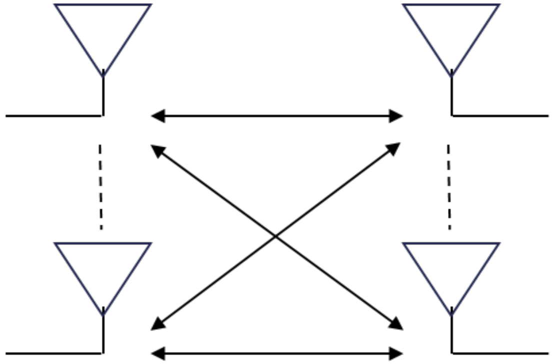

INTRODUCTION

Part I of this thesis investigates channel equalization in MIMO FBMC-OQAM wireless systems. More specifically, Part I addresses various MIMO scenarios characterized by highly frequency and/or time selective channels. The different works presented in Part I share a common approach to characterize the channel variations in the time and/or frequency domains. The chosen approach, initially introduced in [53], relies on a Taylor approximation of these variations and an asymptotic characterization of the residual approximation error.

We now give a brief example of the approach. Formal proofs will be given in the following chapters. For the sake of clarity, we consider a simple case in order to give a general intuition to the reader. Following this idea, we make a few simplifying assumptions that will not always be made in the following chapters. We first consider that the channel is only frequency selective and time-invariant, *i.e.*, $\mathbf{C}[b,n] = \mathbf{C}[b]$ (as in Chapter 3 and 4). We will assume that no pre-equalizer is used, *i.e.*, $\mathbf{A}_m = \mathbf{I}_{N_T}$ (as in Chapter 4, 5 and 6). Furthermore, a single-tap equalizer is used so that the estimated symbols are given by $\hat{\mathbf{d}}_{m,l} = \Re\left(\mathbf{B}_m \mathbf{z}_{m,l}\right)$. The single-tap equalizer is designed to perfectly invert the channel at the receiver, *i.e.*, $\mathbf{B}_m \mathbf{H}_m = \mathbf{I}_{N_T}$ (as in Chapter 6). We define the MSE of the estimated symbols at subcarrier m as

$$\begin{aligned} \mathrm{MSE}(m) &= \mathbb{E}\left(\|\mathbf{d}_{m,l} - \hat{\mathbf{d}}_{m,l}\|^2\right) \\ &= P_d(m) + P_n(m), \end{aligned} \tag{2.14}$$

where the expectation is taken over transmitted symbols and noise. Since the noise and symbols are uncorrelated, their contribution to MSE(m) can be separated in the two terms $P_d(m)$ and $P_n(m)$ and they can be studied independently. The term $P_n(m)$ accounts for the additive noise power and can be easily computed. On the other hand, the term $P_d(m)$ accounts for the distortion due to channel frequency selectivity or, in other words, ICI, ISI and IUI. The exact expression of $P_d(m)$ is an intricate function of the transmitted data, channel and pulses. We now show how to obtain a very compact first order approximation of $P_d(m)$. To do this, we remove the additive noise terms, which are straightforward to compute and can be added afterwards. In the noiseless case, the received signal and the demodulated symbols are respectively given by

$$\begin{aligned}
\mathbf{r}[n] &= \sum_{b=-\infty}^{+\infty} \mathbf{C}[b]\mathbf{s}[n-b] \\
\mathbf{z}_{m_0,l_0} &= \sum_{n=0}^{2M\tilde{N}_s-1} \mathbf{r}[n] g^*_{m_0,l_0}[n] \qquad (2.15) \\
&= \sum_{l=0}^{2N_s-1} \sum_{m=0}^{2M-1} \sum_{n=0}^{2M\tilde{N}_s-1} \sum_{b=-\infty}^{+\infty} \mathbf{C}[b]\mathbf{d}_{m,l} p_{m,l}[n-b] g^*_{m_0,l_0}[n].
\end{aligned}$$

Setting $n' = n - b$ and using the definition of $g_{m_0,l_0}[n]$ introduced just after (2.2), we can rewrite (2.15) as

$$\begin{aligned}
\mathbf{z}_{m_0,l_0} &= \sum_{m,l} \sum_{n'} \sum_{b} \mathbf{C}[b]\mathbf{d}_{m,l} p_{m,l}[n'] g^*_{m_0,l_0}[n'+b]. \qquad (2.16) \\
&= \sum_{m,l,n',b} \mathbf{C}[b]\mathbf{d}_{m,l} p_{m,l}[n'](-\jmath)^{l_0+m_0} g[n'+b-l_0M] e^{-\jmath\omega_{m_0}(b+n'-\frac{2M\kappa-1}{2})},
\end{aligned}$$

where $\omega_{m_0} = \frac{2\pi m_0}{2M}$. We now introduce one of the central assumptions of Part I: the discrete receive prototype filter $g[n]$ is assumed to be obtained by discretization of a smooth, real-valued and even analog waveform

$g(t)$, which is only non zero for $t \in [-\kappa/2, \kappa/2]$, so that

$$g[n] = g\left(\left(n - \frac{2M\kappa - 1}{2}\right)\frac{1}{2M}\right),\ n = 0, \ldots, 2M\kappa - 1.$$

Furthermore, we define the q-th derivative of $g(t)$ in time as $g^{(q)}(t) = \frac{d^{(q)}}{dt^q}g(t)$ and its sampled version as

$$g^{(q)}[n] = g^{(q)}\left(\left(n - \frac{2M\kappa - 1}{2}\right)\frac{1}{2M}\right),\ n = 0, \ldots, 2M\kappa - 1.$$

Hence, $g[n' + b - l_0M]$ can be seen as the evaluation of the function $g(t)$ at $\tilde{t} = (n' + b - l_0M - \frac{2M\kappa-1}{2})\frac{1}{2M}$. Let us perform a Taylor expansion of $g(t)$ around point $\tilde{t}_{l_0} = (n' - l_0M - \frac{2M\kappa-1}{2})\frac{1}{2M}$ that we evaluate at $\tilde{t}$

$$\begin{aligned} g[n' + b - l_0M] &= \sum_{q=0}^{+\infty} \frac{g^{(q)}\left(\tilde{t}_{l_0}\right)}{q!}(\tilde{t} - \tilde{t}_{l_0})^q \\ &= \sum_{q=0}^{+\infty} \frac{g^{(q)}[n' - l_0M]}{(2M)^q q!} b^q. \end{aligned}$$

Replacing the expression of $g[n' + b - l_0M]$ by its Taylor expansion in (2.16), we obtain

$$\begin{aligned} \mathbf{z}_{m_0,l_0} &= \sum_{q=0}^{+\infty} \frac{\jmath^q}{(2M)^q q!} \sum_b (-\jmath b)^q \mathbf{C}[b] e^{-\jmath\omega_{m_0} b} \sum_{m,l} \mathbf{d}_{m,l} \sum_{n'} p_{m,l}[n'] g^{(q)*}_{m_0,l_0}[n'] \\ &= \sum_{q=0}^{+\infty} \frac{\jmath^q}{(2M)^q q!} \mathbf{H}^{(q)}_{m_0} \mathbf{y}^{(q)}_{m_0,l_0}, \end{aligned} \tag{2.17}$$

where we defined $g^{(q)}_{m_0,l_0}[n] = \jmath^{l_0+m_0} g^{(q)}[n - l_0M] e^{\jmath\omega_{m_0}(n - \frac{2M\kappa-1}{2})}$ and

$$\begin{aligned} \mathbf{H}^{(q)}_{m_0} &= \sum_b (-\jmath b)^q \mathbf{C}[b] e^{-\jmath\omega_{m_0} b} \\ \mathbf{y}^{(q)}_{m_0,l_0} &= \sum_{m,l} \mathbf{d}_{m,l} \sum_{n'} p_{m,l}[n'] g^{(q)*}_{m_0,l_0}[n']. \end{aligned}$$

Defining the channel frequency response as $\mathbf{H}(\omega) = \sum_b \mathbf{C}[b]e^{-\jmath\omega b}$, $\mathbf{H}_{m_0}^{(q)}$ can be seen as its q-th derivative evaluated at subcarrier m_0 so that $\mathbf{H}_{m_0}^{(0)} = \mathbf{H}_{m_0}$. The samples $\mathbf{y}_{m_0,l_0}^{(q)}$ can be seen as the complex demodulated symbols at subcarrier m_0 and multicarrier symbol l_0, if the symbols $\mathbf{d}_{m,l}$ are FBMC-OQAM modulated using a prototype pulse $p[n]$, demodulated using a prototype pulse $g^{(q)}[n]$ and for an ideal channel, *i.e.*, $\mathbf{C}[b] = \delta[b]\mathbf{I}_{N_T}$. We also have that $\mathbf{y}_{m_0,l_0}^{(0)} = \mathbf{y}_{m_0,l_0}$ as defined in (2.2).

Equation (2.17) allows us to make several important remarks. If the channel is frequency flat, we have $\mathbf{H}_m^{(q)} = \mathbf{0}$ for $q > 0$, which corresponds to the conventional 0-th order approximation of the demodulated symbol presented in Section 2.1.5 relying on the assumption of a frequency flat channel at the subcarrier level. As the channel frequency selectivity increases, the derivatives of the channel ($\mathbf{H}_m^{(q)}$ for $q > 0$) are amplified and the accuracy of the 0-th order approximation of the demodulated symbol deteriorates.

The estimated symbols are obtained, after single-tap equalization, as $\hat{\mathbf{d}}_{m,l} = \Re\left(\mathbf{B}_m\mathbf{z}_{m,l}\right)$. Let us approximate $\mathbf{z}_{m,l}$ by its first order approximation $\mathbf{z}_{m,l}^{(1)}$, defined as the truncation of (2.17) to the first order,

$$\mathbf{z}_{m,l}^{(1)} = \mathbf{H}_m\mathbf{y}_{m,l} + \frac{\jmath}{(2M)}\mathbf{H}_m^{(1)}\mathbf{y}_{m,l}^{(1)}.$$

Since we assumed that the equalizer $\mathbf{B}_m$ perfectly inverts the channel at the receiver, we have[5] $\mathbf{B}_m\mathbf{H}_m = \mathbf{I}_{N_T}$. We recall that, if the pulses satisfy the PR conditions, we have $\Re\left(\mathbf{y}_{m,l}\right) = \mathbf{d}_{m,l}$, which leads to

$$\hat{\mathbf{d}}_{m,l} \approx \Re\left(\mathbf{B}_m\mathbf{z}_{m,l}^{(1)}\right) = \mathbf{d}_{m,l} + \Re\left(\mathbf{B}_m\frac{\jmath}{(2M)}\mathbf{H}_m^{(1)}\mathbf{y}_{m,l}^{(1)}\right)$$

and the MSE in (2.14) becomes (noiseless case, $P_n(m) = 0$)

$$\mathrm{MSE}(m) = P_d(m) \approx \mathbb{E}\left(\left\|\Re\left(\mathbf{B}_m\frac{\jmath}{(2M)}\mathbf{H}_m^{(1)}\mathbf{y}_{m,l}^{(1)}\right)\right\|^2\right).$$

[5]This assumption will not always be made in the following chapters.

To go further, we use a result, proven in Section 5.5.3,[6] implying that

$$\mathbb{E}\left(\mathbf{y}_{m,l}^{(1)}\left(\mathbf{y}_{m,l}^{(1)}\right)^{T}\right)=\mathbf{0}$$
$$\mathbb{E}\left(\mathbf{y}_{m,l}^{(1)}\left(\mathbf{y}_{m,l}^{(1)}\right)^{H}\right)=2\eta E_s\mathbf{I}_{N_T},$$

where η is a quantity related to the transmit and receive pulses. Using this identity and the trace cyclic property, we finally find that

$$P_d(m)\approx E_s\frac{\eta}{(2M)^2}\mathrm{tr}\left[\left(\mathbf{B}_m\mathbf{H}_m^{(1)}\right)\left(\mathbf{B}_m\mathbf{H}_m^{(1)}\right)^{H}\right].$$

We will refer to this expression as a first order approximation of the distortion due to channel frequency selectivity. The expression is very compact and allows to very easily analyze the performance of an FBMC-OQAM system under strong channel selectivity. As we will show in following chapters, the approximation is very accurate to model highly selective channel conditions. Furthermore, the expression is intuitive as it explains the effect of channel frequency selectivity on an FBMC-OQAM system. As the channel frequency selectivity increases, the derivative of the channel $\mathbf{H}_m^{(1)}$ is amplified and the FBMC-OQAM system will suffer from stronger distortion, composed of IUI, ISI and ICI. One can note that the amount of distortion will depend on the combination with the equalizer, *i.e.*, $\mathbf{B}_m\mathbf{H}_m^{(1)}$.

In Part I, we greatly extend the approach proposed in [53] by considering more general types of equalizers and pre-equalizers. We also consider channels that are both frequency and time selective. Moreover, we investigate different MIMO scenarios. To avoid confusing the reader and to help him identify the specificity of each chapter, we give here below a short description of the different scenarios[7] investigated in Part I

[6]Relying on the results of [53, Appendix B] and Lemma 3 presented in Section 3.5.2.

[7]For a reminder on the different types of MIMO systems that we consider (PTP MIMO, MU MIMO and massive MIMO), we refer the reader to Section 2.2.1.

and the related publications. Moreover, we refer the reader to Fig. 2.15 for a summary of the different scenarios.

Chapter 3 considers a MU-MIMO FBMC-OQAM scenario characterized by a highly frequency selective channel. Both the DL and the UL are investigated. In the UL (resp. DL), single-tap equalizers (resp. pre-equalizers) at the BS are optimized under a ZF or a MMSE criterion.

- F. Rottenberg, X. Mestre, and J. Louveaux, "Optimal zero forcing precoder and decoder design for multi-user MIMO FBMC under strong channel selectivity," in *2016 IEEE International Conference on Acoustics, Speech and Signal Processing (ICASSP)*, pp. 3541–3545, March 2016
- F. Rottenberg, X. Mestre, F. Horlin, and J. Louveaux, "Single-Tap Precoders and Decoders for Multiuser MIMO FBMC-OQAM Under Strong Channel Frequency Selectivity," *IEEE Transactions on Signal Processing*, vol. 65, pp. 587–600, Feb 2017

Chapter 4 analyzes the performance of an uplink massive MIMO FBMC-OQAM system, taking into account high channel frequency selectivity. The performance in terms of the MSE of the decoded symbols is evaluated for three types of classical single-tap equalizers, namely, ZF, LMMSE and MF.

- X. Mestre, F. Rottenberg, and M. Navarro, "Linear receivers for massive MIMO FBMC/OQAM under strong channel frequency selectivity," in *2016 IEEE Statistical Signal Processing Workshop (SSP)*, pp. 1–5, June 2016
- F. Rottenberg, X. Mestre, F. Horlin, and J. Louveaux, "Performance Analysis of Linear Receivers for Uplink Massive MIMO FBMC-OQAM Systems," *IEEE Transactions on Signal Processing*, vol. 66, pp. 830–842, Feb 2018

Chapter 5 proposes a parallel equalization structure for PTP MIMO FBMC-OQAM systems under channels that are both highly frequency and time selective.

- F. Rottenberg, X. Mestre, D. Petrov, F. Horlin, and J. Louveaux, "Parallel Equalization Structure for MIMO FBMC-OQAM Systems Under Strong Time and Frequency Selectivity," *IEEE Transactions on Signal Processing*, vol. 65, pp. 4454–4467, Sept 2017

Chapter 6 also considers a PTP MIMO FBMC-OQAM system under channels that are both highly frequency and time selective. Relatively to the design in Chapter 5, a design with lower complexity is considered, relying on a single-tap per-subcarrier equalizer. This chapter can be seen as an extension of Chapter 3 to doubly selective channels.

- F. Rottenberg, X. Mestre, F. Horlin, and J. Louveaux, "Single-tap equalizer for MIMO FBMC systems under doubly selective channels," in *2017 IEEE International Conference on Acoustics, Speech and Signal Processing (ICASSP)*, pp. 3784–3788, March 2017

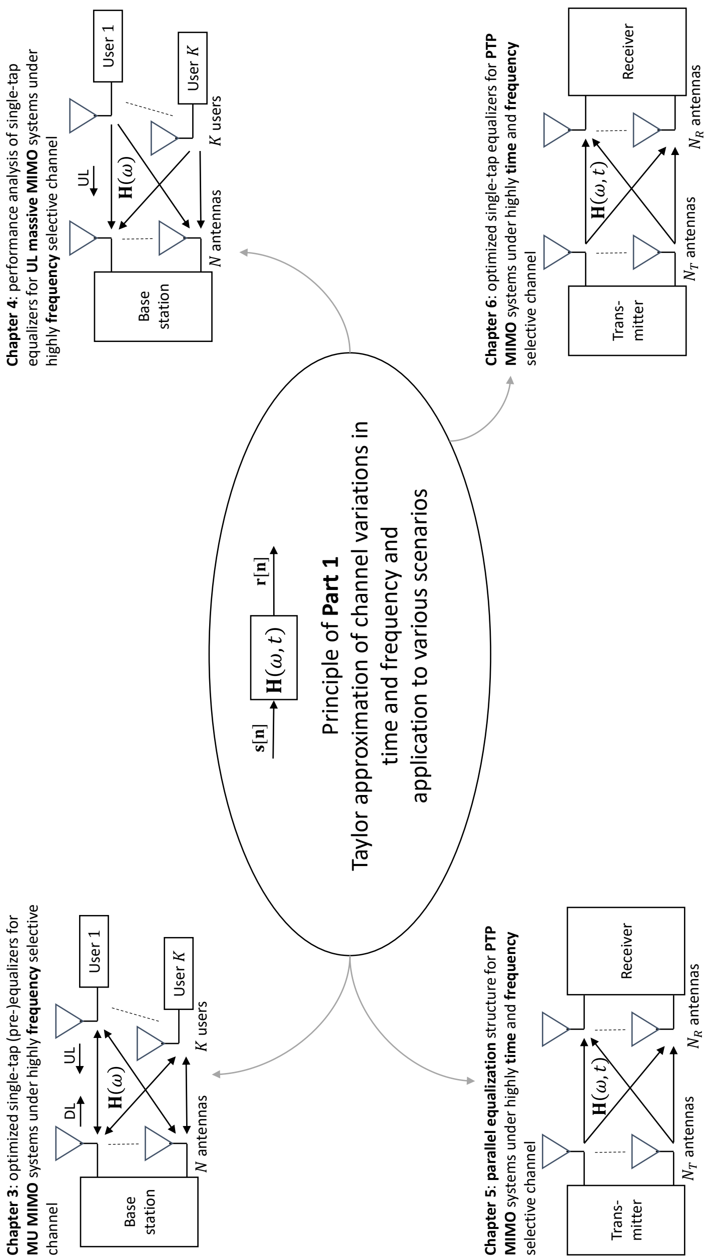

Figure 2.15 General principle used in Part I and application to various MIMO scenarios.

CHAPTER 3

OPTIMIZED SINGLE-TAP PRE-EQUALIZERS AND EQUALIZERS FOR MU MIMO SYSTEMS UNDER STRONG CHANNEL FREQUENCY SELECTIVITY

As the channel becomes more selective in frequency, the FBMC-OQAM modulation begins to suffer from ISI and ICI and the orthogonality is progressively destroyed. As detailed in Section 2.1.5.2, many works in the literature have investigated this problem and proposed various compensation methods. One should however note that the proposed solutions in the literature enhance the system implementation complexity by using more complicated designs such as multi-tap filters, iterative methods, parallel receivers... Here, in contrast to most of the proposed approaches to deal with channel frequency selectivity, we consider the conventional low complexity approach based on single-tap pre-equalizers and equalizers, as represented in Fig. 3.1 and Fig. 3.2. We show that, as soon as the receiver has more antennas than the number of transmit antennas, *i.e.*, $N_R > N_T$, the equalizer can use these extra degrees of freedom to cancel the distortion due to channel frequency selectivity. The same result holds for the design of the pre-equalizer at the transmitter as soon as $N_T > N_R$.

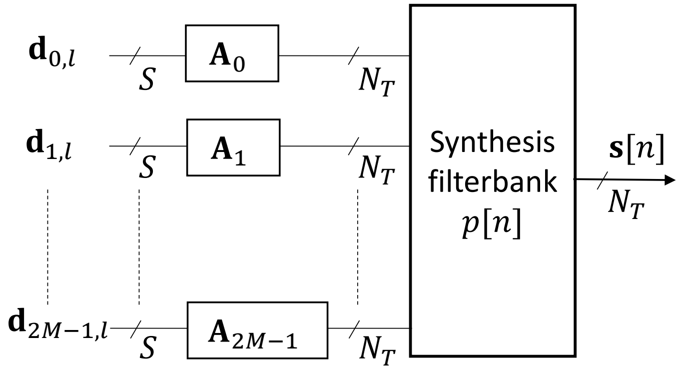

Figure 3.1 Per-subcarrier pre-equalization at the transmitter.

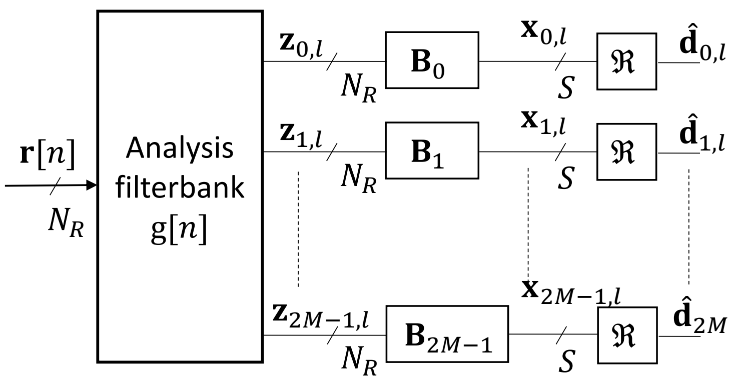

Figure 3.2 Per-subcarrier equalization at the receiver.

In a first step, a first order approximation of the per-subcarrier MSE for a MIMO FBMC-OQAM system, including the effects of noise, MSI, ISI and ICI, is proposed, relying not only on the channel frequency response evaluated at this subcarrier but also on its derivatives. As opposed to most of the works in the literature, the assumption of a frequency flat channel at the subcarrier level (as in (2.6)) is not made. The derived MSE expression is general and can be applied to various MIMO scenarios such as PTP MIMO, MU MIMO and massive MIMO.

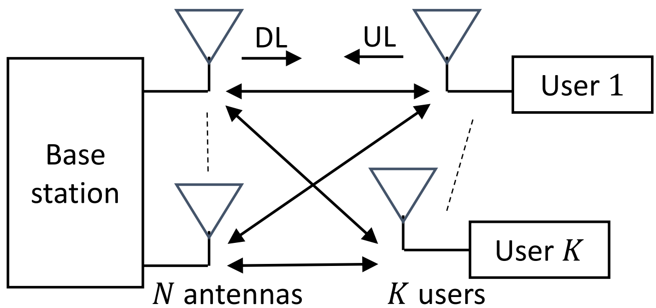

Figure 3.3 Multi-user MIMO scenario: K single-antenna users and one base station with N antennas communicate simultaneously in UL and DL using space division multiple access.

This approximation generalizes the one given in [55] that is valid only for the ZF case.

In a second step, we optimize the MSE formula to design single-tap pre-equalizers and equalizers in a MU MIMO context. As shown in Fig. 3.3, we consider a MU MIMO system with one BS equipped with N antennas and K single-antenna users that are not able to cooperate with one another[1]. The users and the BS are assumed to use SDMA, *i.e.*, they simultaneously communicate using the same time and frequency resources [83, Chap. 10]. As soon as $N > K$, we show that even with the simple single-tap chosen structure, one can exploit the degrees of freedom offered by the $(N - K)$ extra BS antennas to compensate for the distortion due to frequency selectivity. In both the UL and DL cases, two design criteria are considered, namely ZF or MMSE. From the asymptotic study at high SNR, it is shown that the first order approximation of the distortion can be completely removed as soon as the number of BS antennas is twice as large as the number of users.

Chapter 3 is structured as follows. Section 3.1 proposes an approximation of the MSE for a general MIMO FBMC-OQAM system under

[1]Note that one could straightforwardly apply our results to a PTP communication link transmitting with pure spatial multiplexing.

strong channel frequency selectivity. Section 3.2 optimizes the previously derived MSE formula for a MU MIMO scenario as a function of the single-tap pre-equalizer or equalizer under a ZF or a MMSE criterion. Section 3.3 validates the accuracy of MSE approximation and the performance of the optimized single-tap pre-equalizer and equalizer through simulations. Finally, Section 3.4 concludes the chapter and Section 3.5 contains the mathematical proofs of previous sections.

3.1 MSE formulation for general MIMO FBMC-OQAM systems under strong channel frequency selectivity

We consider a general MIMO FBMC-OQAM system with N_T and N_R antennas at the transmit and receive sides, respectively. The number of streams is denoted by S. The block diagrams of the transmitter and receiver are depicted in Fig. 3.1 and Fig. 3.2. This work makes a quasi-static assumption on the channel variations in time meaning that we assume that the channel does not change over the transmitted frame duration. At the transmitter, the pre-equalizer at the m-th subcarrier is denoted by $\mathbf{A}_m \in \mathbb{C}^{N_T \times S}$. At the receiver, the equalizer at the m-th subcarrier is denoted by $\mathbf{B}_m \in \mathbb{C}^{S \times N_R}$.[2] We define the MSE at the output of the transceiver chain corresponding to all streams as

$$\begin{aligned}\mathrm{MSE}(m) &= \mathbb{E}\left(\|\hat{\mathbf{d}}_{m,l} - \mathbf{d}_{m,l}\|^2\right) \\ &= P_d(m) + \frac{N_0}{2}\mathrm{tr}\left[\mathbf{B}_m\mathbf{B}_m^H\right], \end{aligned} \tag{3.1}$$

where the expectation is taken over transmitted symbols and noise. Since noise and symbols are uncorrelated, their effect can be separated in the two terms of (3.1). The term $P_d(m)$ corresponds to the distortion due to

[2]Note that, as explained in Section 2.1.5, we remove the l subscript to emphasize that $\mathbf{A}_m$ and $\mathbf{B}_m$ do not vary over time ($\mathbf{A}_{m,l} = \mathbf{A}_m$ and $\mathbf{B}_{m,l} = \mathbf{B}_m$).

MSI, ISI and ICI. The designs of Fig. 3.1 and Fig. 3.2 usually rely on the assumption of a channel sufficiently flat in frequency at the subcarrier level. When the variation of the channel becomes non-negligible, this assumption becomes inaccurate and distortion will increase with the appearance of MSI, ISI and ICI (, *i.e.*, the term $P_d(m)$ increases). To be able to give an approximation of $P_d(m)$, we make the following assumptions:

($\mathbf{As1}$) There exist two smooth functions $\mathbf{A}(\omega)$ and $\mathbf{B}(\omega)$, defined on the torus $\mathbb{R}/2\pi\mathbb{Z}$, such that the actual pre-equalizers and equalizers implemented at the m-th subcarrier result from the evaluation of $\mathbf{A}(\omega)$ and $\mathbf{B}(\omega)$ at frequency $\omega_m = \frac{2\pi m}{2M}$, *i.e.*, $\mathbf{A}_m = \mathbf{A}(\omega_m)$ and $\mathbf{B}_m = \mathbf{B}(\omega_m)$. Similarly, the channel frequency response $\mathbf{H}(\omega)$ is assumed to be a smooth function and such that $\mathbf{H}_m = \mathbf{H}(\omega_m)$. In the following, the superscript $^{(q)}$ applied to a frequency-depending quantity refers to the q-th derivative with respect to frequency, *i.e.*, the first derivative of $\mathbf{A}(\omega)$ evaluated at ω_m is denoted by $\mathbf{A}_m^{(1)}$ while $\mathbf{H}_m^{(1)}$ and $\mathbf{H}_m^{(2)}$ denote the first and second derivatives of the channel frequency response.

($\mathbf{As2}$) The prototype pulse $g[n]$ is assumed identical at transmit and receive sides, so that $p[n] = g[n]$ and of energy normalized to one. It is either symmetric or anti-symmetric in the time domain and it meets the PR conditions. Furthermore, $g[n]$ is obtained by discretization of a smooth real-valued analog waveform $g(t)$, which is only non zero for $t \in [-\kappa/2, \kappa/2]$, so that

$$g[n] = g\left(\left(n - \frac{2M\kappa - 1}{2}\right)\frac{1}{2M}\right),\ n = 0, \ldots, 2M\kappa - 1.$$

Furthermore, the pulse $g(t)$ and its derivatives are null at the end-points of the support, namely at $t = \pm\kappa/2$. Thanks to the above assumption, we can define $g^{(q)}[n]$ as the sampled version of the q-th derivative of $g(t)$, *i.e.*,

$$g^{(q)}[n] = g^{(q)}\left(\left(n - \frac{2M\kappa - 1}{2}\right)\frac{1}{2M}\right), n = 0, \ldots, 2M\kappa - 1.$$

We are now in a position to introduce the main result of this section.

Theorem 2. *Under* $(\mathbf{As1}) - (\mathbf{As2})$*, the aggregated distortion* $P_d(m)$ *at the* m*-th subcarrier can be expressed as*

$$\begin{aligned}
P_d(m) &= \frac{E_s}{2} tr\left[\left(\mathbf{B}_m\mathbf{H}_m\mathbf{A}_m - \mathbf{I}_S\right)\left(\mathbf{B}_m\mathbf{H}_m\mathbf{A}_m - \mathbf{I}_S\right)^H\right] \\
&+ E_s\frac{\eta}{(2M)^2} tr\left[\left(\mathbf{B}_m\mathbf{H}_m^{(1)}\mathbf{A}_m\right)\left(\mathbf{B}_m\mathbf{H}_m^{(1)}\mathbf{A}_m\right)^H\right] \\
&+ E_s\frac{\eta}{(2M)^2}\Re\, tr\left[\left(\mathbf{B}_m\mathbf{H}_m\mathbf{A}_m - \mathbf{I}_S\right)\left(\mathbf{B}_m\mathbf{H}_m^{(2)}\mathbf{A}_m\right)^H\right] \\
&+ E_s\frac{2(\eta+\zeta)}{(2M)^2} tr\left[\Im\left(\mathbf{B}_m\mathbf{H}_m\mathbf{A}_m - \mathbf{I}_S\right)\Im^T\left(\mathbf{B}_m\left(\mathbf{H}_m\mathbf{A}_m^{(1)}\right)^{(1)}\right)\right] \\
&+ E_s\frac{2(\eta+\zeta)}{(2M)^2} tr\left(\Im\left(\mathbf{B}_m\mathbf{H}_m\mathbf{A}_m^{(1)}\right)\Im^T\left(\mathbf{B}_m\left(\mathbf{H}_m\mathbf{A}_m\right)^{(1)}\right)\right) \\
&+ O\left(M^{-2}\right),
\end{aligned} \tag{3.2}$$

where η *and* ζ *are pulse-related quantities defined in Section 3.5.*

Proof. See Section 3.5. □

Comments: equations (3.1) and (3.2) show that the MSE expression is composed of many terms including the effects of noise, MSI, ISI and ICI. One may recognize some usual terms, *i.e.*, the noise term in (3.1) or the first term of (3.2) related to the fact that the channel is not perfectly inverted ($\mathbf{B}_m\mathbf{H}_m\mathbf{A}_m \neq \mathbf{I}_S$). Those two terms would be the only ones remaining if the channel was frequency flat ($\mathbf{H}^{(1)} = \mathbf{0}$) and the pre-equalizer non-frequency selective ($\mathbf{A}_m^{(1)} = \mathbf{0}$). Those are also the two only terms of distortion in an OFDM system if the cyclic prefix is longer than the channel length and the system well synchronized. Furthermore, the dependence of (3.2) on $\mathbf{H}_m^{(1)}$ and $\mathbf{H}_m^{(2)}$ comes directly from the fact that the channel variation breaks the FBMC-OQAM orthogonality while the dependence in the derivatives of the pre-equalizer $\mathbf{A}_m^{(1)}$ and $\mathbf{A}_m^{(2)}$ shows that the precoding operations on adjacent subcarriers may influence the MSE at the current subcarrier. Notice that this effect, also known as intrinsic interference, also occurs if the channel is non-varying ($\mathbf{H}_m^{(1)} = \mathbf{0}$) but the pre-equalizer varies over the subcarriers ($\mathbf{A}_m^{(1)} \neq \mathbf{0}$).

3.2 Single-tap pre-equalizers and equalizers design for MU MIMO systems

The goal of this section is to optimize the general MSE formulation of (3.1), applied to a MU MIMO scenario, as a function of the pre-equalizer or the equalizer. As shown in Fig. 3.3, we consider a MU MIMO system with one BS equipped with N antennas and K users, each one equipped with a single antenna[3] and not able to cooperate with each other. The users and the BS are assumed to use SDMA, *i.e.*, they communicate simultaneously using the same time and frequency resources. The number of streams is equal to $S = K$ with $N \geq K$. The channel frequency response matrix $\mathbf{H}(\omega)$ is assumed to be perfectly known by the BS. For the sake of clarity, $\mathbf{H}(\omega)$ is denoted by $\mathbf{H}_{\mathrm{DL}}(\omega) \in \mathbb{C}^{K \times N}$ when referred to the specific DL scenario and $\mathbf{H}_{\mathrm{UL}}(\omega) \in \mathbb{C}^{N \times K}$ resp. in the UL case. We use the same subscript to denote the equalizer and pre-equalizer in UL and DL. Furthermore, we remove the subscript m to clarify expressions even though every frequency-depending quantity are evaluated at $\omega = \omega_m$, *e.g.*, $\mathbf{H}^{(1)} = \mathbf{H}_m^{(1)}$, $\mathbf{A} = \mathbf{A}_m$.

While optimizing the equalizer in UL (resp. pre-equalizer in DL), the pre-equalizer (resp. equalizer in DL) at the other end is fixed to a real positive scalar $\xi_{\mathrm{UL}}(\omega)$ (resp. $\xi_{\mathrm{DL}}(\omega)$) since the users cannot collaborate, *i.e.*, $\mathbf{A}_{\mathrm{UL}} = \xi_{\mathrm{UL}}\mathbf{I}_K$ (resp. $\mathbf{B}_{\mathrm{DL}} = \xi_{\mathrm{DL}}\mathbf{I}_K$). Moreover, a per-subcarrier transmit power constraint is considered so that

$$\mathrm{tr}\left[\mathbf{A}\mathbf{A}^H\right] = G_T. \tag{3.3}$$

[3]Note that the approach could be generalized to the case where each user terminal is equipped with multiple antennas, although the extension does not seem trivial.

Table 3.1 Summary of the different designs under consideration and their respective assumptions.

	Equalizer (Uplink, MAC channel) $\mathbf{A}_{\mathrm{UL}} = \xi_{\mathrm{UL}}\mathbf{I}_K, \mathbf{H}_{\mathrm{UL}} \in \mathbb{C}^{N\times K}$	Pre-equalizer (Downlink, BC channel) $\mathbf{B}_{\mathrm{DL}} = \xi_{\mathrm{DL}}\mathbf{I}_K, \mathbf{H}_{\mathrm{DL}} \in \mathbb{C}^{K\times N}$
ZF ($\mathbf{BHA} = \mathbf{I}_K$)	$\xi_{\mathrm{UL}}^{\mathrm{ZF}}$ independent of ω	$\xi_{\mathrm{DL}}^{\mathrm{ZF}}$ depends on ω
MMSE ($\mathbf{BHA} \neq \mathbf{I}_K$)	$\xi_{\mathrm{UL}}^{\mathrm{MMSE}}$ independent of ω	$\xi_{\mathrm{DL}}^{\mathrm{MMSE}}$ depends on ω

Two design criteria will be investigated, namely the ZF criterion and the MMSE criterion. A summary of the different designs under study with their corresponding assumptions is given in Table 3.1. Note that, in UL, the users cannot pre-equalize the streams, so that $\xi_{\mathrm{UL}}(\omega)$ is constant over frequency. Conversely, in the DL, the BS pre-equalizes the channel at the subcarrier level. This processing depends on the channel frequency response at this subcarrier and hence, the normalization factor $\xi_{\mathrm{DL}}(\omega)$ will generally depend on frequency. Finally, the computation complexity of the proposed designs will be studied.

3.2.1 Zero forcing design

For this design, a channel inverting constraint is considered, namely

$$\mathbf{BHA} = \mathbf{I}_K, \tag{3.4}$$

where we recall that every frequency-depending quantity should be understood as evaluated at the subcarrier of interest. The channel matrix $\mathbf{H}$ is assumed to be of full rank, which is a quite natural assumption in the considered MU MIMO scenario. Using (3.4) and the fact that $(\mathbf{BHA})^{(1)} = \mathbf{B}(\mathbf{HA})^{(1)} + \mathbf{B}^{(1)}\mathbf{HA} = \mathbf{0}$,[4] many terms of the distortion

[4]As a reminder, the subscript $^{(q)}$ applied to a frequency-depending quantity refers to the q-th derivative with respect to frequency evaluated at the subcarrier of interest.

expression of (3.2) vanish and the MSE in (3.1) simplifies to

$$\begin{aligned}\mathrm{MSE}(m) = & E_s\tilde{\eta}\mathrm{tr}\Big[\Big(\mathbf{BH}^{(1)}\mathbf{A}\Big)\Big(\mathbf{BH}^{(1)}\mathbf{A}\Big)^H\Big] \\ & - E_s 2(\tilde{\eta}+\tilde{\zeta})\mathrm{tr}\Big[\Im(\mathbf{BHA}^{(1)})\Im(\mathbf{B}^{(1)}\mathbf{HA})^T\Big] \\ & + \frac{N_0}{2}\mathrm{tr}\big[\mathbf{BB}^H\big] + O\left(2M^{-2}\right),\end{aligned} \tag{3.5}$$

where $\tilde{\eta} = \frac{\eta}{(2M)^2}$ and $\tilde{\zeta} = \frac{\zeta}{(2M)^2}$.

Equalizer (multiple access channel (MAC), UL)

In the UL case, $\mathbf{H}_{\mathrm{UL}}$ and $\mathbf{H}_{\mathrm{UL}}^{(1)} \in \mathbb{C}^{N\times K}$ correspond to the tall channel frequency response matrix and its derivative evaluated at the subcarrier of interest. From the power normalization (3.3) and channel inversion (3.4) constraints, the general solution of the problem can be written in the following form

$$\begin{aligned}\mathbf{A}_{\mathrm{UL}}^{\mathrm{ZF}} &= \xi_{\mathrm{UL}}^{\mathrm{ZF}}\mathbf{I}_K \\ \mathbf{B}_{\mathrm{UL}}^{\mathrm{ZF}} &= \frac{1}{\xi_{\mathrm{UL}}^{\mathrm{ZF}}}\Big(\mathbf{H}_{\mathrm{UL}}^{\dagger} + \tilde{\mathbf{B}}\mathbf{P}_{\mathrm{UL}}\Big),\end{aligned} \tag{3.6}$$

where

$$\begin{aligned}\xi_{\mathrm{UL}}^{\mathrm{ZF}} &= \sqrt{G_T/K} \quad \text{(Power normalization)} \\ \mathbf{H}_{\mathrm{UL}}^{\dagger} &= (\mathbf{H}_{\mathrm{UL}}^H\mathbf{H}_{\mathrm{UL}})^{-1}\mathbf{H}_{\mathrm{UL}}^H \quad \text{(Left pseudo-inverse of } \mathbf{H}_{\mathrm{UL}}) \\ \mathbf{P}_{\mathrm{UL}} &= \mathbf{I}_N - \mathbf{H}_{\mathrm{UL}}\mathbf{H}_{\mathrm{UL}}^{\dagger} \quad \text{(Projection in left null space of } \mathbf{H}_{\mathrm{UL}}),\end{aligned}$$

and where $\tilde{\mathbf{B}}$ is a $K\times N$ matrix to be optimized. This shows that the equalizer in (3.6) can be written as the left pseudo-inverse of the channel plus a matrix lying on the left null space of $\mathbf{H}_{\mathrm{UL}}$. In the trivial case $N = K$, the equalizer is the inverse of the channel since there are no extra degrees of freedom, *i.e.*, $\mathbf{P}_{\mathrm{UL}} = \mathbf{0}$, $\mathbf{H}_{\mathrm{UL}}^{\dagger} = \mathbf{H}_{\mathrm{UL}}^{-1}$.

One can check that the second term of the distortion in (3.5) is null due to the fact that $\Im(\mathbf{B}_{\mathrm{UL}}^{\mathrm{ZF}}\mathbf{H}_{\mathrm{UL}}(\mathbf{A}_{\mathrm{UL}}^{\mathrm{ZF}})^{(1)}) = \Im\left((\xi_{\mathrm{UL}}^{\mathrm{ZF}})^{(1)}/\xi_{\mathrm{UL}}^{\mathrm{ZF}}\right)\mathbf{I}_K = \mathbf{0}$ with $\xi_{\mathrm{UL}}^{\mathrm{ZF}}$ purely real (and not depending on frequency). Therefore, the optimization problem can be turned into the minimization of a quadratic expression in $\tilde{\mathbf{B}}$

$$\begin{aligned}\min_{\tilde{\mathbf{B}}} \mathrm{tr}\Big[&\left(\mathbf{H}_{\mathrm{UL}}^{\dagger}\mathbf{H}_{\mathrm{UL}}^{(1)} + \tilde{\mathbf{B}}\mathbf{P}_{\mathrm{UL}}\mathbf{H}_{\mathrm{UL}}^{(1)}\right)\left(\mathbf{H}_{\mathrm{UL}}^{\dagger}\mathbf{H}_{\mathrm{UL}}^{(1)} + \tilde{\mathbf{B}}\mathbf{P}_{\mathrm{UL}}\mathbf{H}_{\mathrm{UL}}^{(1)}\right)^{H}\Big] \\ &+ \frac{N_0 K\tilde{\eta}}{G_T E_s}\mathrm{tr}\Big[\left(\mathbf{H}_{\mathrm{UL}}^{H}\mathbf{H}_{\mathrm{UL}}\right)^{-1} + \tilde{\mathbf{B}}\mathbf{P}_{\mathrm{UL}}\tilde{\mathbf{B}}^{H}\Big]. \end{aligned} \tag{3.7}$$

Setting the derivative of this expression with respect to $\tilde{\mathbf{B}}^{*}$ to $\mathbf{0}$, we find that the optimum solution is such that

$$\tilde{\mathbf{B}} = -\mathbf{H}_{\mathrm{UL}}^{\dagger}\mathbf{H}_{\mathrm{UL}}^{(1)}\left(\mathbf{H}_{\mathrm{UL}}^{(1)H}\mathbf{P}_{\mathrm{UL}}\mathbf{H}_{\mathrm{UL}}^{(1)} + \frac{N_0 K\tilde{\eta}}{G_T E_s}\mathbf{I}_K\right)^{-1}\mathbf{H}_{\mathrm{UL}}^{(1)H}, \tag{3.8}$$

where we used the matrix inversion lemma.

Pre-equalizer (broadcast channel (BC), DL)

In the DL case, $\mathbf{H}_{\mathrm{DL}}, \mathbf{H}_{\mathrm{DL}}^{(1)} \in \mathbb{C}^{K\times N}$ denote the fat channel frequency response matrix and its derivative evaluated at the subcarrier of interest. From the constraints (3.3) and (3.4), the general solution can be written as

$$\begin{aligned}\mathbf{A}_{\mathrm{DL}}^{\mathrm{ZF}} &= \frac{1}{\xi_{\mathrm{DL}}^{\mathrm{ZF}}}\left(\mathbf{H}_{\mathrm{DL}}^{\dagger} + \mathbf{P}_{\mathrm{DL}}\tilde{\mathbf{A}}\right) \\ \mathbf{B}_{\mathrm{DL}}^{\mathrm{ZF}} &= \xi_{\mathrm{DL}}^{\mathrm{ZF}}\mathbf{I}_K,\end{aligned}$$

where

$$\begin{aligned}
\xi_{\mathrm{DL}}^{\mathrm{ZF}} &= \sqrt{\mathrm{tr}\Big((\mathbf{H}_{\mathrm{DL}}\mathbf{H}_{\mathrm{DL}}^{H})^{-1} + \tilde{\mathbf{A}}^{H}\mathbf{P}_{\mathrm{DL}}\tilde{\mathbf{A}}\Big)/G_T} \quad \text{(Power normalization)}\\
\mathbf{H}_{\mathrm{DL}}^{\dagger} &= \mathbf{H}_{\mathrm{DL}}^{H}(\mathbf{H}_{\mathrm{DL}}\mathbf{H}_{\mathrm{DL}}^{H})^{-1} \quad \text{(Right pseudo-inverse of } \mathbf{H}_{\mathrm{DL}})\\
\mathbf{P}_{\mathrm{DL}} &= \mathbf{I}_N - \mathbf{H}_{\mathrm{DL}}^{\dagger}\mathbf{H}_{\mathrm{DL}} \quad \text{(Projection in right null space of } \mathbf{H}_{\mathrm{DL}}).
\end{aligned}$$

As in the equalizer case, the second term of the distortion in (3.5) also disappears due to the fact that $\Im((\mathbf{B}_{\mathrm{DL}}^{\mathrm{ZF}})^{(1)}\mathbf{H}_{\mathrm{DL}}\mathbf{A}_{\mathrm{DL}}^{\mathrm{ZF}}) = \Im((\xi_{\mathrm{DL}}^{\mathrm{ZF}})^{(1)}/\xi_{\mathrm{DL}}^{\mathrm{ZF}})\mathbf{I}_K = \mathbf{0}$ with ξ_{DL} purely real. The optimization problem then simplifies to

$$\begin{aligned}
\min_{\tilde{\mathbf{A}}} \mathrm{tr}\Big[&\Big(\mathbf{H}_{\mathrm{DL}}^{(1)}\mathbf{H}_{\mathrm{DL}}^{\dagger} + \mathbf{H}_{\mathrm{DL}}^{(1)}\mathbf{P}_{\mathrm{DL}}\tilde{\mathbf{A}}\Big)\Big(\mathbf{H}_{\mathrm{DL}}^{(1)}\mathbf{H}_{\mathrm{DL}}^{\dagger} + \mathbf{H}_{\mathrm{DL}}^{(1)}\mathbf{P}_{\mathrm{DL}}\tilde{\mathbf{A}}\Big)^{H}\Big]\\
&+ \frac{N_0K\tilde{\eta}}{G_TE_s}\mathrm{tr}\Big[(\mathbf{H}_{\mathrm{DL}}\mathbf{H}_{\mathrm{DL}}^{H})^{-1} + \tilde{\mathbf{A}}^{H}\mathbf{P}_{\mathrm{DL}}\tilde{\mathbf{A}}\Big],
\end{aligned}$$

the solution of which is, after applying the matrix inversion lemma,

$$\tilde{\mathbf{A}} = -\mathbf{H}_{\mathrm{DL}}^{(1)H}\left(\mathbf{H}_{\mathrm{DL}}^{(1)}\mathbf{P}_{\mathrm{DL}}\mathbf{H}_{\mathrm{DL}}^{(1)H} + \frac{N_0K\tilde{\eta}}{G_TE_s}\mathbf{I}_K\right)^{-1}\mathbf{H}_{\mathrm{DL}}^{(1)}\mathbf{H}_{\mathrm{DL}}^{\dagger}.$$

One can check that the asymptotic MSE of the optimized pre-equalizer and equalizer will be exactly the same if the channels are the Hermitian of one another, *i.e.*, $\mathbf{H}_{\mathrm{DL}} = \mathbf{H}_{\mathrm{UL}}^{H}$.

Asymptotic study at low and high SNR

We concentrate here on the behavior of the optimized single-tap equalizer in the UL (MAC) channel. Similar conclusions also hold for the pre-equalizer in the DL (BC) channel. We assume that the number of users K and the transmit power G_T remain constant while we let N_0 go to 0 or $+\infty$ (high and low SNR respectively). At low SNR ($N_0 \to +\infty$), the expression in (3.8) tends to zero ($\tilde{\mathbf{B}} \to \mathbf{0}$) and the optimized equalizer converges to

$$\lim_{N_0 \to \infty} \mathbf{B}_{\mathrm{UL}}^{\mathrm{ZF}} = \frac{1}{\xi_{\mathrm{UL}}^{\mathrm{ZF}}} \mathbf{H}_{\mathrm{UL}}^{\dagger}.$$

As one would expect, when noise power is large, the distortion caused by channel selectivity is comparatively negligible. The best thing to do is to use the classical pseudo-inverse of the channel to combine the signals of each antenna.

At high SNR, assuming that $\mathbf{H}_{\mathrm{UL}}^{(1)}$ is of full rank K, the equalizer converges to a limit that depends on the rank of $\mathbf{P}_{\mathrm{UL}}$. Indeed, two cases must be considered depending on whether matrix $\mathbf{H}_{\mathrm{UL}}^{(1)H} \mathbf{P}_{\mathrm{UL}} \mathbf{H}_{\mathrm{UL}}^{(1)}$ is invertible or not. One can rewrite $\mathbf{P}_{\mathrm{UL}}$ as a function of the singular value decomposition (SVD) of $\mathbf{H}_{\mathrm{UL}}$

$$\mathbf{H}_{\mathrm{UL}} = \begin{bmatrix} \mathbf{U}_1 & \mathbf{U}_2 \end{bmatrix} \begin{bmatrix} \mathbf{\Sigma}_{K \times K} & \mathbf{0}_{N-K \times K}^{H} \end{bmatrix}^{H} \mathbf{V}^{H}.$$

We then find $\mathbf{P}_{\mathrm{UL}} = \mathbf{U}_2 \mathbf{U}_2^H$ where $\mathbf{U}_2$ is the $N \times N-K$ matrix composed of the $N-K$ left singular vectors of $\mathbf{H}_{\mathrm{UL}}$ associated to its zero singular values. It is then straightforward to see that the rank of $\mathbf{P}_{\mathrm{UL}}$ is the dimension of the left null space of $\mathbf{H}_{\mathrm{UL}}$, *i.e.*, $N-K$. First, if $N-K \geq K$, matrix $\mathbf{H}_{\mathrm{UL}}^{(1)H} \mathbf{P}_{\mathrm{UL}} \mathbf{H}_{\mathrm{UL}}^{(1)}$ is full rank and the limit becomes

$$\lim_{N_0 \to 0} \tilde{\mathbf{B}} = -\mathbf{H}_{\mathrm{UL}}^{\dagger} \mathbf{H}_{\mathrm{UL}}^{(1)} \left(\mathbf{H}_{\mathrm{UL}}^{(1)H} \mathbf{P}_{\mathrm{UL}} \mathbf{H}_{\mathrm{UL}}^{(1)} \right)^{-1} \mathbf{H}_{\mathrm{UL}}^{(1)H}.$$

Replacing this expression of $\tilde{\mathbf{B}}$ into (3.7), it can be seen that the limit of the asymptotic MSE at high SNR will tend to zero. This means that for twice as many antennas as the number of served users, we can completely remove the first order approximation of the distortion caused by channel frequency selectivity.

As for the case $N-K < K$, using the fact that $\mathbf{P}_{\mathrm{UL}} = \mathbf{U}_2 \mathbf{U}_2^H$, one can reapply the matrix inversion lemma on $\tilde{\mathbf{B}} \mathbf{P}_{\mathrm{UL}}$ in order to show that the limit becomes

$$\lim_{N_0 \to 0} \tilde{\mathbf{B}}\mathbf{P}_{\mathrm{UL}} = -\mathbf{H}_{\mathrm{UL}}^{\dagger}\mathbf{H}_{\mathrm{UL}}^{(1)}\mathbf{H}_{\mathrm{UL}}^{(1)H}\mathbf{U}_2\left(\mathbf{U}_2^H\mathbf{H}_{\mathrm{UL}}^{(1)}\mathbf{H}_{\mathrm{UL}}^{(1)H}\mathbf{U}_2\right)^{-1}\mathbf{U}_2^H.$$

In this case, the noise term of the MSE will tend to zero but the first order approximation of the distortion will only be partially compensated for.

We can conclude that the optimized ZF equalizer and pre-equalizer can be written in a compact expression as the pseudo-inverse of the channel plus a matrix lying on the null space of the channel. This design can compensate for the degradation due to channel frequency selectivity and even completely remove the first order approximation of the distortion for twice as many BS antennas as the number of served users.

3.2.2 Minimum mean squared error design

The previous designs rely on a ZF criterion which restricts the solution domain. In the following, we do not make this assumption and we look at the general MMSE design which will achieve an optimized performance. Indeed, for low SNR situations or highly selective subchannels, inverting the channel might strongly degrade the performance. Furthermore, the channel matrix $\mathbf{H}$ does not generally need to be full rank.

Equalizer (multiple access channel, UL)

For the equalizer case, due to the power normalization constraint (3.3), we impose

$$\mathbf{A}_{\mathrm{UL}}^{\mathrm{MMSE}} = \xi_{\mathrm{UL}}^{\mathrm{MMSE}}\mathbf{I}_K$$
$$\mathbf{B}_{\mathrm{UL}}^{\mathrm{MMSE}} = \frac{1}{\xi_{\mathrm{UL}}^{\mathrm{MMSE}}}\hat{\mathbf{B}},$$

where $\xi_{\mathrm{UL}}^{\mathrm{MMSE}} = \sqrt{\frac{G_T}{K}}$. The notation $\hat{\mathbf{B}} = \xi_{\mathrm{UL}}^{\mathrm{MMSE}} \mathbf{B}_{\mathrm{UL}}^{\mathrm{MMSE}}$ is introduced to clarify the following expressions by suppressing the dependence in $\xi_{\mathrm{UL}}^{\mathrm{MMSE}}$. The two imaginary terms of the distortion in (3.2) again disappear since the pre-equalizer is frequency independent, $((\mathbf{A}_{\mathrm{UL}}^{\mathrm{MMSE}})^{(1)} = \mathbf{0})$ and the optimization problem takes the following quadratic form in $\hat{\mathbf{B}}$

$$\begin{aligned}\min_{\hat{\mathbf{B}}} \mathrm{MSE}(m) = & \frac{E_s}{2} \mathrm{tr}\Big[(\hat{\mathbf{B}}\mathbf{H}_{\mathrm{UL}} - \mathbf{I})(\hat{\mathbf{B}}\mathbf{H}_{\mathrm{UL}} - \mathbf{I})^H\Big] \\ & + E_s \tilde{\eta} \mathrm{tr}\Big[\left(\hat{\mathbf{B}}\mathbf{H}_{\mathrm{UL}}^{(1)}\right)\left(\hat{\mathbf{B}}\mathbf{H}_{\mathrm{UL}}^{(1)}\right)^H\Big] \\ & + E_s \tilde{\eta} \Re \mathrm{tr}\Big[(\hat{\mathbf{B}}\mathbf{H}_{\mathrm{UL}} - \mathbf{I})(\hat{\mathbf{B}}\mathbf{H}_{\mathrm{UL}}^{(2)})^H\Big] \\ & + \frac{N_0 K}{2 G_T} \mathrm{tr}\Big[\hat{\mathbf{B}}\hat{\mathbf{B}}^H\Big].\end{aligned}$$

Setting the derivative of this expression with respect to $\hat{\mathbf{B}}^*$ to $\mathbf{0}$ yields the MMSE equalizer given by

$$\begin{aligned}\hat{\mathbf{B}} = & \left(\mathbf{H}_{\mathrm{UL}}^H + \tilde{\eta}\mathbf{H}_{\mathrm{UL}}^{(2)H}\right)\Big(\mathbf{H}_{\mathrm{UL}}\mathbf{H}_{\mathrm{UL}}^H + 2\tilde{\eta}\mathbf{H}_{\mathrm{UL}}^{(1)}\mathbf{H}_{\mathrm{UL}}^{(1)H} \\ & + \tilde{\eta}\left(\mathbf{H}_{\mathrm{UL}}\mathbf{H}_{\mathrm{UL}}^{(2)H} + \mathbf{H}_{\mathrm{UL}}^{(2)}\mathbf{H}_{\mathrm{UL}}^H\right) + \frac{N_0 K}{G_T E_s}\mathbf{I}_N\Big)^{-1}.\end{aligned} \tag{3.9}$$

Pre-equalizer (broadcast channel, DL)

In the pre-equalizer case, due to the normalization constraint, we have

$$\begin{aligned}\mathbf{A}_{\mathrm{DL}}^{\mathrm{MMSE}} &= \frac{1}{\xi_{\mathrm{DL}}^{\mathrm{MMSE}}} \hat{\mathbf{A}} \\ \mathbf{B}_{\mathrm{DL}}^{\mathrm{MMSE}} &= \xi_{\mathrm{DL}}^{\mathrm{MMSE}} \mathbf{I}_K,\end{aligned}$$

with $\xi_{\mathrm{DL}}^{\mathrm{MMSE}} = \sqrt{\frac{\mathrm{tr}\left[\hat{\mathbf{A}}\hat{\mathbf{A}}^H\right]}{G_T}}$. As opposed to all of the previous designs, the imaginary terms of the distortion in (3.2) do not cancel out. The optimization of those two terms is difficult due to the dependence in $(\mathbf{A}_{\mathrm{DL}}^{\mathrm{MMSE}})^{(1)}$. The derivative implies that the optimization of the pre-equalizer of one subcarrier depends on the neighboring subcarriers and the optimization can no longer be done locally at the subcarrier level, which increases the problem complexity and is not comparable to the other designs. Hence, we propose to impose an additional constraint which cancels the imaginary terms of (3.2), *i.e.*, $\Im(\mathbf{H}_{\mathrm{DL}}\mathbf{A}_{\mathrm{DL}}^{\mathrm{MMSE}}) = \mathbf{0}$. This somehow means that we have a ZF design on the imaginary part of $\mathbf{H}_{\mathrm{DL}}\mathbf{A}_{\mathrm{DL}}^{\mathrm{MMSE}}$ and a MMSE design on its real part. We then have to minimize the following Lagrangian formulation including the constraint via the Lagrange multiplier $\mathbf{\Theta}$

$$\begin{aligned}\min_{\hat{\mathbf{A}}} L = {} & \frac{E_s}{2}\mathrm{tr}\Big[(\mathbf{H}_{\mathrm{DL}}\hat{\mathbf{A}} - \mathbf{I})(\mathbf{H}_{\mathrm{DL}}\hat{\mathbf{A}} - \mathbf{I})^H\Big] \\ & + E_s\tilde{\eta}\mathrm{tr}\left[\left(\mathbf{H}_{\mathrm{DL}}^{(1)}\hat{\mathbf{A}}\right)\left(\mathbf{H}_{\mathrm{DL}}^{(1)}\hat{\mathbf{A}}\right)^H\right] \\ & + E_s\tilde{\eta}\Re\,\mathrm{tr}\Big[(\mathbf{H}_{\mathrm{DL}}\hat{\mathbf{A}} - \mathbf{I})(\mathbf{H}_{\mathrm{DL}}^{(2)}\hat{\mathbf{A}})^H\Big] \\ & + \frac{N_0 K}{2G_T}\mathrm{tr}\Big[\hat{\mathbf{A}}\hat{\mathbf{A}}^H\Big] \\ & + \frac{\jmath}{2}\mathrm{tr}\Big[\mathbf{\Theta}^T(\mathbf{H}_{\mathrm{DL}}\hat{\mathbf{A}} - \mathbf{H}_{\mathrm{DL}}^*\hat{\mathbf{A}}^*)\Big].\end{aligned}$$

Setting the derivative of L with respect to $\hat{\mathbf{A}}$ to $\mathbf{0}$ yields the pre-equalizer given by

$$\begin{aligned}\hat{\mathbf{A}} = {} & \left(\mathbf{H}_{\mathrm{DL}}^H\mathbf{H}_{\mathrm{DL}} + 2\tilde{\eta}\mathbf{H}_{\mathrm{DL}}^{(1)H}\mathbf{H}_{\mathrm{DL}}^{(1)} + \tilde{\eta}\left(\mathbf{H}_{\mathrm{DL}}^H\mathbf{H}_{\mathrm{DL}}^{(2)} + \mathbf{H}_{\mathrm{DL}}^{(2)H}\mathbf{H}_{\mathrm{DL}}\right)\right. \\ & \left. + \frac{N_0 K}{G_T E_s}\mathbf{I}_N\right)^{-1}\left(\mathbf{H}_{\mathrm{DL}}^H + \tilde{\eta}\mathbf{H}_{\mathrm{DL}}^{(2)H} + \frac{\jmath}{E_s}\mathbf{H}_{\mathrm{DL}}^H\mathbf{\Theta}\right),\end{aligned}$$

where the value of $\mathbf{\Theta}$ is fixed thanks to the constraint $\Im(\mathbf{H}_{\mathrm{DL}}\mathbf{A}) = \mathbf{0}$. Denoting $\mathbf{X} = \mathbf{H}_{\mathrm{DL}}^H\mathbf{H}_{\mathrm{DL}} + 2\tilde{\eta}\mathbf{H}_{\mathrm{DL}}^{(1)H}\mathbf{H}_{\mathrm{DL}}^{(1)} + \tilde{\eta}\left[\mathbf{H}_{\mathrm{DL}}^H\mathbf{H}_{\mathrm{DL}}^{(2)} + \mathbf{H}_{\mathrm{DL}}^{(2)H}\mathbf{H}_{\mathrm{DL}}\right] + \frac{N_0 K}{G_T}\mathbf{I}_N$, we find

$$\mathbf{\Theta} = -E_s\left(\Re\left(\mathbf{H}_{\mathrm{DL}}\mathbf{X}^{-1}\mathbf{H}_{\mathrm{DL}}^H\right)\right)^{-1}\Im(\mathbf{H}_{\mathrm{DL}}\mathbf{X}^{-1}(\mathbf{H}_{\mathrm{DL}}^H + \tilde{\eta}\mathbf{H}_{\mathrm{DL}}^{(2)H})).$$

Table 3.2 Complexity of calculating the proposed pre-equalizers and equalizers.

	Equalizer (Uplink, MAC channel)	Pre-equalizer (Downlink, BC channel)
Classical ZF	$O(2NK^2 + K^3)$	$O(3NK^2 + K^3)$
Opt. ZF	$O(4NK^2 + 4N^2K + 2K^3)$	$O(5NK^2 + 4N^2K + 2K^3)$
Classical MMSE	$O(2N^2K + N^3)$	$O(2N^2K + NK^2 + N^3)$
Opt. MMSE	$O(5N^2K + N^3)$	$O(6N^2K + 3NK^2 + 2K^3 + N^3)$

3.2.3 Complexity of computation of the proposed pre-equalizers and equalizers

Table 3.2 gives an order of complexity of computing the proposed optimized designs with respect to classical designs. By classical designs, we mean pre-equalizers and equalizers that rely on the hypothesis of channel frequency flatness at the subcarrier level, *i.e.*, $\mathbf{H}^{(1)}(\omega_m) = \mathbf{H}^{(2)}(\omega_m) = \mathbf{0}$. For the calculation, only matrix multiplications and inversions are taken into account given that they are the most complex operations. It is assumed that for general matrices $\mathbf{D} \in \mathbb{C}^{l\times m}, \mathbf{E} \in \mathbb{C}^{m\times n}, \mathbf{F} \in \mathbb{C}^{m\times m}$, performing matrix multiplication $\mathbf{DE}$ has complexity $O(lmn)$ and matrix inversion $\mathbf{F}^{-1}$ has complexity $O(m^3)$. One can check that the calculation complexity of the optimized designs remains similar to the classical. Note that the designs in DL are more complex since they require one more matrix multiplication for the calculation of ξ_{DL}. Furthermore, the opt. MMSE pre-equalizer is slightly more complex than the opt. MMSE equalizer due to the required calculation of $\boldsymbol{\Theta}$.

3.3 Simulation results

The following simulations first aim at demonstrating the accuracy of the derived asymptotic MSE expression in practical situations. Secondly, they validate the performance of the optimized pre-equalizers and equalizers w.r.t. classical pre-equalizer and equalizer designs. A FBMC-OQAM system is considered with $2M = 128$ subcarriers and subcarrier spacing 15 kHz as in LTE. The channels are randomly drawn

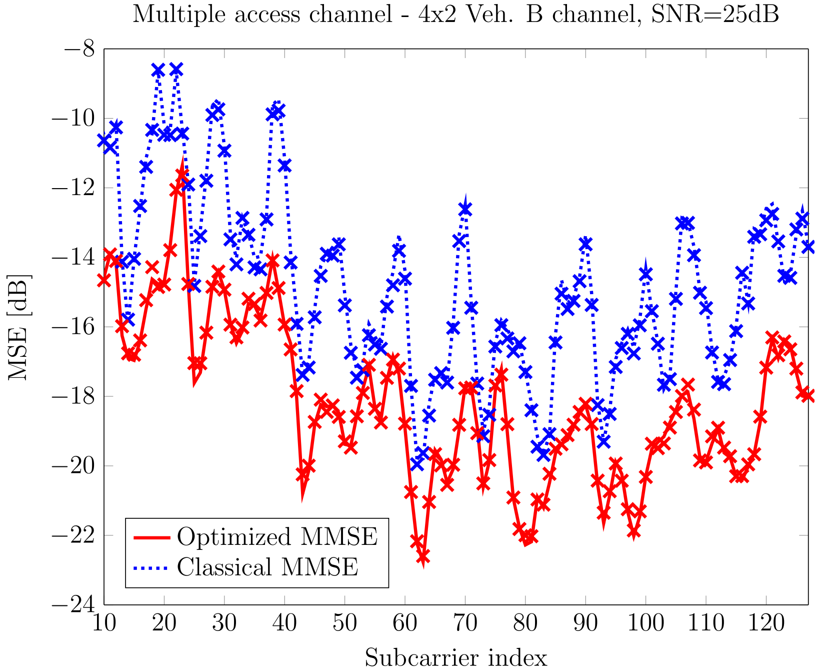

Figure 3.4 The optimized MMSE equalizer clearly outperforms the classical MMSE equalizer. The asymptotic approximation of the MSE represented in a solid line matches perfectly the simulated MSE in crosses.

from the ITU Vehicular A or B channel model, *i.e.* a mildly or highly frequency selective channel respectively. Furthermore, they remain constant during the frame transmission (quasi-static assumption). The Phydyas prototype pulse with overlapping factor $\kappa = 4$ is used in the simulations [6]. This pulse does not fully satisfy the PR constraints but is of the NPR type. Given that it almost fulfills PR constraints, the derived MSE expression (3.1) remains a very good approximation of the distortion, as will be shown in the following.

Fig. 3.4 shows the MSE of the classical and optimized MMSE equalizers for a specific channel realization. The channel model simulated is the Vehicular B channel. The BS is assumed to have $N = 4$ antennas serving $K = 2$ users and the SNR of the system is 25 dB. One can first check that

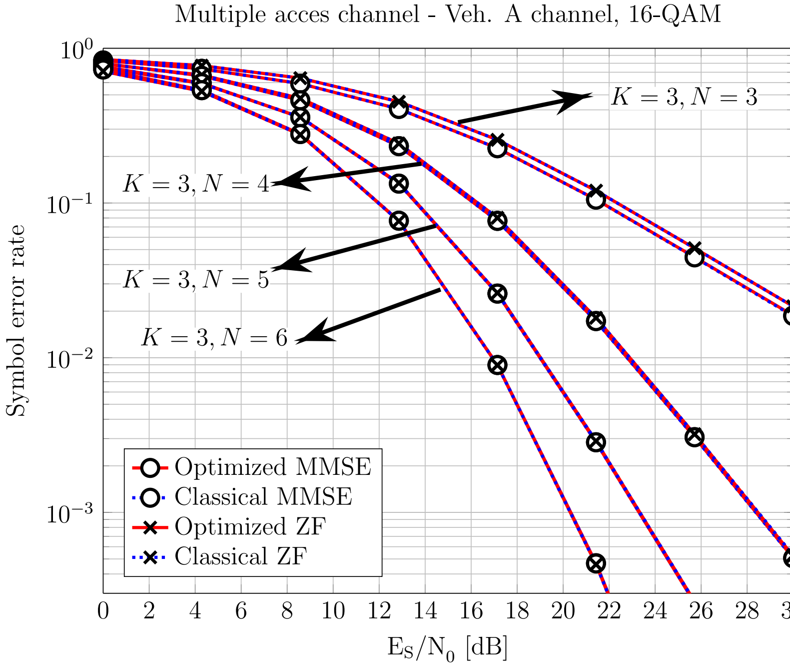

Figure 3.5 SER of the optimized and classical ZF/MMSE equalizers and Veh. A channel model.

the simulated MSE (in cross markers) perfectly matches the theoretical approximation (in solid line) of (3.1). Furthermore, in the high SNR regime considered here, the classical MMSE equalizer is limited by the distortion induced by the channel frequency selectivity. On the other hand, the optimized MMSE equalizer uses the two extra antennas to cancel the distortion, giving a clear gain of performance.

In Fig. 3.5 and Fig. 3.6, the symbol error rate (SER) for the classical and optimized equalizers are plotted for a fixed number of users $K = 3$ and different number of BS antennas N. The signal constellation is a 16-QAM. In Fig. 3.5, the Veh. A channel model is considered and the classical equalizers can achieve the same performance as the optimized ones. This comes from the fact that the assumption of an approximately flat channel inside each subchannel is accurate. On the other hand, in Fig. 3.6, the Veh. B channel model is considered, *i.e.*, a highly selective

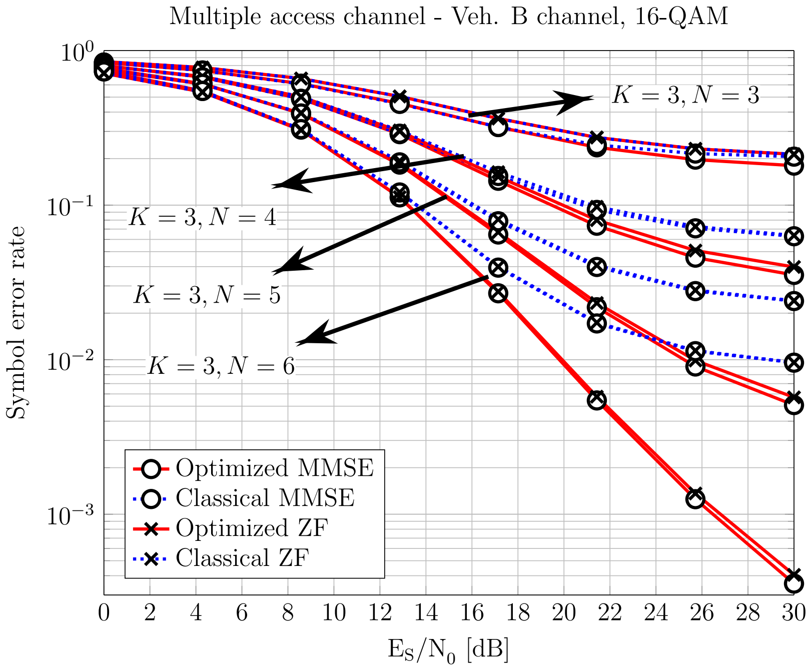

Figure 3.6 SER of the optimized and classical ZF/MMSE equalizer and Veh. B channel model

channel. The SER saturates very quickly with a classical equalizer while the optimized ZF or MMSE equalizer can compensate for the distortion as the number of BS antennas N grows and the SER therefore saturates at higher SNR. In the case $K = 3, N = 6$, the SER does not even saturate in the considered SNR range since the BS has twice as many antennas and can completely remove the first order approximation of the distortion. This is in accordance with the asymptotic study at high SNR conducted in Section 3.2.1. As expected, the MMSE designs outperform the ZF designs, and this gain is larger for a small number of BS antennas. Indeed, as the number of BS antennas increases, the interference can be better handled and the regularization gain of the MMSE equalizer is reduced.

In Fig. 3.7, a 4-QAM constellation and the Veh. B channel model are considered in the UL. The proposed equalizer designs are compared

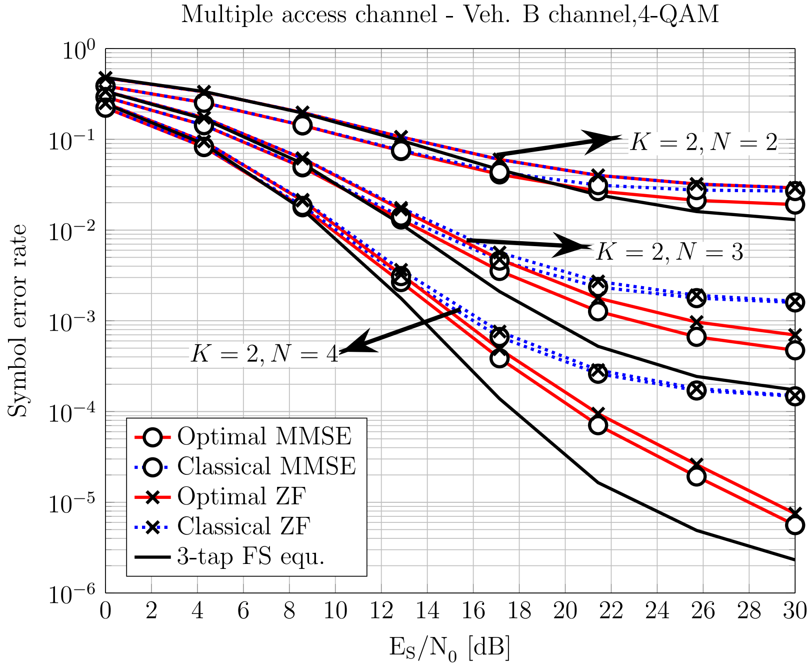

Figure 3.7 SER of the optimized and classical ZF/MMSE equalizer and a 3-tap frequency sampling equalizer.

with a 3-tap frequency sampling equalizer that follows the design of [44] with target frequency points chosen according to a ZF criterion. One can check that the 3-tap equalizer has a gain of performance relative to the proposed designs for the same antenna configuration. Note however that the multi-tap design has a much larger complexity in terms of hardware implementation and calculation of the equalizer coefficients. Moreover, it adds a reconstruction delay to the demodulation chain.

Fig. 3.8 has exactly the same simulation parameters as Fig. 3.7 but for the DL. One can check that the performance of the ZF pre-equalizer in DL is similar to the equalizer one in UL. Note that the SER performances of the pre-equalizer and equalizer might differ. Indeed, even though the MSE expression is dual in UL and in DL, the distribution of the per-stream SER might differ due to the correlation of the noise arising in UL

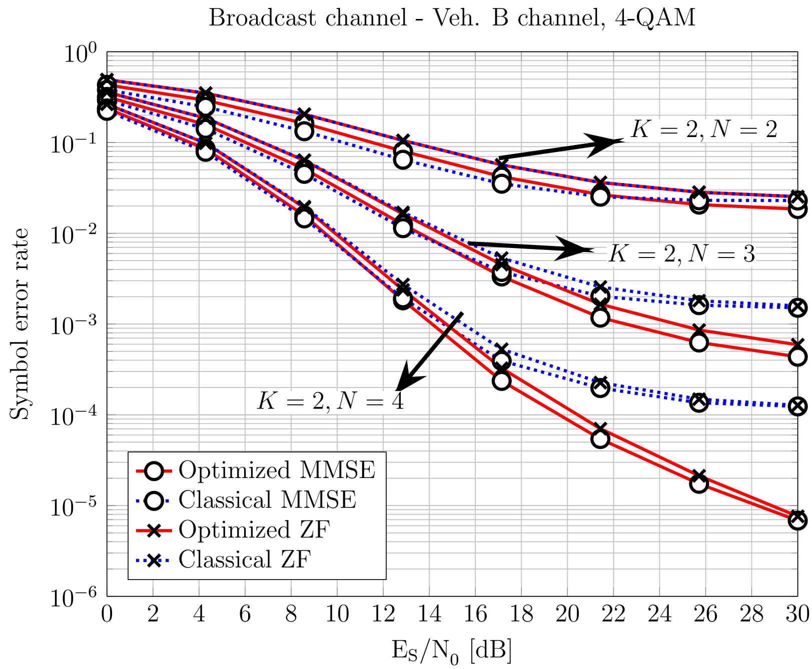

Figure 3.8 SER of the optimized, classical ZF/MMSE pre-equalizer.

but not in DL. Moreover, due to the ZF constraint on $\Im(\mathbf{H}_{\mathrm{DL}}\mathbf{A}_{\mathrm{DL}}^{\mathrm{MMSE}}) = 0$, the optimized MMSE pre-equalizer performs slightly worse than the classical MMSE pre-equalizer at low SNR.

3.4 Conclusion

We investigated the design of optimized FBMC-OQAM single-tap pre-equalizers and equalizers for a MU MIMO scenario highly selective channel. The asymptotic expression of the MSE of a FBMC-OQAM transceiver was recalled, simplified and generalized. Optimizing the MSE expression, expressions of the optimized single-tap pre-equalizers and equalizers were found under either a ZF criterion or a MMSE criterion. As soon as the BS has more antennas than the number of users, the optimized structures use those extra degrees of freedom to compensate for the distortion induced by channel frequency selectivity. From an asymptotic study at high SNR, it was shown that the first order approximation of the distortion can even be completely removed if the BS has at least twice as many antennas as the number of users. Simulation results have demonstrated the accuracy of the new asymptotic expression of the distortion as well as the performance of the optimized pre-equalizers and equalizers.

3.5 Proofs

3.5.1 Distortion expression

In this appendix, we are interested only in the intrinsic distortion caused by the FBMC signal itself in the presence of channel frequency selectivity. Since the additive noise samples are assumed to be uncorrelated with the signal of interest, we will assume a noise-free received signal. In order to derive the distortion expression, we will first define different notations and recall one Lemma of [55].

We define $\mathbf{y}^{p,g}_{m_0,l_0} \in \mathbb{C}^{S\times 1}$ as

$$\mathbf{y}^{p,g}_{m_0,l_0} = \sum_{l=0}^{2N_s-1} \sum_{m=0}^{2M-1} \mathbf{d}_{m,l} \sum_{n=0}^{L_q-1} p_{m,l}[n] g^*_{m_0,l_0}[n].$$

The symbols $\mathbf{y}^{p,g}_{m_0,l_0}$ can be seen as the complex demodulated samples at subcarrier m_0 and multicarrier symbol l_0, before de-staggering, if the real-valued symbols streams $\mathbf{d}_{m,l}$ are FBMC/OQAM modulated using a prototype pulse $p[n]$ and demodulated using a prototype pulse $g[n]$ and for an ideal channel, *i.e.*, $\mathbf{H}(\omega) = \mathbf{I}_S$. To compensate for the effect of the channel, a single-tap precoding matrix $\mathbf{A}(\omega)$ and decoding matrix $\mathbf{B}(\omega)$ are used, operating at the per-subcarrier level. At the transmitter, the symbols $\mathbf{d}_{m,l}$ are precoded by matrix $\mathbf{A}(\omega_m)$. At the receiver, the equalized symbols are denoted by $\mathbf{x}_{m_0,l_0} = \mathbf{B}(\omega_{m_0})\mathbf{z}_{m_0,l_0}$ where $\mathbf{z}_{m_0,l_0}$ are the demodulated symbols at the receiver before equalization.

To derive the result of Theorem 2, we will use the following result, proven in [55]. We will basically assume that all frequency depending quantities are smooth functions of ω and that the prototype pulses are sampled versions of smooth analog waveforms, namely, $(\mathbf{As1})$-$(\mathbf{As2})$.

Lemma 1. *Under assumptions* $(\mathbf{As1})$-$(\mathbf{As2})$*, we have*

$$\mathbf{z}_{m_0,l_0} = \sum_{q=0}^{Q} \sum_{q'=0}^{Q-q} \frac{(-j)^{q+q'}}{(2M)^{q+q'} q! q'!} \mathbf{H}^{(q)} \mathbf{A}^{(q')} \mathbf{y}_{m_0,l_0}^{p,g^{(q)}}(q') + O(M^{-Q})$$

where

$$\mathbf{y}_{m_0,l_0}^{p,g^{(q)}}(q') = \sum_{r=0}^{q'} \frac{q'!}{r!(q'-r)!} (-1)^r \mathbf{y}_{m_0,l_0}^{p^{(r)},g^{(q+q'-r)}}$$

and where $p^{(r)}$, $g^{(r)}$ are the sampled versions of the r-th time domain derivatives of the original prototype pulses. Superscript $^{(q)}$ denotes the q-th order derivative of the corresponding frequency dependent quantity, which always is evaluated at subcarrier m_0 (here and in the following of Section 3.5).

A direct application of the above lemma for $Q = 2$ allows us to write

$$\mathbf{x}_{m_0,l_0} = \mathbf{BHAy}_{m_0,l_0} - \frac{j}{2M} \boldsymbol{\epsilon}_1 - \frac{1}{2(2M)^2} \boldsymbol{\epsilon}_2 + O(M^{-2}) \tag{3.10}$$

where we have defined

$$\begin{aligned}
\boldsymbol{\epsilon}_1 &= \mathbf{B} \left(\mathbf{HA}\right)^{(1)} \mathbf{y}_{m_0,l_0}^{p,g^{(1)}} - \mathbf{BHA}^{(1)} \mathbf{y}_{m_0,l_0}^{p^{(1)},g} \\
\boldsymbol{\epsilon}_2 &= \mathbf{B} \left(\mathbf{HA}\right)^{(2)} \mathbf{y}_{m_0,l_0}^{p,g^{(2)}} - 2\mathbf{B} \left(\mathbf{HA}^{(1)}\right)^{(1)} \mathbf{y}_{m_0,l_0}^{p^{(1)},g^{(1)}} + \mathbf{BHA}^{(2)} \mathbf{y}_{m_0,l_0}^{p^{(2)},g}.
\end{aligned}$$

At this point, force $p = g$ so that the same prototype pulse is used at both transmitter and receiver. The distortion power $P_d(m)$ was defined in (6.1) as (in the absence of noise)

$$P_d(m) = \mathbb{E}\left(\|\Re(\mathbf{x}_{m_0,l_0}) - \mathbf{d}_{m_0,l_0}\|^2\right). \tag{3.11}$$

We now need to define some pulse-related quantities. Given two generic pulses, p, q of length $2M\kappa$ and let $\mathbf{P}$ and $\mathbf{Q}$ denote two $2M \times \kappa$ matrices obtained by arranging the samples of the respective pulses in columns from left to right. We will define

$$\begin{aligned}\mathcal{R}(p,q) &= \mathbf{P} \circledast \mathbf{J}_{2M}\mathbf{Q}\\ \mathcal{S}(p,q) &= (\mathbf{J}_2 \otimes \mathbf{I}_M)\, \mathbf{P} \circledast \mathbf{J}_{2M}\mathbf{Q}\end{aligned}$$

where $\circledast$ denotes row-wise convolution, $\otimes$ denotes Kronecker product, $\mathbf{I}_M$ (resp. $\mathbf{J}_M$) are the identity (resp. exchange) matrices of order M. Given four generic pulses p, q, r, s, we define

$$\begin{aligned}\eta^{\pm}(p,q,r,s) &= \frac{M}{2}\mathrm{tr}\left[\mathbf{U}^{+}\mathcal{R}(p,q)\,\mathcal{R}^{T}(r,s) + \mathbf{U}^{-}\mathcal{S}(p,q)\,\mathcal{S}^{T}(r,s)\right]\\ \eta^{\mp}(p,q,r,s) &= \frac{M}{2}\mathrm{tr}\left[\mathbf{U}^{-}\mathcal{R}(p,q)\,\mathcal{R}^{T}(r,s) + \mathbf{U}^{+}\mathcal{S}(p,q)\,\mathcal{S}^{T}(r,s)\right],\end{aligned}$$

where $\mathbf{U}^{\pm} = \mathbf{I}_2 \otimes (\mathbf{I}_M \pm \mathbf{J}_M)$. In order to simplify the notations, given four integers m, n, r, s, we will define $\eta^{(+,-)}_{mnrs} = \eta^{\pm}\left(p^{(m)}, p^{(n)}, p^{(r)}, p^{(s)}\right)$.

Assuming that the pulse has PR properties $(\mathbf{As2})$ so that $\mathbf{d}_{m_0,l_0} = \Re(\mathbf{y}^{p,g}_{m_0,l_0})$, we can obtain an asymptotic expression for this distortion by simply inserting (3.10) in (3.11) for $p = q$ and by using the fact that [53, Appendix B]

$$\begin{aligned}\mathbb{E}\left(\Re(\mathbf{y}^{p^{(m)},q^{(n)}}_{m_0,l_0})\Re^{T}(\mathbf{y}^{p^{(r)},q^{(s)}}_{m_0,l_0})\right) &= E_s\eta^{(+,-)}_{mnrs}\mathbf{I}_S\\ \mathbb{E}\left(\Im(\mathbf{y}^{p^{(m)},q^{(n)}}_{m_0,l_0})\Im^{T}(\mathbf{y}^{p^{(r)},q^{(s)}}_{m_0,l_0})\right) &= E_s\eta^{(-,+)}_{mnrs}\mathbf{I}_S\\ \mathbb{E}\left(\Re(\mathbf{y}^{p^{(m)},q^{(n)}}_{m_0,l_0})\Im^{T}(\mathbf{y}^{p^{(r)},q^{(s)}}_{m_0,l_0})\right) &= \mathbf{0}.\end{aligned}$$

The resulting expression can be more compactly expressed by using the fact that $\eta^{(+,-)}_{mnrs} = \eta^{(+,-)}_{rsmn}$, $\eta^{(+,-)}_{mnrs} = \eta^{(+,-)}_{nmsr}$,[5] as established in Lemma 2 of Appendix 3.5.2. Furthermore, if we assume that the prototype pulse is either symmetric or anti-symmetric, one can establish that $\eta^{(+,-)}_{0000} =$

[5]Obviously, the same identities hold if $(+,-)$ is replaced by $(-,+)$.

$\eta_{0000}^{(-,+)}$, $\eta_{0001}^{(+,-)} = \eta_{0001}^{(-,+)}$, $\eta_{0101}^{(+,-)} = \eta_{0101}^{(-,+)}$ and $\eta_{0020}^{(+,-)} = \eta_{0020}^{(-,+)}$, a fact that is proven in Lemma 3 of Appendix 3.5.2. If, additionally, the prototype pulse meets the PR conditions, we can guarantee that $\eta_{0001}^{(+,-)} = 0$ as established in Lemma 4 of Appendix 3.5.2.

Using all this, together with the fact that

$$\begin{aligned}
\text{tr}\left[\Re(\mathbf{X})\Re^T(\mathbf{Y}) + \Im(\mathbf{X})\Im^T(\mathbf{Y})\right] &= \Re\text{tr}\left[\mathbf{X}\mathbf{Y}^H\right] \\
\text{tr}\left[\Im(\mathbf{X})\Re^T(\mathbf{Y}) - \Re(\mathbf{X})\Im^T(\mathbf{Y})\right] &= \Im\text{tr}\left[\mathbf{X}\mathbf{Y}^H\right]
\end{aligned}$$

for any complex valued matrices $\mathbf{X}$, $\mathbf{Y}$ of appropriate dimensions, we see that

$$P_d(m) = E_s\xi_{0,m} + E_s\frac{1}{(2M)^2}\xi_{2,m} + O\left(M^{-2}\right) \tag{3.12}$$

where we have defined

$$\begin{aligned}
\xi_{0,m} &= \eta_{0000}^{(+,-)}\text{tr}\left[(\mathbf{BHA}-\mathbf{I})(\mathbf{BHA}-\mathbf{I})^H\right] \\
\xi_{2,m} &= \eta_{1010}^{(+,-)}\left(\text{tr}\left[\mathbf{BHA}^{(1)}\left(\mathbf{BHA}^{(1)}\right)^H\right]\right. \\
&\quad \left.+\text{tr}\left[\mathbf{B}\left(\mathbf{HA}\right)^{(1)}\left(\mathbf{B}\left(\mathbf{HA}\right)^{(1)}\right)^H\right]\right) \\
&\quad - \eta_{2000}^{(+,-)}\left(\Re\text{tr}\left[(\mathbf{BHA}-\mathbf{I})\left(\mathbf{BHA}^{(2)}\right)^H\right]\right. \\
&\qquad \left.+\Re\text{tr}\left[(\mathbf{BHA}-\mathbf{I})\left(\mathbf{B}\left(\mathbf{HA}\right)^{(2)}\right)^H\right]\right) \\
&\quad + 2\eta_{0011}^{(+,-)}\text{tr}\left[\Re\left(\mathbf{BHA}-\mathbf{I}\right)\Re^T\left(\mathbf{B}\left(\mathbf{HA}^{(1)}\right)^{(1)}\right)\right] \\
&\quad + 2\eta_{0011}^{(-,+)}\text{tr}\left[\Im\left(\mathbf{BHA}-\mathbf{I}\right)\Im^T\left(\mathbf{B}\left(\mathbf{HA}^{(1)}\right)^{(1)}\right)\right] \\
&\quad - 2\eta_{1001}^{(+,-)}\text{tr}\left[\Im\left(\mathbf{B}\left(\mathbf{HA}\right)^{(1)}\right)\Im^T\left(\mathbf{BHA}^{(1)}\right)\right] \\
&\quad - 2\eta_{1001}^{(-,+)}\text{tr}\left[\Re\left(\mathbf{B}\left(\mathbf{HA}\right)^{(1)}\right)\Re^T\left(\mathbf{BHA}^{(1)}\right)\right]
\end{aligned}$$

and where all frequency-depending matrices are evaluated at $\omega = \omega_m$.

It is easy to see that, thanks to the PR property of the prototype pulse, we will have $\eta_{0000}^{(+,-)} = 1/2$. Therefore, the asymptotic distortion power depends on six different pulse-related quantities, which present some non-trivial interrelationships. To establish these interrelationships, we invoke again Lemma 3 of Section 3.5.2. In particular, the relationships in (3.17)-(3.18) allow us to establish

$$\left[\eta_{1001}^{(+,-)} - \eta_{1001}^{(-,+)}\right] - \left[\eta_{0011}^{(+,-)} - \eta_{0011}^{(-,+)}\right] = 0 \tag{3.13}$$

$$\eta_{0011}^{(+,-)} + \eta_{1010}^{(+,-)} = 0. \tag{3.14}$$

We can find further equivalences between the different pulse quantities by considering here the asymptotic domain as $M \to \infty$ together with the fact that the prototype pulse is, by assumption, a sampled version of a smooth analog waveform.

Indeed, applying the result in Proposition 1, Corollary 1 and Lemma 6 in Section 3.5.2 together with the fact that the prototype pulse is symmetric and PR compliant, we obtain

$$\eta_{2000}^{(+,-)} - \eta_{0011}^{(+,-)} + \eta_{1010}^{(+,-)} - \eta_{1001}^{(-,+)} = O(M^{-1}) \tag{3.15}$$

$$\eta_{0011}^{(+,-)} - \eta_{2000}^{(+,-)} = O(M^{-2}). \tag{3.16}$$

We may consider the system of equations formed by (3.13),(3.14),(3.15) and (3.16). Denoting $\eta = \eta_{1010}^{(+,-)}$ and $\zeta = \eta_{0011}^{(-,+)}$, we can express the system of equations as

$$\begin{bmatrix} 1 & -1 & -1 & 0 \\ 0 & 0 & 1 & 0 \\ 0 & -1 & -1 & 1 \\ 0 & 0 & 1 & -1 \end{bmatrix} \begin{bmatrix} \eta_{1001}^{(+,-)} \\ \eta_{1001}^{(-,+)} \\ \eta_{0011}^{(+,-)} \\ \eta_{2000}^{(+,-)} \end{bmatrix} = \begin{bmatrix} -\zeta \\ -\eta \\ -\eta \\ 0 \end{bmatrix} + O(M^{-1})$$

so that we can conclude that

$$\begin{bmatrix} \eta_{1001}^{(+,-)} \\ \eta_{1001}^{(-,+)} \\ \eta_{0011}^{(+,-)} \\ \eta_{2000}^{(+,-)} \end{bmatrix} = \begin{bmatrix} -\zeta \\ \eta \\ -\eta \\ -\eta \end{bmatrix} + O(M^{-1}).$$

Using this in (3.12), we obtain (3.2).

3.5.2 Some properties of the quantities $\eta_{mnrs}^{(+,-)}$

We now provide some identities on the quantities $\eta_{mnrs}^{(+,-)}$, $\eta_{mnrs}^{(-,+)}$ that will clearly simplify the expression for the asymptotic distortion derived above. We will begin by presenting some properties that hold exactly for all values of M.

Non-asymptotic properties

Let us begin with general properties that hold regardless of whether the pulses are symmetric or not.

Lemma 2. *By the definition of the $\eta^{\pm}(p,q,r,s)$, and regardless of the pulse symmetries, we have*

$$\eta^{\pm}(p,q,r,s) = \eta^{\pm}(r,s,p,q)$$

and

$$\eta^{\pm}(p,q,r,s) = \eta^{\pm}(q,p,s,r).$$

The same identities hold if $\pm$ is replaced by $\mp$ everywhere.

Proof. Indeed, the first result is a consequence of the fact that

$$\left(\mathbf{U}^{\pm}\mathcal{R}(p,q)\,\mathcal{R}^{T}(r,s)\right)^{T} = \mathcal{R}(r,s)\,\mathcal{R}^{T}(p,q)\,\mathbf{U}^{\pm}$$
$$\left(\mathbf{U}^{\pm}\mathcal{S}(p,q)\,\mathcal{S}^{T}(r,s)\right)^{T} = \mathcal{S}(r,s)\,\mathcal{S}^{T}(p,q)\,\mathbf{U}^{\pm}$$

whereas the second one follows from the identities

$$\begin{aligned}\mathcal{R}\left(p,q\right)\mathcal{R}^{T}\left(r,s\right)&=\mathbf{J}_{2M}\mathcal{R}\left(q,p\right)\mathcal{R}^{T}\left(s,r\right)\mathbf{J}_{2M},\\ \mathcal{S}\left(p,q\right)\mathcal{S}^{T}\left(r,s\right)&=\left(\mathbf{I}_{2}\otimes\mathbf{J}_{M}\right)\mathcal{S}\left(q,p\right)\mathcal{S}^{T}\left(s,r\right)\left(\mathbf{I}_{2}\otimes\mathbf{J}_{M}\right)\end{aligned}$$

and the definition of $\mathbf{U}^{\pm}$. □

Sometimes, it is useful to consider a relationship between quantities of the type $\eta^{\pm}$ and $\eta^{\mp}$. In order to obtain such relationships, we impose that the pulses are either symmetric or anti-symmetric in the time domain.

Lemma 3. *Assume that all the pulses p, q, r, s are either symmetric or anti-symmetric in the time domain. Let $s(p)$ be defined so that $s(p) = 0$ if the pulse p has even symmetry and $s(p) = 1$ if the pulse is anti-symmetric. Then, we can write*

$$\begin{aligned}&(-1)^{s(p)}\left[\eta^{\pm}(p,q,r,s)-\eta^{\mp}(p,q,r,s)\right]\\&+(-1)^{s(r)}\left[\eta^{\pm}(r,q,p,s)-\eta^{\mp}(r,q,p,s)\right]=0\end{aligned}\tag{3.17}$$

and also

$$\begin{aligned}&(-1)^{s(p)}\left[\eta^{\pm}(p,q,r,s)+\eta^{\mp}(p,q,r,s)\right]\\&\pm(-1)^{s(p)}\left[\eta^{\pm}(p,q,s,r)-\eta^{\mp}(p,q,s,r)\right]\\&=(-1)^{s(s)}\left[\eta^{\pm}(s,q,r,p)+\eta^{\mp}(s,q,r,p)\right]\end{aligned}\tag{3.18}$$

In particular, for the specific case where $p = r$ we have

$$\eta^{\pm}(p,q,p,s)=\eta^{\mp}(p,q,p,s).$$

Finally, if $q = s$ and the pulses p and r have the same type of symmetry, we have

$$\eta^{\pm}(p,q,r,q)=\eta^{\mp}(p,q,r,q).$$

Proof. Let us denote by $\mathcal{R}_1(p,q)$ and $\mathcal{R}_2(p,q)$ the upper and lower matrices of $\mathcal{R}(p,q)$, and equivalently for $\mathcal{S}_1(p,q)$ and $\mathcal{S}_2(p,q)$. Let $\mathbf{P}$ denote a $2M \times \kappa$ matrix obtained by arranging the pulse $p[n]$ in columns, and let $\mathbf{P}_1$ and $\mathbf{P}_2$ respectively denote the matrices obtained by selecting the M upper and lower rows of $\mathbf{P}$ respectively. By the symmetry of $p[n]$, we know that

$$\mathbf{P}_1 = (-1)^{s(p)}\mathbf{J}_M\mathbf{P}_2\mathbf{J}_{2\kappa-1}.$$

On the other hand, we can prove that, for any four matrices $\mathbf{A}, \mathbf{B}, \mathbf{C}$ and $\mathbf{D}$ of dimensions $M\times\kappa$, the diagonal entries of $(\mathbf{A} \circledast \mathbf{B}\mathbf{J}_\kappa)(\mathbf{C} \circledast \mathbf{D}\mathbf{J}_\kappa)^T \mathbf{J}_M$ are equal to the diagonal entries of $\mathbf{J}_M(\mathbf{C} \circledast \mathbf{J}_M\mathbf{B})(\mathbf{A} \circledast \mathbf{J}_M\mathbf{D})^T$. This shows that, using pulse symmetry,

$$\begin{aligned}
&\operatorname{tr}\left[\mathcal{R}_1(p,q)\,\mathcal{R}_1^T(r,s)\,\mathbf{J}_M\right] \\
&= \operatorname{tr}\left[\mathbf{J}_M(\mathbf{J}_M\mathbf{P}_1 \circledast \mathbf{Q}_2)(\mathbf{J}_M\mathbf{R}_1 \circledast \mathbf{S}_2)^T\right] \\
&= (-1)^{s(p)+s(r)}\operatorname{tr}\left[(\mathbf{P}_2\mathbf{J}_\kappa \circledast \mathbf{Q}_2)(\mathbf{R}_2\mathbf{J}_\kappa \circledast \mathbf{S}_2)^T\mathbf{J}_M\right] \\
&\overset{(*)}{=} (-1)^{s(p)+s(r)}\operatorname{tr}\left[\mathbf{J}_M(\mathbf{S}_2 \circledast \mathbf{J}_M\mathbf{P}_2)(\mathbf{Q}_2 \circledast \mathbf{J}_M\mathbf{R}_2)^T\right] \\
&= (-1)^{s(p)+s(r)}\operatorname{tr}\left[\mathbf{J}_M(\mathbf{P}_2 \circledast \mathbf{J}_M\mathbf{S}_2)(\mathbf{R}_2 \circledast \mathbf{J}_M\mathbf{Q}_2)^T\right] \\
&= (-1)^{s(p)+s(r)}\operatorname{tr}\left[\mathbf{J}_M\mathcal{S}_1(p,s)\,\mathcal{S}_1^T(r,q)\right] \\
&= (-1)^{s(p)+s(r)}\operatorname{tr}\left[\mathbf{J}_M\mathcal{S}_1(r,q)\,\mathcal{S}_1^T(p,s)\right]
\end{aligned}\tag{3.19}$$

where the identity in $(*)$ follows from the above convolution result. Equivalently, we will obviously have

$$\operatorname{tr}\left[\mathcal{R}_2(p,q)\,\mathcal{R}_2^T(r,s)\,\mathbf{J}_M\right] = (-1)^{s(p)+s(r)}\operatorname{tr}\left[\mathbf{J}_M\mathcal{S}_2(r,q)\,\mathcal{S}_2^T(p,s)\right]$$

and the two above identities directly prove (3.17). Regarding the identity in (3.18), it follows easily from the above identities together with the fact that $\mathbf{J}_M\mathcal{R}_i(p,q) = \mathcal{R}_{3-i}(q,p)$, $\mathbf{J}_M\mathcal{S}_i(p,q) = \mathcal{S}_i(q,p)$, $i = 1,2$, and the fact that

$$\begin{aligned}\mathrm{tr}\left[\mathcal{R}_1(p,q)\,\mathcal{R}_2^T(r,s)\,\mathbf{J}_M\right] &= (-1)^{s(p)+s(r)}\,\mathrm{tr}\left[\mathcal{R}_1(r,q)\,\mathcal{R}_2^T(p,s)\,\mathbf{J}_M\right]\\ \mathrm{tr}\left[\mathcal{S}_1(p,q)\,\mathcal{S}_2^T(r,s)\,\mathbf{J}_M\right] &= (-1)^{s(p)+s(r)}\,\mathrm{tr}\left[\mathcal{S}_1(r,q)\,\mathcal{S}_2^T(p,s)\,\mathbf{J}_M\right],\end{aligned}$$

which can be established following the same approach as in (3.19). The last two identities in the statement of the lemma are obtained as special cases of (3.17). □

We finalize the description of the non-asymptotic properties of the $\eta^{\pm}(p,q,r,s)$ with a result that will be useful whenever two of the pulses meet the PR conditions.

Lemma 4. *Assume that the two pulses p,q meet the perfect reconstruction conditions, and that r and s are either symmetric or anti-symmetric in the time domain and have the opposite symmetry. Then $\eta^{\pm}(p,q,r,s)=0$.*

Proof. Since p,q have PR conditions, we know that $\mathbf{U}^{-}\mathcal{S}(p,q)$ is an all-zero matrix whereas $\mathbf{U}^{+}\mathcal{R}(p,q)$ has zeros everywhere except for the central column, which is filled with 1s. Therefore, we are able to write

$$\eta^{\pm}(p,q,r,s) = \frac{1}{2M}\sum_{n=0}^{2M\tilde{N}_s-1} r[n]s[2M\kappa-n+1] = 0$$

where the last equality follows from the fact that r and s have the opposite symmetry. □

Asymptotic properties

Let us now consider some properties of the $\eta^{\pm}(p,q,p,s)$ that are obtained by assuming that the pulses are sampled versions of a smooth analog waveform. In other words, we assume that $p[n]$, $q[n]$, $r[n]$ and $s[n]$ are sampled versions of the waveforms $p(t), q(t), r(t)$ and $s(t)$ respectively, according to the properties in ($\mathbf{As2}$). This means that we can express

$$p[n] = p\left(\left(n - \frac{2M\kappa - 1}{2}\right)\frac{1}{2M}\right)$$

where $p\,(t)$ has the usual properties in ($\mathbf{As2}$). The same holds for the rest of the pulses.

Let us denote $p_m[n]$ the m-th polyphase component of $p[n]$, which can be expressed as

$$p_m[n] = p_m\left(\left(n - \frac{1}{2}\right)\frac{1}{2M}\right)$$

where $p_m(t)$ is the m-th section of $p(t)$, namely

$$p_m(t) = p\left(t - \left(m + \frac{\kappa}{2} - 1\right)\right)$$

which has support $[0, 1]$. The definition of $p_m(t)$ is only valid for $m = 1, \ldots, \kappa$, but we will consider $p_m(t) = 0$ for values of m outside this range. The same definitions carry over to the other pulses, namely q, r and s. With all these definitions, we are now in a position to establish the first asymptotic result associated with $\eta^{\pm}(p, q, p, s)$. The following result asymptotically relates the original quantity $\eta^{\pm}(p, q, p, s)$ with an equivalent definition that is constructed using the analog waveforms instead of the sampled ones.

Lemma 5. *Under the above assumptions, we can write*

$$\eta^{\pm}(p, q, r, s) = \bar{\eta}^{\pm}(p, q, r, s) + O(M^{-2})$$

where

$$\bar{\eta}^{\pm}(p, q, r, s) = \sum_{\ell=1}^{2\kappa-1}\sum_{m=1}^{\kappa}\sum_{n=1}^{\kappa} A^{(\ell,m,n)}\left[p, q, r, s\right] \pm B^{(\ell,m,n)}\left[p, q, r, s\right]$$

and where $A^{(\ell,m,n)}[p,q,r,s]$ *and* $B^{(\ell,m,n)}[p,q,r,s]$ *are defined as:*

$$\begin{aligned}A^{(\ell,m,n)}[p,q,r,s] &= \int_0^1 p_m(t)q_{\ell-m+1}(1-t)r_n(t)s_{\ell-n+1}(1-t)dt\\ &+\int_0^{\frac{1}{2}} p_m(t)q_{\ell-m+1}(\frac{1}{2}-t)r_n(t)s_{\ell-n+1}(\frac{1}{2}-t)dt\\ &+\int_{\frac{1}{2}}^1 p_m(t)q_{\ell-m+1}(\frac{3}{2}-t)r_n(t)s_{\ell-n+1}(\frac{3}{2}-t)dt\end{aligned}$$

and

$$\begin{aligned}B^{(\ell,m,n)}[p,q,r,s] &= \int_0^{\frac{1}{2}} p_m(t)q_{\ell-m+1}(1-t)r_n(\frac{1}{2}-t)s_{\ell-n+1}(\frac{1}{2}+t)dt\\ &+\int_{\frac{1}{2}}^1 p_m(t)q_{\ell-m+1}(1-t)r_n(\frac{3}{2}-t)s_{\ell-n+1}(t-\frac{1}{2})dt\\ &+\int_0^{\frac{1}{2}} p_m(t)q_{\ell-m+1}(\frac{1}{2}-t)r_n(\frac{1}{2}-t)s_{\ell-n+1}(t)dt\\ &+\int_{\frac{1}{2}}^1 p_m(t)q_{\ell-m+1}(\frac{3}{2}-t)r_n(\frac{3}{2}-t)s_{\ell-n+1}(t)dt.\end{aligned}$$

Proof. The proof is a direct consequence of the definition of $\eta^{\pm}(p,q,r,s)$ and the Riemann integral. Details are omitted due to the space constraints. □

The above lemma allows us to express $\eta^{\pm}(p,q,r,s)$ as a function of integrals of the analog waveform sections $p_m(t), q_m(t), r_m(t), s_m(t)$. This turns out to be very convenient for the following result, which provides an asymptotic relationship among different $\eta^{\pm}(p,q,r,s)$ with respect to the derivatives of the corresponding pulses.

Proposition 1. *Under the above assumptions and definitions, we can write*

$$\begin{aligned}\eta^{\pm}\left(p',q,r,s\right) - & \eta^{\pm}\left(p,q',r,s\right)+\eta^{\mp}\left(p,q,r',s\right)-\eta^{\mp}\left(p,q,r,s'\right)\\ &= -\left[\mathbf{U}^{\mp}\mathcal{R}\left(p,q\right)\mathcal{R}^{1}\left(r,s\right)\mathbf{U}^{\pm}\right]_{1,1}\\ &\quad -\left[\mathbf{U}^{\mp}\mathcal{R}\left(p,q\right)\mathcal{R}^{T}\left(r,s\right)\mathbf{U}^{\pm}\right]_{M+1,M+1}\\ &\quad -\left[\mathbf{U}^{\pm}\mathcal{S}\left(p,q\right)\mathcal{S}^{T}\left(r,s\right)\mathbf{U}^{\mp}\right]_{1,1}\\ &\quad -\left[\mathbf{U}^{\pm}\mathcal{S}\left(p,q\right)\mathcal{S}^{T}\left(r,s\right)\mathbf{U}^{\mp}\right]_{M+1,M+1}+O(M^{-1})\end{aligned} \quad (3.20)$$

Proof. Consider the definition of $A^{(\ell,m,n)}\left[p,q,r,s\right]$ and $B^{(\ell,m,n)}\left[p,q,r,s\right]$. These terms consist of a number of integrals of a differentiable function on a compact interval of the positive real axis. Hence, we can use the fundamental theorem of calculus to write

$$\begin{aligned}&\bar{\eta}^{\pm}\left(p',q,r,s\right)-\bar{\eta}^{\pm}\left(p,q',r,s\right)+\bar{\eta}^{\mp}\left(p,q,r',s\right)\\ &-\bar{\eta}^{\mp}\left(p,q,r,s'\right)=\sum_{\ell=1}^{2\kappa-1}\phi_{\ell}\end{aligned}$$

where

$$\begin{aligned}\phi_{\ell} &= \mu_{\ell}\left(1,0\right)\xi_{\ell}\left(1,0\right)-\mu_{\ell}\left(0,1\right)\xi_{\ell}\left(0,1\right)\\ &\pm\left[\mu_{\ell}\left(1,0\right)-\mu_{\ell}\left(0,1\right)\right]\xi_{\ell}\left(1/2,1/2\right)\\ &\pm\mu_{\ell}\left(1/2,1/2\right)\left[\xi_{\ell}\left(0,1\right)-\xi_{\ell}\left(1,0\right)\right]\\ &+\mu_{\ell}\left(1/2,0\right)\xi_{\ell}\left(1/2,0\right)-\mu_{\ell}\left(0,1/2\right)\xi_{\ell}\left(0,1/2\right)\\ &+\mu_{\ell}\left(1,1/2\right)\xi_{\ell}\left(1,1/2\right)-\mu_{\ell}\left(1/2,1\right)\xi_{\ell}\left(1/2,1\right)\\ &\mp\mu_{\ell}\left(1/2,0\right)\xi_{\ell}\left(0,1/2\right)\pm\mu_{\ell}\left(0,1/2\right)\xi_{\ell}\left(1/2,0\right)\\ &\mp\mu_{\ell}\left(1,1/2\right)\xi_{\ell}\left(1/2,1\right)\pm\mu_{\ell}\left(1/2,1\right)\xi_{\ell}\left(1,1/2\right)\end{aligned}$$

and where we have defined

$$\mu_\ell\left(t_1,t_2\right)=\sum_{m=1}^{\kappa}p_m(t_1)q_{\ell-m+1}(t_2)$$
$$\xi_\ell\left(t_1,t_2\right)=\sum_{m=1}^{\kappa}r_m(t_1)s_{\ell-m+1}(t_2).$$

Now, according to Lemma 5 we can replace each term $\bar{\eta}^{\pm}\left(p,q,r,s\right)$ by the corresponding $\eta^{\pm}\left(p,q,r,s\right)$ up to an error of order $O(M^{-2})$. Therefore, it suffices to prove that the right hand side of (3.20) is equal to $\sum_{\ell=1}^{2\kappa-1}\phi_\ell+O(M^{-1})$. But this follows directly from the fact that

$$\begin{aligned}
\mu_\ell\left(1,0\right)&=\left[\mathcal{R}_2\left(p,q\right)\right]_{M,\ell}+O(M^{-1})\\
\mu_\ell\left(0,1\right)&=\left[\mathcal{R}_1\left(p,q\right)\right]_{1,\ell}+O(M^{-1})\\
\mu_\ell\left(1/2,1/2\right)&=\left[\mathcal{R}_1\left(p,q\right)\right]_{M,\ell}+O(M^{-1})\\
&=\left[\mathcal{R}_2\left(p,q\right)\right]_{1,\ell}+O(M^{-1})\\
\mu_\ell\left(0,1/2\right)&=\left[\mathcal{S}_2\left(p,q\right)\right]_{1,\ell}+O(M^{-1})\\
\mu_\ell\left(1/2,0\right)&=\left[\mathcal{S}_2\left(p,q\right)\right]_{M,\ell}+O(M^{-1})\\
\mu_\ell\left(1,1/2\right)&=\left[\mathcal{S}_1\left(p,q\right)\right]_{M,\ell}+O(M^{-1})\\
\mu_\ell\left(1/2,1\right)&=\left[\mathcal{S}_1\left(p,q\right)\right]_{1,\ell}+O(M^{-1})
\end{aligned}$$

and equivalently for ξ_ℓ, replacing p,q with r,s. This concludes the proof of the proposition. $\square$

The application of the above proposition may prove to be difficult due the presence of the term on the right hand side of (3.20), which is difficult to interpret. The following corollary establishes that under PR conditions, this term is zero.

Corollary 1. *Under the above assumptions and definitions, if (r,s) are PR-compliant and p,q are symmetric or anti-symmetric but have the opposite* *symmetry, we can write*

$$\eta^{+}\left(p',q,r,s\right)-\eta^{+}\left(p,q',r,s\right)+\eta^{-}\left(p,q,r',s\right)-\eta^{-}\left(p,q,r,s'\right)=O(M^{-1}).$$

Proof. It follows from the PR conditions that $\mathbf{U}^{-}\mathcal{S}\left(r,s\right)$ is an all-zero matrix, whereas $\mathbf{U}^{+}\mathcal{R}\left(r,s\right)$ contains zeros everywhere except for the central column, which is filled with 1s. Proposition 1 therefore establishes that

$$\begin{aligned}&\eta^{+}\left(p',q,r,s\right)-\eta^{+}\left(p,q',r,s\right)+\eta^{-}\left(p,q,r',s\right)-\eta^{-}\left(p,q,r,s'\right)=\\&[\mathcal{R}\left(p,q\right)]_{2M,\kappa}-[\mathcal{R}\left(p,q\right)]_{1,\kappa}+[\mathcal{R}\left(p,q\right)]_{M,\kappa}-[\mathcal{R}\left(p,q\right)]_{M+1,\kappa}+O(M^{-1})\end{aligned}$$

and the result follows from symmetry. □

Before we conclude this proof section, we introduce another asymptotic result that will prove useful in the situation where two of the pulses meet the PR conditions.

Lemma 6. *Under the above definitions and hypotheses, assume additionally that p and q are perfect reconstruction pulses and that the analog waveforms r,s and r',s' are zero at the extreme of their support. Then, we can write*

$$\eta^{\pm}\left(p,q,r',s\right)-\eta^{\pm}\left(p,q,r,s'\right)=O(M^{-2})$$

Proof. We know that $\mathbf{U}^{-}\mathcal{S}\left(p,q\right)$ is an all zero matrix whereas the entries of $\mathbf{U}^{+}\mathcal{R}\left(p,q\right)$ are all zero except for the central column, which is filled with ones. This means that $\mathrm{tr}\left[\mathbf{U}^{+}\mathcal{S}(p,q)\mathcal{S}(r,s)^{T}\right]=0$ and

$$\begin{aligned}\frac{1}{2M}\mathrm{tr}\left[\mathbf{U}^{+}\mathcal{R}(p,q)\mathcal{R}(r,s)^{T}\right]&=\frac{1}{2M}\sum_{n=1}^{2M\kappa}r[n]s[2M\kappa-n+1]\\&=\int_{0}^{\kappa}r(t)s(\kappa-t)dt+O(M^{-2})\end{aligned}$$

where the last identity follows from the Riemann integral definition. Therefore, since

$$\int_0^\kappa r'(t)s(\kappa - t)dt - \int_0^\kappa r(t)s'(\kappa - t)dt \quad = r(\kappa)s(0) - r(\kappa)s(0) = 0,$$

we obtain the result. □

CHAPTER 4

PERFORMANCE ANALYSIS OF SINGLE-TAP EQUALIZERS FOR UPLINK MASSIVE MIMO SYSTEMS

In recent years, massive MIMO systems have received a lot of attention. These architectures are able to achieve the high data rate requirements targeted by 5G communication networks in terms of capacity and energy efficiency [109–111]. By using a very large number of antennas at the BS, these systems are able to simultaneously serve multiple users occupying the same time-frequency resources and separated using SDMA.

FBMC-OQAM modulations in combination with massive MIMO communications was first analyzed in [112]. As detailed in Chapter 3, the FBMC-OQAM orthogonality is well known to be progressively destroyed as the channel frequency selectivity becomes large, *i.e.*, when the channel cannot be approximated as flat at the subcarrier level. Somewhat surprisingly, in massive MIMO systems, it appears that the distortion induced by channel frequency selectivity decreases as the number of BS antennas increases, even in the case of strong channel selectivity and for simple single-tap per-subcarrier equalizers [112]. It is stated in [112] that, thanks to this so called "self-equalization effect", the subcarrier spacing can be increased in massive MIMO FBMC systems, reducing the number of subcarriers and leading to a lower sensitivity to CFO and peak-to-average-power-ratio. In [113], the same authors propose

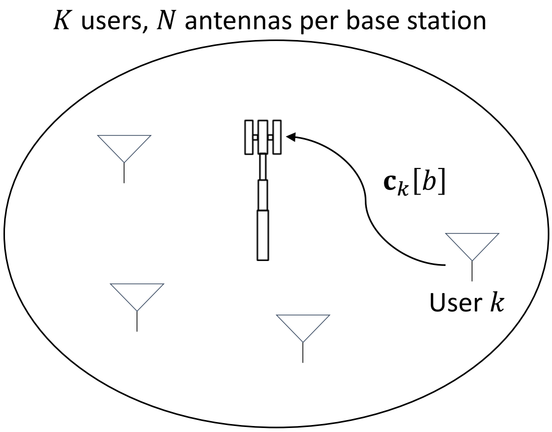

Figure 4.1 Uplink massive MIMO system.

to use the frequency spreading implementation of FBMC [38, 39] in the massive MIMO setting. This would allow for a more accurate channel equalization, which would result in a further reduction of the number of subcarriers. In [114, 115], it is shown that a distortion floor remains even if the number of BS antennas grow without bounds, meaning that ICI and ISI are not completely removed. To get rid of this performance floor, the authors propose an efficient equalization method.

As explained above, the combination of FBMC and massive MIMO has been studied in several previous works. However, to the best of our knowledge, there does not exist a theoretical analysis of the FBMC performance in a massive MIMO scenario. In [114, 115], bounds for the signal-to-interference-plus-noise ratio (SINR) are derived. However, these bounds only hold when the number of BS antennas N grows to infinity, for a fixed number of users K. In practice however, N is finite and may not be sufficiently large with respect to K, so that the derived bounds are very far from the actual SINR value for practical K and N. Furthermore, the work of [114] assumes a common PDP per-user, equal channel gains for each user and does not consider spatial channel correlation at the BS.

Here, the performance of an FBMC-OQAM uplink massive MIMO system is theoretically characterized in terms of the MSE of the estimated transmitted symbols and at the output of ZF, LMMSE and MF single-tap equalizers. Using random matrix theory, the MSE approximation derived in [104] is asymptotically analyzed as N and K grow to infinity, while keeping a finite ratio N/K, for each type of equalizer. Even if the results are only asymptotically true, it is shown that for practical values of N and K, the MSE is very close to its asymptotic equivalent, so that the approximations are very accurate and useful in practice. The obtained asymptotic MSE expressions are very compact and give a lot of insight on how the different scenario parameters affect the MSE, *i.e.*, the number of BS antennas N, the number of users K, the spatial correlation between the BS antennas, the small-scale and large-scale fading and the different PDP of each user. More specifically, we draw the following conclusions:

- For each type of equalizer under study, the asymptotic MSE almost surely converges to a deterministic quantity that does not depend on the subcarrier index, meaning that the MSE becomes flat across the frequency band.

- A good synchronization of the users and the BS is crucial in the considered SDMA uplink massive MIMO scenario. Indeed, it is shown here that a sizable part of the distortion is related to the average delay of the channel or in other words, the timing synchronization. This part of the output distortion does not go to zero as N/K grows large. This performance floor was earlier noticed in [112, 114], though its relationship with timing synchronization was not established.

- It is shown that, if users are well synchronized, the different terms that compose the MSE, such as noise, inter-user interference (IUI) and the distortion caused by the channel frequency selectivity, are inversely proportional to the ratio N/K and hence can be made arbitrarily

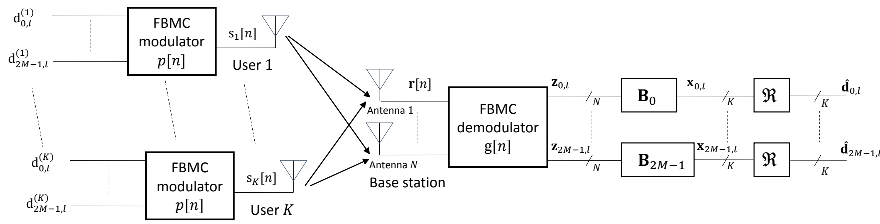

Figure 4.2 Uplink massive MIMO FBMC-OQAM transmission chain.

small for large N/K. This effect was previously referred to as "self-equalization" in [112, 114].

The rest of this chapter is structured as follows. Section 4.1 provides details on the system model of the considered uplink massive MIMO scenario. A per-subcarrier MSE approximation previously derived is recalled, which holds for general types of single-tap equalizers. Furthermore, the channel model under study in the current massive MIMO scenario is described. In Section 4.2, the asymptotic performance of FBMC is studied for the three types of single-tap equalizers. Section 4.3 validates the theoretical study of the self-equalization effect in massive MIMO FBMC systems in practical situations. Finally, Section 4.4 concludes the chapter and Section 4.5 contain the mathematical proofs of previous sections.

4.1 System model

4.1.1 Massive MIMO FBMC-OQAM transmission model

Let us consider a massive MIMO uplink transmission with one BS, equipped with N antennas, and K single-antenna users. The transmission chain considered in the following is depicted in Fig. 4.2. Each user simultaneously transmits one data stream to the the BS at the same frequency resources, using SDMA. It is assumed that the BS has knowledge of the channel response of all the users in the system. As in the rest of this thesis, the symbols $\mathbf{d}_{m,l} \in \mathbb{R}^{K\times 1}$ are assumed bounded, independent and identically distributed random variables with zero mean and variance $E_s/2$. In practice, users may have a different transmit power. This can be taken into account by the channel gain of each user, that is specified in the channel model presented in the next section. The channel is assumed to be quasi-static and its impulse response, denoted by $\mathbf{C}[b] \in \mathbb{C}^{N\times K}$, is assumed to be of finite length[1] L.

4.1.2 MSE approximation under high channel frequency selectivity

In practice, as we saw in Chapter 3, the presence of channel frequency selectivity will deteriorate the symbol estimate, which will be affected by ICI and ISI. Moreover if the channel is not perfectly inverted at the receiver, *i.e.*, $\mathbf{B}_{m_0}\mathbf{H}_{m_0} \neq \mathbf{I}_K$, IUI coming from the other users will impact the symbol estimate. We use the same definition of the aggregated MSE at subcarrier m as was defined in (3.1), *i.e.*,

$$\mathrm{MSE}(m) = \mathbb{E}\left(\|\mathbf{d}_{m,l} - \hat{\mathbf{d}}_{m,l}\|^2\right),$$

where the expectation is taken over transmitted symbols and noise samples. The exact expression of the MSE is an intricate function of the channel impulse response. Therefore, we utilize the approximation derived in Theorem 2. Under $(\mathbf{As1}) - (\mathbf{As2})$ and when no pre-equalizer is used at the transmitter side implying that $\mathbf{A}(\omega) = \mathbf{I}_K$ and $\mathbf{A}'(\omega) = \mathbf{0}$,

[1]Note that the channel of each user may have a different length. L would then be the supremum of all the channel lengths, which we assume bounded.

the approximation of the MSE leads to[2]

$$\begin{aligned}\mathrm{MSE}(m) &= \frac{E_T}{2K}\mathrm{tr}\left[\left(\mathbf{B}_m\mathbf{H}_m - \mathbf{I}_K\right)\left(\mathbf{B}_m\mathbf{H}_m - \mathbf{I}_K\right)^H\right] \\ &+ \frac{E_T}{K}\frac{\eta}{(2M)^2}\mathrm{tr}\left[\left(\mathbf{B}_m\mathbf{H}_m^{(1)}\right)\left(\mathbf{B}_m\mathbf{H}_m^{(1)}\right)^H\right] \\ &+ \frac{E_T}{K}\frac{\eta}{(2M)^2}\Re\,\mathrm{tr}\left[\left(\mathbf{B}_m\mathbf{H}_m - \mathbf{I}_K\right)\left(\mathbf{B}_m\mathbf{H}_m^{(2)}\right)^H\right] \\ &+ \frac{N_0}{2}\mathrm{tr}\big[\mathbf{B}_m\mathbf{B}_m^H\big] + \epsilon, \end{aligned} \tag{4.1}$$

where $E_T = KE_s$ and $\eta = \eta^{\pm}\left(p, g^{(1)}, p, g^{(1)}\right)$ is a pulse-related quantity, with $\eta^{\pm}(p,q,r,s)$ properly defined in Section 3.5. For an integer q, $\mathbf{H}_m^{(q)}$ denotes the q-th order derivative of the channel in the frequency domain and evaluated at subcarrier m, *i.e.*,

$$\mathbf{H}_m^{(q)} = \sum_{b=0}^{L-1}(-\jmath b)^q\mathbf{C}[b]e^{-\jmath\frac{2\pi}{2M}mb}. \tag{4.2}$$

Note that $\mathbf{H}_m^{(0)} = \mathbf{H}_m$. The term ϵ in (4.1) is an error contribution that depends on the degree of frequency selectivity of the channel, which can be characterized by the ratio $\frac{L}{2M}$. As will be shown in the simulations, for practical channel lengths and number of subcarriers, the approximation is very accurate. Therefore, we will neglect the error term ϵ. Note that the approximation takes into account the effect of IUI, ICI, ISI and additive noise, as explained in Section 3.1.

4.1.3 Channel model

To study the MSE behavior when the number of antennas grows large, we first need to define a channel model that is relevant in the considered uplink massive MIMO scenario. We denote by $\mathbf{c}_k[b] \in \mathbb{C}^{N\times 1}$, $k =$

[2]Note that in the case of no pre-equalizer, the derivations performed in Section 3.5 can be simplified and are holding even in the case where a different pulse is used at transmit and receive sides.

$1, \ldots, K$, the b-th tap of the channel impulse response between the k-th user and the BS antennas, namely the k-th column of $\mathbf{C}[b]$. In the following, we will assume that vector $\mathbf{c}_k[b]$ is modeled as

$$\mathbf{c}_k[b] = \underbrace{\mathbf{C}_{\mathrm{BS}}^{1/2}}_{\text{BS correlation}} \overbrace{\mathbf{g}_k[b]}^{\text{Small-scale fading}} \underbrace{\sqrt{\beta_k}}_{\text{Channel gain}} \overbrace{\sqrt{p_k[b]}}^{\text{PDP}}. \tag{4.3}$$

The positive matrix $\mathbf{C}_{\mathrm{BS}} \in \mathbb{C}^{N \times N}$ models the spatial correlation between the BS antennas, normalized such that $\mathrm{tr}[\mathbf{C}_{\mathrm{BS}}] = N$. We assume that the matrix matrix $\mathbf{C}_{\mathrm{BS}}$ does not depend on the user index k, which is the case if the spectrum of angle of arrival is the same for each user. The vector $\mathbf{g}_k[b] \in \mathbb{C}^{N \times 1}$ is made of i.i.d. zero mean and unit variance Gaussian entries that accounts for the small-scale fading. The coefficient $\sqrt{\beta_k}$ accounts for the channel gain related to user k,[3] normalized such that $\sum_{k=1}^{K} \beta_k = K$. The coefficient $p_k[b]$ models the power of the b-th tap, normalized such that $\sum_{b=0}^{L-1} p_k[b] = 1$. Note that since $p_k[b]$ depends both on k and b, the model can take into account different PDP's for each user, depending on its own environment. Collecting the vectors $\mathbf{c}_k[b]$ for all users $k = 1, \ldots, K$, the matrix $\mathbf{C}[b] \in \mathbb{C}^{N \times K}$ can be formulated as

$$\mathbf{C}[b] = \mathbf{C}_{\mathrm{BS}}^{1/2} \mathbf{G}[b] \mathbf{D}_{\beta,b}^{1/2}, \quad b = 0, \ldots, L-1, \tag{4.4}$$

where the diagonal matrix $\mathbf{D}_{\beta,b}^{1/2} \in \mathbb{C}^{K \times K}$ is given by

$$\mathbf{D}_{\beta,b}^{1/2} = \mathrm{diag}(\sqrt{\beta_1}\sqrt{p_1[b]}, ..., \sqrt{\beta_K}\sqrt{p_K[b]})$$

and $\mathbf{G}[b] = (\mathbf{g}_1[b], ..., \mathbf{g}_K[b])$. The fact that $\mathbf{D}_{\beta,b}^{1/2}$ is diagonal comes from the fact that users are assumed to be located at different positions in the cell and we assume no correlation among them. Inserting (4.4) in (4.2), the q-th derivative of the channel frequency response at subcarrier m

[3]The coefficient β_k includes the effect of large-scale fading and power control.

can be expressed as

$$\begin{aligned}\mathbf{H}_m^{(q)} &= \mathbf{C}_{\mathrm{BS}}^{1/2} \sum_{b=0}^{L-1} (-\jmath b)^q \mathbf{G}[b] \mathbf{D}_{\beta,b}^{1/2} e^{-\jmath \frac{2\pi}{2M} mb} \\ &= \mathbf{C}_{\mathrm{BS}}^{1/2} \mathbf{G} \mathbf{\Phi}^q \mathbf{D}_{1/2,m}, \end{aligned} \tag{4.5}$$

where we defined

$$\begin{aligned}\mathbf{G} &= \Big(\mathbf{G}[0], \ldots, \mathbf{G}[L-1]\Big), \qquad (4.6) \\ \mathbf{\Phi} &= (-\jmath \mathbf{\Gamma} \otimes \mathbf{I}_K), \\ \mathbf{\Gamma} &= \mathrm{diag}(0, ..., L-1), \\ \mathbf{D}_{1/2,m} &= \Big(e^{-\jmath \frac{2\pi}{2M} m0} \mathbf{D}_{\beta,0}^{1/2}, \ldots, e^{-\jmath \frac{2\pi}{2M} m(L-1)} \mathbf{D}_{\beta,L-1}^{1/2}\Big)^T\end{aligned}$$

and matrix $\mathbf{\Phi}^0$ is defined as the identity $\mathbf{I}_{LK}$. Furthermore, we define key channel statistics that will help characterize the distortion induced by the channel frequency selectivity. The average delay $\tau_{k,\mathrm{av}}$ and the delay spread $\tau_{k,\mathrm{rms}}$ associated to user k are defined as

$$\begin{aligned}\tau_{k,\mathrm{av}} &= \sum_{b=0}^{L-1} b p_k[b], \\ \tau_{k,\mathrm{rms}} &= \sqrt{\sum_{b=0}^{L-1} b^2 p_k[b] - \tau_{k,\mathrm{av}}^2}.\end{aligned}$$

Note that the average delay of each user $\tau_{k,\mathrm{av}}$ depends on the BS synchronization. By changing the demodulation window, a delay is added or removed to the PDP of each user $p_k[b]$. However, the delay spread $\tau_{k,\mathrm{rms}}$ is an intrinsic property of the channel of each user and does not depend on the BS synchronization.

Further, we define the three following diagonal matrices of size $K \times K$

$$\mathbf{D}_\beta = \mathrm{diag}(\beta_1, \ldots, \beta_K),$$
$$\mathbf{D}_{\mathrm{av}} = \mathrm{diag}(\tau_{1,\mathrm{av}}, \ldots, \tau_{K,\mathrm{av}}),$$
$$\mathbf{D}_{\mathrm{rms}} = \mathrm{diag}(\tau_{1,\mathrm{rms}}, \ldots, \tau_{K,\mathrm{rms}}),$$

which respectively contain on their diagonal the channel gain, the average delay and the delay spread of each user.

4.2 Performance in massive MIMO systems

In this section, we aim at characterizing the performance of FBMC-OQAM in an uplink massive MIMO scenario for three types of classical single-tap equalizers, namely, the ZF, the LMMSE and the MF equalizers. These are designed based on the assumption of a frequency flat channel at the subcarrier level, *i.e.*, $\mathbf{H}_m^{(1)} \approx \mathbf{0}$ and $\mathbf{H}_m^{(2)} \approx \mathbf{0}$. In practice, it will not be the case and this simple design will lead to ICI, ISI and IUI, which is taken into account by the second and third terms of (4.1). In the following, we study the asymptotic behavior of the MSE in (4.1) for each type of single-tap equalizer. We will show that (4.1) converges in each case almost surely to an asymptotic equivalent as N and K grow infinitely large, for a finite ratio N/K. Of course, in a massive MIMO scenario, the number of BS antennas N and the number of users K are finite but they are sufficiently large so that the actual MSE becomes very close to its asymptotic equivalent, as will be shown via simulations.

In the sequel, as N and K grow large, we will assume that

$(\mathbf{As3})$: $0 < \liminf \frac{N}{K} \leq \limsup \frac{N}{K} < \infty$,

$(\mathbf{As4})$: $\limsup_N \|\mathbf{C}_{\mathrm{BS}}\| < \infty$,

$(\mathbf{As5})$: $\limsup_K \|\mathbf{D}_{\beta,b}\| < \infty$ for all b.

One should note that $(\mathbf{As4})$ and $(\mathbf{As5})$ practically make sense since it is unlikely that one channel gain grows infinitely large.

4.2.1 ZF and LMMSE equalizers

We will here study the performance of two particular equalizers. The first one, the ZF equalizer, is obtained by minimizing (4.1) under a channel inversion constraint and assuming a frequency flat channel at the subcarrier level ($\mathbf{H}_m^{(1)} = \mathbf{H}_m^{(2)} \approx \mathbf{0}$), *i.e.*,

$$\begin{aligned}\mathbf{B}_m^{\mathrm{ZF}} &= \arg\min_{\mathbf{B}} \mathrm{MSE}_m \text{ s.t. } \mathbf{B}_m\mathbf{H}_m = \mathbf{I}_K \\ &= \left(\mathbf{H}_m^H\mathbf{H}_m\right)^{-1}\mathbf{H}_m^H.\end{aligned}$$

It is well know that inverting the channel may lead to noise amplification, which is particularly detrimental for low SNR. An alternative is to use an LMMSE equalizer, obtained by minimizing (4.1) assuming a frequency flat channel at the subcarrier level ($\mathbf{H}_m^{(1)} = \mathbf{H}_m^{(2)} \approx \mathbf{0}$), *i.e.*,

$$\begin{aligned}\mathbf{B}_m^{\mathrm{LMMSE}} &= \arg\min_{\mathbf{B}} \mathrm{MSE}_m \\ &= \left(\mathbf{H}_m^H\mathbf{H}_m + \frac{N_0K}{E_T}\mathbf{I}_K\right)^{-1}\mathbf{H}_m^H.\end{aligned}$$

As soon as the channel becomes significantly frequency selective, we have $\mathbf{H}_m^{(1)} \neq \mathbf{0}, \mathbf{H}_m^{(2)} \neq \mathbf{0}$. Hence, $\mathbf{B}_m^{\mathrm{ZF}}$ and $\mathbf{B}_m^{\mathrm{LMMSE}}$ are not optimal anymore, as was shown in Chapter 3. Still, in the massive MIMO setting, we will show further that classical single-tap equalizers, designed for the frequency flat case, such as $\mathbf{B}_m^{\mathrm{ZF}}$ and $\mathbf{B}_m^{\mathrm{LMMSE}}$, can lead to very small MSE values for large values of the ratio N/K, even for highly frequency selective channels. In the following, we will more generally study a single-tap equalizer of the form

$$\mathbf{B}_m^{\lambda} = \left(\mathbf{H}_m^H\mathbf{H}_m + K\lambda\mathbf{I}_K\right)^{-1}\mathbf{H}_m^H. \tag{4.7}$$

Note that if $\lambda = 0$, we retrieve the expression of the ZF equalizer whereas if we choose $\lambda = \frac{N_0}{E_T}$, we find the LMMSE equalizer. Inserting the expression of this equalizer in (4.1), the MSE becomes

$$\begin{aligned}\mathrm{MSE}_m(\lambda) &= \frac{E_T}{2K}\lambda^2\mathbf{tr}\left[\left(\frac{\mathbf{H}_m^H\mathbf{H}_m}{K}+\lambda\mathbf{I}_K\right)^{-2}\right]\\ &+\frac{E_T\tilde{\eta}}{K}\mathbf{tr}\left[\left(\frac{\mathbf{H}_m^H\mathbf{H}_m}{K}+\lambda\mathbf{I}_K\right)^{-2}\frac{\mathbf{H}_m^H\mathbf{H}_m^{(1)}}{K}\frac{(\mathbf{H}_m^H\mathbf{H}_m^{(1)})^H}{K}\right]\\ &-\frac{E_T\tilde{\eta}}{K}\lambda\Re\,\mathbf{tr}\left[\left(\frac{\mathbf{H}_m^H\mathbf{H}_m}{K}+\lambda\mathbf{I}_K\right)^{-2}\frac{(\mathbf{H}_m^H\mathbf{H}_m^{(2)})^H}{K}\right]\\ &+\frac{N_0}{2K}\mathrm{tr}\left[\left(\frac{\mathbf{H}_m^H\mathbf{H}_m}{K}+\lambda\mathbf{I}_K\right)^{-2}\left(\frac{\mathbf{H}_m^H\mathbf{H}_m}{K}\right)\right],\end{aligned}\tag{4.8}$$

where $\tilde{\eta}=\eta/(2M)^2$. The MSE expression can be rewritten as a function of the matrix of Gaussian entries $\mathbf{G}$ defined in (4.6).

The following theorem shows that the expression of $\mathrm{MSE}_m(\lambda)$ given in (4.8), almost surely (a.s.) behaves as a deterministic equivalent in a massive MIMO scenario.

Theorem 3. *Under* $(\mathbf{As1})$-$(\mathbf{As5})$*, as* N *and* K *grow infinitely large, for the equalizer in (4.7) and if* $\lambda\in\mathbb{C}\setminus(\mathbb{R}^-\cup\{0\})$*, we have*

$$\mathrm{MSE}_m(\lambda)-\overline{\mathrm{MSE}}(\lambda)\xrightarrow{a.s.}0,$$

and the expression of $\overline{\mathrm{MSE}}(\lambda)$ *is given by*

$$\begin{aligned}\overline{\mathrm{MSE}}(\lambda) &= \frac{E_T}{2}\left(1-\tilde{\delta}(\lambda)\delta(\lambda)\right)+\frac{N_0-\lambda E_T}{2}\frac{\alpha(\lambda)\tilde{\alpha}(\lambda)}{1-\gamma(\lambda)\tilde{\gamma}(\lambda)}\\ &+\frac{E_T\tilde{\eta}}{K}\mathrm{tr}\left[\tilde{\delta}(\lambda)\mathbf{D}_\beta\left(\tilde{\delta}(\lambda)\mathbf{D}_\beta+\lambda\mathbf{I}_K\right)^{-1}\mathbf{D}_{\mathrm{av}}^2\right]\\ &+\frac{E_T\tilde{\eta}}{K}\frac{\alpha(\lambda)\tilde{\gamma}(\lambda)}{1-\gamma(\lambda)\tilde{\gamma}(\lambda)}\mathrm{tr}\left[\mathbf{D}_\beta\mathbf{D}_{\mathrm{rms}}^2\right]\\ &+\frac{E_T\tilde{\eta}}{K}\frac{\lambda\tilde{\alpha}(\lambda)}{1-\gamma(\lambda)\tilde{\gamma}(\lambda)}\mathrm{tr}\left[\mathbf{D}_\beta\left(\tilde{\delta}(\lambda)\mathbf{D}_\beta+\lambda\mathbf{I}_K\right)^{-2}\mathbf{D}_{\mathrm{rms}}^2\right],\end{aligned}\tag{4.9}$$

where $\tilde{\delta}(\lambda)$ and $\delta(\lambda)$ are the unique positive solutions of the following system of equations in $\left(\tilde{\delta}(\lambda), \delta(\lambda)\right)$

$$\delta(\lambda) = \frac{1}{K}\mathrm{tr}\left[\mathbf{D}_\beta\left(\tilde{\delta}(\lambda)\mathbf{D}_\beta + \lambda\mathbf{I}_K\right)^{-1}\right] \tag{4.10}$$

$$\tilde{\delta}(\lambda) = \frac{1}{K}\mathrm{tr}\left[\mathbf{C}_{\mathrm{BS}}(\delta(\lambda)\mathbf{C}_{\mathrm{BS}} + \mathbf{I}_N)^{-1}\right]. \tag{4.11}$$

Furthermore, we have defined

$$\alpha(\lambda) = \frac{1}{K}\mathrm{tr}\left[\mathbf{D}_\beta\left(\tilde{\delta}(\lambda)\mathbf{D}_\beta + \lambda\mathbf{I}_K\right)^{-2}\right] \tag{4.12}$$

$$\gamma(\lambda) = \frac{1}{K}\mathrm{tr}\left[\mathbf{D}_\beta^2\left(\tilde{\delta}(\lambda)\mathbf{D}_\beta + \lambda\mathbf{I}_K\right)^{-2}\right] \tag{4.13}$$

$$\tilde{\alpha}(\lambda) = \frac{1}{K}\mathrm{tr}\left[\mathbf{C}_{\mathrm{BS}}(\delta(\lambda)\mathbf{C}_{\mathrm{BS}} + \mathbf{I}_N)^{-2}\right] \tag{4.14}$$

$$\tilde{\gamma}(\lambda) = \frac{1}{K}\mathrm{tr}\left[\mathbf{C}_{\mathrm{BS}}^2(\delta(\lambda)\mathbf{C}_{\mathrm{BS}} + \mathbf{I}_N)^{-2}\right]. \tag{4.15}$$

The above properties also hold for $\lambda = 0$ when $\inf \frac{N}{K} > 1$.

Proof. The proof is given in Section 4.5. □

The expression of $\overline{\mathrm{MSE}}(\lambda)$ in (4.9) is not trivial to interpret due to the dependence in the variables $\tilde{\delta}(\lambda)$ and $\delta(\lambda)$. A first remark is that it does not depend on the subcarrier index m, meaning that the MSE becomes flat over frequency. Moreover, the two first terms proportional to N_0 and E_T are terms of additive noise and IUI. The terms proportional to $\tilde{\eta}$, are ICI and ISI caused by the channel frequency selectivity, related to the average delay and the delay spread of the channel. By making further assumptions on the channel statistics, the next corollary will give a better intuition of the different terms of $\overline{\mathrm{MSE}}(\lambda)$.

ZF equalizer

Theorem 3 can be particularized to the ZF equalizer case by setting $\lambda = 0$ and ensuring that $\inf \frac{N}{K} > 1$. Let us define $\overline{\mathrm{MSE}}^{\mathrm{ZF}} = \overline{\mathrm{MSE}}(0)$.

Corollary 2. *If we assume that the channel is spatially uncorrelated at the receiver side, i.e.,* $\mathbf{C}_{\mathrm{BS}} = \mathbf{I}_N$*, the expression of* $\overline{\mathrm{MSE}}^{\mathrm{ZF}}$ *simplifies to*

$$\overline{\mathrm{MSE}}^{\mathrm{ZF}} = \frac{N_0}{2}\frac{1}{\frac{N}{K}-1}\frac{\mathrm{tr}\left[\mathbf{D}_\beta^{-1}\right]}{K} + E_T\tilde{\eta}\frac{\mathrm{tr}\left[\mathbf{D}_{\mathrm{av}}^2\right]}{K}$$
$$+ E_T\tilde{\eta}\frac{1}{\frac{N}{K}-1}\frac{\mathrm{tr}\left[\mathbf{D}_\beta^{-1}\right]}{K}\frac{\mathrm{tr}\left[\mathbf{D}_\beta\mathbf{D}_{\mathrm{rms}}^2\right]}{K}.$$

If, further, we assume a common PDP for all users but different per-user large-scale fading coefficients, we have $p_k[b] = p[b]$*, which does not depend on* k*. The expression of* $\overline{\mathrm{MSE}}^{\mathrm{ZF}}$ *then becomes*

$$\overline{\mathrm{MSE}}^{\mathrm{ZF}} = \frac{N_0}{2}\frac{1}{\frac{N}{K}-1}\frac{\mathrm{tr}\left[\mathbf{D}_\beta^{-1}\right]}{K} + E_T\tilde{\eta}\tau_{\mathrm{av}}^2 + E_T\tilde{\eta}\frac{1}{\frac{N}{K}-1}\frac{\mathrm{tr}\left[\mathbf{D}_\beta^{-1}\right]}{K}\tau_{\mathrm{rms}}^2,$$

where we defined $\tau_{\mathrm{av}} = \tau_{\mathrm{av},k}$*, which does not depend on* k*.*

Proof. The proof is given by particularizing the result of Theorem 3 to the special cases mentioned above. First, if $\mathbf{C}_{\mathrm{BS}} = \mathbf{I}_N$, the solution of the system of equations (4.10) and (4.11) admits a closed-form expression ($\lambda = 0$), given by $\tilde{\delta} = \frac{N}{K} - 1$ and $\delta = \tilde{\delta}^{-1}$. Replacing this expression of δ and $\tilde{\delta}$ in (4.12)-(4.15) for $\lambda = 0$, we find the first result of the Corollary. Moreover, if $p_k[b] = p[b]$, we have $\mathbf{D}_{\mathrm{av}} = \tau_{\mathrm{av}}\mathbf{I}_K$ and $\mathbf{D}_{\mathrm{rms}} = \tau_{\mathrm{rms}}\mathbf{I}_K$. □

By adding some assumptions, Corollary 2 provides additional insights into the physical meaning of the different terms of the MSE. The first term is simply related to the additive noise power after equalization and goes to zero as N/K becomes large. This makes sense since with a larger N/K, the channel inversion will be better conditioned and leads to lower noise amplification. As explained before, the two other terms are related to the channel frequency selectivity. Note that the term related to the delay spread of the channel τ_{rms} also goes to zero as N/K grows large. This is part of the so-called "self-equalization" effect, previously noticed in [112].

Surprisingly, the term related to the delay average of the channel τ_{av} is independent of N and K. Hence, this corresponds to the remaining error floor as N/K grows to infinity, previously noticed in [114]. The presence of this term motivates the need for a strict synchronization of the users at the transmit side in the considered SDMA uplink scenario. In practice, if the users and the BS are well synchronized, this term is negligible relatively to the other terms. Further, it can even be made very close to zero. This can be done by redefining the channel $\mathbf{C}[b]$ as being not causal and having a $\tau_{\mathrm{av}} \approx 0$. In other words, the BS can re-center the demodulation window to minimize the average channel delay.

LMMSE equalizer

Theorem 3 can also be particularized to the LMMSE equalizer case by setting $\lambda = \frac{N_0}{E_T}$. Let us define $\overline{\mathrm{MSE}}^{\mathrm{LMMSE}} = \overline{\mathrm{MSE}}(N_0/E_T)$. Unfortunately, the asymptotic expression $\overline{\mathrm{MSE}}^{\mathrm{LMMSE}}$ is not trivial to interpret due to the dependence in the variables $\delta(\lambda)$ and $\tilde{\delta}(\lambda)$. Even by making more assumptions as in Corollary 2, the expression does not simplify a lot. However, we will see via simulations that the performance of the LMMSE equalizer gets very close to the one of the ZF for relatively high values of N/K and/or high SNR. Hence, in these regimes, the conclusions that were drawn for the ZF equalizer, approximately hold for the LMMSE equalizer.

4.2.2 MF equalizer

A disadvantage of the ZF and LMMSE equalizers is that they require one matrix inversion, which significantly increases their implementation complexity. To overcome this, an alternative equalizer known as MF or maximum-ratio combining, has received a lot of attention in the massive MIMO literature. If we denote by $\mathbf{h}_{j,m} \in \mathbb{C}^{N\times 1}$ the channel frequency response at subcarrier m between user j and the BS antennas, the BS simply processes this stream by a multiplication by its Hermitian transpose $\mathbf{h}_{j,m}^H/\|\mathbf{h}_{j,m}\|^2$. The normalization factor $\|\mathbf{h}_{j,m}\|^2$ ensures a unit gain for the channel of interest. We can write the matrix form of this equalizer as,

$$\mathbf{B}_m^{\mathrm{MF}} = \mathrm{diag}^{-1}\left(\mathbf{H}_m^H\mathbf{H}_m\right)\mathbf{H}_m^H,$$

where the operator diag(.) applied to a square matrix $\mathbf{A}$ returns a diagonal matrix with diagonal entries equal to the diagonal entries of $\mathbf{A}$ and $\mathrm{diag}^r(\mathbf{A})$ is the r-th power of matrix $\mathrm{diag}(\mathbf{A})$.

Inserting the expression of $\mathbf{B}_m^{\mathrm{MF}}$ into (4.1), the MSE expression for the MF equalizer becomes

$$\begin{aligned}\mathrm{MSE}_m^{\mathrm{MF}} &= \frac{E_T}{2K}\mathrm{tr}\left[\mathrm{diag}^{-2}\left(\mathbf{H}_m^H\mathbf{H}_m\right)\left(\mathbf{H}_m^H\mathbf{H}_m\right)^2\right] - \frac{E_T}{2} \\ &+ \frac{E_T\tilde{\eta}}{K}\mathrm{tr}\left[\mathrm{diag}^{-2}\left(\mathbf{H}_m^H\mathbf{H}_m\right)\left(\mathbf{H}_m^H\mathbf{H}_m^{(1)}\right)\left(\mathbf{H}_m^H\mathbf{H}_m^{(1)}\right)^H\right] \\ &+ \frac{E_T\tilde{\eta}}{K}\Re\mathrm{tr}\left[\mathrm{diag}^{-2}(\mathbf{H}_m^H\mathbf{H}_m)(\mathbf{H}_m^H\mathbf{H}_m)(\mathbf{H}_m^H\mathbf{H}_m^{(2)})^H\right] \\ &- \frac{E_T\tilde{\eta}}{K}\Re\mathrm{tr}\left[\mathrm{diag}^{-1}(\mathbf{H}_m^H\mathbf{H}_m)(\mathbf{H}_m^H\mathbf{H}_m^{(2)})^H\right] \\ &+ \frac{N_0}{2}\mathrm{tr}\left[\mathrm{diag}^{-1}\left(\mathbf{H}_m^H\mathbf{H}_m\right)\right], \end{aligned} \tag{4.16}$$

which can be written as a function of $\mathbf{G}$ using (4.5).

The following theorem gives the expression of $\mathrm{MSE}_m^{\mathrm{MF}}$ as the number of BS antennas N and the number of users K grow large for a finite ratio N/K.

Theorem 4. *Under* $(\mathbf{As1})$-$(\mathbf{As5})$, *as N and K grow infinitely large, we have,*

$$\mathrm{MSE}_m^{\mathrm{MF}} - \overline{\mathrm{MSE}}^{\mathrm{MF}} \xrightarrow{a.s.} 0$$

such that the deterministic equivalent of $\mathrm{MSE}_m^{\mathrm{MF}}$ *is given by*

$$\overline{\mathrm{MSE}}^{\mathrm{MF}} = \frac{E_T}{2}\mathrm{tr}\left[\mathbf{D}_\beta^{-1}\right]\frac{\mathrm{tr}\left[\mathbf{C}_{\mathrm{BS}}^2\right]}{N^2} + E_T\tilde{\eta}\frac{\mathrm{tr}\left[\mathbf{D}_{\mathrm{av}}^2\right]}{K} + \frac{N_0}{2}\frac{\mathrm{tr}\left[\mathbf{D}_\beta^{-1}\right]}{N}.$$

Proof. The proof is given in in Section 4.5. □

Note again that $\overline{\mathrm{MSE}}^{\mathrm{MF}}$ is a deterministic quantity that does not depend on the subcarrier index m. $\overline{\mathrm{MSE}}^{\mathrm{MF}}$ is composed of three terms. The first one is related to IUI due to the fact that the channel is not perfectly inverted, $\mathbf{B}_m^{\mathrm{MF}}\mathbf{H}_m \neq \mathbf{I}_K$. This term is generally dominant at mid to high SNR values. The second term is related to the average delay of the PDP of each user, whereas the last term is due to the additive noise. Surprisingly, in contrast to the ZF and LMMSE equalizers, the deterministic equivalent $\overline{\mathrm{MSE}}^{\mathrm{MF}}$ does not depend on the delay spread of the channel, *i.e.*, $\overline{\mathrm{MSE}}^{\mathrm{MF}}$ does not depend on $\mathbf{D}_{\mathrm{rms}}$.

Corollary 3. *If we assume that the channel is spatially uncorrelated at the receiver side, i.e.,* $\mathbf{C}_{\mathrm{BS}} = \mathbf{I}_N$*, the expression of* $\overline{\mathrm{MSE}}^{\mathrm{MF}}$ *simplifies to*

$$\overline{\mathrm{MSE}}^{\mathrm{MF}} = \frac{E_T}{2}\frac{\mathrm{tr}\left[\mathbf{D}_\beta^{-1}\right]}{N} + E_T\tilde{\eta}\frac{\mathrm{tr}\left[\mathbf{D}_{\mathrm{av}}^2\right]}{K} + \frac{N_0}{2}\frac{\mathrm{tr}\left[\mathbf{D}_\beta^{-1}\right]}{N}.$$

If further, we assume a common PDP for all users, as in Corollary 2, $\overline{\mathrm{MSE}}^{\mathrm{MF}}$ *becomes,*

$$\overline{\mathrm{MSE}}^{\mathrm{MF}} = \frac{E_T}{2}\frac{\mathrm{tr}\left[\mathbf{D}_\beta^{-1}\right]}{N} + E_T\tilde{\eta}\tau_{\mathrm{av}}^2 + \frac{N_0}{2}\frac{\mathrm{tr}\left[\mathbf{D}_\beta^{-1}\right]}{N},$$

where τ_{av} *and* τ_{rms} *are defined as in Corollary 2.*

By making some additional assumptions, Corollary 3 allows for a very intuitive understanding of the behavior of the different terms. As mentioned earlier, the first term is related to IUI. As in the ZF and LMMSE cases, we notice the self-equalization impact of massive MIMO on FBMC: for large values of the ratio N/K, the first and third terms will go to zero. The only term that does not go to zero, is the second one, proportional to $\tilde{\eta}$ and τ_{av}^2, similarly as in the ZF and LMMSE cases. This again emphasizes the fact that in an SDMA situation, the BS and the different users should be well synchronized. If this is the case, this term is negligible compared to the other two.

4.3 Simulation results

This section aims at assessing the accuracy of the approximations through simulations. Furthermore, the performance of an uplink massive MIMO FBMC-OQAM system is characterized as a function of different parameters.

In the simulations, the subcarrier spacing is fixed to 15 kHz. The number of subcarriers is $2M = 128$. The prototype filter used in all simulations is the PHYDYAS pulse [6] with overlapping factor $\kappa = 4$. To characterize the PDP's $p_k[b]$ and the channel gains β_k of each user, we will assume that the users are clustered in four groups of equal number $K/4$. The PDP of the users of each cluster follow the same channel model, which is given by an ITU - Veh. A, an ITU - Veh. B, a 3GPP - Typical Urban or a 3GPP - Hilly Terrain channel model. Note that these models correspond to both mildly and highly frequency selective channels. Moreover, the users inside a same cluster have an equal channel gain β_k which takes one of the following four values $[0.4, 0.8, 1.2, 1.6]$. The spatial correlation matrix at the BS $\mathbf{C}_{\mathrm{BS}}$ was fixed using the exponential model [116], *i.e.*, its m, n entry is given by $[\mathbf{C}_{\mathrm{BS}}]_{m,n} = \rho^{|m-n|}$, which models a linear array of antennas. The parameter ρ will be referred to as the correlation coefficient and is fixed to 0.7, if not stated otherwise. The SNR is defined as E_T/N_0.

4.3.1 Accuracy of the MSE approximations and frequency flattening effect

Fig. 4.3 shows the MSE of the three types of single-tap equalizers as a function of the subcarrier index for an SNR of 15 dB. One can first check that the crosses, which corresponds to the MSE approximation of (4.1), perfectly match the simulated MSE. As it could be expected,

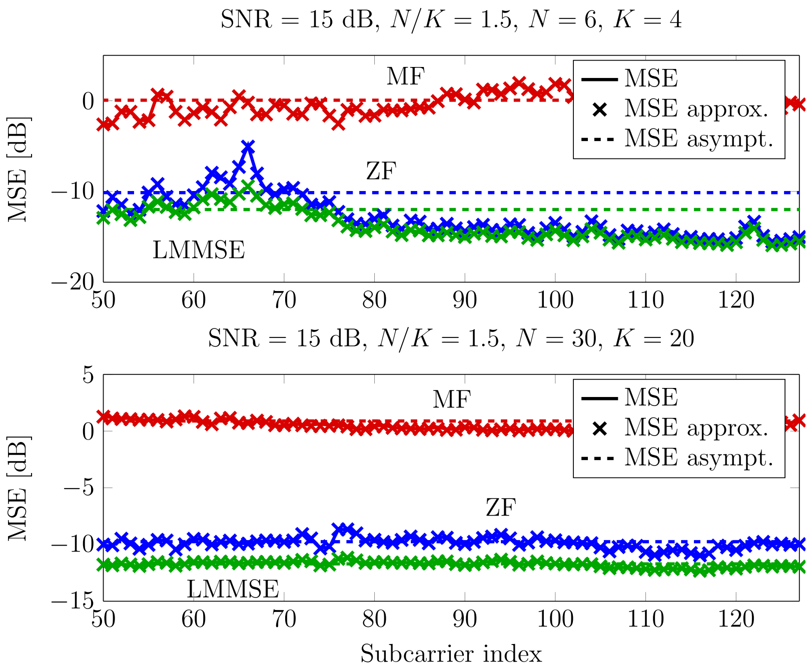

Figure 4.3 MSE across the subcarriers. The MSE approximation in crosses perfectly matches the simulated MSE in continuous lines. As the number of users K and the BS antennas N increases (above figure), the MSE gets flat across frequency and converge to the derived asymptotic MSE.

the LMMSE is the best equalizer closely followed by the ZF, while the MF has a poorer performance. Note that both Figures 4.3 (a) and (b) are plotted for the same ratio $N/K = 1.5$, while in (a), $N = 6$ and in (b), $N = 30$. One can clearly see in (b) that, as expected by Theorems 1-2, when N and K grow, the MSE gets flat across frequency and converges to the asymptotic expressions of the MSE derived in Theorems 3 and 4.

Figures 4.4 (a) and (b) plot the MSE as a function of the SNR for the same antenna configuration as in the previous figure. The dashed lines correspond to the asymptotic approximation of the MSE of Theorems 1-3 while the circles correspond to the MSE averaged over the subcarriers and the channel realizations. The vertical bars indicate the 90% confidence interval of the measured MSE across the spectrum and channel realizations. In other words, 90% of the subcarriers and channel

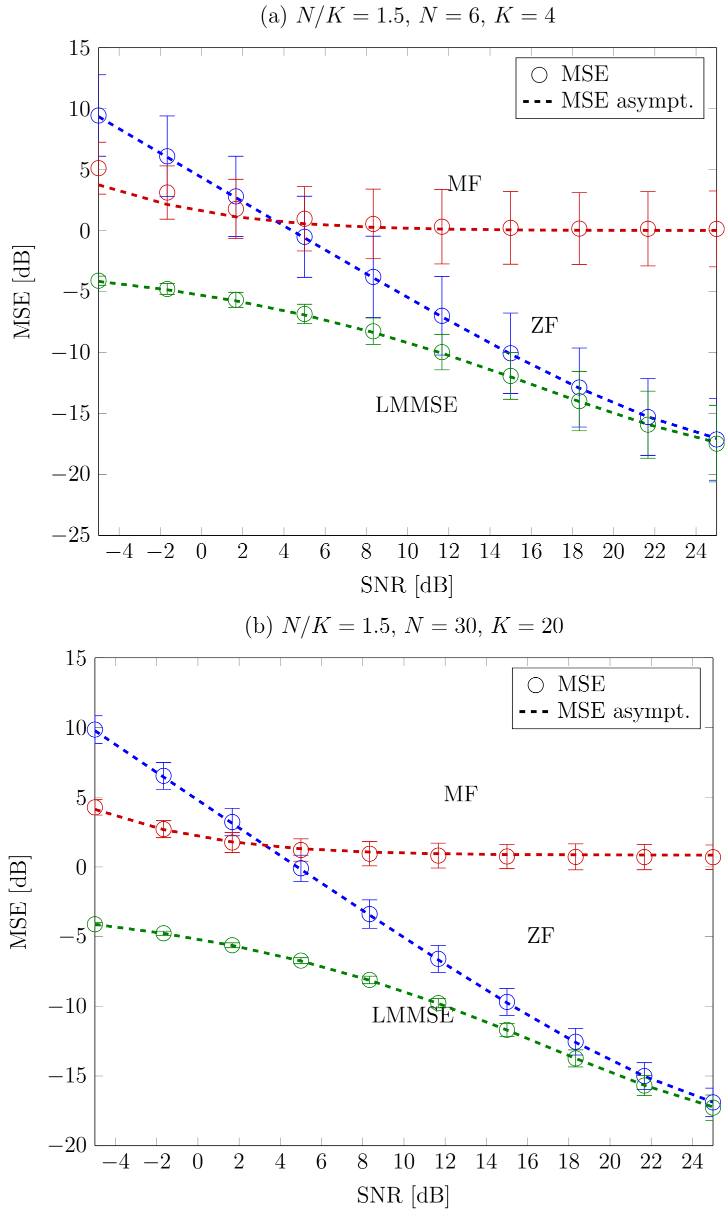

Figure 4.4 Simulated MSE vs. asymptotic MSE as a function of the SNR. Vertical bars represent the 90% confidence interval.

realizations resulted in a simulated MSE within these vertical intervals. Observe that the asymptotic formulas of the MSE provide a very accu-

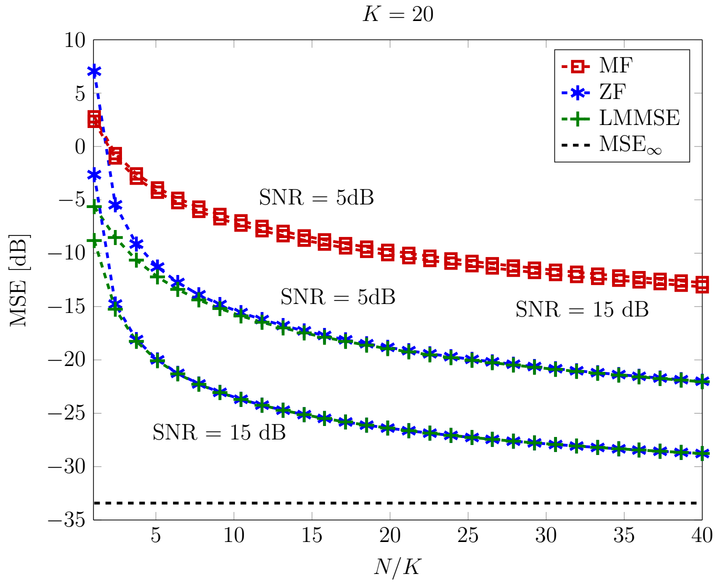

Figure 4.5 Asymptotic MSE as a function of the ratio N/K.

rate description of the average MSE, even for relatively low values of N and K (in Fig. 4.4 (a)). Further, observe in Fig. 4.4 (b) that, as N and K grow, the variance of the simulated MSE is drastically reduced, confirming the convergence predicted by Theorems 1-3. Finally, note that at high SNR, the MSE begins to saturate due to the distortion induced by the channel selectivity, *i.e.*, the terms related to the delay average and delay spread of the channel in Theorems 3 and 4. We will see in the following figure that these terms may go to zero as well.

4.3.2 On the self-equalization effect

Fig. 4.5 plots the asymptotic MSE as a function of the ratio N/K for the three equalizers and two SNR values, *i.e.*, 5 dB and 15 dB. One can clearly observe the self-equalization effect. As N/K increases, the MSE decreases and the different terms of the MSE progressively go to zero, except for the term related to the average delay of the channel. The curve denoted by MSE_∞ corresponds to the performance floor observed

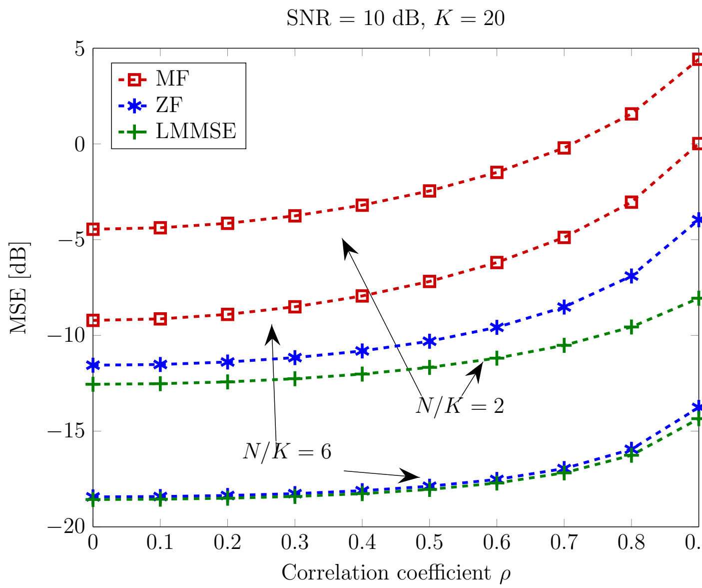

Figure 4.6 Asymptotic MSE as a function of the correlation at the BS.

for the ZF and MF equalizers and is defined as

$$\mathrm{MSE}_\infty = E_T \tilde{\eta} \frac{\mathrm{tr}\left[\mathbf{D}_{\mathrm{av}}^2\right]}{K}.$$

The value of MSE_∞ could be diminished by a better synchronization of the users and the BS, which would decrease the value of $\mathrm{tr}\left[\mathbf{D}_{\mathrm{av}}^2\right]$. Furthermore, one can note that the performance of the LMMSE and ZF equalizers rapidly converge as N/K increases. Moreover, note that increasing the SNR is beneficial for the ZF and LMMSE equalizers while it does not help the MF a lot. Indeed, as predicted by Theorem 3, the MF is especially limited by IUI, which does not depend on the SNR.

Fig. 4.6 plots the asymptotic MSE of the three single-tap equalizers as a function of the correlation coefficient ρ for an SNR of 10 dB and two ratios N/K. Note that ρ models the degree of correlation between the BS antennas. One can see that the ZF and LMMSE equalizers are relatively robust to the correlation between BS antennas except for high values of ρ, especially for the ZF equalizer with a low ratio N/K. On the other hand, the MF appears to be more sensitive to the BS inter-antenna correlation. Again, this makes sense since, following Theorem 3, the MF is especially limited by IUI, which becomes stronger as the channels of the different users get more correlated.

4.4 Conclusion

We have investigated the performance of FBMC-OQAM systems in an uplink massive MIMO scenario. The performance of three types of single-tap equalizers was analyzed as the number of BS antennas and the number of users grow large. For each equalizer, the MSE was shown to converge to a deterministic quantity that does not depend on the subcarrier index. Further, it was shown that a good synchronization of the user is of crucial importance. Finally, the "self-equalization" effect of FBMC-OQAM was verified by theory and simulations. This shows that, under a good synchronization, having a large ratio N/K allows for a low value of the MSE, even in the case of highly selective channels and classical low complexity equalizers.

4.5 Proofs

4.5.1 Proof of Theorem 3

For the sake of the compactness of the expressions, we define $\mathbf{F}_m = \mathbf{D}_{1/2,m}$ and $\mathbf{F}_m^{(1)} = \mathbf{\Phi}\mathbf{D}_{1/2,m}$. Let us first review well known results related to the resolvent $\mathbf{Q}(\lambda)$ defined as

$$\begin{aligned}\mathbf{Q}(\lambda) &= \left(\frac{\mathbf{H}_m^H\mathbf{H}_m}{K} + \lambda\mathbf{I}_K\right)^{-1}\\ &= \left(\mathbf{F}_m^H\frac{\mathbf{G}^H\mathbf{C}_{\mathrm{BS}}\mathbf{G}}{K}\mathbf{F}_m + \lambda\mathbf{I}_K\right)^{-1}.\end{aligned}$$

Theorem 5. *Let $\mathbf{G}$ consist of i.i.d. standardized complex Gaussian entries, and assume that both $\mathbf{C}_{\mathrm{BS}}$ and $\mathbf{D}_\beta = \mathbf{F}_m^H \mathbf{F}_m$ be matrices of appropriate dimensions with uniformly bounded spectral norm. Assume that $K, N \to \infty$ with*

$$0 < \liminf \frac{N}{K} \leq \limsup \frac{N}{K} < \infty.$$

Then, for each sequence of deterministic matrices $\mathbf{A}$ of size $K \times K$ with uniformly bounded spectral norm and assuming $\lambda > 0$, we have

$$\frac{1}{K}\mathrm{tr}[\mathbf{A}\left(\mathbf{Q}\left(\lambda\right) - \mathbf{T}\left(\lambda\right)\right)] \xrightarrow{a.s.} 0, \tag{4.17}$$

where

$$\mathbf{T}\left(\lambda\right) = \left(\lambda \mathbf{I}_K + \tilde{\delta}\left(\lambda\right) \mathbf{D}_\beta\right)^{-1}$$

and where $\left(\tilde{\delta}\left(\lambda\right), \delta\left(\lambda\right)\right)$ are the only positive pair of solutions to the system of equations

$$\begin{aligned}
\delta\left(\lambda\right) &= \frac{1}{K}\mathrm{tr}\left[\mathbf{D}_\beta \left(\lambda \mathbf{I}_K + \tilde{\delta}\left(\lambda\right) \mathbf{D}_\beta\right)^{-1}\right] \\
\tilde{\delta}\left(\lambda\right) &= \frac{1}{K}\mathrm{tr}\left[\mathbf{C}_{\mathrm{BS}}\left(\mathbf{I}_N + \delta\left(\lambda\right)\mathbf{C}_{\mathrm{BS}}\right)^{-1}\right].
\end{aligned}$$

Furthermore, the above convergence can be extended to the case $\lambda = 0$ assuming that $\inf \frac{N}{K} > 1$.

The result is well known in the random matrix theory literature, see e.g. [117, 118] for some early studies of this random matrix model. We here follow the formulation established in [119, 120]. In particular, it follows from [120] and [121] that if the eigenvalues of $\mathbf{D}_\beta$ and $\mathbf{C}_{\mathrm{BS}}$ are uniformly contained in two compact intervals of $\mathbb{R}^+$, the eigenvalues of $\mathbf{F}_m^H \frac{\mathbf{G}\mathbf{C}_{\mathrm{BS}}\mathbf{G}^H}{K}\mathbf{F}_m$ are contained on a compact interval $\mathcal{S} \subset \mathbb{R}^+$ for all large K, N. Furthermore, it was shown in [120] that $0 \notin \mathcal{S}$ if $\inf \frac{N}{K} > 1$. This means that, if $\lambda \in \mathbb{C}\backslash\left(\mathbb{R}^- \cup \{0\}\right)$ we have $\mathrm{dist}\left(-\lambda, \mathcal{S}\right) > 0$ and that this property also holds for $\lambda = 0$ when $\inf \frac{N}{K} > 1$.

Convergence of (4.17) has been usually proven for $\lambda \in \mathbb{C} \backslash \left(\mathbb{R}^{-} \cup \{0\}\right)$, but it can be trivially extended to all the region of interest according to the following reasoning. Observe that the spectral norm of $\mathbf{Q}\left(\lambda\right)$ and $\mathbf{T}\left(\lambda\right)$ is upperbounded by $\left(\mathrm{dist}\left(-\lambda, \mathcal{S}\right)\right)^{-1}$, because they are Stieljes transforms of positive matrix valued measures (see further [122]). Furthermore these matrices are holomorphic functions on all the region of interest. Therefore, by a standard application of Montel's theorem, one can establish almost convergence in all the region of interest.

Next, we present a result that can trivially be established using the same approach as in [119] (details are therefore omitted).

Proposition 2. *Let $\lambda \in \mathbb{C} \backslash \left(\mathbb{R}^{-} \cup \{0\}\right)$. Under the above set of assumptions, and assuming that $\mathbf{A}, \mathbf{B}$ and $\boldsymbol{\Upsilon}$ are sequences of rectangular deterministic matrices of appropriate dimensions with uniformly bounded spectral norm, and define*

$$\widehat{\Psi}_0\left(\lambda\right) = \frac{1}{K}\mathrm{tr}[\mathbf{A}\mathbf{Q}\left(\lambda\right)]$$
$$\widehat{\Psi}_1\left(\lambda\right) = \frac{1}{K}\mathrm{tr}\left[\mathbf{A}\mathbf{Q}\left(\lambda\right)\mathbf{B}\frac{\mathbf{G}\boldsymbol{\Upsilon}\mathbf{G}^H}{K}\right].$$

It holds that

$$\left|\mathbb{E}\widehat{\Psi}_0\left(\lambda\right) - \Psi_0\left(\lambda\right)\right| = \frac{1}{N}P_1(|\lambda|)P_2\left(\frac{1}{|\Im(\lambda)|}\right) \tag{4.18}$$

$$\left|\mathbb{E}\widehat{\Psi}_1\left(\lambda\right) - \Psi_1\left(\lambda\right)\right| = \frac{1}{N}P_1(|\lambda|)P_2\left(\frac{1}{|\Im(\lambda)|}\right) \tag{4.19}$$

where P_1 and P_2 are polynomials of positive coefficients independent of K, N (the values of which may change from line to line), and where we have defined *the deterministic quantities*

$$\Psi_0(\lambda) = \frac{1}{K}\mathrm{tr}[\mathbf{A}\mathbf{T}(\lambda)]$$
$$\Psi_1(\lambda) = \frac{1}{K}\mathrm{tr}[\mathbf{A}\mathbf{T}(\lambda)\mathbf{B}]\frac{1}{K}\mathrm{tr}[\boldsymbol{\Upsilon}]$$
$$-\frac{1}{K}\mathrm{tr}\big[\mathbf{A}\mathbf{T}(\lambda)\mathbf{F}_m^H\big]\frac{1}{K}\mathrm{tr}[\mathbf{T}(\lambda)\mathbf{B}\mathbf{F}_m]\frac{1}{K}\mathrm{tr}\Big[(\mathbf{I}_N+\delta(\lambda)\mathbf{C}_{\mathrm{BS}})^{-1}\mathbf{C}_{\mathrm{BS}}\boldsymbol{\Upsilon}\Big].$$

Furthermore, we can establish that

$$\mathrm{var}\left(\widehat{\Psi}_0(\lambda)\right) = \frac{1}{N^2}P_1(|\lambda|)P_2\left(\frac{1}{|\Im(\lambda)|}\right)$$
$$\mathrm{var}\left(\widehat{\Psi}_1(\lambda)\right) = \frac{1}{N^2}P_1(|\lambda|)P_2\left(\frac{1}{|\Im(\lambda)|}\right).$$

The result in (4.19) accepts an interesting particularization in the case where $\mathbf{B} = \mathbf{F}_m^H$, for which, one trivially obtains

$$\Psi_1(\lambda) = \frac{1}{K}\mathrm{tr}\big[\mathbf{A}\mathbf{T}(\lambda)\mathbf{F}_m^H\big]\frac{1}{K}\mathrm{tr}\Big[(\mathbf{I}_N+\delta(\lambda)\mathbf{C}_{\mathrm{BS}})^{-1}\boldsymbol{\Upsilon}\Big].$$

We now have all the ingredients to prove Theorems 3, which we summarize in the following proposition.

Proposition 3. *Let* $\lambda \in \mathbb{C}\backslash(\mathbb{R}^- \cup \{0\})$*. Consider two sequences of* $N \times N$ *deterministic matrices* $\boldsymbol{\Gamma}_1$*,* $\boldsymbol{\Gamma}_2$ *with uniformly bounded spectral norm, and define*

$$\widehat{\Psi}_2(\lambda) = \frac{1}{K}\mathrm{tr}\left[\mathbf{Q}(\lambda)\mathbf{F}_m^H\frac{\mathbf{G}\boldsymbol{\Gamma}_1\mathbf{G}^H}{K}\mathbf{F}_m^{(1)}(\mathbf{F}_m^{(1)})^H\frac{\mathbf{G}\boldsymbol{\Gamma}_2\mathbf{G}^H}{K}\mathbf{F}_m\right]$$

Under the assumptions of Theorem 1 and 2, we can write

$$\left|\mathbb{E}\widehat{\Psi}_2(\lambda) - \Psi_2(\lambda)\right| = \frac{1}{N}P_1(|\lambda|)P_2\left(\frac{1}{|\Im(\lambda)|}\right) \tag{4.20}$$

where

$$\Psi_2(\lambda) = \tilde{\delta}^2(\lambda) \frac{1}{K} \mathrm{tr}\left[\mathbf{T}(\lambda) \mathbf{F}_m^H \mathbf{F}_m^{(1)} \left(\mathbf{F}_m^{(1)} \right)^H \mathbf{F}_m \right]$$
$$+ \delta(\lambda) \frac{1}{K} \mathrm{tr}\left[\mathbf{C}_{\mathrm{BS}}^2 \left(\mathbf{I}_N + \delta(\lambda) \mathbf{C}_{\mathrm{BS}} \right)^{-1} \right] \frac{1}{K} \mathrm{tr}\left[\mathbf{F}_m^{(1)} (\mathbf{F}_m^{(1)})^H \right].$$

Furthermore,

$$\mathrm{var}\left(\widehat{\Psi}_2(\lambda) \right) = \frac{1}{N^2} P_1(|\lambda|) P_2\left(\frac{1}{|\Im(\lambda)|} \right).$$

Before presenting the proof of this result, let us reason why the above two propositions directly prove almost sure convergence of the MSE quantities in Theorems 3. To see this, observe that, using (4.5), all the terms in the expression of $\mathrm{MSE}_m(\lambda)$ can be expressed in the form of $\widehat{\Psi}_0(\lambda)$, $\widehat{\Psi}_1(\lambda)$ and $\widehat{\Psi}_2(\lambda)$ together with their derivatives with respect to λ,[4] for different choices of the deterministic matrices $\mathbf{A}$, $\mathbf{B}$, $\boldsymbol{\Upsilon}$, $\boldsymbol{\Gamma}_1$, $\boldsymbol{\Gamma}_2$ (all of which have bounded spectral norm). Hence, almost sure convergence of all these quantities and their derivatives will ultimately establish the result. Now, from Propositions 2 and 3, we obtain that

$$\mathbb{E}\left| \widehat{\Psi}_i(\lambda) - \Psi_i(\lambda) \right|^2 = \left| \mathbb{E}\widehat{\Psi}_i(\lambda) - \Psi_i(\lambda) \right|^2 + \mathrm{var}\left(\widehat{\Psi}_i(\lambda) \right)$$
$$= \frac{1}{N^2} P_1(|\lambda|) P_2\left(\frac{1}{|\Im(\lambda)|} \right).$$

A direct application of the Markov inequality and the Borel Cantelli lemma shows that $\widehat{\Psi}_i(\lambda) - \Psi_i(\lambda) \to 0$ almost surely to zero for every fixed $\lambda \in \mathbb{C} \backslash (\mathbb{R}^- \cup \{0\})$ (or $\lambda = 0$ when $\inf \frac{N}{K} > 1$). Indeed, all the terms in the MSE expression are analytic and almost surely bounded for all $\lambda \in \mathbb{C} \backslash (\mathbb{R}^- \cup \{0\})$ (or $\lambda = 0$ when $\inf \frac{N}{K} > 1$). Hence, Montel's theorem shows that convergence holds uniformly in compact sets in the same region, which additionally implies convergence of the corresponding complex derivatives.

[4]Note that the derivative with respect to λ of $\mathbf{Q}(\lambda)$ is $\frac{d\mathbf{Q}}{d\lambda}(\lambda) = -\mathbf{Q}^2(\lambda)$.

We devote the rest of the appendix to the proof of Proposition 3. We first establish the bound of the variance by using the Nash-Poincaré inequality [123], which establishes that (if g_{ij} denotes the (i,j)-th entry of $\mathbf{G}$)

$$\operatorname{var}\left[\widehat{\Psi}\left(\mathbf{G},\mathbf{G}^*\right)\right] \leq \sum_{j=1}^{LK}\sum_{j=1}^{N}\mathbb{E}\left[\left|\frac{\partial\widehat{\Psi}\left(\mathbf{G},\mathbf{G}^*\right)}{\partial g_{ij}^*}\right|^2\right] + \mathbb{E}\left[\left|\frac{\partial\widehat{\Psi}\left(\mathbf{G},\mathbf{G}^*\right)}{\partial g_{ij}}\right|^2\right] \tag{4.21}$$

for any continuously differentiable $\widehat{\Psi}\left(\mathbf{G},\mathbf{G}^*\right)$ such that both itself and its derivatives are polynomially bounded functions of $\mathbf{G}$. One can readily see that

$$\begin{aligned}
&\sum_{j=1}^{LK}\sum_{j=1}^{N}\mathbb{E}\left[\left|\frac{\partial\widehat{\Psi}_2\left(\lambda\right)}{\partial g_{ij}^*}\right|^2\right] \\
&= \frac{1}{K^2}\frac{1}{K}\mathbb{E}\mathrm{tr}\Bigg[\mathcal{Q}\frac{\mathbf{G}\boldsymbol{\Gamma}_1\mathbf{G}^H}{K}\mathcal{F}\frac{\mathbf{G}\boldsymbol{\Gamma}_2\mathbf{G}^H}{K}\mathcal{Q}\frac{\mathbf{G}\mathbf{C}_{\mathrm{BS}}^2\mathbf{G}^H}{K}\mathcal{Q}^H \\
&\qquad\qquad\qquad\qquad \frac{\mathbf{G}\boldsymbol{\Gamma}_2^H\mathbf{G}^H}{K}\mathcal{F}\frac{\mathbf{G}\boldsymbol{\Gamma}_1^H\mathbf{G}^H}{K}\mathcal{Q}^H\Bigg] \\
&+ \frac{1}{K^2}\frac{1}{K}\mathbb{E}\mathrm{tr}\left[\mathcal{F}\frac{\mathbf{G}\boldsymbol{\Gamma}_2\mathbf{G}^H}{K}\mathcal{Q}\frac{\mathbf{G}\boldsymbol{\Gamma}_1\boldsymbol{\Gamma}_1^H\mathbf{G}^H}{K}\mathcal{Q}^H\frac{\mathbf{G}\boldsymbol{\Gamma}_2^H\mathbf{G}^H}{K}\mathcal{F}\right] \\
&+ \frac{1}{K^2}\frac{1}{K}\mathbb{E}\mathrm{tr}\left[\mathcal{Q}\frac{\mathbf{G}\boldsymbol{\Gamma}_1\mathbf{G}^H}{K}\mathcal{F}\frac{\mathbf{G}\boldsymbol{\Gamma}_2\boldsymbol{\Gamma}_2^H\mathbf{G}^H}{K}\mathcal{F}\frac{\mathbf{G}\boldsymbol{\Gamma}_1^H\mathbf{G}^H}{K}\mathcal{Q}^H\right]
\end{aligned}$$

where $\mathcal{Q} = \mathbf{F}_m\mathbf{Q}(\lambda)\mathbf{F}_m^H$, $\mathcal{F} = \mathbf{F}_m^{(1)}(\mathbf{F}_m^{(1)})^H$ and where we have used the fact that

$$\frac{\partial\mathbf{Q}}{\partial g_{ij}^*} = -\mathbf{Q}(\lambda)\mathbf{F}_m^H\frac{\mathbf{G}\mathbf{C}_{\mathrm{BS}}\mathbf{e}_j\mathbf{e}_i^T}{K}\mathbf{F}_m\mathbf{Q}(\lambda)$$

with $\mathbf{e}_j$ denoting the j-th column of the identity matrix. Now, using the fact that $\|\mathbf{Q}(\lambda)\| \leq \frac{1}{|\Im(\lambda)|}$, the uniform boundedness of the spectral norm of $\mathcal{F}$, $\mathbf{C}_{\mathrm{BS}}$, $\mathbf{F}_m$, $\boldsymbol{\Gamma}_1$, $\boldsymbol{\Gamma}_2$ and the result in [124, Lemma 2], we readily obtain that the above term is bounded by a quantity of the type

$N^{-2}P_1(|\lambda|)P_2\left(\frac{1}{|\Im(\lambda)|}\right)$. The same reasoning can be applied to the second term on the right hand side of (4.21), leading to the result (details are omitted).

Next, we prove the identity in (4.20). We will be using the integration by parts formula [123], which establishes that for any continuously differentiable $\widehat{\Psi}\left(\mathbf{G},\mathbf{G}^*\right)$ such that both itself and its derivatives are polynomically bounded functions of $\mathbf{G}$, we have

$$\mathbb{E}\left[g_{ij}\widehat{\Psi}\left(\mathbf{G},\mathbf{G}^*\right)\right] = \mathbb{E}\left[\frac{\partial\widehat{\Psi}\left(\mathbf{G},\mathbf{G}^*\right)}{\partial g_{ij}^*}\right].$$

More specifically, we consider the decomposition of $\mathbf{G}$ as

$$\mathbf{G} = \sum_{j=1}^{LK}\sum_{j=1}^{N} g_{ij}\mathbf{e}_i\mathbf{e}_j^T.$$

Using this decomposition in the definition of $\widehat{\Psi}_2\left(\lambda\right)$, we directly obtain

$$\mathbb{E}\widehat{\Psi}_2\left(\lambda\right) = \sum_{j=1}^{LK}\sum_{j=1}^{N}\frac{1}{K}\mathbb{E}\frac{\partial}{\partial g_{ij}^*}\mathrm{tr}\left[\mathcal{Q}\frac{\mathbf{e}_i\mathbf{e}_j^T\mathbf{\Gamma}_1\mathbf{G}^H}{K}\mathcal{F}\frac{\mathbf{G}\mathbf{\Gamma}_2\mathbf{G}^H}{K}\right]$$

and, after some algebra,

$$\begin{aligned}\mathbb{E}\widehat{\Psi}_2\left(\lambda\right) = &-\mathbb{E}\left[\frac{1}{K}\mathrm{tr}\left[\mathcal{Q}\frac{\mathbf{G}\mathbf{C}_{\mathrm{BS}}\mathbf{\Gamma}_1\mathbf{G}^H}{K}\mathcal{F}\frac{\mathbf{G}\mathbf{\Gamma}_2\mathbf{G}^H}{K}\right]\frac{1}{K}\mathrm{tr}\mathcal{Q}\right]\\ &+\mathbb{E}\left[\frac{1}{K}\mathrm{tr}\left[\mathcal{Q}\mathcal{F}\frac{\mathbf{G}\mathbf{\Gamma}_2\mathbf{G}^H}{K}\right]\frac{1}{K}\mathrm{tr}[\mathbf{\Gamma}_1]\right]\\ &+\mathbb{E}\left[\frac{1}{K}\mathrm{tr}\left[\mathbf{\Gamma}_1\frac{\mathbf{G}^H\mathcal{F}\mathbf{G}}{K}\mathbf{\Gamma}_2\right]\frac{1}{K}\mathrm{tr}\mathcal{Q}\right].\end{aligned}$$

Observe that the first term on the right hand side of the above equation is very similar to $\widehat{\Psi}_2\left(\lambda\right)$. Next, we introduce the following error definition in the first and last terms on the right hand side of the above equation, namely

$$\epsilon_0(\lambda) = \frac{1}{K}\mathrm{tr}\left[\mathbf{F}_m^H \mathbf{F}_m (\mathbf{Q} - \mathbb{E}\mathbf{Q})\right].$$

After some algebra, and replacing $\mathbf{\Gamma}_1$ in the above expression of $\mathbb{E}\widehat{\Psi}_2(\lambda)$ we obtain

$$\begin{aligned}
&\mathbb{E}\frac{1}{K}\mathrm{tr}\left[\mathcal{Q}\frac{\mathbf{G}\mathbf{\Gamma}_1\mathbf{G}^H}{K}\mathcal{F}\frac{\mathbf{G}\mathbf{\Gamma}_2\mathbf{G}^H}{K}\right] \\
&= \frac{1}{K}\mathbb{E}\mathrm{tr}\left[\mathcal{Q}\mathcal{F}\frac{\mathbf{G}\mathbf{\Gamma}_2\mathbf{G}^H}{K}\right]\frac{1}{K}\mathrm{tr}\left[\left(\mathbf{I}_N + \frac{1}{K}\mathbb{E}\mathrm{tr}[\mathcal{Q}]\,\mathbf{C}_{\mathrm{BS}}\right)^{-1}\mathbf{\Gamma}_1\right] \\
&+ \frac{1}{K}\mathrm{tr}\left[\left(\mathbf{I}_N + \frac{1}{K}\mathbb{E}\mathrm{tr}[\mathcal{Q}]\,\mathbf{C}_{\mathrm{BS}}\right)^{-1}\mathbf{\Gamma}_1\mathbf{\Gamma}_2\right]\frac{\mathrm{tr}[\mathcal{F}]}{K}\frac{\mathbb{E}\mathrm{tr}[\mathcal{Q}]}{K} \\
&+ \chi_1 + \chi_2
\end{aligned} \tag{4.22}$$

where

$$\begin{aligned}
\chi_1 &= \mathbb{E}\left[t_1(\lambda)\,\epsilon_0(\lambda)\right] \\
\chi_2 &= -\mathbb{E}\left[t_2(\lambda)\,\epsilon_0(\lambda)\right] \\
t_1(\lambda) &= \mathrm{tr}\left[\frac{1}{K}\left(\mathbf{I}_N + \frac{1}{K}\mathbb{E}\mathrm{tr}[\mathcal{Q}]\,\mathbf{C}_{\mathrm{BS}}\right)^{-1}\mathbf{\Gamma}_1\frac{\mathbf{G}^H\mathcal{F}\mathbf{G}}{K}\mathbf{\Gamma}_2\right] \\
t_2(\lambda) &= \frac{1}{K}\mathrm{tr}\left[\mathcal{Q}\frac{\mathbf{G}\mathbf{C}_{\mathrm{BS}}\left(\mathbf{I}_N + \frac{1}{K}\mathbb{E}\mathrm{tr}[\mathcal{Q}]\,\mathbf{C}_{\mathrm{BS}}\right)^{-1}\mathbf{\Gamma}_1\mathbf{G}^H}{K}\mathcal{F}\frac{\mathbf{G}\mathbf{\Gamma}_2\mathbf{G}^H}{K}\right].
\end{aligned}$$

Now, a direct application of the Cauchy-Schwarz inequality shows that

$$|\chi_1| \leq \sqrt{\mathrm{var}\left(t_1(\lambda)\right)\mathrm{var}\left(\epsilon_0(\lambda)\right)}.$$

By Proposition 2, we see that $|\chi_1| = N^{-1}P_1(|\lambda|)P_2\left(\frac{1}{|\Im(\lambda)|}\right)$. A similar reasoning shows that $|\chi_2| = N^{-1}P_1(|\lambda|)P_2\left(\frac{1}{|\Im(\lambda)|}\right)$. Using this in (4.22), particularizing the resulting expression for $\mathbf{\Gamma}_1 = \mathbf{\Gamma}_2 = \mathbf{C}_{\mathrm{BS}}$ and observe that, by Proposition 2,

$$\left|\frac{1}{K}\mathbb{E}\mathrm{tr}[\mathcal{Q}] - \delta\right| = N^{-1}P_1(|\lambda|)P_2\left(\frac{1}{|\Im(\lambda)|}\right),$$

$$\left|\frac{1}{K}\mathbb{E}\mathrm{tr}\left[\mathcal{Q}\mathcal{F}\frac{\mathbf{G}\mathbf{C}_{\mathrm{BS}}\mathbf{G}^H}{K}\right] - \tilde{\delta}\frac{1}{K}\mathrm{tr}\left[\mathbf{T}\left(\lambda\right)\mathbf{F}_m^H\mathcal{F}\mathbf{F}_m\right]\right|$$
$$= N^{-1}P_1(|\lambda|)P_2\left(\frac{1}{|\Im(\lambda)|}\right),$$

we obtain the result of the proposition.

4.5.2 Proof of Theorem 4

rewriting $\mathrm{MSE}_m^{\mathrm{MF}}$ in (4.16) as a function of the matrix $\mathbf{G}$ using (4.5), as we did for the ZF and LMMSE equalizers, one will observe terms that have the following general form,

$$\frac{1}{K}\mathbb{E}\mathrm{tr}\left[\hat{\mathbf{Y}}^{-1}\Psi\left(\mathbf{G},\mathbf{G}^H\right)\right],$$

where $\hat{\mathbf{Y}}$ is a diagonal matrix defined as

$$\hat{\mathbf{Y}} = \mathrm{diag}\left(\frac{\mathbf{H}_m^H\mathbf{H}_m}{K}\right) = \mathrm{diag}\left(\mathbf{F}_m^H\frac{\mathbf{G}\mathbf{C}_{\mathrm{BS}}\mathbf{G}^H}{K}\mathbf{F}_m\right).$$

The proof of Theorem 4 consists in showing that $\hat{\mathbf{Y}}$ can be replaced by its asymptotic equivalent $\mathbf{Y}$. Then, one only needs to compute the expectation of $\mathbb{E}\Psi\left(\mathbf{G},\mathbf{G}^H\right)$, which can be easily computed. Here below, in Proposition 4, we only give the first part of the proof. The other one is omitted due to space constraints.

Proposition 4. *Assume that $\Psi\left(\mathbf{G},\mathbf{G}^H\right)$ is a function of $\mathbf{G}$ such that*

$$\sup_{K,N}\frac{1}{K}\mathbb{E}\mathrm{tr}\left[\Psi\left(\mathbf{G},\mathbf{G}^H\right)\Psi\left(\mathbf{G},\mathbf{G}^H\right)^H\right] < \infty$$

and let

$$\mathbf{Y} = \mathbb{E}\left(\hat{\mathbf{Y}}\right) = \operatorname{diag}\left(\mathbf{F}_m^H \mathbf{F}_m\right) \frac{1}{K} \operatorname{tr}[\mathbf{C}_{\mathrm{BS}}] .$$

Assume that the eigenvalues of $\mathbf{F}_m^H \mathbf{F}_m$ *are located on a compact set of* $\mathbb{R}^+$ *independent of* K, N *and that* $\inf \frac{1}{K}\operatorname{tr}[\mathbf{C}_{\mathrm{BS}}] > 0$*. Then, as* $K, N \to \infty$ *at the same rate,*

$$\frac{1}{K}\operatorname{tr}\left[\left(\mathbf{Y}^{-1} - \hat{\mathbf{Y}}^{-1}\right) \Psi\left(\mathbf{G}, \mathbf{G}^H\right)\right] \to 0$$

almost surely.

Indeed, observe that we can write, by the Cauchy-Schwarz inequality,

$$\begin{aligned}
&\left|\frac{1}{K}\operatorname{tr}\left[\left(\mathbf{Y}^{-1} - \hat{\mathbf{Y}}^{-1}\right) \Psi\left(\mathbf{G}, \mathbf{G}^H\right)\right]\right| \\
&= \left|\frac{1}{K}\operatorname{tr}\left[\left(\hat{\mathbf{Y}} - \mathbf{Y}\right) \hat{\mathbf{Y}}^{-1} \Psi\left(\mathbf{G}, \mathbf{G}^H\right) \mathbf{Y}^{-1}\right]\right| \\
&\leq \sqrt{\frac{1}{K}\operatorname{tr}\left[\mathbf{Y}^{-2}\left(\hat{\mathbf{Y}} - \mathbf{Y}\right) \hat{\mathbf{Y}}^{-2}\left(\hat{\mathbf{Y}} - \mathbf{Y}\right)\right]} \\
&\qquad \sqrt{\frac{1}{K}\operatorname{tr}\left[\Psi\left(\mathbf{G}, \mathbf{G}^H\right) \Psi\left(\mathbf{G}, \mathbf{G}^H\right)^H\right]} \\
&\leq \alpha \left\|\hat{\mathbf{Y}}^{-1}\right\| \left\|\mathbf{Y}^{-1}\right\| \left\|\hat{\mathbf{Y}} - \mathbf{Y}\right\|
\end{aligned}$$

for some positive constant α. Observe that $\left\|\mathbf{Y}^{-1}\right\| < \infty$ by assumption, whereas $\left\|\hat{\mathbf{Y}}^{-1}\right\|$ will also be bounded for sufficiently large K, N because of the norm convergence. Hence, we only we now prove that $\left\|\hat{\mathbf{Y}} - \mathbf{Y}\right\| \to 0$ almost surely to prove the theorem.

In order to see $\left\|\hat{\mathbf{Y}} - \mathbf{Y}\right\| \to 0$, let $\hat{d}_{ii}$ and d_{ii} denote the i-th diagonal entry of $\hat{\mathbf{Y}}$ and $\mathbf{Y}$ respectively. Then, for an arbitrary $\epsilon > 0$, we have

$$P\left[\left\|\hat{\mathbf{Y}} - \mathbf{Y}\right\| > \epsilon\right] = P\left[\max_i \left|\hat{d}_{ii} - d_{ii}\right| > \epsilon\right] \leq \sum_{i=1}^{K} P\left[\left|\hat{d}_{ii} - d_{ii}\right| > \epsilon\right].$$

However, the i-th entry of $\hat{\mathbf{Y}}$ can be expressed as

$$\hat{d}_{ii} = \mathbf{x}_i^H \frac{\mathbf{C}_{\mathrm{BS}}}{K} \mathbf{x}_i$$

where $\mathbf{x}_i$ is a circular Gaussian vector with zero mean and variance $\mathbb{E}\left[\mathbf{x}_i \mathbf{x}_i^H\right] = \mathbb{E}\left[\mathbf{G}^H \mathbf{f}_i \mathbf{f}_i^H \mathbf{G}\right] = \|\mathbf{f}_i\|^2 \mathbf{I}$ with $\mathbf{f}_i$ denoting the i-th column of $\mathbf{F}_m$. Using, e.g. [125, Lemma 2.7], for $p \geq 2$

$$\mathbb{E}\left[\left|\hat{d}_{ii} - d_{ii}\right|^p\right] \leq \frac{\alpha_1}{K^{p/2}} \left(\frac{1}{K} \mathrm{tr}\left[\left(\|\mathbf{f}_i\|^2 \mathbf{C}_{\mathrm{BS}}\right)^2\right]\right)^{p/2} + \frac{\alpha_2}{K^p} \mathrm{tr}\left[\left(\|\mathbf{f}_i\|^2 \mathbf{C}_{\mathrm{BS}}\right)^p\right].$$

Choosing, e.g. $p = 5$ we see that $\mathbb{E}\left[\left|\hat{d}_{ii} - d_{ii}\right|^5\right] = O\left(K^{-5/2}\right)$ and therefore, using Markov inequality, $P\left[\left\|\hat{\mathbf{Y}} - \mathbf{Y}\right\| > \epsilon\right] \leq O\left(K^{-3/2}\right)$. Applying the Borel-Cantelli lemma we obtain the result.

CHAPTER 5

PARALLEL EQUALIZATION STRUCTURE FOR PTP MIMO DOUBLY SELECTIVE CHANNELS

If the channel is slowly varying in time and frequency, single-tap equalization is sufficient to compensate for the channel distortion and restore the FBMC-OQAM orthogonality. However, as the channel gets more selective in time and frequency, distortion will appear and FBMC will suffer from so-called intrinsic interference caused by ISI and ICI. As detailed in Section 2.1.5.2, many papers have proposed algorithms to compensate for the distortion induced by the frequency selectivity of the channel while the case of time selective channels has received much less attention. The interested reader is referred to Section 2.1.5.3 for a review on the associated literature.

In this work, we first characterize the effect of time and frequency variations of the channel on the FBMC transceiver chain. Second, we propose a new receiver structure for PTP MIMO FBMC-OQAM systems that can compensate for both the time and frequency selectivity of the channel. This receiver uses multiple AFB working in parallel on the received signal. Each AFB is using a different derivative of the prototype pulse with respect to time and frequency. The demodulated symbols coming from each parallel AFB are then equalized and re-combined in order to mitigate the distortion caused by the channel variations. This processing does not require any additional delay as opposed to multi-tap equalizers and has a relatively low complexity of implementation. Furthermore, analytical approximations of the residual distortion and noise power after equalization are given, which results in a very compact expression, as compared with [63]. The proposed parallel equalization structure may be seen as an extension of the work of [53, 55] to the doubly selective channel case. Another related work that aimed at characterizing the FBMC distortion based on the same approach but restricted to the frequency selective only case, was performed in [126–128].

The rest of this chapter is structured as follows. Section 5.1 details the system model for a general FBMC-OQAM MIMO transceiver and proposes different orders of approximation of the demodulated symbol for doubly selective channels. Section 5.2 proposes the new parallel receiver structure and gives a theoretical expression of the residual distortion and noise power. Section 5.3 validates the accuracy of the distortion approximation and the performance of the proposed equalization structure. Finally, Section 5.4 concludes the chapter.

5.1 System model

5.1.1 FBMC-OQAM transmission model

We consider a MIMO FBMC-OQAM transmission chain as described in Section 2.1 and shown in Fig. 2.5. Let us omit the effect of additive noise to simplify the exposition. Since the noise is not correlated with the data, its impact may be studied independently, as will be shown later (see Section 5.2.2). As a reminder, the signal after demodulation, at subcarrier m_0 and multicarrier symbol l_0, denoted by $\mathbf{z}_{m_0,l_0} \in \mathbb{C}^{N_R \times 1}$, may be written as (in the noiseless case)

$$\begin{aligned}\mathbf{z}_{m_0,l_0} &= \sum_{n=0}^{2M\tilde{N}_s-1} \mathbf{r}[n] g^*_{m_0,l_0}[n] \\ &= \sum_{l=0}^{2N_s-1} \sum_{m=0}^{2M-1} \sum_{n=0}^{2M\tilde{N}_s-1} \sum_{b=-\infty}^{+\infty} \mathbf{C}[b,n] \mathbf{d}_{m,l} p_{m,l}[n-b] g^*_{m_0,l_0}[n],\end{aligned}$$

where $\mathbf{C}[b,n] \in \mathbb{C}^{N_R \times N_T}$ is the time-variant channel impulse response at time instant n and corresponding to delay b. The effect of the channel $\mathbf{C}[b,n]$ on $\mathbf{z}_{m_0,l_0}$ is a mixed function of the transmitted data, channel and pulses. It is then convenient to find accurate approximations and more practical expressions of $\mathbf{z}_{m_0,l_0}$. Since we here consider the case of strongly doubly selective channels, a conventional 0-th order approximation of $\mathbf{z}_{m_0,l_0}$ as given in (2.6),

$$\mathbf{z}_{m_0,l_0} \approx \mathbf{H}_{m_0,l_0} \sum_{l=0}^{2N_s-1} \sum_{m=0}^{2M-1} \mathbf{d}_{m,l} \sum_{n=0}^{2M\tilde{N}_s-1} p_{m,l}[n] g^*_{m_0,l_0}[n], \tag{5.1}$$

is highly non accurate. The work of [53] initially proposed the idea of considering higher order approximations of the demodulated signal $\mathbf{z}_{m_0,l_0}$ in the presence of channel frequency selectivity. Here, we extend the approach of [53] to doubly selective channels. To be able to write this higher order approximation of the demodulated symbol, we need to give a deeper description of the channel model. In the same way, smoothness conditions on the prototype pulses are necessary.

5.1.2 Doubly selective channel model

Let us introduce the continuous time-frequency response of the channel, denoted by $\mathbf{H}(\omega, t)$ and defined in terms of normalized time and angular frequency, *i.e.*, $t \in [0,1], \omega \in [0, 2\pi]$. The normalized time $t = 0$ denotes the beginning of the data transmission and $t = 1$, its end or unnormalized time $\tilde{N}_s T$ [s]. The normalized angular frequency $\omega = 0$ and $\omega = 2\pi$

corresponds to the edges of the system bandwidth, *i.e.*, unnormalized frequencies 0 and $\frac{2M}{T}$ [Hz].

Since the function $\mathbf{H}(\omega, t)$ is limited to unnormalized frequency $\frac{2M}{T}$ and time $\tilde{N}_s T$, we know from the Shannon sampling theorem that the inverse Fourier transform of $\mathbf{H}(\omega, t)$ with respect to frequency ω can be sampled in the delay domain with a spacing $\frac{T}{2M}$, without causing any aliasing in the frequency domain. Similarly, the Fourier transform of $\mathbf{H}(\omega, t)$ with respect to time t can be sampled in the Doppler domain with a spacing $\frac{1}{\tilde{N}_s T}$. Hence, $\mathbf{H}(\omega, t)$ is equivalently defined by the discrete-delay-Doppler spreading function of the channel [129], which we denote by $\mathbf{\Psi}[b, \nu]$. The index b denotes the delay tap index while ν denotes the Doppler tap index. The functions $\mathbf{H}(\omega, t)$ and $\mathbf{\Psi}[b, \nu]$ are related through the relations

$$\begin{aligned}
\mathbf{H}(\omega, t) &= \sum_{b=-\infty}^{+\infty} \sum_{\nu=-\infty}^{+\infty} \mathbf{\Psi}[b, \nu] e^{\jmath\left(\frac{\omega 2M}{T}\right)\left(\frac{bT}{2M}\right)} e^{-\jmath 2\pi\left(t\tilde{N}_s T\right)\left(\frac{\nu}{\tilde{N}_s T}\right)} \\
&= \sum_{b=-\infty}^{+\infty} \sum_{\nu=-\infty}^{+\infty} \mathbf{\Psi}[b, \nu] e^{-\jmath\omega b} e^{\jmath 2\pi t\nu}, \qquad (5.2) \\
\mathbf{\Psi}[b, \nu] &= \frac{1}{2\pi} \int_0^{2\pi} \left[\int_0^1 \mathbf{H}(\omega, t) e^{-\jmath 2\pi t\nu} dt \right] e^{\jmath\omega b} \, d\omega.
\end{aligned}$$

Functions $\mathbf{H}(\omega, t)$ and $\mathbf{\Psi}[b, \nu]$ equivalently define the channel and all channel frequency quantities can be derived from them. Equation (5.2) highlights the fact that $\mathbf{H}(\omega, t)$ can be seen as the linear superposition of multiple scatterers, each having a particular delay and Doppler shift. The time-variant channel impulse response $\mathbf{C}[b, n]$ at time instant n and corresponding to delay b can be obtained from $\mathbf{\Psi}[b, \nu]$ as

$$\mathbf{C}[b, n] = \sum_{\nu=-\infty}^{+\infty} \mathbf{\Psi}[b, \nu] e^{\jmath \frac{2\pi}{2\tilde{N}_s M} n\nu},$$

for $n = 0, \ldots, 2\tilde{N}_s M - 1$. The derivatives of the channel with respect to time and frequency at the subcarrier and multicarrier symbol of interest can also be expressed as a function of $\boldsymbol{\Psi}[b, \nu]$

$$\mathbf{H}_{m,l}^{(q,r)} = \frac{d^q}{d\omega^q}\frac{d^r}{dt^r}\mathbf{H}(\omega, t)\bigg|_{\omega=\omega_m, t=t_l} \tag{5.3}$$
$$= \sum_{b=-\infty}^{+\infty}\sum_{\nu=-\infty}^{\infty}(-\jmath b)^q(\jmath 2\pi\nu)^r\boldsymbol{\Psi}[b, \nu]e^{-\jmath\omega_m b+\jmath 2\pi t_l \nu},$$

for $l = 0, \ldots, 2N_s - 1$, $m = 0, \ldots, 2M - 1$ and where we defined $\omega_m = \frac{2\pi}{2M}m$ and $t_l = \frac{1}{2\tilde{N}_s M}(lM + \frac{2M\kappa-1}{2})$. Note that $\mathbf{H}_{m,l}^{(0,0)} = \mathbf{H}_{m,l}$. Equation (5.3) highlights the fact that the variations of $\mathbf{H}(\omega, t)$ with respect to frequency and time can be related to the support of $\boldsymbol{\Psi}[b, \nu]$. If the function $\boldsymbol{\Psi}[b, \nu]$ is very spread out in the delay and/or Doppler domains, one can expect large variations of $\mathbf{H}(\omega, t)$ in the frequency and/or time domains respectively. To characterize those variations, we make the following assumption:

(**As6**) The spreading function $\boldsymbol{\Psi}[b, \nu]$ is assumed to be causal and finitely supported in the delay and Doppler domains (as was assumed in [64]). This implies that $\boldsymbol{\Psi}[b, \nu]$ is non zero only for $b = 0, \ldots, L_b$ and $\nu = -L_\nu, \ldots, L_\nu$. Moreover, we assume that the parameters L_b and L_ν are related to the maximal delay τ_{max} [s] and Doppler shift f_d [Hz] of the underlying analog channel, given by $L_b = \lfloor \frac{\tau_{max} 2M}{T} \rfloor$ and $L_\nu = \lfloor f_d \tilde{N}_s T \rfloor$ with T being the multicarrier symbol period. The channel is assumed to be perfectly known by the receiver. Furthermore, we assume that

$$\inf_{(\omega,t)\in[0,2\pi]\times[0,1]} \lambda_{\min}\left(\mathbf{H}^H(\omega, t)\mathbf{H}(\omega, t)\right) > 0,$$
$$\sup_{(\omega,t)\in[0,2\pi]\times[0,1]} \lambda_{\max}\left(\mathbf{H}^H(\omega, t)\mathbf{H}(\omega, t)\right) < +\infty$$

where $\lambda_{\min}(\mathbf{A})$ and $\lambda_{\max}(\mathbf{A})$ denote the minimum and maximum eigenvalue of matrix $\mathbf{A}$ respectively.

Intuitively, $(\mathbf{As6})$ implies that the channel can be equivalently described by the combination of the effects of a finite number of scatterers, such that the number of delay taps and Doppler shifts are finite. Further, it implies that the channel is periodic in time and frequency, *i.e.*, $\mathbf{H}(\omega, 0) = \mathbf{H}(\omega, 1)$ and $\mathbf{H}(0, t) = \mathbf{H}(2\pi, t)$, which makes sense if a sufficiently large observation window is used both in time and frequency. The equivalent channel should then be zero at the edges due to the time-frequency windowing effect of the analog filters at the transmitter and the receiver. Still, the channel model remains quite general under $(\mathbf{As6})$. For instance, it can address the special cases of a timing or carrier frequency offset. A timing offset of x samples would be modeled by imposing that $\mathbf{\Psi}[b, \nu] = \mathbf{0}$ if $b < x$.

Moreover, $(\mathbf{As6})$ implies that the channel is perfectly known at the receiver. In practice, this is of course not the case and the receiver should estimate the function $\mathbf{\Psi}[b, \nu]$ based on pilots scattered in time and frequency inside the transmitted frame. If the support of the function $\mathbf{\Psi}[b, \nu]$ is not known in advance, one has to estimate the channel frequency response and its derivatives at each subcarrier and multicarrier symbol of interest by interpolation between the scattered pilots. Due to the OQAM modulation and the MIMO scenario, the pilot symbols may be impacted by ISI, ICI and inter-antenna interference. Many works in the literature have looked at this issue, see [33] for a general review or [68, 77] for more recent works on the challenges and solutions in pilot-aided channel estimation for FBMC-OQAM systems.

5.1.3 Conditions on the prototype pulses

We introduce the following assumptions on the prototype pulses:

$(\mathbf{As7})$ The transmit and receive prototype pulses $p[n]$ and $g[n]$ are of the perfect reconstruction type and of energy normalized to one. They are either symmetric or anti-symmetric. Furthermore, $g[n]$ is obtained by the discretization of an analog waveform $\tilde{g}(t) : \mathbb{R} \to \mathbb{R}$ so that

$$g[n] = \tilde{g}\left(\left(n - \frac{2M\kappa - 1}{2}\right)\frac{1}{2M}\right),$$

for $n = 0, \ldots, 2M\kappa - 1$ and zero elsewhere. The additional shift of $\frac{2M\kappa-1}{2}$ units is performed in order to obtain a causal pulse. Further, $\tilde{g}(t)$ is analytic and only non zero if $t \in [-\kappa/2, \kappa/2]$.

Moreover, we define $g^{(q,r)}[n]$ as

$$g^{(q,r)}[n] = \tilde{g}^{(q,r)}\left(\left(n - \frac{2M\kappa - 1}{2}\right)\frac{1}{2M}\right),$$

where $\tilde{g}^{(q,r)}(t) = \frac{d^q}{dt^q}(t^r \tilde{g}(t))$. Further, we define $\mathbf{y}^{(q,r)}_{m_0,l_0}$ as

$$\mathbf{y}^{(q,r)}_{m_0,l_0} = \sum_{l=0}^{2N_s-1} \sum_{m=0}^{2M-1} \mathbf{d}_{m,l} \sum_{n=0}^{2M\tilde{N}_s-1} p_{m,l}[n] g^{(q,r)*}_{m_0,l_0}[n], \tag{5.4}$$

where $g^{(q,r)}_{m_0,l_0}[n] = \jmath^{l_0+m_0} g^{(q,r)}[n-l_0M] e^{\jmath \frac{2\pi}{2M} m_0 (n - \frac{2M\kappa-1}{2})}$. Note that $\mathbf{y}^{(0,0)}_{m_0,l_0} = \mathbf{y}_{m_0,l_0}$ as defined in (2.2) and that, for perfect reconstruction pulses $p[n]$ and $g[n]$, the perfect reconstruction property is not generally fulfilled by $p[n]$ and $g^{(q,r)}[n]$ if $(q, r) \neq (0, 0)$.

5.1.4 Higher order approximation of the demodulated symbol

We are now in the position of introducing our higher order approximation of the demodulated symbol $\mathbf{z}_{m_0,l_0}$.

Proposition 5. *Under* $(\mathbf{As6}) - (\mathbf{As7})$*, an approximation of* $\mathbf{z}_{m_0,l_0}$ *of order* Q *with respect to channel variation in frequency and of order* R *with respect to channel variation in time is given by*

$$\mathbf{z}^{(Q,R)}_{m_0,l_0} = \sum_{r=0}^{R} \sum_{q=0}^{Q} \frac{\jmath^q}{(2M)^q q! (\tilde{N}_s)^r r!} \mathbf{H}^{(q,r)}_{m_0,l_0} \mathbf{y}^{(q,r)}_{m_0,l_0} \tag{5.5}$$

and as $\frac{\tau_{max}}{T} \to 0$ *and* $f_d T \to 0$*, the approximation error can be bounded by*

$$\left\| \mathbf{z}_{m_0,l_0} - \mathbf{z}^{(Q,R)}_{m_0,l_0} \right\| = O\left(\left(\frac{\tau_{max}}{T} \right)^Q \right) + O\left((f_d T)^R \right). \tag{5.6}$$

Proof. The proof is based on the truncation of a double Taylor expansion of the channel and the pulse with respect to time and frequency. See Section 5.5 for the complete proof. □

Equation (5.5) gives more understanding of what is happening to the demodulated signal in the presence of channel selectivity. As the channel gets more selective, the derivatives of the channel $\mathbf{H}^{(q,r)}_{m_0,l_0}$ are amplified and distortion will be superimposed on the demodulated signal. Equation (5.6) shows that the approximation is more accurate when $\frac{\tau_{max}}{T}$ and $T f_d$ are small. As one would expect, a larger symbol period T is beneficial regarding frequency selectivity since the maximal delay of the channel will be smaller with respect to the symbol duration. At the same time, a larger T means that the channel will have stronger variations in time during one symbol period, which is detrimental regarding time selectivity. In practice, the choice of T should be made according to a trade-off between time and frequency selectivity. For a fixed T, the approximation is more accurate as τ_{max} and f_d decrease, *i.e.*, the time and frequency channel selectivity decreases. Furthermore, for a higher accuracy regarding time and frequency selectivity, one can always increase R and Q respectively. Moreover, one can check that $\mathbf{z}^{(0,0)}_{m_0,l_0}$ corresponds to the 0-th order approximation given in (2.6) and recalled in (5.1).

5.2 Parallel equalization structure

We here extend the proposed receiver structure of [53, 55] to doubly selective channels. Let us consider that the receiver uses $(R+1)(Q+1)$ AFB's working in parallel on the received signal, as shown in Fig. 5.1. Each

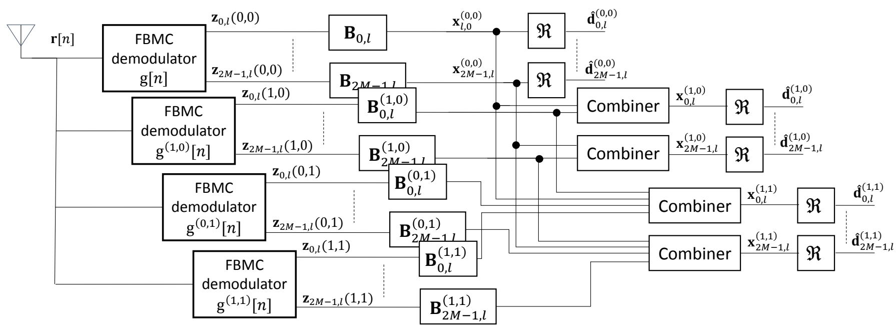

Figure 5.1 Parallel equalization structure at the receiver for different designs: $Q = 0, R = 0$ (classical), $Q = 1, R = 0$ and $Q = 1, R = 1$.

AFB has a different index pair (q, r) with $q = 0, \dots, Q$ and $r = 0, \dots, R$ and uses $g^{(q,r)}[n]$ as prototype pulse. After the $(R+1)(Q+1)$ parallel AFB's, the signals coming from each AFB are first equalized and then combined to cancel the distortion caused by the channel selectivity. To formalize this new receiver structure, we need to introduce the following assumption on the per-subcarrier decoding matrices:

($\mathbf{As8}$) There exists a function $\mathbf{B}(\omega, t)$ such that the per-subcarrier equalizers $\mathbf{B}_{m,l}$ at subcarrier m and multicarrier symbol l result from the evaluation of $\mathbf{B}(\omega, t)$ at frequency $\omega = \omega_m$ and time $t = t_l$. We define $\mathbf{B}(\omega, t)$ as

$$\mathbf{B}(\omega, t) = \left(\mathbf{H}(\omega, t)^H \mathbf{H}(\omega, t)\right)^{-1} \mathbf{H}(\omega, t)^H.$$

and its derivatives with respect to time and frequency as

$$\mathbf{B}_{m,l}^{(q,r)} = \frac{d^q}{d\omega^q} \frac{d^r}{dt^r} \mathbf{B}(\omega, t) \bigg|_{\omega=\omega_m, t=t_l}.$$

One can note that $\mathbf{B}_{m,l}^{(0,0)} = \mathbf{B}_{m,l}$. The following results can be extended to equalizers that do not invert the channel. However, we restricted the analysis to this case for the sake of compactness of the results and readability of the chapter.

Let us denote by $\mathbf{z}_{m_0,l_0}(q,r)$ the demodulated symbol at subcarrier m_0 and multicarrier symbol l_0 of the (q,r) AFB, such that $\mathbf{z}_{m_0,l_0}(0,0) = \mathbf{z}_{m_0,l_0}$. The following theorem gives the weights to combine the outputs of the $(R+1)(Q+1)$ parallel AFB's so that the combined equalized symbol is free from the distortion caused by the frequency selectivity up to an error term, the magnitude of which depends on Q and R.

Theorem 6. *Under* $(\mathbf{As6})$-$(\mathbf{As8})$*, the demodulated symbols* $\mathbf{z}_{m_0,l_0}(q,r)$ *of each AFB are combined into the symbol* $\mathbf{x}_{m_0,l_0}^{(Q,R)}$ *in the following way*

$$\begin{aligned}\mathbf{x}_{m_0,l_0}^{(Q,R)} &= \sum_{r=0}^{R}\sum_{q=0}^{Q} \frac{\jmath^q}{(2M)^q q! (\tilde{N}_s)^r r!} \mathbf{B}_{m_0,l_0}^{(q,r)} \mathbf{z}_{m_0,l_0}(q,r) \\ &= \mathbf{y}_{m_0,l_0} + \boldsymbol{\epsilon}_{m_0,l_0}^{\mathbb{C}}\end{aligned} \tag{5.7}$$

and as $\frac{\tau_{max}}{T} \to 0$ *and* $f_d T \to 0$*, the residual error after parallel processing,* $\boldsymbol{\epsilon}_{m_0,l_0}^{\mathbb{C}} = \mathbf{x}_{m_0,l_0}^{(Q,R)} - \mathbf{y}_{m_0,l_0}$*, is bounded by*

$$\left\|\boldsymbol{\epsilon}_{m_0,l_0}^{\mathbb{C}}\right\| = O\left(\left(\frac{\tau_{max}}{T}\right)^Q\right) + O\left((f_d T)^R\right).$$

Proof. The proof is given in Section 5.5. □

As it is classical in FBMC-OQAM systems, to recover the purely real transmitted symbol, the real part of the equalized signal is taken, *i.e.*, $\hat{\mathbf{d}}_{m_0,l_0}^{(Q,R)} = \Re(\mathbf{x}_{m_0,l_0}^{(Q,R)})$. Note that $\hat{\mathbf{d}}_{m_0,l_0}^{(0,0)} = \hat{\mathbf{d}}_{m_0,l_0}$.

Table 5.1 Implementation complexity of the different receivers under comparison.

Considered system	**Real-valued multiplications**
Classical FBMC ($Q = R = 0$)	$2MN_R(\log_2(2M) + 2\kappa + 2N_T - 3) + 4N_R$
Parallel equalization	$(2MN_R(\log_2(2M) + 2\kappa + 2N_T - 3) + 4N_R)(Q+1)(R+1)$
CP-OFDM	$N_R M(\log_2(2M) + 4N_T - 3) + 2N_R$

Regarding the complexity of implementation of the proposed design, one can check in Fig. 5.1 that it scales linearly with the number of parallel AFB's. Each parallel stage has its own filterbank and performs a per-subcarrier single-tap decoding. This shows that the complexity is about $(Q+1)(R+1)$ times the complexity of the classical FBMC-OQAM design. Table 5.1 shows the comparison of complexity of the classical designs, the proposed equalization structure and a similar CP-OFDM system, in terms of real-valued multiplications. For the calculation, we assume that the number of subcarriers is a power of two and that an FFT/IFFT of size $2M$ requires $2M(\log_2(2M)-3)+4$ real-valued multiplications using the split-radix algorithm [130]. Note that each parallel AFB can be efficiently implemented by the combination of a $2M$-FFT and a polyphase network [30].

We have proposed here a parallel equalization structure at the receiver side. A similar approach could be implemented at the transmitter side, in order to implement a pre-equalizer robust to time and frequency selectivity, as was done in [55] for the frequency selective case only.

5.2.1 Error model for the residual distortion after parallel processing

The next theorem proposes a model for the residual distortion power after parallel processing, equalization and real part conversion, which correlation matrix is defined as

$$\begin{aligned}\mathbf{P}^{d,(Q,R)}_{m,l|H} &= \mathbb{E}\left(\left(\mathbf{d}_{m,l}-\hat{\mathbf{d}}^{(Q,R)}_{m,l}\right)\left(\mathbf{d}_{m,l}-\hat{\mathbf{d}}^{(Q,R)}_{m,l}\right)^T\right)\\ &= \mathbb{E}\left(\Re\left(\boldsymbol{\epsilon}^{\mathbb{C}}_{m,l}\right)\left(\Re\left(\boldsymbol{\epsilon}^{\mathbb{C}}_{m,l}\right)\right)^T\right),\end{aligned}$$

where the expectation is taken over the transmitted symbols, for one specific channel realization[1]. Note that $\mathbf{P}^{d,(Q,R)}_{m,l|H}$ is a $N_T\times N_T$ error

[1] To highlight that the expectation is taken conditionally to the channel realization, we added the subscript $|H$ in the notation $\mathbf{P}^{d,(Q,R)}_{m,l|H}$.

correlation matrix. The distortion associated to the k-th stream is given by its k-th diagonal element while its trace gives the total distortion of all streams.

Theorem 7. *Under* $(\mathbf{As6})$-$(\mathbf{As8})$ *and up to an error term, we can write that*

$$
\begin{aligned}
\mathbf{P}^{d,(Q,R)}_{m,l|H} &= E_s \frac{\eta_{(0,R+1),(0,R+1)}}{\left((R+1)!(\tilde{N}_s)^{R+1}\right)^2} \left(\mathbf{B}^{(0,R+1)}_{m,l}\mathbf{H}_{m,l}\right)\left(\mathbf{B}^{(0,R+1)}_{m,l}\mathbf{H}_{m,l}\right)^H \\
&+ E_s \frac{\eta_{(Q+1,0),(Q+1,0)}}{((Q+1)!(2M)^{Q+1})^2} \left(\mathbf{B}^{(Q+1,0)}_{m,l}\mathbf{H}_{m,l}\right)\left(\mathbf{B}^{(Q+1,0)}_{m,l}\mathbf{H}_{m,l}\right)^H \\
&+ E_s \frac{\eta_{(0,R+1),(Q+1,0)}}{(R+1)!(\tilde{N}_s)^{R+1}(Q+1)!(2M)^{Q+1}} \\
&\qquad \left[\Re\left(\left(\mathbf{B}^{(0,R+1)}_{m,l}\mathbf{H}_{m,l}\right)\left(\jmath^{Q+1}\mathbf{B}^{(Q+1,0)}_{m,l}\mathbf{H}_{m,l}\right)^H\right)\right. \\
&\qquad\qquad \left. +\Re\left(\left(\jmath^{Q+1}\mathbf{B}^{(Q+1,0)}_{m,l}\mathbf{H}_{m,l}\right)\left(\mathbf{B}^{(0,R+1)}_{m,l}\mathbf{H}_{m,l}\right)^H\right)\right],
\end{aligned}
\tag{5.8}
$$

where the different η's are pulse-related quantities properly defined in Section 5.5.

Proof. The proof is given in Section 5.5. □

Theorem 7 gives a compact approximation for the residual distortion power of a receiver that would use $(R+1)(Q+1)$ parallel AFB's. The approximation is very accurate, as will be shown in the simulations. By inspection of the three terms of $\mathbf{P}^{d,(Q,R)}_{m,l|H}$, one can see that the first two are related to the distortion caused by time or frequency selectivity respectively while the third term of the sum is a cross term due to the fact that the channel is both selective in time and in frequency. In practice, by evaluating $\mathbf{P}^{d,(Q,R)}_{m,l|H}$, the receiver could make the best choice of R and Q by trading-off complexity and performance.

Note that the particularization of $\mathbf{P}^{d,(Q,R)}_{m,l|H}$ to $Q = 0, R = 0$ gives the expression of the distortion associated with the classical FBMC demodulator of Fig. 2.5 using only one AFB. These results are important to develop link abstraction model for FBMC system-level simulators, as was done in [126–128] but under a quasi-static assumption of the channel. Moreover, by particularizing the channel model, the performance analysis of an FBMC system with errors of synchronization can be performed, such as carrier frequency offset or timing offset.

5.2.2 Noise effect

In the previous analysis, the effect of the noise was discarded. Given that it is assumed uncorrelated with the data samples, its effect can be analyzed independently. If the receive antennas are corrupted by additive circularly-symmetric white Gaussian noise samples $\mathbf{w}[n]$, with zero mean and variance N_0, the noise samples after the AFB using $g^{(q,r)}[n]$ as prototype filter are given by

$$\mathbf{w}_{m,l}(q,r) = \sum_{n=0}^{2M\tilde{N}_s-1} g_{m,l}^{(q,r)*}[n]\mathbf{w}[n],$$

such that, after parallel combining, the noise samples become

$$\mathbf{w}_{m,l}^{(Q,R)} = \sum_{r=0}^{R}\sum_{q=0}^{Q} \frac{\jmath^q}{(2M)^q q!(\tilde{N}_s)^r r!}\mathbf{B}_{m,l}^{(q,r)}\mathbf{w}_{m,l}(q,r).$$

Then, the real part is taken such that the noise correlation matrix is

$$\mathbf{P}_{m,l|H}^{n,(Q,R)} = \mathbb{E}\left(\Re\left(\mathbf{w}_{m,l}^{(Q,R)}\right)\left(\Re\left(\mathbf{w}_{m,l}^{(Q,R)}\right)\right)^T\right), \tag{5.9}$$

where the expectation is taken over the noise statistics, for one specific channel realization. $\mathbf{P}_{m,l|H}^{wn,(Q,R)}$ is a $N_T \times N_T$ matrix, which k-th diagonal entry corresponds to the noise power associated to stream k. The following theorem gives the expression of $\mathbf{P}_{m,l|H}^{wn,(Q,R)}$.

Theorem 8. *The noise correlation matrix after parallel processing is given by*

$$\mathbf{P}_{m,l|H}^{wn,(Q,R)} = \frac{N_0}{2} \sum_{r'=0}^{R} \sum_{r=0}^{R} \sum_{q=0}^{Q} \sum_{q'=0}^{Q} \frac{(-1)^{q'} \alpha^{(q,r,q',r')} \Re \left(\jmath^{q+q'} \mathbf{B}_{m,l}^{(q,r)} \mathbf{B}_{m,l}^{(q',r')H} \right)}{(2M)^{q+q'} q! q'! (\tilde{N}_s)^{r+r'} r! r'!},$$

where

$$\alpha^{(q,r,q',r')} = \sum_{n=0}^{2M\tilde{N}_s - 1} g^{(q,r)}[n] g^{(q',r')}[n].$$

Due to the symmetry of the pulse $g[n]$, the evaluation of the noise can be greatly simplified by using the fact that $\alpha^{(q,r,q',r')} = 0$ if $q + r \neq q' + r' \mod 2$ ($g^{(q,r)}[n]$ and $g^{(q',r')}[n]$ do not share the same type of symmetry).

Proof. The proof is given in Section 5.5. □

This expression is exact and not an approximation as opposed to Theorems 6 and 7.

5.3 Simulation results

This section aims at assessing the performance of the proposed designs and approximations through simulations. Most results of previous sections show that the accuracy of the approximations depend on quantities $\frac{\tau_{max}}{T}$ and $T f_d$. We will show in the following that, even for high time and frequency channel selectivity, the symbol period T can be considered large enough with respect to τ_{max} and small with respect to f_d such that the assumption holds and the approximations closely match the simulations results.

Hereby, we assume that the symbol period and subcarrier spacing are fixed to $T = 66,67\mu s$ and 15 kHz, as in LTE systems. The number of real multicarrier symbols is $2N_s = 1000$ and the number of subcarriers is $2M = 128$. The carrier frequency is fixed to $f_c = 2000$ MHz, which corresponds to the E-UTRA band 23. We consider a terminal moving at

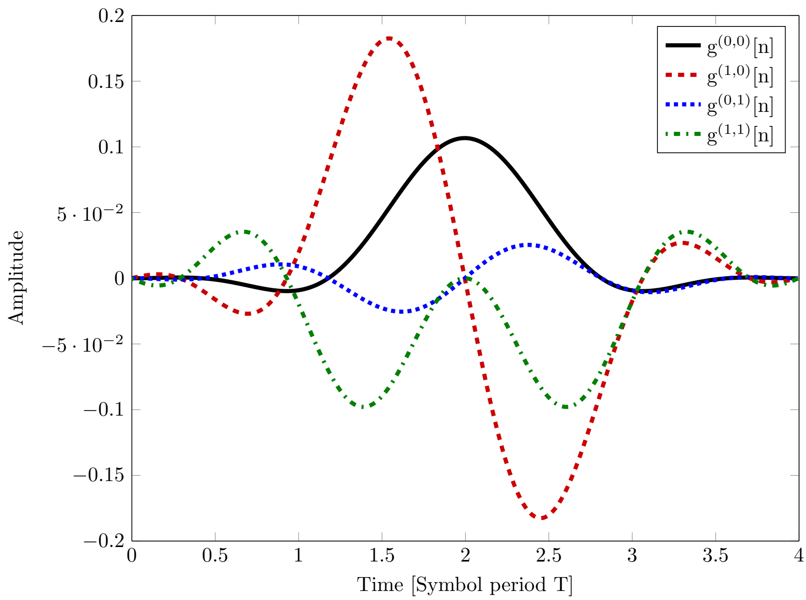

Figure 5.2 The prototype pulse and its derivatives used in the simulations.

speed $V = 400$ km/h, which corresponds to a maximal Doppler shift of $f_d = \frac{f_c V}{c} \approx 741$ Hz where c is the speed of light. To characterize the power delay profile of the channel, we will use the 3GPP - Hilly Terrain model [84], which corresponds to a highly frequency selective channel. The ITU - Veh. A channel model will also be used in one figure as an example of mildly frequency selective channel. Note that for both channel models, the Doppler spectrum of each tap is characterized by a classical Jakes model.

The per-stream signal-to-noise-and-distortion ratio (SNDR) is defined as

$$\mathrm{SNDR}_{m,l|H}(k) = \frac{E_s/2}{[\mathbf{P}^{d,(Q,R)}_{m,l|H}]_{k,k} + [\mathbf{P}^{n,(Q,R)}_{m,l|H}]_{k,k}},$$

where $k = 1, \ldots, N_T$ is the stream index. The SNDR is a very useful metric in practice since it characterizes the scale of the signal of interest

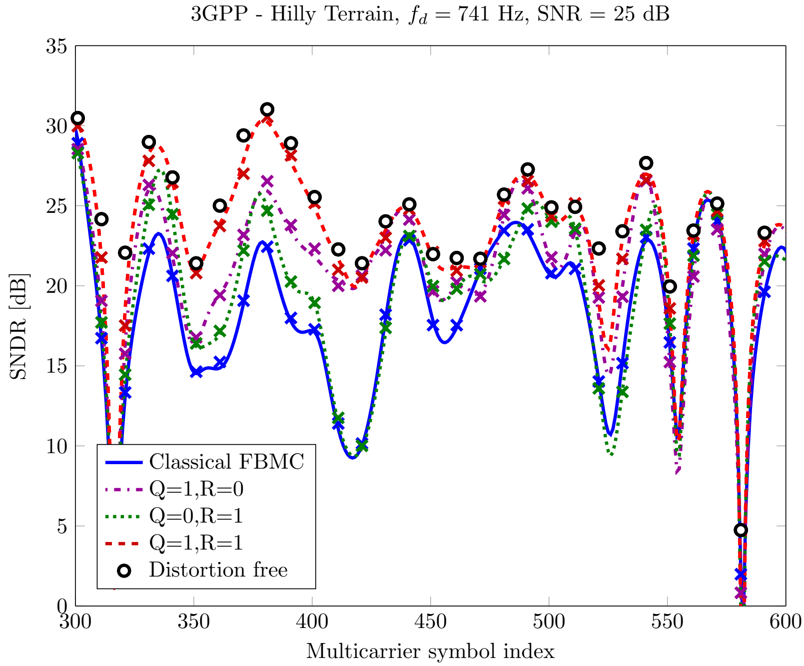

Figure 5.3 SNDR at one subcarrier as a function of the multicarrier symbol index and for one SISO channel realization. The simulated performance of the proposed receivers, plotted with crosses, is very close from the lines that represent the proposed SNDR approximation.

relatively to the power of the additive noise, ICI and ISI. We recall that $\mathbf{P}^{d,(Q,R)}_{m,l|H}$ and $\mathbf{P}^{n,(Q,R)}_{m,l|H}$ come from computing the expectation with respect to the transmitted symbols and noise for a specific channel realization. The SNR is defined as $\mathrm{SNR} = E_s/N_0$.

In the following simulations, the prototype pulse at transmit and receive sides is the PHYDYAS filter [6] with overlapping factor $\kappa = 4$. The pulse and its first derivatives are shown in Fig. 5.2.

Furthermore, the performance of a CP-OFDM system is also shown in several figures as a reference. For the sake of comparison, the same number of subcarriers $2M$, the same bandwidth and the same frame duration were considered as in the filterbank multicarrier (FBMC) case. The CP length used here is 10 samples, as it is defined for the first OFDM

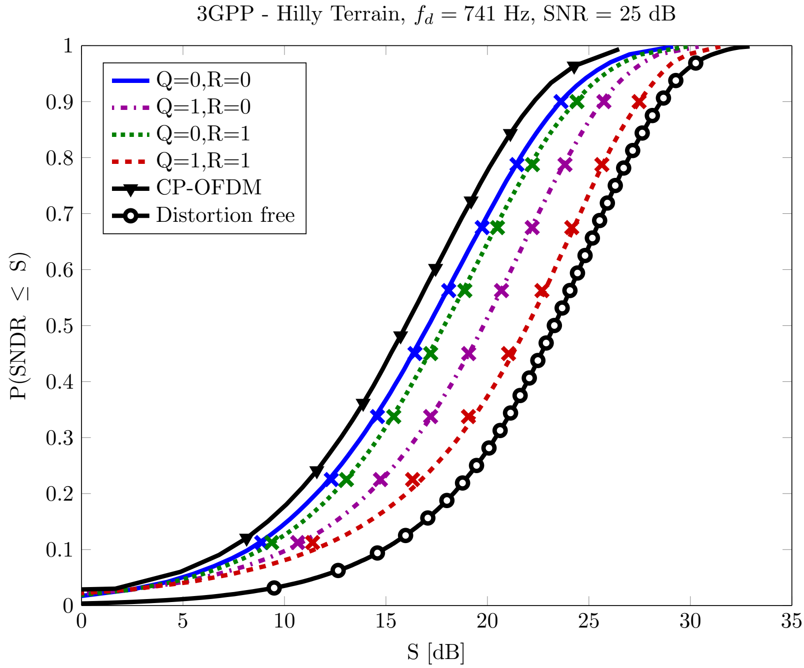

Figure 5.4 CDF of the SNDR for different types of parallel receiver structure in the SISO case, for one channel realization. The simulated performance of the proposed receivers, plotted with crosses, is very close from the lines that represent the proposed SNDR approximation. The simulated performance of a CP-OFDM system is also shown.

symbol of each slot in the normal mode of the LTE standard. Hence, for the same frame duration, less information bits are transmitted and the CP-OFDM system has a lower throughput rate than the corresponding FBMC system. Perfect channel estimation was also considered and the decoding matrices at each subcarrier were chosen as the pseudo-inverse of the channel evaluated at that frequency and multicarrier symbol, *i.e.*, zero-forcing equalization.

5.3.1 Validation of the theoretic expressions of Theorems 7 and 8

In Fig. 5.3, we consider a SISO case, *i.e.*, $N_R = N_T = 1$ and only one channel realization. For this channel realization, we plotted the SNDR at one subcarrier as a function of time, expressed in terms of the multicarrier symbol index, and for a fixed SNR of 25 dB. We used a high SNR regime to highlight the gain of the proposed designs. Indeed, at low SNR's, the distortion power is negligible compared to the noise power. Different versions of the proposed designs are plotted together with the classical FBMC implementation having only one AFB, as depicted in Fig. 2.5. The $Q = 0, R = 1$ (resp. $Q = 1, R = 0$) receiver has a second AFB which is used to cancel the first order of the distortion due to time (resp. frequency) selectivity. The $Q = 1, R = 1$ receiver uses four AFB's. The theoretical performance of a distortion free system is also shown, which corresponds to the theoretical case of a perfectly flat channel at the subcarrier level and during the pulse duration, *i.e.*, $\mathbf{H}_{m,l}^{(q,r)} = \mathbf{0}$ for $q > 0$ or $r > 0$. In other words, only additive noise impacts the equalized symbols. Furthermore, the crosses correspond to the simulated SNDR while the lines (continuous and dashed) correspond to the theoretical SNDR values from Theorems 7 and 8.

One can first notice in Fig. 5.3 the close match between the lines and the crosses, which imply that the proposed expressions of Theorems 7 and 8 are very accurate. There is visible gain of the proposed designs with respect to classical FBMC implementation. The $Q = 1, R = 1$ curve is even very close to the distortion free curve. At a few points however, we can see that the classical FBMC receiver performs better than the $Q = 0, R = 1$ and $Q = 1, R = 0$ designs. This is in accordance with the theoretical expression of $\mathbf{P}_{m,l|H}^{d,(Q,R)}$ and is more specifically related to the third term of (5.8), which is not restricted to be positive and may decrease the distortion, depending on the value of $\eta_{(0,R+1),(Q+1,0)}$. Still, we will see in the next figure that the proposed designs perform better "statistically", looking at their cumulative density function (CDF).

For the same channel realization as in Fig. 5.3, Fig. 5.4 shows the CDF of the SNDR, evaluated at all subcarriers and multicarrier symbols[2]. Again, one can note the close match between the lines (continuous and dashed) and the crosses, demonstrating the accuracy of Theorems 7 and 8. Next, increasing the number of AFB's is in each case statistically beneficial. The $Q = 1, R = 1$ curve gets close to the theoretical distortion free curve. To be even closer, it is possible to increase the number of AFB's, at the price of a higher receiver complexity. Furthermore, the performance of a CP-OFDM system is also shown, which is outperformed by all FBMC receivers. Indeed, since the length of the cyclic prefix is much smaller than the channel delay spread, CP-OFDM strongly suffers from the channel frequency selectivity. Furthermore, the bad time-frequency localization of the rectangular pulse in OFDM makes it very sensitive to time selectivity as well [131].

One can also see that the $Q = 0, R = 1$ design performs worse than the $Q = 1, R = 0$. This is due to the fact that the channel is comparatively more frequency selective than time selective. This is also related to the choice of the LTE symbol duration T, which is relatively low and provides high robustness to channel time variations. If it was chosen to be larger, the system would be more sensitive to time selectivity and less to frequency selectivity. The authors in [65, 132] provide a detailed performance analysis on the choice of the symbol duration as a function of the channel delay and Doppler spread.

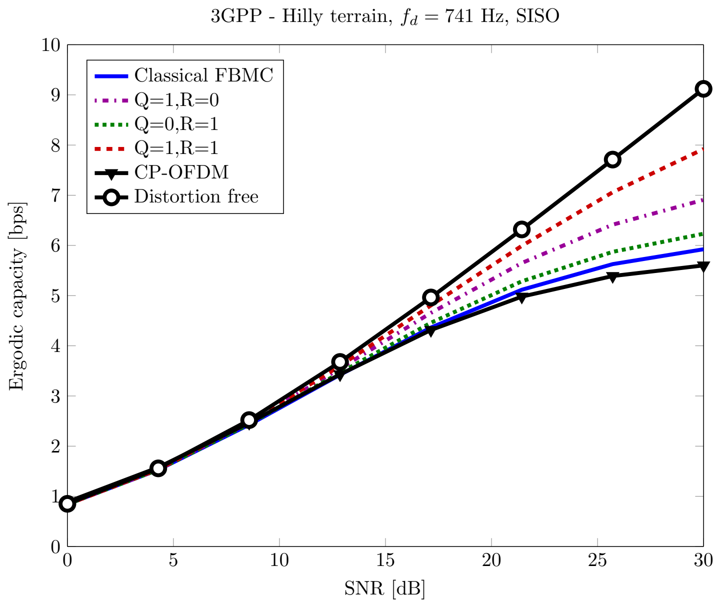

Figure 5.5 Ergodic capacity comparison of the proposed different parallel receivers, classical FBMC receiver and CP-OFDM system.

5.3.2 Ergodic capacity and outage symbol error rate for random channels

In Fig. 5.5, the ergodic capacity as a function of the SNR is plotted for the different designs under comparison, in the SISO case and averaged over multiple channel realizations. The distortion plus noise distribution at one subcarrier and multicarrier symbol, for one specific channel realization is approximated by a Gaussian distribution.

The ergodic capacity is defined as

$$\mathrm{R} = \mathbb{E}_H \left(\frac{1}{2M2N_s} \sum_{l=0}^{2N_s-1} \sum_{m=0}^{2M-1} \log_2 \left(1 + \mathrm{SNDR}_{m,l|H}(1)\right) \right),$$

[2]As a reminder, the SNDR metric come from taking the expectation with respect to the statistics of the noise and the transmitted symbols, conditionally to the channel realization.

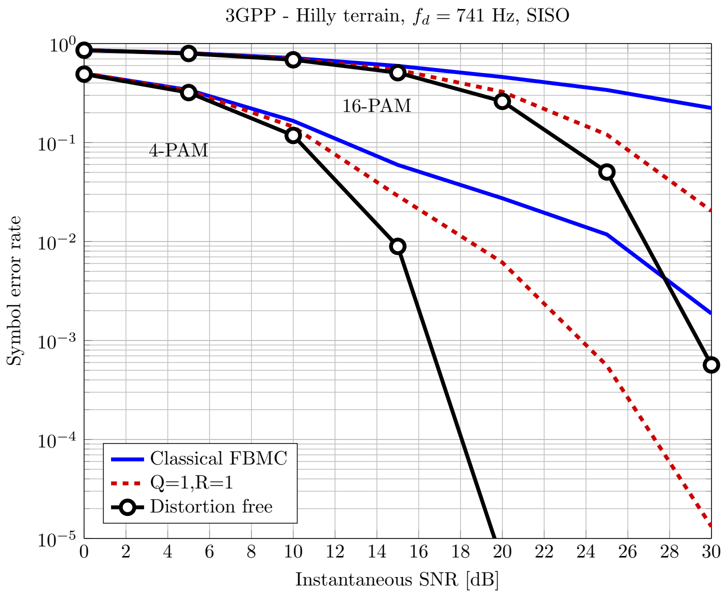

Figure 5.6 SER of the classical FBMC system, the proposed $Q = 1, R = 1$ design and the distortion free curve.

expressed in bits per symbol and where the expectation $\mathbb{E}_H$ is taken over the channel statistics. As could be expected, the proposed designs provide more robustness to channel selectivity. Furthermore, CP-OFDM exhibits the worst performance. In Fig. 5.6, the uncoded SER is plotted as a function of the instantaneous SNR for the classical FBMC system, the proposed $Q = 1, R = 1$ design and the distortion free curve. The instantaneous SNR is defined as the SNR at one particular subcarrier and multicarrier symbol, taking the channel gain into account. The curves are obtained by considering average SNR ranging from 0 to 30 dB and computing for each channel realization, each subcarrier and each multicarrier symbol, the corresponding instantaneous SNR. We plotted the results for a 4-PAM and a 16-PAM constellation sizes. Again, the proposed design outperforms the classical FBMC receiver.

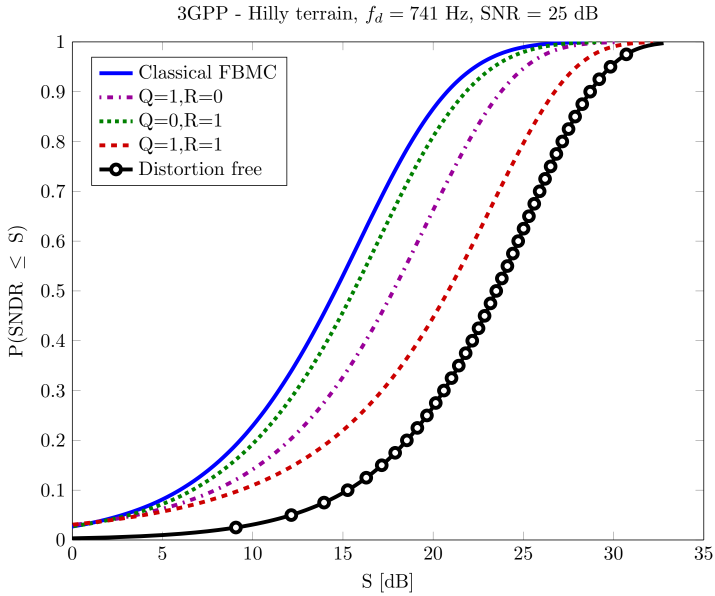

Figure 5.7 CDF of the SNDR for different types of parallel receiver structure in the $N_R = N_T = 2$ MIMO case.

5.3.3 Multiple-antenna case

In Fig. 5.7, the CDF of the SNDR's of the proposed designs evaluated at each subcarrier and multicarrier symbol is plotted for the MIMO case $N_R = N_T = 2$, for a fixed SNR of 25 dB and for multiple channel realizations. The same conclusion as in the SISO case holds. Note that the simulations of all figures were realized for a 3GPP-Hilly Terrain channel model and a maximal Doppler frequency $f_d = 741$ Hz, which corresponds to a channel highly selective both in time and frequency. The results demonstrated the superiority of the receiver structure $Q = 1, R = 1$. However, if the channel was for instance higly time selective but only slightly frequency selective, there would be no large gains of increasing Q to one. To illustrate this, we plotted in Fig. 5.8 the performance of the same system for the ITU - Veh. A channel model and for the same maximal Doppler frequency, *i.e.*, a channel which is strongly time selective but mildly frequency selective. As one can see,

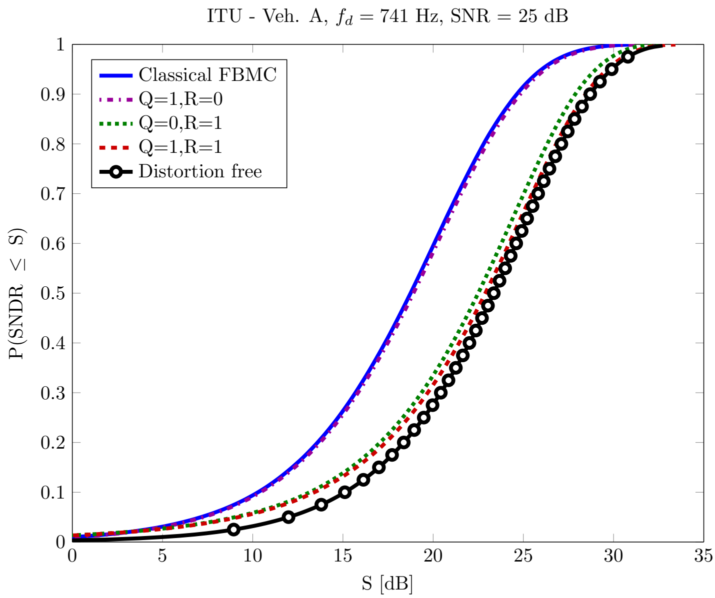

Figure 5.8 CDF of the SNDR for different types of parallel receiver structure in the $N_R = N_T = 2$ MIMO case. The channel is strongly time selective and mildly frequency selective.

the $Q = 1, R = 1$ and $Q = 0, R = 1$ curves are very close to the distortion free curve.

5.4 Conclusion

We investigated the effect of time and frequency selectivity on the performance of a FBMC-OQAM system. As the channel becomes more selective in the time-frequency plane, the demodulated symbol are affected by distortion caused by ICI and ISI. A new parallel equalization structure was proposed, such that the performance of a distortion free system can be retrieved by the use of multiple AFB's at the receiver side. A theoretical approximation of the residual distortion and noise powers after equalization was derived. The accuracy of the approximation as well as the performance of the proposed equalization structure were validated through simulations in the single-antenna and multiple-antenna cases.

5.5 Proofs

5.5.1 Proof of Proposition 5

Let us rewrite (2.5) by setting $n' = n - b$ as

$$\begin{aligned}\mathbf{z}_{m_0,l_0} &= \sum_{m,l}\sum_{n'}\sum_{b=0}^{L_b}\mathbf{C}[b, n'+b]g^*_{m_0,l_0}[n'+b]\mathbf{d}_{m,l}p_{m,l}[n'].\\ &= \sum_{m,l}\sum_{n'}\boldsymbol{\Delta}_{m_0,l_0}[n']\mathbf{d}_{m,l}p_{m,l}[n'],\end{aligned} \tag{5.10}$$

where we have defined

$$\begin{aligned}\boldsymbol{\Delta}_{m_0,l_0}[n'] &= \sum_{b=0}^{L_b}\mathbf{C}[b, n'+b]g^*_{m_0,l_0}[n'+b]\\ &= \beta^*_{m_0,l_0}\sum_{b=0}^{L_b}\mathbf{C}[b, n'+b]g[n'+b-l_0M]e^{-\jmath\omega_{m_0}b},\end{aligned} \tag{5.11}$$

with $\beta_{m_0,l_0} = \jmath^{l_0+m_0}e^{\jmath\omega_{m_0}(n'-\frac{2M\kappa-1}{2})}$. We are now going to develop the expression of $\boldsymbol{\Delta}_{m_0,l_0}[n']$.

Note that $\mathbf{C}[b, n'+b]$ comes from the evaluation at time $t = \frac{n'+b}{2\tilde{N}_sM}$ of the smooth function $\mathbf{F}_b(t)$ defined by

$$\mathbf{F}_b(t) = \sum_{\nu=-L_\nu}^{L_\nu}\boldsymbol{\Psi}[b,\nu]e^{\jmath 2\pi t\nu},$$

which can be seen as the time variant response of the b-th tap of the channel. We have

$$\mathbf{C}[b, n'+b] = \mathbf{F}_b(t)\big|_{t=\frac{n'+b}{2\tilde{N}_sM}}.$$

Since $\mathbf{C}[b, n'+b]g[n'+b-l_0 M]$ is non zero only for $n'+b \in \{l_0 M, \ldots, l_0 M + 2M\kappa - 1\}$, let us perform a Taylor expansion of $\mathbf{F}_b(t)$ around time instant $t_{l_0} = \frac{1}{2\tilde{N}_s M}(l_0 M + \frac{2M\kappa-1}{2})$ that we evaluate at $t = \frac{n'+b}{2\tilde{N}_s M}$. Note that this Taylor expansion converges for any t since the convergence radius of the exponential function is infinite. We obtain

$$\mathbf{C}[b, n'+b] = \sum_{r=0}^{+\infty} \frac{\mathbf{F}_b^{(r)}(t_{l_0})}{r!}(t - t_{l_0})^r \Bigg|_{t=\frac{n'+b}{2\tilde{N}_s M}}$$

$$= \sum_{r=0}^{+\infty} \sum_{\nu=-L_\nu}^{L_\nu} \frac{(\jmath 2\pi\nu)^r}{(\tilde{N}_s)^r r!} \boldsymbol{\Psi}[b,\nu] e^{\jmath 2\pi t_{l_0}\nu} \left(\frac{n'+b-l_0 M - \frac{2M\kappa-1}{2}}{2M} \right)^r .$$

Replacing this expression of $\mathbf{C}[b, n'+b]$ in (5.11), we obtain

$$\boldsymbol{\Delta}_{m_0,l_0}[n'] = \beta^*_{m_0,l_0} \sum_{r=0}^{+\infty} \sum_{\nu=-L_\nu}^{L_\nu} \frac{(\jmath 2\pi\nu)^r}{(\tilde{N}_s)^r r!} e^{\jmath 2\pi t_{l_0}\nu}$$

$$\sum_{b=0}^{L_b} \boldsymbol{\Psi}[b,\nu] g^{(0,r)}[n'+b-l_0 M] e^{-\jmath \omega_{m_0} b}. \tag{5.12}$$

Remember that $g^{(0,r)}[n'+b-l_0 M]$ can be seen as the evaluation of the function $\tilde{g}^{(0,r)}(t)$ at $\tilde{t} = (n'+b-l_0 M - \frac{2M\kappa-1}{2})\frac{1}{2M}$. Let us perform a Taylor expansion of $\tilde{g}^{(0,r)}(t)$ around point $\tilde{t}_{l_0} = (n' - l_0 M - \frac{2M\kappa-1}{2})\frac{1}{2M}$ that we evaluate at $\tilde{t}$

$$g^{(0,r)}[n'+b-l_0 M] = \sum_{q=0}^{+\infty} \frac{\tilde{g}^{(q,r)}\left(\tilde{t}_{l_0}\right)}{q!}(\tilde{t} - \tilde{t}_{l_0})^q$$

$$= \sum_{q=0}^{+\infty} \frac{g^{(q,r)}[n' - l_0 M]}{(2M)^q q!} b^q.$$

Note that, due to $(\mathbf{As7})$, $\tilde{g}(t)$ is analytic and the same holds for $\tilde{g}^{(q,r)}(t)$ since the product and derivatives of analytic functions are also analytic. Hence the above Taylor expansion is ensured to converge to $g^{(0,r)}[n'+b-l_0 M]$, which is bounded. Replacing the expression of $g^{(0,r)}[n'+b-l_0 M]$

by its Taylor expansion in (5.12), we obtain

$$
\begin{aligned}
\boldsymbol{\Delta}_{m_0,l_0}[n'] = \beta^*_{m_0,l_0} \sum_{r=0}^{+\infty}\sum_{q=0}^{+\infty} \frac{g^{(q,r)}[n'-l_0M]}{(2M)^q q!(\tilde{N}_s)^r r!} \\
\sum_{b=0}^{L_b}\sum_{\nu=-L_\nu}^{L_\nu} b^q (\jmath 2\pi\nu)^r \boldsymbol{\Psi}[b,\nu] e^{\jmath 2\pi t_{l_0}\nu} e^{-\jmath\omega_{m_0} b} \\
\overset{(5.3)}{=} \sum_{r=0}^{+\infty}\sum_{q=0}^{+\infty} \frac{\jmath^q \mathbf{H}^{(q,r)}_{m_0,l_0}}{(2M)^q q!(\tilde{N}_s)^r r!} g^{(q,r)*}_{m_0,l_0}[n'].
\end{aligned}
$$

If we replace this expression of $\boldsymbol{\Delta}_{m_0,l_0}[n']$ in (5.10), we finally obtain

$$
\begin{aligned}
\mathbf{z}_{m_0,l_0} &= \sum_{r=0}^{+\infty}\sum_{q=0}^{+\infty} \frac{\jmath^q \mathbf{H}^{(q,r)}_{m_0,l_0}}{(2M)^q q!(\tilde{N}_s)^r r!} \sum_{m,l} \mathbf{d}_{m,l} \sum_{n'} p_{m,l}[n'] g^{(q,r)*}_{m_0,l_0}[n'] \\
&= \sum_{r=0}^{+\infty}\sum_{q=0}^{+\infty} \frac{\jmath^q}{(2M)^q q!(\tilde{N}_s)^r r!} \mathbf{H}^{(q,r)}_{m_0,l_0} \mathbf{y}^{(q,r)}_{m_0,l_0}. \qquad (5.13)
\end{aligned}
$$

The above repeated series can be replaced by a double series, which allows to swap the order of the two indexes q and r. To see this, it is enough to see that the double series is absolutely convergent. Indeed, this can be deduced by looking at the different terms of $\mathbf{z}_{m_0,l_0}$ in (5.10). First, we have just shown that $\boldsymbol{\Delta}_{m_0,l_0}[n']$ can be replaced by a double series, which converges and remains bounded. Further, the transmitted symbols $\mathbf{d}_{m,l}$ and the energy of the pulse $p[n]$ are bounded by assumption.

The (Q,R)-th order approximation of $\mathbf{z}_{m_0,l_0}$ is given by the truncation of the Taylor expansion to its (Q,R) first terms

$$
\mathbf{z}^{(Q,R)}_{m_0,l_0} = \sum_{r=0}^{R}\sum_{q=0}^{Q} \frac{\jmath^q}{(2M)^q q!(\tilde{N}_s)^r r!} \mathbf{H}^{(q,r)}_{m_0,l_0} \mathbf{y}^{(q,r)}_{m_0,l_0}.
$$

and the approximation error is

$$\mathbf{z}_{m_0,l_0} - \mathbf{z}_{m_0,l_0}^{(Q,R)} = \sum_{(q,r)\in\Omega} \frac{\jmath^q}{(2M)^q q!(\tilde{N}_s)^r r!} \mathbf{H}_{m_0,l_0}^{(q,r)} \mathbf{y}_{m_0,l_0}^{(q,r)}$$

where Ω denotes the set (q,r) such that $q > Q$ or $r > R$. Using the triangular inequality and the fact that the channel power is bounded, we can write

$$\begin{aligned}\left\|\mathbf{z}_{m_0,l_0} - \mathbf{z}_{m_0,l_0}^{(Q,R)}\right\| &\leq \sum_{(r,q)\in\Omega} \frac{\left\|\mathbf{H}_{m_0,l_0}^{(q,r)}\right\|}{(2M)^q(\tilde{N}_s)^r} \left\|\frac{\mathbf{y}_{m_0,l_0}^{(q,r)}}{q!r!}\right\| \\ &\overset{(5.3)}{\leq} \sum_{(r,q)\in\Omega} \sum_{b=0}^{L_b} \sum_{\nu=-L_\nu}^{L_\nu} \left(\frac{b}{2M}\right)^q \left(\frac{2\pi\nu}{\tilde{N}_s}\right)^r \|\mathbf{\Psi}[b,\nu]\| \left\|\frac{\mathbf{y}_{m_0,l_0}^{(q,r)}}{q!r!}\right\|.\end{aligned}$$

Since the channel has finite energy, we can bound

$$\sum_{b=0}^{L_b} \sum_{\nu=-L_\nu}^{L_\nu} \|\mathbf{\Psi}[b,\nu]\| \leq C_{\mathbf{\Psi}},$$

and we obtain

$$\left\|\mathbf{z}_{m_0,l_0} - \mathbf{z}_{m_0,l_0}^{(Q,R)}\right\| \leq C_{\mathbf{\Psi}} \sum_{(r,q)\in\Omega} \left(\frac{L_b}{2M}\right)^q \left(\frac{2\pi L_\nu}{\tilde{N}_s}\right)^r \left\|\frac{\mathbf{y}_{m_0,l_0}^{(q,r)}}{q!r!}\right\|.$$

Under $(\mathbf{As6})$, we have $L_b = \lfloor\frac{\tau_{max}2M}{T}\rfloor$ and $L_\nu = \lfloor f_d\tilde{N}_sT\rfloor$. Using the fact that the symbols are bounded, the definition of $\mathbf{y}_{m_0,l_0}^{(q,r)}$ in (5.4) and under $(\mathbf{As7})$, we can write that, as $\frac{\tau_{max}}{T} \to 0$ and $f_dT \to 0$, we have

$$\left\|\mathbf{z}_{m_0,l_0} - \mathbf{z}_{m_0,l_0}^{(Q,R)}\right\| = O\left(\left(\frac{\tau_{max}}{T}\right)^Q\right) + O\left((f_dT)^R\right),$$

which completes the proof of Proposition 5.

5.5.2 Proof of Theorem 6

We will begin by showing that the equalizer and its derivatives are bounded. Under $(\mathbf{As8})$, we have that $\mathbf{B}(\omega, t)\mathbf{H}(\omega, t) = \mathbf{I}_{N_T}$, which is not dependent on time and frequency and hence

$$
\begin{aligned}
(\mathbf{B}_{m,l}\mathbf{H}_{m,l})^{(\tilde{q},\tilde{r})} &= \sum_{q=0}^{\tilde{q}} \sum_{r=0}^{\tilde{r}} \binom{\tilde{q}}{q} \binom{\tilde{r}}{r} \mathbf{B}_{m,l}^{(q,r)} \mathbf{H}_{m,l}^{(\tilde{q}-q,\tilde{r}-r)} \\
&= \mathbf{I}_{N_T} \delta[\tilde{q}]\delta[\tilde{r}]. \qquad (5.14)
\end{aligned}
$$

We can reason by induction to show that $\sup_{m,l} \|\mathbf{B}_{m,l}^{(q,r)}\| < +\infty$ for each q and r. First, for $q = r = 0$, we have

$$
\begin{aligned}
\sup_{m,l} \|\mathbf{B}_{m,l}\| &\leq \sup_{m,l} \| \left(\mathbf{H}_{m,l}^H \mathbf{H}_{m,l}\right)^{-1} \| \sup_{m,l} \|\mathbf{H}_{m,l}^H\| \\
&\leq \frac{\sup_{(\omega,t)} \lambda_{\max}^{1/2} \left(\mathbf{H}^H(\omega, t)\mathbf{H}(\omega, t)\right)}{\inf_{(\omega,t)} \lambda_{\min} \left(\mathbf{H}^H(\omega, t)\mathbf{H}(\omega, t)\right)},
\end{aligned}
$$

which is bounded under $(\mathbf{As6})$. Otherwise, using (5.14), we have,

$$
\begin{aligned}
\|\mathbf{B}_{m,l}^{(q,r)}\| &\leq \frac{\|\mathbf{B}_{m,l}^{(q,r)}\mathbf{H}_{m,l}\|}{\lambda_{\min}^{1/2} \left(\mathbf{H}^H(\omega, t)\mathbf{H}(\omega, t)\right)} \\
&\leq \sum_{\substack{(i,j)=(0,0),\\ (i,j)\neq(q,r)}}^{(q,r)} \binom{q}{i} \binom{r}{j} \|\mathbf{B}_{m,l}^{(i,j)}\| \frac{\|\mathbf{H}_{m,l}^{(q-i,r-j)}\|}{\lambda_{\min}^{1/2} \left(\mathbf{H}^H(\omega, t)\mathbf{H}(\omega, t)\right)}
\end{aligned}
$$

and the result follows from taking the supremum with respect to m, l and applying the induction hypothesis. This concludes the proof that $\sup_{m,l} \|\mathbf{B}_{m,l}^{(q,r)}\| < +\infty$. In the following, we drop the subscript m_0, l_0 for the sake of clarity. Let us define $\alpha = \frac{\tau_{max}}{T}$ and $\beta = f_d T$. Using the result of Proposition 5, we can write

$$\mathbf{z}(q,r) = \sum_{r_1=0}^{R-r} \sum_{q_1=0}^{Q-q} \frac{\jmath^{q_1} \mathbf{H}^{(q_1,r_1)}}{(2M)^{q_1} q_1! (\tilde{N}_s)^{r_1} r_1!} \mathbf{y}^{(q+q_1,r+r_1)} + \boldsymbol{\epsilon}(q,r)$$

where $\|\boldsymbol{\epsilon}(q,r)\| = O\left(\alpha^{Q-q}\right) + O\left(\beta^{R-r}\right)$. Using the definition of $\mathbf{x}^{(Q,R)}$ in (5.7), we can write

$$\mathbf{x}^{(Q,R)} = \sum_{r=0}^{R} \sum_{q=0}^{Q} \sum_{r_1=0}^{R-r} \sum_{q_1=0}^{Q-q} \frac{\jmath^{q+q_1} \mathbf{B}^{(q,r)} \mathbf{H}^{(q_1,r_1)} \mathbf{y}^{(q+q_1,r+r_1)}}{(2M)^{q+q_1} q_1! q! (\tilde{N}_s)^{r+r_1} r! r_1!} + \boldsymbol{\epsilon}^{\mathbb{C}},$$

where the error $\boldsymbol{\epsilon}^{\mathbb{C}}$ is given by

$$\begin{aligned} \boldsymbol{\epsilon}^{\mathbb{C}} &= \sum_{r=0}^{R} \sum_{q=0}^{Q} \frac{\jmath^{q}}{(2M)^{q} q! (\tilde{N}_s)^{r} r!} \mathbf{B}^{(q,r)} \boldsymbol{\epsilon}(q,r) \\ &= O\left(\alpha^{Q}\right) + O\left(\beta^{R}\right), \end{aligned}$$

where we used the fact that $\sup_{m,l} \|\mathbf{B}_{m,l}^{(q,r)}\| < +\infty$ and $\frac{1}{2M} \leq \frac{L_b}{2M} \leq \frac{\tau_{max}}{T}$ and $\frac{1}{\tilde{N}_s} \leq \frac{L_\nu}{\tilde{N}_s} \leq f_d T$. Let us take $\tilde{q} = q + q_1$ and $\tilde{r} = r + r_1$, $\mathbf{x}^{(Q,R)}$ can be rewritten as

$$\begin{aligned} \mathbf{x}^{(Q,R)} - \boldsymbol{\epsilon}^{\mathbb{C}} &= \sum_{r=0}^{R} \sum_{q=0}^{Q} \sum_{\tilde{r}=r}^{R} \sum_{\tilde{q}=q}^{Q} \frac{\jmath^{\tilde{q}} \mathbf{B}^{(q,r)} \mathbf{H}^{(\tilde{q}-q,\tilde{r}-r)} \mathbf{y}^{(\tilde{q},\tilde{r})}}{r! q! (\tilde{r}-r)! (\tilde{q}-q)! (2M)^{\tilde{q}} (\tilde{N}_s)^{\tilde{r}}} \\ &= \sum_{\tilde{r}=0}^{R} \sum_{\tilde{q}=0}^{Q} \frac{\jmath^{\tilde{q}}}{\tilde{q}! (2M)^{\tilde{q}} \tilde{r}! (\tilde{N}_s)^{\tilde{r}}} \sum_{q=0}^{\tilde{q}} \sum_{r=0}^{\tilde{r}} \frac{\mathbf{B}^{(q,r)} \mathbf{H}^{(\tilde{q}-q,\tilde{r}-r)} \mathbf{y}^{(\tilde{q},\tilde{r})}}{r! q! (\tilde{r}-r)! (\tilde{q}-q)!}. \end{aligned}$$

Using the identity in (5.14), we finally find that $\mathbf{x}^{(Q,R)} = \mathbf{y} + \boldsymbol{\epsilon}^{\mathbb{C}}$, which completes the proof.

5.5.3 Proof of Theorem 7

Using Theorem 6, we have[3]

$$\mathbf{x}^{(Q+1,R+1)} = \sum_{r=0}^{R+1}\sum_{q=0}^{Q+1} \frac{\jmath^q}{(2M)^q q!(\tilde{N}_s)^r r!}\mathbf{B}^{(q,r)}\mathbf{z}(q,r)$$

and $\left\|\mathbf{x}^{(Q+1,R+1)} - \mathbf{y}\right\| = O\left(\alpha^{Q+1}\right) + O\left(\beta^{R+1}\right)$. Note that,

$$\begin{aligned}\mathbf{x}^{(Q+1,R+1)} - \mathbf{y} &= \mathbf{x}^{(Q,R)} - \mathbf{y} + \frac{\jmath^{Q+1}\mathbf{B}^{(Q+1,0)}\mathbf{z}(Q+1,0)}{(2M)^{Q+1}(Q+1)!} \\ &+ \frac{\mathbf{B}^{(0,R+1)}\mathbf{z}(0,R+1)}{(\tilde{N}_s)^{R+1}(R+1)!} + \sum_{r=1}^{R+1}\frac{\jmath^{Q+1}\mathbf{B}^{(Q+1,r)}\mathbf{z}(Q+1,r)}{(2M)^{Q+1}(Q+1)!(\tilde{N}_s)^r r!} \\ &+ \sum_{q=1}^{Q}\frac{\jmath^q\mathbf{B}^{(q,R+1)}\mathbf{z}(q,R+1)}{(2M)^q q!(\tilde{N}_s)^{R+1}(R+1)!}.\end{aligned}$$

Combining the two previous equations, we can write the following approximation of the residual distortion

$$\begin{aligned}\boldsymbol{\epsilon}^{\mathbb{C}} &= \mathbf{x}^{(Q,R)} - \mathbf{y} \\ &= -\frac{\jmath^{Q+1}\mathbf{B}^{(Q+1,0)}\mathbf{z}(Q+1,0)}{(2M)^{Q+1}(Q+1)!} - \frac{\mathbf{B}^{(0,R+1)}\mathbf{z}(0,R+1)}{(\tilde{N}_s)^{R+1}(R+1)!} + \boldsymbol{\epsilon}_1,\end{aligned}$$

where $\boldsymbol{\epsilon}_1$ is the error on the approximation of the residual distortion itself, which can be bounded as

$$\begin{aligned}\|\boldsymbol{\epsilon}_1\| &\leq \left\|\sum_{r=1}^{R+1}\frac{\jmath^{Q+1}\mathbf{B}^{(Q+1,r)}\mathbf{z}(Q+1,r)}{(2M)^{Q+1}(Q+1)!(\tilde{N}_s)^r r!}\right\| + \left\|\sum_{q=1}^{Q}\frac{\jmath^q\mathbf{B}^{(q,R+1)}\mathbf{z}(q,R+1)}{(2M)^q q!(\tilde{N}_s)^{R+1}(R+1)!}\right\| \\ &+ O\left(\alpha^{Q+1}\right) + O\left(\beta^{R+1}\right) \\ &= O\left(\alpha^Q\beta\right) + O\left(\alpha\beta^R\right) + O\left(\alpha^{Q+1}\right) + O\left(\beta^{R+1}\right),\end{aligned}$$

[3]Here again, we dropped the subscript m_0, l_0 for the sake of clarity.

where we used the same bounding methodology as in Appendices 5.5.1 and 5.5.2. Then, we can write, using the result of Proposition 5,

$$\begin{aligned} \boldsymbol{\epsilon}^{\mathbb{C}} &= -\frac{\jmath^{Q+1}\mathbf{B}^{(Q+1,0)}\mathbf{H}\mathbf{y}^{(Q+1,0)}}{(2M)^{Q+1}(Q+1)!} - \frac{\mathbf{B}^{(0,R+1)}\mathbf{H}\mathbf{y}^{(0,R+1)}}{(\tilde{N}_s)^{R+1}(R+1)!} + \boldsymbol{\epsilon}_2 \\ \|\boldsymbol{\epsilon}_2\| &= O\left(\alpha^Q\beta\right) + O\left(\alpha\beta^R\right) + O\left(\alpha^{Q+1}\right) + O\left(\beta^{R+1}\right). \end{aligned} \tag{5.15}$$

We now need to compute $\mathbf{P}^{d,(Q,R)}_{m_0,l_0|H} = \mathbb{E}\left(\Re\left(\boldsymbol{\epsilon}^{\mathbb{C}}\right)\left(\Re\left(\boldsymbol{\epsilon}^{\mathbb{C}}\right)\right)^T\right)$. To do this, we need to define some pulse-related quantities. Given two generic pulses, p, q of length $2M\kappa$, let $\mathbf{P}$ and $\mathbf{Q}$ denote two $2M \times \kappa$ matrices obtained by arranging the samples of the respective pulses in columns from left to right. We will define

$$\begin{aligned} \mathcal{R}(p,q) &= \mathbf{P} \circledast \mathbf{J}_{2M}\mathbf{Q} \\ \mathcal{S}(p,q) &= \left(\mathbf{J}_2 \otimes \mathbf{I}_M\right)\mathbf{P} \circledast \mathbf{J}_{2M}\mathbf{Q}, \end{aligned}$$

where $\circledast$ denotes row-wise convolution, $\otimes$ denotes Kronecker product, $\mathbf{I}_M$ (resp. $\mathbf{J}_M$) are the identity (resp. exchange) matrices of order M. Given four generic pulses p, q, r, s, we recall the definition of $\eta^{\pm}\left(p,q,r,s\right)$ and $\eta^{\mp}\left(p,q,r,s\right)$ from Section 3.5.1

$$\begin{aligned} \eta^{\pm}\left(p,q,r,s\right) &= \frac{M}{2}\mathrm{tr}\left[\mathbf{U}^{+}\mathcal{R}\left(p,q\right)\mathcal{R}^T\left(r,s\right) + \mathbf{U}^{-}\mathcal{S}\left(p,q\right)\mathcal{S}^T\left(r,s\right)\right] \\ \eta^{\mp}\left(p,q,r,s\right) &= \frac{M}{2}\mathrm{tr}\left[\mathbf{U}^{-}\mathcal{R}\left(p,q\right)\mathcal{R}^T\left(r,s\right) + \mathbf{U}^{+}\mathcal{S}\left(p,q\right)\mathcal{S}^T\left(r,s\right)\right], \end{aligned}$$

where $\mathbf{U}^{\pm} = \mathbf{I}_2 \otimes (\mathbf{I}_M \pm \mathbf{J}_M)$. In order to simplify the notations and since the pulse at the transmit side always is p and the pulse at the receiver is a derivative of g, given four integers q_1, r_1, q_2, r_2, we will define $\eta^{(+,-)}_{(q_1,r_1),(q_2,r_2)} = \eta^{\pm}\left(p, g^{(q_1,r_1)}, p, g^{(q_2,r_2)}\right)$.

We can now obtain an expression of the residual distortion by using the fact that, under ((**As7**)) [53, Appendix B] and neglecting tail effects,

$$\begin{aligned}
\mathbb{E}\left(\Re(\mathbf{y}^{(q_1,r_1)})\Re^T(\mathbf{y}^{(q_2,r_2)})\right) &= E_s\eta^{(+,-)}_{(q_1,r_1),(q_2,r_2)}\mathbf{I}_{N_T},\\
\mathbb{E}\left(\Im(\mathbf{y}^{(q_1,r_1)})\Im^T(\mathbf{y}^{(q_2,r_2)})\right) &= E_s\eta^{(-,+)}_{(q_1,r_1),(q_2,r_2)}\mathbf{I}_{N_T},\\
\mathbb{E}\left(\Re(\mathbf{y}^{(q_1,r_1)})\Im^T(\mathbf{y}^{(q_2,r_2)})\right) &= \mathbf{0}.
\end{aligned}$$

The resulting expression can be simplified using Lemma 3 presented in Section 3.5.2 showing that, in the particular case considered here, we have $\eta^{(+,-)}_{(q_1,r_1),(q_2,r_2)} = \eta^{(-,+)}_{(q_1,r_1),(q_2,r_2)}$ (the transmit pulse does not change). Hence, we will omit the superscripts $^{(+,-)}$ and $^{(-,+)}$. The result of Theorem 7 is then found by computing $\mathbf{P}^{d,(Q,R)}_{m_0,l_0|H} = \mathbb{E}\left(\Re\left(\boldsymbol{\epsilon}^{\mathbb{C}}\right)\left(\Re\left(\boldsymbol{\epsilon}^{\mathbb{C}}\right)\right)^T\right)$ with the expression of $\boldsymbol{\epsilon}^{\mathbb{C}}$ given in (5.15) (neglecting the error term $\boldsymbol{\epsilon}_2$) and using the above definition of $\eta_{(q_1,r_1),(q_2,r_2)}$.

5.5.4 Proof of Theorem 8

Let us develop the expression of $\mathbf{P}^{n,(Q,R)}_{m_0,l_0|H}$,

$$\begin{aligned}
\mathbf{P}^{n,(Q,R)}_{m_0,l_0|H} &= \mathbb{E}\left(\Re\left(\mathbf{w}^{(Q,R)}_{m_0,l_0}\right)\left(\Re\left(\mathbf{w}^{(Q,R)}_{m_0,l_0}\right)\right)^T\right)\\
&= \sum_{r'=0}^{R}\sum_{r=0}^{R}\sum_{q=0}^{Q}\sum_{q'=0}^{Q}\frac{1}{(2M)^{q+q'}q!q'!(\tilde{N}_s)^{r+r'}r!r'!}\\
&\quad \mathbb{E}\left(\Re\left(\jmath^q\mathbf{B}^{(q,r)}_{m_0,l_0}\sum_{n=0}^{2M\tilde{N}_s-1}g^{(q,r)*}_{m_0,l_0}[n]\mathbf{w}[n]\right)\right.\\
&\quad \left.\Re\left(\jmath^{q'}\sum_{n'=0}^{2M\kappa-1}g^{(q',r')*}_{m_0,l_0}[n']\mathbf{w}[n']^T\left(\mathbf{B}^{(q',r')}_{m_0,l_0}\right)^T\right)\right)
\end{aligned}$$

Using the fact that for any complex matrix $\mathbf{A}$, $\Re(\mathbf{A}) = \frac{1}{2}(\mathbf{A}+\mathbf{A}^*)$ and that $\mathbf{w}[n]$ is white and circularly symmetric, $\mathbb{E}(\mathbf{w}[n]\mathbf{w}^T[n']) = \mathbf{0}$ and $\mathbb{E}(\mathbf{w}[n]\mathbf{w}^H[n']) = N_0\mathbf{I}_{N_R}\delta[n-n']$, the expression of $\mathbf{P}^{n,(Q,R)}_{m_0,l_0|H}$ simplifies to

$$\mathbf{P}^{n,(Q,R)}_{m_0,l_0|H} = \sum_{r'=0}^{R}\sum_{r=0}^{R}\sum_{q=0}^{Q}\sum_{q'=0}^{Q} \frac{1}{(2M)^{q+q'}q!q'!(\tilde{N}_s)^{r+r'}r!r'!}$$
$$\frac{N_0}{4}\mathrm{tr}\left[\jmath^q(-\jmath)^{q'}\mathbf{B}^{(q,r)}_{m_0,l_0}\left(\mathbf{B}^{(q',r')}_{m_0,l_0}\right)^H \sum_{n=0}^{2M\tilde{N}_s-1} g^{(q,r)*}_{m_0,l_0}[n]g^{(q',r')}_{m_0,l_0}[n]\right.$$
$$\left.+(-\jmath)^q\jmath^{q'}\mathbf{B}^{(q,r)*}_{m_0,l_0}\left(\mathbf{B}^{(q',r')}_{m_0,l_0}\right)^T \sum_{n=0}^{2M\tilde{N}_s-1} g^{(q,r)}_{m_0,l_0}[n]g^{(q',r')*}_{m_0,l_0}[n]\right].$$

Defining

$$\alpha^{(q,r,q',r')} = \sum_{n=0}^{2M\tilde{N}_s-1} g^{(q,r)*}_{m_0,l_0}[n]g^{(q',r')}_{m_0,l_0}[n] = \sum_{n=0}^{2M\tilde{N}_s-1} g^{(q,r)}[n]g^{(q',r')}[n],$$

we find the expression given in Theorem 8. Using the fact that $g[n]$ is even or odd and that $g^{(q,r)}[n]$ shares the same type of symmetry as $g[n]$ if $q+r=0 \mod 2$ and the opposite otherwise, one can easily check that $\alpha^{(q,r,q',r')} \neq 0$ only if $q+r = q'+r' \mod 2$. This completes the proof.

CHAPTER 6

OPTIMIZED SINGLE-TAP EQUALIZERS FOR PTP MIMO SYSTEMS UNDER DOUBLY SELECTIVE CHANNELS

As explained in Chapter 5, the techniques to deal with channel frequency selectivity have been extensively studied in numerous works. Conversely, equalization for time selective channels has only been studied in very few works (see Section 2.1.5.3 for a review of the related literature). In this chapter, we propose a very simple design based on single-tap per-subcarrier equalizers. The equalizing matrices are designed to minimize the MSE of the symbol estimate at each subcarrier and each multicarrier symbol of interest, taking into account a first order approximation of the distortion caused by channel time and frequency selectivity. It is shown that, as soon as the equalizer has more antennas than the number of transmitted streams, it can tune those extra degrees of freedom to compensate for the channel distortion. This chapter can be seen as an extension of Chapter 3 to doubly selective channels.

6.1 MSE expression

We consider a PTP MIMO FBMC-OQAM transmission chain as described in Section 2.1 and shown in Fig. 2.5. We define the MSE at the subcarrier m and multicarrier symbol l as

$$\begin{aligned}\mathrm{MSE}(m,l) &= \mathbb{E}\left(\left\|\hat{\mathbf{d}}_{m,l}-\mathbf{d}_{m,l}\right\|^2\right) \\ &= P_d(m,l)+P_n(m,l).\end{aligned} \tag{6.1}$$

Since the noise and symbol samples are uncorrelated, their effect can be studied separately and we divided the MSE expression into two contributions, namely, the distortion power $P_d(m,l)$ and the noise power $P_n(m,l)$. The noise term is simply due to the additive noise and is given by (for the receive pulse energy normalized to one)

$$P_n(m,l)=\mathrm{tr}\left[\mathbf{P}^{n,(0,0)}_{m,l|H}\right]=\frac{N_0}{2}\mathrm{tr}\left[\mathbf{B}_{m,l}\mathbf{B}^H_{m,l}\right],$$

where $\mathbf{P}^{n,(Q,R)}_{m,l|H}$ was defined in (5.9) and computed in Theorem 8. The distortion term $P_d(m,l)$, including the ISI and ICI power, comes from channel selectivity or in other words the fact that the channel is not flat and constant at the subcarrier and multicarrier symbol of interest. Under $(\mathbf{As6})$-$(\mathbf{As8})$ and up to an error term, it can be approximated using a particularization of Theorem 7 to the case $Q=R=0$,

$$\begin{aligned}P_d(m,l) &= \mathrm{tr}\left[\mathbf{P}^{d,(0,0)}_{m,l|H}\right] \\ &= E_s\frac{\eta_{(0,1),(0,1)}}{(N_s')^2}\mathrm{tr}\left[\left(\mathbf{B}_{m,l}\mathbf{H}^{(0,1)}_{m,l}\right)\left(\mathbf{B}_{m,l}\mathbf{H}^{(0,1)}_{m,l}\right)^H\right] \\ &+ E_s\frac{\eta_{(1,0),(1,0)}}{(2M)^2}\mathrm{tr}\left[\left(\mathbf{B}_{m,l}\mathbf{H}^{(1,0)}_{m,l}\right)\left(\mathbf{B}_{m,l}\mathbf{H}^{(1,0)}_{m,l}\right)^H\right] \\ &+ E_s\frac{2\eta_{(0,1),(1,0)}}{2MN_s'}\Im\mathrm{tr}\left[\left(\mathbf{B}_{m,l}\mathbf{H}^{(0,1)}_{m,l}\right)\left(\mathbf{B}_{m,l}\mathbf{H}^{(1,0)}_{m,l}\right)^H\right],\end{aligned}$$

where $\mathbf{P}^{d,(Q,R)}_{m,l|H}$ was defined in (5.8). Hence, $\mathrm{MSE}(m,l)$ defined in (6.1) can be approximated as

$$\begin{aligned}\mathrm{MSE}(m,l) \approx\ & E_s \frac{\eta_{(0,1),(0,1)}}{(N_s')^2} \mathrm{tr}\left[\left(\mathbf{B}_{m,l}\mathbf{H}^{(0,1)}_{m,l}\right)\left(\mathbf{B}_{m,l}\mathbf{H}^{(0,1)}_{m,l}\right)^H\right] \\ &+ E_s \frac{\eta_{(1,0),(1,0)}}{(2M)^2} \mathrm{tr}\left[\left(\mathbf{B}_{m,l}\mathbf{H}^{(1,0)}_{m,l}\right)\left(\mathbf{B}_{m,l}\mathbf{H}^{(1,0)}_{m,l}\right)^H\right] \\ &+ E_s \frac{2\eta_{(0,1),(1,0)}}{2MN_s'} \Im\mathrm{tr}\left[\left(\mathbf{B}_{m,l}\mathbf{H}^{(0,1)}_{m,l}\right)\left(\mathbf{B}_{m,l}\mathbf{H}^{(1,0)}_{m,l}\right)^H\right] \\ &+ \frac{N_0}{2}\mathrm{tr}\left[\mathbf{B}_{m,l}\mathbf{B}^H_{m,l}\right]. \end{aligned} \tag{6.2}$$

6.2 Single-tap equalizer design

The goal now is to optimize the MSE formula in (6.2) to obtain the expression of the optimal single-tap equalizer in the asymptotic regime. Due to the channel inversion constraint $(\mathbf{As8})$, we have

$$\mathbf{B}_{m,l}\mathbf{H}_{m,l} = \mathbf{I}_{N_T},$$

and the multi-stream interference is mitigated. The optimal equalizer should then compensate for time and frequency selectivity of the channel while keeping the noise level low enough. The general expression of any equalizer that satisfies $(\mathbf{As8})$ is given by

$$\mathbf{B}_{m,l} = \mathbf{H}^{\dagger}_{m,l} + \tilde{\mathbf{B}}_{m,l}\mathbf{P}^{\dagger}_{m,l}, \tag{6.3}$$

where $\mathbf{H}^{\dagger}_{m,l} = \left(\mathbf{H}^H_{m,l}\mathbf{H}_{m,l}\right)^{-1}\mathbf{H}^H_{m,l}$, $\mathbf{P}^{\dagger}_{m,l} = \mathbf{I}_{N_R} - \mathbf{H}_{m,l}\mathbf{H}^{\dagger}_{m,l}$ and $\tilde{\mathbf{B}}_{m,l}$ is a matrix left to be optimized. The above expression of $\mathbf{B}_{m,l}$ shows that the optimal equalizer can be written as the pseudo inverse of the channel plus a matrix lying on the left null space of $\mathbf{H}_{m,l}$. In the case $N_R = N_T$, it is obvious to see that $\mathbf{B}_{m,l}$ is fixed to the inverse of the channel and there are no extra degrees of freedom. On the contrary, as N_R increases relatively to N_T, there is more and more degrees of freedom left to optimize and one can expect a better compensation of the noise and distortion. Note that the assumption that $N_R > N_T$ makes for instance particular sense in the uplink of cellular networks where the number of base station antennas could be drastically increased in a massive MIMO scenario [109].

6.2.1 Equalizer optimization

By using the expression of the MSE in (6.2) and the expression of $\mathbf{B}_{m,l}$ in (6.3), the optimization problem can be formulated as follows,

$$\begin{aligned}&\min_{\tilde{\mathbf{B}}_{m,l}} \mathrm{MSE}(m,l)\\ &\quad= \mathrm{tr}\left[\left(\mathbf{H}^{\dagger}_{m,l} + \tilde{\mathbf{B}}_{m,l}\mathbf{P}^{\dagger}_{m,l}\right)\left(\mathbf{\Theta}_{m,l} + \frac{N_0}{2}\mathbf{I}_{N_R}\right)\left(\mathbf{H}^{\dagger}_{m,l} + \tilde{\mathbf{B}}_{m,l}\mathbf{P}^{\dagger}_{m,l}\right)^H\right],\end{aligned}$$

where matrix $\mathbf{\Theta}_{m,l}$ is given by

$$\begin{aligned}\mathbf{\Theta}_{m,l} = {}& E_s\frac{\eta_{(0,1),(0,1)}}{(N_s')^2}\mathbf{H}^{(0,1)}_{m,l}\mathbf{H}^{(0,1)}_{m,l}{}^H + E_s\frac{\eta_{(1,0),(1,0)}}{(2M)^2}\mathbf{H}^{(1,0)}_{m,l}\mathbf{H}^{(1,0)}_{m,l}{}^H\\ &+ \jmath E_s\frac{\eta_{(0,1),(1,0)}}{2MN_s'}\left(\mathbf{H}^{(1,0)}_{m,l}\mathbf{H}^{(0,1)}_{m,l}{}^H - \mathbf{H}^{(0,1)}_{m,l}\mathbf{H}^{(1,0)}_{m,l}{}^H\right).\end{aligned}$$

This problem is a quadratic form in the variable $\tilde{\mathbf{B}}_{m,l}$ which can be easily solved by differentiation with respect to $\tilde{\mathbf{B}}^*_{m,l}$ and setting the derivative to zero. The expression of the optimized equalizer is then given by

$$\mathbf{B}_{m,l} = \mathbf{H}^{\dagger}_{m,l}\left(\mathbf{I}_{N_R} - \mathbf{\Theta}_{m,l}\mathbf{P}^{\dagger}_{m,l}\left(\mathbf{\Theta}_{m,l}\mathbf{P}^{\dagger}_{m,l} + \frac{N_0}{2}\mathbf{I}_{N_R}\right)^{-1}\right).$$

6.2.2 Asymptotic behavior at low and high SNR

It is easy to see that at low SNR, *i.e.*, when $N_0 \longrightarrow +\infty$, the optimized equalizer converges to the classical pseudo inverse of the channel $\mathbf{B}_{m,l} = \mathbf{H}^{\dagger}_{m,l}$. Indeed, in that regime, the noise power is dominant relatively to the distortion power and the best to do is to invert the channel combining the signals coming from each receive antenna to prevent noise amplification.

As explained above, the distortion will be better compensated as N_R increases. One could be interested to know the number of receive antennas N_R required to completely compensate the distortion caused by the channel selectivity in the high SNR regime, *i.e.*, when $N_0 \to 0$. In Section 3.2.1, it was shown that, when the equalizer has twice as many antennas as the number of transmit antennas, it can completely remove the first order approximation of the distortion at high SNR. However, in that section, a quasi-static channel was assumed such that only the effect of frequency selectivity was regarded. Here, the channel time selectivity should also be mitigated.

When $N_0 \to 0$, the MSE is given by the distortion power only, $\mathrm{MSE} = \mathbf{B}_{m,l}\boldsymbol{\Theta}_{m,l}\mathbf{B}_{m,l}$. Hence, in order to completely remove the first order distortion power, matrix $\mathbf{B}_{m,l}$ should on the one hand satisfy $(\mathbf{As8})$ and on the other hand lie in the null space of $\boldsymbol{\Theta}_{m,l}$. Let us define the i-th decoding vector as $\mathbf{b}_i^H = \mathbf{e}_i^H\mathbf{B}_{m,l}$ where $\mathbf{e}_i$ is the i-th column of the identity matrix $\mathbf{I}_{N_T}$. Vector $\mathbf{b}_i^H \in \mathbb{C}^{1\times N_R}$ should generally satisfy

$$\mathbf{b}_i^H\mathbf{H}_{m,l} = \mathbf{e}_i^H, \mathbf{b}_i^H\mathbf{H}_{m,l}^{(0,1)} = \mathbf{0}, \mathbf{b}_i^H\mathbf{H}_{m,l}^{(1,0)} = \mathbf{0}, \quad i = 1, \dots, N_T.$$

For this problem to be feasible, N_R has to be larger than the number of linearly independent constraints. We will assume that all matrices are full rank. Depending on the channel selectivity, we differentiate three cases:

- No channel selectivity ($\mathbf{H}_{m,l}^{(0,1)} = \mathbf{H}_{m,l}^{(1,0)} = \mathbf{0}$): in this trivial case, the MSE is zero by assumption ($N_R \geq N_T$).

- Channel with frequency or time selectivity only ($\mathbf{H}_{m,l}^{(0,1)} = \mathbf{0}$ or $\mathbf{H}_{m,l}^{(1,0)} = \mathbf{0}$): in that case, at least $2N_T$ receive antennas are required, as was the case in Section 3.2.1.

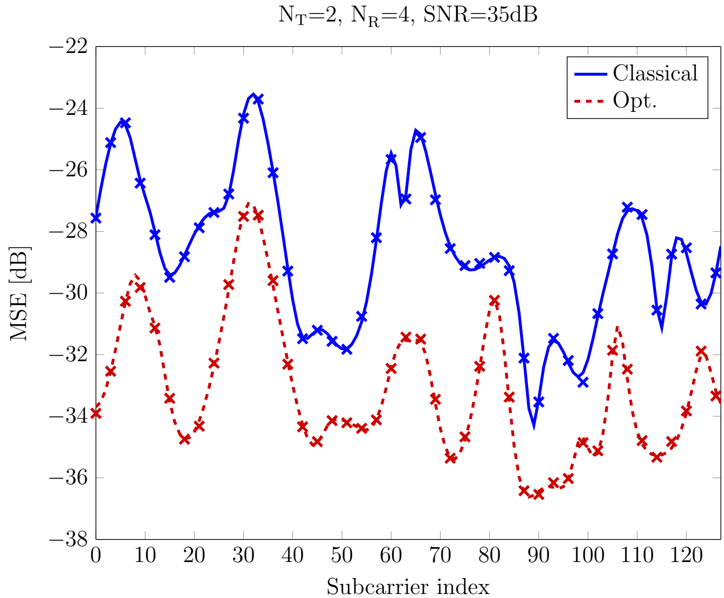

Figure 6.1 MSE at multicarrier symbol $l = 35$ as a function of the subcarrier. Crosses correspond to simulated SNDR and solid/dashed lines to the theoretical proposed approximation.

- Channel with time and frequency selectivity: in that case, at least $3N_T$ receive antennas are required.

6.3 Simulation results

This section aims at demonstrating the performance of the proposed equalizer design with respect to classical designs. By "classical" equalizer, we refer to single-tap per-subcarrier decoding matrices that assume a constant and flat channel at the subcarrier level, *i.e.*, the pseudo inverse of the channel, $\mathbf{B}_{m,l} = \mathbf{H}^{\dagger}_{m,l}$. We consider an FBMC-OQAM system with $2M = 128$ subcarriers and a frame transmission composed of $2N_s = 100$ real multicarrier symbols. The subcarrier spacing is fixed to $1/T = 15$ kHz as in LTE systems. The transmit and receive pulses are the Phydyas prototype pulse with $\kappa = 4$ [6].

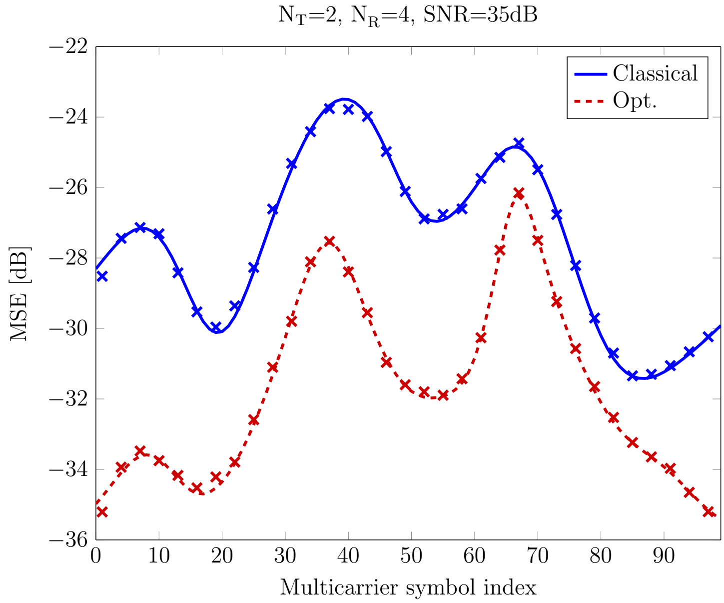

Figure 6.2 MSE at subcarrier $m = 35$ as a function of the multicarrier symbol. Crosses correspond to simulated SNDR and solid/dashed lines to the theoretical proposed approximation.

In the simulations, one channel realization is drawn and the performances are averaged over multiple frame transmission where data and noise samples are regenerated. The SNR of the system is 35dB. The delay-Doppler discrete channel coefficients $\boldsymbol{\Psi}[b,\nu]$ are assumed zero-mean and independent with variance

$$\mathbb{E}\left(\operatorname{vec}\left(\boldsymbol{\Psi}[b,\nu]\right)\operatorname{vec}^H\left(\boldsymbol{\Psi}[b,\nu]\right)\right) = \mathbf{I}_{N_R N_T} p_b^2[b] p_\nu^2[\nu]$$
$$p_b^2[b] = \alpha_b 10^{-2\frac{bT}{\tau_{max}2M}}; \quad p_\nu^2[\nu] = \frac{\alpha_\nu}{\sqrt{1-\left(\frac{\nu}{f_d N_s' T}\right)^2}},$$

which models an exponentially decaying power delay profile and a classical Jake's Doppler spectrum. The constants α_b and α_ν are chosen to normalize $\sum_b p_b^2[b]$ and $\sum_\nu p_\nu^2[\nu]$ to one. In the simulations, we fixed $\tau_{max} = 5\mu s$ and $f_d = 400$Hz.

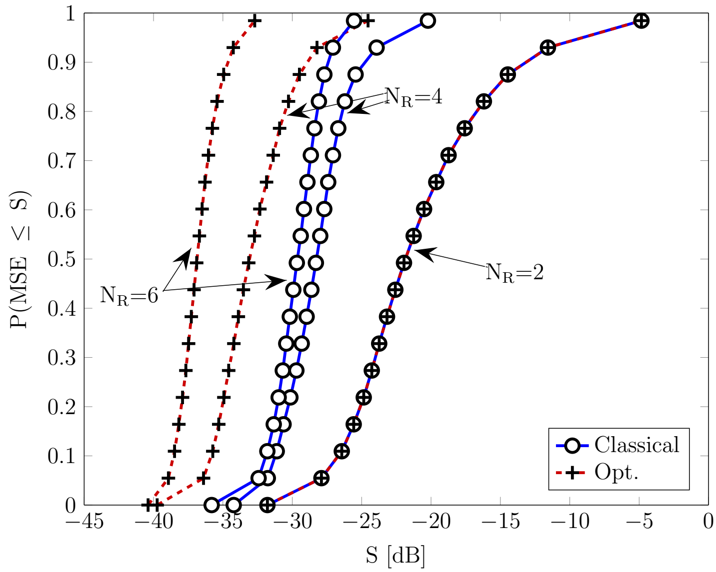

Figure 6.3 CDF of the MSE for different number of antennas at the receiver using a classical equalizer or the optimized one.

Fig. 6.1 and Fig. 6.2 show the MSE in an $N_R = 4, N_T = 2$ scenario at one subcarrier and one multicarrier symbol respectively. As can be seen, the optimized equalizer has a large gain of performance over the classical one. One can further check that the crosses that represent the simulated MSE perfectly match the theoretical one in dashed/solid lines, which validates the accuracy of the approximation in (6.2).

Fig. 6.3 plots the CDF of the MSE of the classical and optimized equalizers. A channel realization for $N_T = 2$ and $N_R = 6$ antennas is drawn and the performance of the equalizer using only two, four or all its six antennas is shown. One can check that in the $N_R = N_T = 2$, the performance of the classical and optimized equalizers is the same, which is logical since they are the same (no extra degrees of freedom at the receiver). As the number of receive antennas increases, the distortion cannot be compensated for efficiently with a classical equalizer while the optimized equalizers can use their extra antennas to mitigate the distortion.

6.4 Conclusion

We investigated the design of equalizers for MIMO doubly selective channels. The proposed design is based on a single-tap per-subcarrier decoding matrix and has a very low complexity. It is shown that, as soon as the receiver has more antennas than the number of streams, these extra degrees of freedom can be used to compensate for the distortion induced by the channel selectivity.

Part II

Linear impairments compensation in optical fiber systems

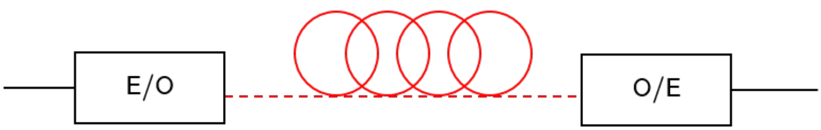

INTRODUCTION

This part of the thesis investigates the compensation of linear impairments in FBMC-OQAM optical fiber systems. More specifically, two major impairments are considered, *i.e.*, PN and CD. PN and CD are assumed to follow the model detailed in Section 2.2.2. We here detail the impairments studied in each chapter and the related publications.

Chapter 7 proposes a ML and a MAP PN estimators for optical fiber FBMC-OQAM systems.

- F. Rottenberg, T. H. Nguyen, S. P. Gorza, F. Horlin, and J. Louveaux, "ML and MAP phase noise estimators for optical fiber FBMC-OQAM systems," in *2017 IEEE International Conference on Communications (ICC)*, pp. 1–6, May 2017

Chapter 8 considers the application of advanced CD compensation algorithms to optical fiber FBMC-OQAM systems.

- F. Rottenberg, T.-H. Nguyen, S.-P. Gorza, F. Horlin, and J. Louveaux, "Advanced Chromatic Dispersion Compensation in Optical Fiber FBMC-OQAM Systems," *IEEE Photonics Journal*, vol. 9, pp. 1–10, Dec 2017

In **Chapter 9**, the joint compensation of CD and PN in optical fiber FBMC-OQAM systems is studied.

- T.-H. Nguyen, F. Rottenberg, S. P. Gorza, J. Louveaux, and F. Horlin, "Efficient Chromatic Dispersion Compensation and Carrier Phase Tracking for Optical Fiber FBMC/OQAM Systems," *IEEE/OSA Journal of Lightwave Technology*, vol. 35, pp. 2909–2916, July 2017

Chapter 7

ML and MAP phase noise estimators

Thanks to the recent advents in electronic circuits, digital signal processing is becoming more prevalent in modern optical coherent systems. The laser PN is one of the crucial impairments in such systems. The PN induces a rotation of the signal after the demodulation process at the receiver. Multicarrier systems are particularly sensitive to PN, especially if the number of subcarriers is large. Indeed, increasing the number of subcarriers (for a fixed bandwidth) induces a larger multicarrier symbol period and hence, the PN will have more varied during one multicarrier symbol duration. Different CPR algorithms have already been proposed in the literature. Because of the particular structure of the intrinsic interference inherent to OQAM modulations, the extension to OQAM systems is not straightforward. The work of [85] proposed a modified-blind phase search (M-BPS) algorithm which takes advantage of the OQAM modulation to track the phase variations of the laser. The M-BPS algorithm tries to find the optimal phase estimate by performing a certain number of phase trials. The final phase estimate is given at each multicarrier symbol by the phase trial that minimizes a certain cost function. The approach has a significant complexity of implementation, even though simplified versions have been proposed in [86, 136, 137] with negligible performance loss. Moreover, in practice, only a finite number of phase trials can be tested, which induces a discretization error.

In this work, we propose two new estimators for the laser PN in optical FBMC-OQAM systems, namely, a ML estimator and a MAP estimator. The novelty of the approach is plural. Since the phase is assumed to change slowly over time, the measurement model is formulated as a function of the phase error with respect to the previous phase estimate. This allows to easily exploit the *a priori* known statistics of the PN. By linearization of the system model, closed-form expressions are found that avoid the need of multiple phase tests. This decreases the complexity of the algorithm and at the same time suppresses the discretization error due to the limited number of phase tests of the M-BPS algorithm. Furthermore, a part of the intrinsic interference is estimated based on previous and current decoded symbols. The ML and MAP estimates are obtained by combining the outputs of all subcarriers, which makes the system more robust to additive noise effect. Moreover, the ML and MAP estimators do not suffer from phase ambiguity problems as opposed to the M-BPS algorithm. The performance of the proposed estimators is demonstrated by simulations. It is shown that the proposed algorithms outperform the state of the art M-BPS algorithm in the low SNR region and when a small number of subcarriers used.

7.1 System model

We consider a conventional FBMC-OQAM system, as shown in Fig. 2.5. To focus on the PN impact, we consider only one polarization mode and we will assume that the CD is perfectly compensated at the receiver. The model of the PN that we are using was detailed in Section 2.2.2, we recall it here. The received signal, only impacted by PN and additive noise is given by

$$r[n] = s[n]e^{\jmath\phi[n]} + w[n].$$

The PN is modeled as a Wiener process, *i.e.*, $\phi[n+1] = \phi[n] + \nu[n]$ where $\nu[n]$ is an independent real Gaussian random variable with zero mean and variance $\sigma_\nu^2 = 2\pi\Delta\nu\frac{T}{2M}$ [92]. The parameter $\Delta\nu$ refers to the combined laser linewidth. The noise samples $w[n]$ are additive circularly-symmetric white Gaussian noise samples with zero mean and variance N_0. At the receiver, the signal after demodulation, at subcarrier m_0 and multicarrier symbol l_0, denoted by z_{m_0,l_0}, may be written as

$$\begin{aligned} z_{m_0,l_0} &= \sum_{n=0}^{2M\tilde{N}_s-1} r[n] g^*_{m_0,l_0}[n] \\ &= \sum_{l,m} d_{m,l} \sum_{n=0}^{2M\tilde{N}_s-1} p_{m,l}[n] g^*_{m_0,l_0}[n] e^{\jmath\phi[n]} + w_{m_0,l_0}. \end{aligned}$$

Furthermore, we assume that the PN is slowly varying with respect to the symbol duration. Hence, the PN can be viewed as constant during one multicarrier symbol transmission,

$$z_{m_0,l_0} \approx d_{m_0,l_0} e^{\jmath\phi_{l_0}} + \jmath u_{m_0,l_0} e^{\jmath\phi_{l_0}} + w_{m_0,l_0}$$

where $\jmath u_{m_0,l_0} = \sum_{(m,l)\neq(m_0,l_0)} d_{m,l} t_{m,m_0,l,l_0}$ with

$$t_{m,m_0,l,l_0} = \sum_{n=0}^{2M\tilde{N}_s-1} p_{m,l}[n] g^*_{m_0,l_0}[n].$$

The symbol $\jmath u_{m_0,l_0}$ is purely imaginary and is commonly referred to as intrinsic interference. The equalization is performed by simply applying a phase correction and real conversion, *i.e.*, $\hat{d}_{m_0,l_0} = \Re\{z_{m_0,l_0} e^{-\jmath\hat{\phi}_{l_0}}\}$ where $\hat{\phi}_{l_0}$ is the estimate of the PN at multicarrier symbol l_0. Accurate estimation of the PN is of crucial importance to avoid leakage of the intrinsic interference on the symbol of interest.

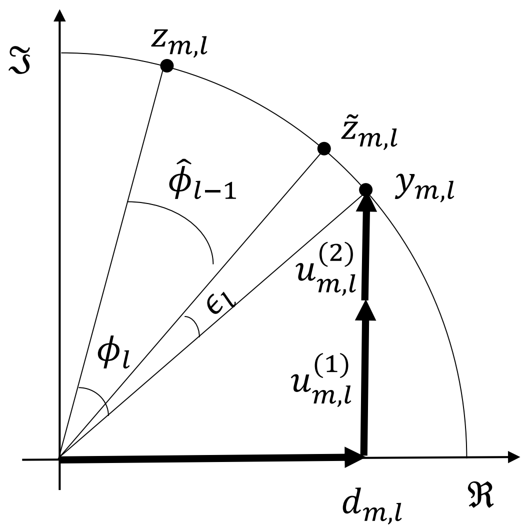

Figure 7.1 Illustration of the signal model on the complex plane without additive noise.

7.2 ML and MAP estimators

Let us assume that an initial phase estimate can be obtained at the beginning of the transmission. After this initialization phase, the modem switches in tracking mode and does not use pilot symbols. Let us denote the estimate of the previous phase at multicarrier symbol $l-1$ by $\hat{\phi}_{l-1}$. We want an estimate of the current phase ϕ_l that we denote by $\hat{\phi}_l$.

Since the PN is assumed to be slowly varying over the symbol duration, we propose to estimate the phase error, defined as $\epsilon_l = \phi_l - \hat{\phi}_{l-1}$ and its estimate, $\hat{\epsilon}_l = \hat{\phi}_l - \hat{\phi}_{l-1}$, instead of re-estimating ϕ_l from scratch as in [85, 86]. At first, we perform a rotation of angle $-\hat{\phi}_{l-1}$ on $z_{m,l}$,

$$\begin{aligned}\tilde{z}_{m,l} &= e^{-\jmath\hat{\phi}_{l-1}} z_{m,l} \\ &= d_{m,l}e^{\jmath\epsilon_l} + \jmath u_{m,l}e^{\jmath\epsilon_l} + \tilde{w}_{m,l}.\end{aligned}$$

Since the PN is assumed to vary slowly, a first estimation of the symbols $d_{m,l}$ at multicarrier symbol l can be obtained by taking the real part of

$\tilde{z}_{m,l}$ and performing a direct decision. Moreover, thanks to the current and previously decoded symbols, a part of the intrinsic interference can be estimated. We rewrite $u_{m,l}$ as

$$\begin{aligned} u_{m_0,l_0} &= u^{(1)}_{m_0,l_0} + u^{(2)}_{m_0,l_0} \\ u^{(i)}_{m_0,l_0} &= \sum_{(m,l)\in\Omega^{(i)}_{m_0,l_0}} d_{m,l}\Im\left\{t_{m,m_0,l,l_0}\right\}, \quad i=1,2, \end{aligned}$$

where $u^{(1)}_{m,l}$ corresponds to the intrinsic interference due to previous and current decoded symbols which can be estimated based on decisions, *i.e.*, $\Omega^{(1)}_{m_0,l_0}$ is the set of indices (m,l) such that $m \in \{0,...,2M-1\}, l \leq l_0$ and $u^{(2)}_{m,l}$ is the intrinsic interference due to future symbols, *i.e.*, $\Omega^{(2)}_{m_0,l_0}$ is the set of indices (m,l) such that $m \in \{0,...,2M-1\}, l > l_0$. Fig. 7.1 illustrates the signal model under consideration with no additive noise ($w_{m_0,l_0} = 0$). Of course, the knowledge of $u^{(1)}_{m,l}$ can help to improve the performance but also increases the complexity of the algorithm due to the necessary computation of $u^{(1)}_{m,l}$. In practice, if the prototype pulse is well localized in time and frequency, the set $\Omega^{(1)}_{m_0,l_0}$ can be restricted to the close neighbors of (m_0,l_0) and the complexity might be decreased by considering less neighboring symbols in the estimation of $u^{(1)}_{m,l}$. The complexity-performance trade-off will be further discussed in Section 7.3. Note that the symbol $d_{m,l} + \jmath u^{(1)}_{m,l}$ can be seen as a kind of pseudo-pilot symbol [33]. However, it includes only one part of the intrinsic interference and it is based on direct decisions and not pilots.

Since the PN at instant l does not depend on the subcarrier index, it makes sense to combine all subcarriers to jointly estimate this phase factor. Moreover, the use of all subcarriers makes the estimator more robust against the noise effect. In the following sections, the outputs of all subcarriers will be considered.

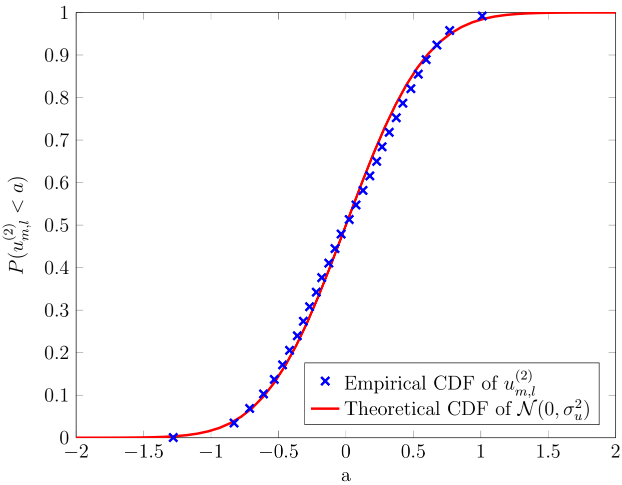

Figure 7.2 Empirical cumulative density function (CDF) of $u_{m,l}^{(2)}$ versus CDF of a zero mean Gaussian random variable with variance σ_u^2.

7.2.1 ML estimator

The ML estimator of ϵ_l is the one that maximizes the likelihood of the demodulated symbols given ϵ_l, based on current available decisions,

$$\hat{\epsilon}_l^{\mathrm{ML}} = \arg\max_{\epsilon_l} f(\tilde{z}_{0,l}, ..., \tilde{z}_{2M-1,l}|\epsilon_l).$$

Since one part of the intrinsic interference, $u_{0,l}^{(2)}, ..., u_{2M-1,l}^{(2)}$, cannot be estimated, we will consider it as noise. The distribution of $u_{m,l}^{(2)}$ is an intricate combination of the real transmitted symbols. To simplify the design, we will assume that $u_{m,l}^{(2)}$ is normally distributed with zero mean and variance σ_u^2, *i.e.*, $u_{m,l}^{(2)} \sim \mathcal{N}(0, \sigma_u^2)$. Assuming that the transmitted symbols $d_{m,l}$ are independent and of variance $E_s/2$, the variance σ_u^2 is given by

$$\sigma_u^2 = \frac{E_s}{2} \sum_{(m,l)\in\Omega_{m_0,l_0}^{(2)}} \Im^2 \left\{t_{m,m_0,l,l_0}\right\}.$$

Note that depending on the number of neighboring symbols included in the set $\Omega^{(2)}_{m_0,l_0}$, the value of σ_u^2 might change. In the limit case where $\Omega^{(1)}_{m_0,l_0} = \emptyset$, there is no estimation of the intrinsic interference, *i.e.*, $u_1 = 0$. Fig. 7.2 plots the empirical distribution of $u^{(2)}_{m,l}$ compared to the distribution of a Gaussian random variable with variance σ_u^2. This justifies the assumption of approximating the distribution $u^{(2)}_{m,l}$ as Gaussian. One should remember that $u^{(2)}_{m,l}$ is purely real. Hence, the noise statistics are not circularly symmetric. To take this into account, we rewrite the measurement model at all subcarriers in an extended all-real form as

$$\mathbf{z} = \mathbf{C}\boldsymbol{\theta} + \mathbf{w},$$

where we defined

$$\begin{aligned}
\mathbf{z} &= \left(\tilde{z}^R_{0,l}, \tilde{z}^I_{0,l}, \ldots, \tilde{z}^R_{2M-1,l}, \tilde{z}^I_{2M-1,l}\right)^T \\
\mathbf{C} &= \left(\mathbf{C}^T_{0,l}, \ldots, \mathbf{C}^T_{2M-1,l}\right)^T \\
\boldsymbol{\theta} &= \left(\cos(\epsilon_l), \sin(\epsilon_l)\right)^T \\
\mathbf{w} &= \left(\tilde{\mathbf{w}}^T_{0,l}, \ldots, \tilde{\mathbf{w}}^T_{2M-1,l}\right)^T
\end{aligned}$$

and

$$\begin{aligned}
\mathbf{C}_{m,l} &= \begin{pmatrix} d_{m,l} & -u^{(1)}_{m,l} \\ u^{(1)}_{m,l} & d_{m,l} \end{pmatrix} \\
\tilde{\mathbf{w}}_{m,l} &= \begin{pmatrix} -u^{(2)}_{m,l}\sin(\epsilon_l) + \tilde{w}^R_{m,l} \\ u^{(2)}_{m,l}\cos(\epsilon_l) + \tilde{w}^I_{m,l} \end{pmatrix}.
\end{aligned}$$

One can verify that, under previous assumptions, the vector of real noise samples $\mathbf{w}$ is normally distributed with zero mean and a covariance matrix $\mathbf{R}_w$ that depends on ϵ_l. In FBMC-OQAM systems, the prototype pulse, modulated around a specific time-frequency bin (m, l), overlaps with neighboring subcarriers and multicarrier symbols. This implies correlation of the additive noise and the intrinsic interference, *i.e.*, $\mathbf{R}_w$

is not diagonal. Taking into account this interference could help to average the noise effect. However, this would significantly increase the complexity of the design. Therefore, we here choose to neglect inter-carrier correlation. Matrix $\mathbf{R}_w$ then becomes block diagonal, *i.e.*, $\mathbf{R}_w = \mathbf{I}_{2M} \otimes \mathbf{R}_m$, with $\mathbf{R}_m$ given by

$$\mathbf{R}_m = \begin{pmatrix} \frac{N_0}{2} + \sigma_u^2 \sin^2(\epsilon_l) & -\sigma_u^2 \sin(\epsilon_l)\cos(\epsilon_l) \\ -\sigma_u^2 \sin(\epsilon_l)\cos(\epsilon_l) & \frac{N_0}{2} + \sigma_u^2 \cos^2(\epsilon_l) \end{pmatrix}.$$

We are now in the position to write the expression of the likelihood $f(\mathbf{z}|\epsilon_l) = f(\tilde{z}_{0,l}, ..., \tilde{z}_{2M-1,l}|\epsilon_l)$,

$$f(\mathbf{z}|\epsilon_l) = \frac{1}{\sqrt{(2\pi)^{4M}|\mathbf{R}_w|}} e^{-\frac{1}{2}(\mathbf{z}-\mathbf{C}\boldsymbol{\theta})^T \mathbf{R}_w^{-1}(\mathbf{z}-\mathbf{C}\boldsymbol{\theta})}.$$

Noting that $|\mathbf{R}_w| = (\frac{N_0}{2}(\frac{N_0}{2} + \sigma_u^2))^{2M}$ which does not depend on ϵ_l and that $\mathbf{R}_w^{-1} = \mathbf{I}_{2M} \otimes \mathbf{R}_m^{-1}$ is block diagonal with

$$\mathbf{R}_m^{-1} = \frac{\begin{pmatrix} \frac{N_0}{2} + \sigma_u^2 \cos^2(\epsilon_l) & \sigma_u^2 \sin(\epsilon_l)\cos(\epsilon_l) \\ \sigma_u^2 \sin(\epsilon_l)\cos(\epsilon_l) & \frac{N_0}{2} + \sigma_u^2 \sin^2(\epsilon_l) \end{pmatrix}}{\frac{N_0}{2}(\frac{N_0}{2} + \sigma_u^2)},$$

the ML estimator is given by

$$\begin{aligned} \hat{\epsilon}_l^{\mathrm{ML}} &= \arg\max_{\epsilon_l} \log f(\tilde{\mathbf{z}}|\epsilon_l) \\ &= \arg\max_{\epsilon_l} -\frac{1}{2}(\mathbf{z} - \mathbf{C}\boldsymbol{\theta})^T \mathbf{R}_w^{-1}(\mathbf{z} - \mathbf{C}\boldsymbol{\theta}) \end{aligned}$$

where we removed the constant term of the log-likelihood that does not depend on ϵ_l. After several mathematical manipulations and keeping only the terms that depend on ϵ_l, the expression simplifies to

$$\hat{\epsilon}_l^{\mathrm{ML}} = \arg\max_{\epsilon_l} -\frac{\sigma_u^2}{2}\sum_{m=0}^{2M-1}\Re\{\tilde{z}_{m,l}e^{-\jmath\epsilon_l}\}\left(\Re\{\tilde{z}_{m,l}e^{-\jmath\epsilon_l}\}-2d_{m,l}\right) + \frac{N_0}{2}\sum_{m=0}^{2M-1}\Re\left\{\tilde{z}_{m,l}\left(d_{m,l}-\jmath u_{m,l}^{(1)}\right)e^{-\jmath\epsilon_l}\right\}.$$

The two terms in the above expression have an intuitive meaning. The maximization of the first term, proportional to $-\sigma_u^2$ tends to find the rotation ϵ_l such that, after taking the real part, the contribution due to remaining intrinsic interference disappears and the symbol $d_{m,l}$ is recovered, *i.e.*, $\Re\{\tilde{z}_{m,l}e^{-\jmath\epsilon_l}\} = d_{m,l}$. The maximization of the second term aims at finding the value of ϵ_l that aligns the observations $\tilde{z}_{m,l}$ with the "partial" pseudo-pilots $d_{m,l} + \jmath u_{m,l}^{(1)}$, especially when the additive noise power N_0 is large. This problem is not trivial to optimize due to the non polynomial dependence in ϵ_l. One idea would be to test different phase trials, evaluate the likelihood and keep the best test, as it was done in [85, 86] but using a different metric. However, this would significantly increase the complexity of the algorithm. Moreover, the fact that, in practice, only a finite number of phase trials can be tested induces a discretization error.

In order to reduce the complexity, we derive a closed-form solution. Due to the fact that ϵ_l is close to zero, the term $e^{-\jmath\epsilon_l}$ can be well approximated by the first order Taylor expansion given by $e^{-\jmath\epsilon_l} \approx 1 - \jmath\epsilon_l$. Note that this assumption makes sense due to the slowly varying nature of the PN. We will further show, through simulations, that the error induced by this linearization is negligible and does not impact the system performance. This leads to

$$
\begin{aligned}
\hat{\epsilon}_l^{\mathrm{ML}} \approx \arg\max_{\epsilon_l} & -\frac{\sigma_u^2}{2}\sum_{m=0}^{2M-1}\left(\Re\{\tilde{z}_{m,l}(1-\jmath\epsilon_l)\}\right)^2 \\
& + \sigma_u^2 \sum_{m=0}^{2M-1}\left(\Re\{\tilde{z}_{m,l}(1-\jmath\epsilon_l)\}\right) d_{m,l} \\
& + \frac{N_0}{2}\sum_{m=0}^{2M-1}\Re\left\{\tilde{z}_{m,l}\left(d_{m,l}-\jmath u_{m,l}^{(1)}\right)(1-\jmath\epsilon_l)\right\},
\end{aligned}
$$

which is a quadratic expression in ϵ_l. We finally obtain

$$
\hat{\epsilon}_l^{\mathrm{ML}} \approx \frac{\sum_m(\tilde{z}_{m,l}^I(\frac{N_0}{2}+\sigma_u^2)d_{m,l} - \tilde{z}_{m,l}^R\frac{N_0}{2}u_{m,l}^{(1)} - \sigma_u^2\tilde{z}_{m,l}^R\tilde{z}_{m,l}^I)}{\sigma_u^2\sum_m(\tilde{z}_{m,l}^I)^2}.
$$

Hence, the current phase can be estimated as $\hat{\phi}_l = \hat{\phi}_{l-1} + \hat{\epsilon}_l^{\mathrm{ML}}$ and the symbols $d_{m,l}$ can be re-estimated using this update of the phase.

7.2.2 MAP estimator

The ML estimator does not use the *a priori* distribution of ϵ_l. In practice, the transmit and receive lasers are known. Hence the linewidth can be estimated and we can use this knowledge to improve the estimation. The MAP estimator of ϵ_l is given by

$$
\hat{\epsilon}_l^{\mathrm{MAP}} = \arg\max_{\epsilon_l} f(\mathbf{z}|\epsilon_l)f(\epsilon_l). \tag{7.1}
$$

Assuming that the previous phase estimate is close to the actual phase, we can approximate $\epsilon_l = \phi_l - \hat{\phi}_{l-1}$ by $\epsilon_l \approx \phi_l - \phi_{l-1}$. Under this assumption, ϵ_l is normally distributed with zero mean and variance $\sigma_\epsilon^2 = M\sigma_\nu^2 = \pi\Delta\nu T$, *i.e.*,

$$
f(\epsilon_l) = \frac{1}{\sqrt{2\pi\sigma_\epsilon^2}}e^{-\frac{\epsilon_l^2}{2\sigma_\epsilon^2}}, \quad \log f(\epsilon_l) = D - \frac{\epsilon_l^2}{2\sigma_\epsilon^2},
$$

where D is a constant that does not depend on ϵ_l. Taking the logarithm of the expression in (7.1), the MAP estimator of ϵ_l is the solution of

$$\hat{\epsilon}_l^{\mathrm{MAP}} = \arg\max_{\epsilon_l} -\frac{\sigma_u^2}{2}\sum_{m=0}^{2M-1} \Re\{\tilde{z}_{m,l}e^{-\jmath\epsilon_l}\}\left(\Re\{\tilde{z}_{m,l}e^{-\jmath\epsilon_l}\} - 2d_{m,l}\right)$$
$$+\frac{N_0}{2}\sum_{m=0}^{2M-1} \Re\left\{\tilde{z}_{m,l}\left(d_{m,l} - \jmath u_{m,l}^{(1)}\right)e^{-\jmath\epsilon_l}\right\} - \frac{\epsilon_l^2}{2}\sigma_{\mathrm{MAP}}^2,$$

where $\sigma_{\mathrm{MAP}}^2 = \frac{\frac{N_0}{2}(\frac{N_0}{2}+\sigma_u^2)}{\sigma_\epsilon^2}$. If, as in the derivations of the ML estimator, we use the first order approximation of $e^{-\jmath\epsilon_l}$, we obtain

$$\hat{\epsilon}_l^{\mathrm{MAP}} \approx \frac{\sum_m(\tilde{z}_{m,l}^I(\frac{N_0}{2}+\sigma_u^2)d_{m,l} - \tilde{z}_{m,l}^R\frac{N_0}{2}u_{m,l}^{(1)} - \sigma_u^2\tilde{z}_{m,l}^R\tilde{z}_{m,l}^I)}{\sigma_u^2\sum_m(\tilde{z}_{m,l}^I)^2 + \sigma_{\mathrm{MAP}}^2}.$$

One can see that the MAP estimator expression is very close to the ML estimator. Intuitively, the parameter σ_{MAP}^2 adjusts the estimation depending on the linewidth of the laser. If the linewidth is small, σ_ϵ^2 will be low as well and σ_{MAP}^2 will be high, which will decrease in the end the value of the estimate. This makes sense since we have the *a priori* knowledge that ϵ_l is low and we should then penalize large values of ϵ_l. Finally, the current PN is estimated as $\hat{\phi}_l = \hat{\phi}_{l-1} + \hat{\epsilon}_l^{\mathrm{MAP}}$ and the symbols $d_{m,l}$ are re-estimated using this update of the phase. Note that, the ML and MAP estimators do not suffer from ambiguity problem [138] as could be the case for the M-BPS algorithm, which can recover the phase only up to a multiple of π.

Note that in the case where no part of the intrinsic interference is estimated, the MAP estimator simplifies to

$$\hat{\epsilon}_{l,u^{(1)}=0}^{\mathrm{MAP}} \approx \frac{(\frac{N_0}{2}+\sigma_u^2)\sum_m \tilde{z}_{m,l}^I d_{m,l} - \sigma_u^2\sum_m \tilde{z}_{m,l}^R\tilde{z}_{m,l}^I}{\sigma_u^2\sum_m(\tilde{z}_{m,l}^I)^2 + \sigma_{\mathrm{MAP}}^2},$$

where σ_u^2 should be re-computed based on the new neighborhood defined by $\Omega^{(2)}_{m_0,l_0}$. One can see that the estimator $\hat{\epsilon}^{\mathrm{MAP}}_{l,u^{(1)}=0}$ has a very low complexity of implementation.

7.3 Simulation results

This sections aims at validating the performance of the proposed estimators through simulations. We will assume a laser linewidth $\Delta\nu$ of 1 MHz and a bandwidth of 30 GHz, which corresponds to a sampling period $\frac{T}{2M}$ of 33 ps. Note that since the bandwidth is fixed, if we increase the number of subcarriers $2M$, the symbol period T is increased as well. As a consequence, the system becomes more sensitive to the laser PN since the phase has experienced a larger variation during one symbol duration. To take that into account, we define the normalized bandwidth as the product of the combined linewidth and symbol duration, *i.e.*, $\Delta\nu T$. In the simulations, the theoretical curve of a system without PN is also plotted, as a benchmark. The transmit and receive prototype filters used in the simulations is the Phydyas filter [6] with overlapping factor set to four.

In Fig. 7.3, the symbol error rate (SER) is simulated for FBMC-OQAM systems using different implementations of the proposed estimators. A 4-OQAM and a 16-OQAM constellations are considered. The ML curve corresponds to the derived ML estimator denoted by $\hat{\epsilon}^{\mathrm{ML}}_l$, based on the linearization of $e^{-\jmath\epsilon_l}$ and where $u^{(1)}_{m,l}$ is estimated based on all current and previously decoded symbols. The MAP curve corresponds to the derived MAP estimator denoted by $\hat{\epsilon}^{\mathrm{MAP}}_l$ which is very similar to the ML estimator but includes the *a priori* distribution of the PN. As can be seen, the MAP estimator does not provide a high gain with respect to the ML estimator, except at very low SNR for the 4-OQAM constellation. Furthermore, the MAP curve with $u^{(1)} = 0$ corresponds to the MAP estimator with no estimation at all of the intrinsic interference, denoted by $\hat{\epsilon}^{\mathrm{MAP}}_{l,u^{(1)}=0}$. Note that this estimator is less complex and achieves the

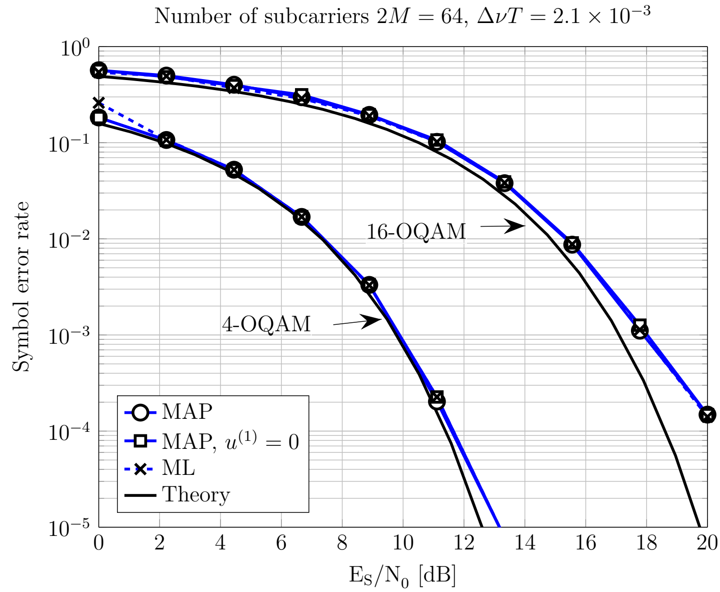

Figure 7.3 Comparison of different proposed estimators.

same performance as the the estimator $\hat{\epsilon}_l^{\mathrm{MAP}}$. Therefore, we conclude that estimating part of the intrinsic interference is not really useful and should be avoided to decrease the estimation complexity. In the following, we only consider the MAP estimator $\hat{\epsilon}_{l,u^{(1)}=0}^{\mathrm{MAP}}$ since it achieves the best trade-off between performance and complexity.

In Fig. 7.4 and Fig. 7.5, the SER of an FBMC-OQAM system using the proposed MAP estimator $\hat{\epsilon}_{l,u^{(1)}=0}^{\mathrm{MAP}}$ is compared to the state of the art M-BPS algorithm, as detailed in [86]. The M-BPS algorithm is here implemented with a number of phase tests B set to 20. The complexity of those two algorithms is compared in Table 7.1. One can see that the proposed estimator uses about 4 times less real multiplications and 10 times less decisions than the M-BPS algorithm (for $B = 20$).

Fig. 7.4 compares the two methods as a function of the SNR. Again, two constellation sizes are considered, namely, a 4-OQAM and a 16-OQAM. The results show that M-BPS performs significantly worse at low SNR level, especially for a higher constellation size. At medium

Table 7.1 Complexity of the algorithms in terms of real multiplications and decisions. B is the number of phase tests.

	Real multiplications	Decisions
M-BPS	$4MB$	$2MB$
MAP, $u^{(1)} = 0$	$18M + 4$	$4M$

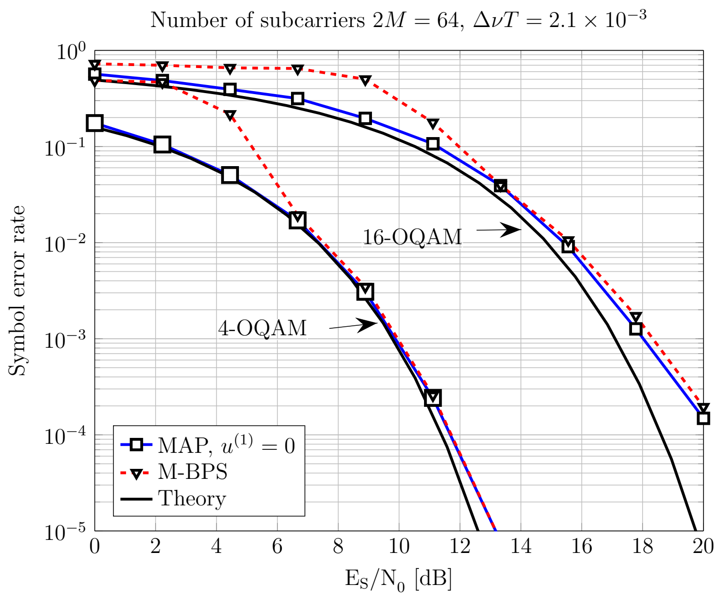

Figure 7.4 Comparison of the proposed MAP estimator with the state of the art M-BPS algorithm as a function of the SNR.

and high SNR values, the performances of the two algorithms are equivalent. The worse performance of the M-BPS algorithm at low SNR can be explained by the M-BPS metric, which is obtained based on the assumption of a high SNR regime. On the other hand, the proposed MAP estimator does not make that assumption and performs well at low SNR. Furthermore, it does not suffer from the discretization error due the limited number of phase tests of the M-BPS algorithm. It can also use its *a priori* information on the phase error to improve the PN estimation. On top of that, the complexity of the MAP estimator is drastically reduced.

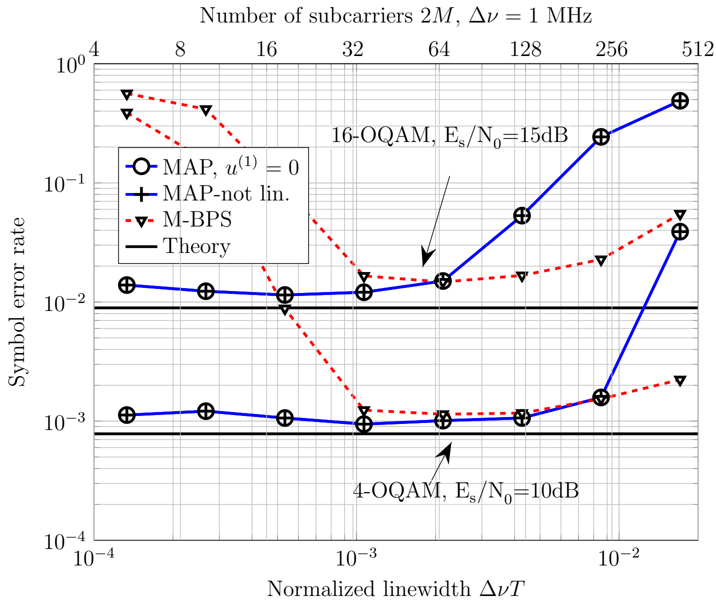

Figure 7.5 Comparison of the proposed MAP estimator with the state of the art M-BPS algorithm as a function of the normalized linewidth.

Fig. 7.5 compares the proposed MAP estimator and the M-BPS algorithm as a function of the normalized linewidth for fixed SNR values. For the 16-OQAM constellation, the SNR is fixed to $E_s/N_0 = 15$ dB while for the 4-OQAM constellation, the SNR is fixed to $E_s/N_0 = 10$ dB. To better understand the figure, one should remember that the transmission bandwidth is fixed and hence the ratio $\frac{T}{2M}$. This means that, if the normalized linewidth $\Delta\nu T = \Delta\nu \frac{T}{2M} 2M$ increases, the number of subcarriers $2M$ has increased as well, as indicated in the upper x axis of Fig. 7.5.

It can readily be seen in Fig. 7.5 that the M-BPS algorithm performs very poorly for low normalized linewidth. This comes from the fact that the number of subcarriers is low and the noise effect is not well averaged by the algorithm. As the normalized linewidth increases, and hence the number of subcarriers, the M-BPS starts to perform better. On the other hand, the MAP estimator performs well at low to moderate normalized linewidth since it does not make any assumption on the working SNR regime.

Furthermore, for high normalized linewidth values, the performance of the two algorithms begins to decrease. This comes from the fact that the basic assumption that the phase is constant during one multicarrier symbol transmission is not true anymore. One can see that the MAP estimator is more sensitive and is outperformed for high normalized linewidth by the M-BPS algorithm. One could think that the degradation comes from the linearization error of the approximation $e^{-\jmath\epsilon_l} \approx 1 - \jmath\epsilon_l$. To show the impact of this error, we plotted a MAP curve with no linearization, which achieves exactly the same performance as the MAP estimator. This curve is obtained by computing the MAP criterion for a high number of phase tests and keeping the best phase test. Therefore, we explain the worse performance of the MAP algorithm by the fact that the algorithm first estimates the current real symbols by performing a direct decision using the estimate of the phase at the previous multicarrier symbol, which is not the case for the M-BPS algorithm. In other words, the algorithm is limited by the propagation of the decision errors. One could avoid it by changing our algorithm and considering the current multicarrier symbol as an unknown random variable too and try a different number of phase trials. For each phase test, we would perform a direct decision and compute the *a posteriori* probability and keep the best test, as in the M-BPS algorithm but using a different cost function. Of course, this would increase the complexity.

7.4 Conclusion

Two estimators have been proposed for carrier phase recovery in optical FBMC-OQAM systems. The first one was obtained by maximization of the likelihood of the demodulated signal while the second one was found by maximizing the *a posteriori* distribution of the received signal. For both estimators, a closed form expression was derived, based on a first order approximation of the signal model, which leads to a significant reduction of complexity with respect to state of the art solutions. The impact of estimating part of the intrinsic interference based on previous and current decoded symbols was studied. It was shown through simulations that it does not provide significant gain of performance. Simulation results have also shown that the proposed estimators outperform state of the art solution in the low SNR regime and for a small number of subcarriers.

CHAPTER 8

CHROMATIC DISPERSION COMPENSATION

The CD is one of the main transmission impairments in optical fiber systems. It comes from the fact that spectral components of the transmitted signal travel at different speeds inside the fiber. The classical way to handle channel frequency variations in FBMC-OQAM systems is to increase the number of subcarriers, so that the channel can be approximated as flat at the subcarrier level. Then, simple one-tap equalization can be used, providing an efficient replacement of the well-known overlap and save algorithm [87]. However, Chapter 7 has shown that, for a fixed bandwidth, having more subcarriers induces a larger symbol period and hence, more sensitivity to PN [137].

In this work, we consider a system with a sufficiently high number of subcarriers such that it can achieve high SE. At the same time, we keep the number of subcarriers low enough such that the system remains robust against PN. In other words, a low complexity PN estimator as proposed in Chapter 7 is sufficient to compensate for PN. In that case, for wideband systems and for relatively long fibers, simple one-tap equalization is not sufficient to compensate for CD and more advanced methods are necessary [87], [139], [140]. Here, we review several compensation algorithms and we show that these methods, initially designed to handle channel frequency selectivity in wireless systems, can be applied to optical fiber communications. The different algorithms are compared in terms of performance and complexity.

8.1 System model

In order to focus on the CD effect and its compensation methods, an FBMC-OQAM transmission with only one polarization is considered. Dual polarization systems can straightforwardly be achieved by using some existing techniques in OFDM systems for both polarization multiplexing and demultiplexing [141]. Ideal time/frequency synchronization is assumed. As detailed in Section 2.2.2, the CD is assumed to have the following baseband frequency response

$$H\left(f\right) = e^{-\jmath \frac{\pi D \lambda^2 L}{c} f^2}, \tag{8.1}$$

where D is the dispersion coefficient [ps/nm/km], λ is the central wavelength, c is the speed of light and L is the fiber length [91]. The baseband received signal, impacted by CD, PN and additive noise, can be written as

$$r\left[n\right] = \left(\int\limits_{-1/2T_s}^{1/2T_s} S\left(f\right) H\left(f\right) e^{\jmath 2\pi f T_s n} df \right) e^{\jmath \phi[n]} + w[n], \tag{8.2}$$

where $S(f)$ is the Fourier transform of the transmitted signal. The PN is modeled as detailed in Section 2.2.2.

In classical approaches of FBMC-OQAM transmissions, the channel is assumed to be frequency flat at the subcarrier level and the phase noise is assumed to slowly vary with respect to the symbol duration. Under these conditions and if the pulse $g[n]$ is well localized in time and frequency, an approximation of z_{m_0,l_0} is given by (neglecting additive noise)

$$
\begin{aligned}
z_{m_0,l_0} &= \sum_{n=0}^{2M\kappa-1} r\left[n\right] g^{*}_{m_0,l_0}\left[n\right] \\
&\approx e^{\jmath\phi_{l_0}} H_{m_0} \sum_{l=-\infty}^{+\infty} \sum_{m=0}^{2M-1} d_{m,l} \sum_{n=0}^{2M\kappa-1} p_{m,l}\left[n\right] g^{*}_{m_0,l_0}\left[n\right]
\end{aligned} \tag{8.3}
$$

where $H_m = H\left(f_m\right)$ with f_m being the frequency of subcarrier m. CD equalization is performed by a simple one-tap multiplication. Assuming that the PN ϕ_{l_0} is estimated and compensated after the CD compensation and using the fact that the pulses are assumed to have PR conditions, the transmitted symbols can be recovered by taking the real part

$$
\hat{d}_{m_0,l_0} = \Re\left\{\frac{z_{m_0,l_0} e^{-\jmath\hat{\phi}_{l_0}}}{H_{m_0}}\right\}. \tag{8.4}
$$

The quality of the detection will critically depend on the accuracy of the approximation in (8.3). For long fibers, the channel will exhibit fast phase variations, especially at the edges of the band [140], which can be seen as a highly selective channel. To counterbalance this effect and to improve the accuracy of (8.3), one could decrease the subcarrier spacing $1/T$. This can be achieved by increasing the number of subcarriers in the system, while the transmission bandwidth, $1/T_s$, remains fixed. However, as was shown in Chapter 7 (for instance Fig. 7.5), increasing the number of subcarriers also means an increased symbol period $T = 2MT_s$, making the system more sensitive to time variations of the channel and hence to PN. In other words, more advanced equalization techniques should be analyzed to compensate for CD, especially for long communication links and for a relatively low number of subcarriers.

8.2 Equalization algorithms for chromatic dispersion compensation

In this work, we consider and compare several equalization algorithms for the CD compensation: a multi-tap per-subcarrier equalizer, a parallel equalization structure, a frequency-spreading receiver and the overlap and save algorithm. All these algorithms were detailed in Section 2.1.5.2. Except for the overlap and save algorithm [87], the other techniques were initially proposed for wireless FBMC-OQAM communications under high channel frequency selectivity and can be adapted straightforwardly to FBMC-OQAM communications on optical fiber to compensate for CD.

8.3 Complexity comparison

Since the CD effect is assumed to be static over time, the equalizer coefficients should be computed only once and for all at the beginning of the transmission or off-line. Therefore we omitted this type of complexity in the comparison.

In Table 8.1, the complexity of implementation of the different algorithms, in terms of real-valued multiplications, is compared. For the calculation, we assume that the number of subcarriers is a power of two and that an FFT/IFFT of size $2M$ requires $2M(\log_2(2M) - 3) + 4$ real-valued multiplications using the split-radix algorithm [130]. The classical receiver using single-tap per-subcarrier equalization, as described in Section 8.1, can be efficiently implemented using a $2M-$FFT, a PPN and a single-tap per-subcarrier equalizer. The multi-tap fractionally spaced per-subcarrier equalizer has an increased complexity due to the additional filtering by a $N_{\text{taps}}-$equalizer. The parallel multi-stage structure has a complexity that simply scales linearly with the number of parallel AFB's Q. The frequency-spreading receiver uses a FFT of size $2M\kappa$. Each bin of the FFT is equalized and filtered to retrieve the trans-

Table 8.1 Complexity of implementation of the algorithms.

Equalization structure	Real-valued multiplications
Single-tap, per-subcarrier	$2M(\log_2(2M) + 2\kappa + 1) + 4$
Multi-tap, per-subcarrier	$2M(\log_2(2M) + 2\kappa + 4N_{\text{taps}} - 3) + 4$
Parallel multi-stage	$(2M(\log_2(2M) + 2\kappa + 1) + 4)Q$
Frequency-spreading	$2M\kappa(\log_2(2M\kappa) + 5) - 8M + 4$
Overlap and save	$\frac{M}{N_{\text{FFT}}-K_{\text{ov}}}(2N_{\text{FFT}} \log_2(N_{\text{FFT}}) - 2N_{\text{FFT}} + 8)$ $+2M(\log_2(2M) + 2\kappa - 3) + 4$

Table 8.2 Equalizers complexity for the considered parameters: $2M = 256$ and $\kappa = 4$.

Single-tap, per-subcarrier	4356
Multi-tap, per-subcarrier	$N_{\text{taps}} = 3 \to 6404$, $N_{\text{taps}} = 7 \to 10500$
Parallel multi-stage	$Q = 2 \to 8712$, $Q = 3 \to 13608$
Frequency-spreading	14340
Overlap and save	$N_{\text{FFT}} = 512, K_{\text{ov}} = 128 \to 6065$ $N_{\text{FFT}} = 512, K_{\text{ov}} = 256 \to 7432$ $N_{\text{FFT}} = 1024, K_{\text{ov}} = 512 \to 7942$

mitted symbol. Finally, the overlap and save algorithm is composed of an FFT of size N_{FFT}, N_{FFT} complex multiplications and another IFFT of size N_{FFT}, followed by one AFB. The penalty due to the K_{ov} discarded samples was also taken into account. Table 8.2 gives the complexity of the different CD equalization methods when the number of subcarriers is 256 and the Phydyas prototype filter with overlapping factor equal to 4 is used [6].

8.4 Numerical results

In order to evaluate the effectiveness of the proposed CD compensation methods, a 30-GBaud ($1/T_s$ = 30 GHz) FBMC-OQAM system is simu-

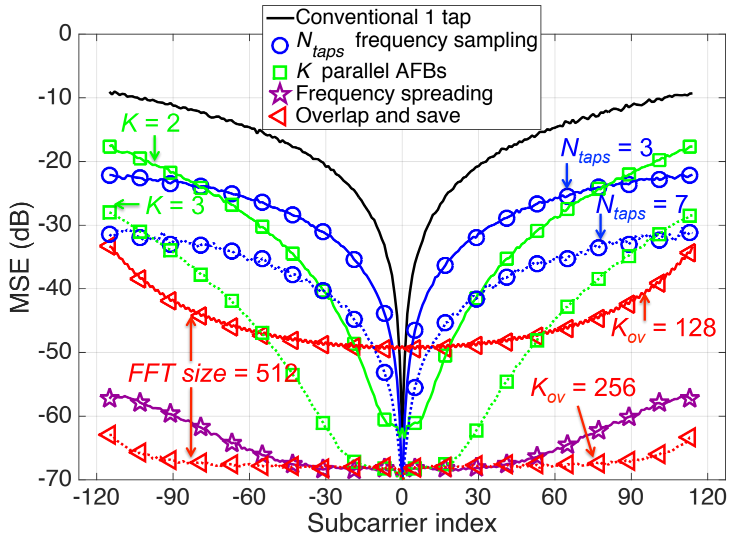

Figure 8.1 MSE of symbols versus subcarrier index. Normalized chromatic dispersion, $DL = 1.7 \times 10^4$ ps/nm.

lated and 4- and 16-OQAM modulations are considered. The combined linewidth of the transmitter and receiver lasers is set to $\Delta\nu = 200$ kHz, which is a typical value of the commercial external cavity laser. The adaptive maximum likelihood algorithm, which will be later presented in Chapter 9, is used for the compensation of the PN after CD equalization. We fix the number of subcarriers $2M = 256$ such that the normalized linewidth becomes $\Delta\nu T = \Delta\nu T_s 2M = 1.7 \times 10^{-3}$. As shown in Chapter 7, it ensures that the assumption of a sufficiently slow varying PN during one multicarrier symbol duration is accurate. Ten percents of the subcarriers at the edges of the band and the center (DC) subcarrier remain inactive. In the simulations, the frequency sampling method is used to compute the coefficients of the multi-tap per-subcarrier equalizer.

First, additive noise is not included in the simulations. This allows to clearly identify the impact of CD on the system performance. Fig. 8.1 shows the MSE of received symbols for each subcarrier after a 1000 km optical fiber transmission using different CD compensation methods. The dispersion coefficient D of standard single-mode fiber (SSMF) used in simulations is chosen equal to 17 ps/nm/km. The normalized CD is defined as the product of the dispersion coefficient and the fiber length, *i.e.*, DL [ps/nm]. It can be seen that the MSE exhibits the highest values on the edges of the frequency band since the phase variations of the channel are increasing with the absolute value of frequency. As it would be expected, the MSE reduces when applying the CD compensation methods. The performance is improved by increasing the block size of the overlap and save method, the number of taps of the fractionally-spaced per-subcarrier equalizer, the number of parallel AFBs equalizer, at the cost of increasing the receiver complexity. The high CD tolerance of the frequency spreading structure comes from the efficient equalization being performed at the very high frequency resolution $1/2M\kappa$. A basic assumption of the parallel equalization structure is that the derivatives of the channel frequency response should remain bounded [53], which becomes less accurate at the edges of the band and explain the performance degradation for these subcarriers. The frequency sampling multi-tap equalizer does not suffer from this limitation and outperforms the parallel equalization structure at the spectrum edges while performing relatively worse in the center frequencies.

In the next step, the FBMC system under the impact of CD is investigated in the presence of additive noise. The commonly used optical signal-to-noise ratio (OSNR) can be linked to the SNR per bit SNR_b used in wireless communications by [142]

$$OSNR = \frac{R_b}{2B_{ref}} SNR_b, \tag{8.5}$$

where R_b is the information bit rate and B_{ref} is the reference bandwidth, which is commonly 12.5 GHz corresponding to a 0.1 nm resolution bandwidth of optical spectrum analyzers at 1550 nm carrier wavelength.

Fig. 8.2(a) and (b) present the bit-error-ratio (BER) as a function of the OSNR after a 1000 km optical fiber transmission for 4- and 16-OQAM modulations, respectively. Considering the BER of 3.8×10^{-3} as the soft forward error correction (FEC) limit [143], the conventional single-tap equalizer is not sufficient to compensate for the CD induced by 1000 km fiber transmission for both modulation formats. By applying the proposed CD compensation methods, the OSNR penalties of the CD compensation curves compared to that of back-to-back (B2B, no transmission) curve at the 3.8×10^{-3} BER are negligible for 4-OQAM modulations (Fig. 8.2(a)). However, for 16-OQAM modulations (Fig. 8.2(b)), the CD compensation by using the 3 tap frequency sampling equalizer and the two parallel-AFBs equalizer are less effective than the other CD compensations. More specifically, at the soft FEC limit, the former CD compensations exhibit about 2 dB OSNR penalty whereas the latter CD compensations present only about 0.3 dB OSNR penalty compared to the B2B level.

Finally, the OSNR penalty at the 3.8×10^{-3} BER as a function of the normalized CD using different CD compensation methods is shown in Fig. 8.3(a) and (b) for 4- and 16-OQAM modulations, respectively. Considering a 1-dB OSNR penalty and 4-OQAM modulations (Fig. 8.3(a)), the tolerated CD of the conventional single-tap equalizer is only 9×10^3 ps/nm. The tolerated CD of the 3 taps and 7 taps frequency sampling equalizers are increased to 5×10^4 ps/nm and 1.1×10^5 ps/nm, respectively. Whereas the two and three parallel-AFBs equalizers show the corresponding tolerated CD of 2.5×10^4 ps/nm and 3.5×10^4 ps/nm. The frequency spreading method can provide the tolerated CD as high as the 7 taps frequency sampling equalizer, however, at the cost of higher complexity (Table 8.2). The tolerated CD of the overlap-and-save method can vary by adjusting the FFT size and overlapping factor. For example, when the FFT size and overlapping factor are 1024 and 512, respectively, the tolerated CD is 8×10^4 ps/nm. Similar to the other methods, the tolerated CD can be increased at the price of increasing

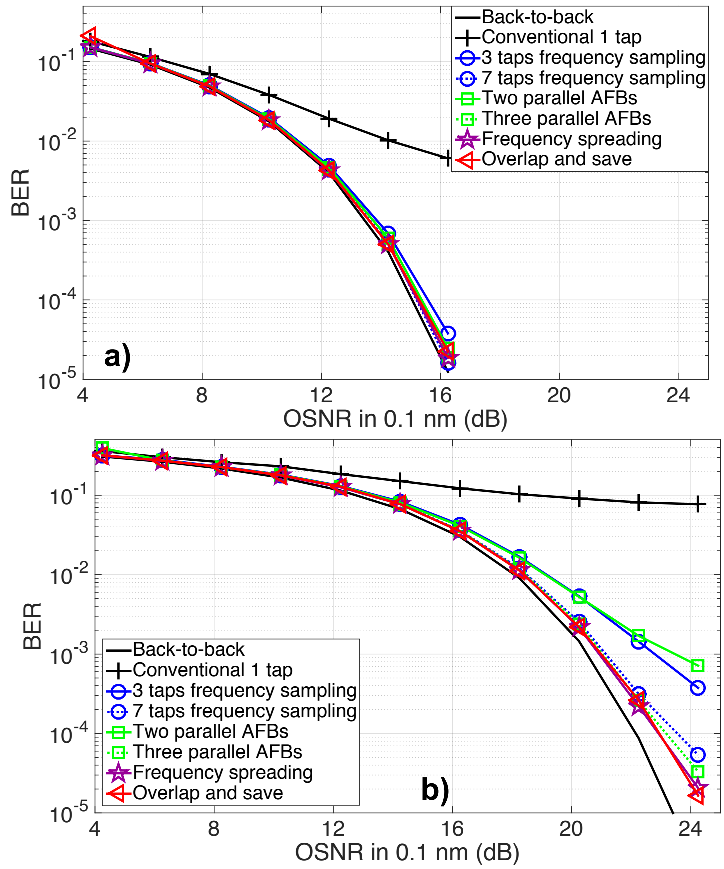

Figure 8.2 BER versus OSNR for a) 4-OQAM and b) 16-OQAM modulations. Normalized chromatic dispersion, $DL = 1.7 \times 10^4$ ps/nm.

the complexity. For 16-OQAM modulations (Fig. 8.3(b)), the similar tendencies are observed for different CD compensation methods, however, the tolerated CD is reduced compared to the case of 4-OQAM modulations. It is worth noticing that the frequency sampling equalizer seems to be more sensitive to higher modulation formats than the other methods. More particularly, at the 1-dB OSNR penalty, the tolerated CD of the 3 taps frequency sampling equalizer is reduced to that of the two parallel-AFBs equalizer. While the tolerated CD of the 7 taps frequency sampling equalizer is no longer similar to that of the frequency spread-

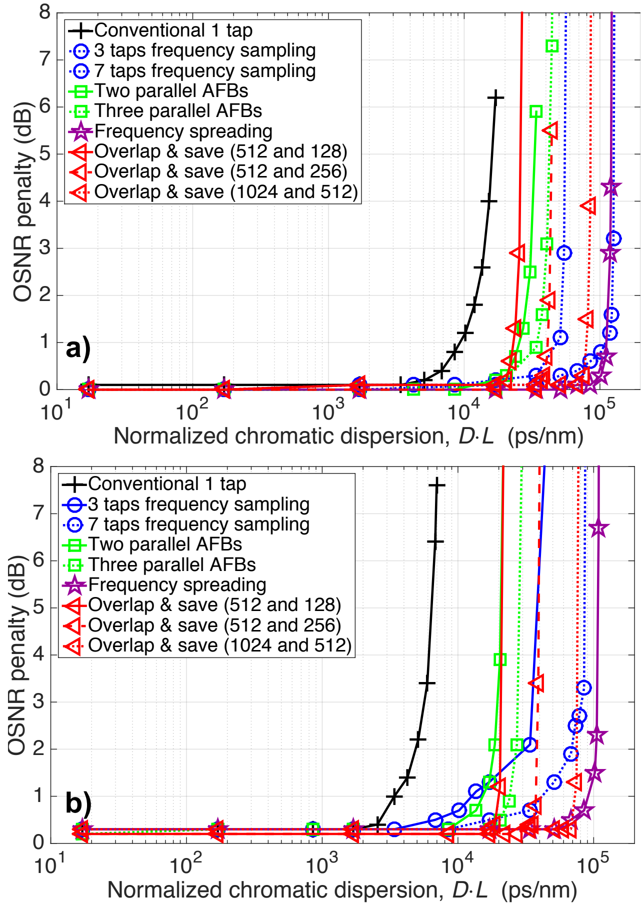

Figure 8.3 OSNR penalty as a function of the normalized CD for a) 4-OQAM and b) 16-OQAM modulations.

ing equalizer, as in 4-OQAM modulations case. Note that, although a varying number of subcarriers is not studied here, it is pointed out in [139] that the CD tolerance can scale linearly with the increase of the number of subcarriers. However, the PN compensation algorithm may become the main limitation of the system if the number of subcarriers is too large, which would require more efficient PN algorithms.

8.5 Conclusion

We investigated the compensation of CD in optical fiber FBMC-OQAM systems. It was shown that several equalization structures, initially proposed for wireless systems, can be applied to optical FBMC-OQAM systems even when the number of subcarriers is moderate. This allows for simple PN compensation methods working in the frequency domain. The various algorithms propose different trade-off between performance and complexity of implementation. The frequency spreading and parallel multi-stage architectures do not add any delay to the demodulation chain as opposed to the overlap and save and the multi-tap equalizers. The frequency spreading receiver and certain versions of the overlap and save algorithms showed very high robustness to CD. The disadvantage of the frequency spreading is its implementation complexity. The multi-tap equalizer is flexible in the sense that it can be applied on a subcarrier-basis depending on the CD frequency response.

CHAPTER 9

JOINT PHASE NOISE AND CHROMATIC DISPERSION COMPENSATION

In this chapter, we investigate long-haul terrestrial optical fiber FBMC-OQAM systems in the presence of both CD and PN. The number of subcarriers is kept sufficiently high in order to get a high spectral efficiency, *i.e.*, at least 128 subcarriers so that discarding one subcarrier at the spectrum edge to create a guard band between two optical channels leads to less than 1% spectral loss. However, it has been shown in Chapter 7 that the number of subcarriers should not be too high to ensure that the PN can be compensated in the frequency domain, allowing for a low complexity algorithm. At the same time, we know from Chapter 8 that the CD tolerance of single-tap equalization is reduced as the fiber dispersion or the propagation distance increases and/or the number of subcarriers decreases. In this work, we propose to use the frequency sampling multi-tap equalizer (as detailed in Section 2.1.5.2) for improving the CD tolerance. Moreover, a new simple PN estimation algorithm is derived following the same methodology as in Chapter 7 and which can be seen as an adaptive maximum likelihood (AML) algorithm. The proposed algorithms are numerically validated with 4- and 16-OQAM modulations after transmission over $L = 1000$ km of SSMF, with a combined laser linewidth $\Delta\nu$ of 400 kHz. The sampling rate $1/T_s$ is set to 60 GHz. Finally, we show how to optimize an FBMC-OQAM system in terms of the performance of both CD and PN compensation and their complexity. It is shown that the number of subcarriers should be carefully chosen so that the trade-off between efficient CD and PN compensation is optimized while the complexity is kept relatively low.

The chapter is organized as follows: in Section 9.1, the system model under study is detailed. In Section 9.2, the CD compensation performance of the FS multi-tap equalizer is studied as a function of the number of taps of the equalizer. In Section 9.3, the AML algorithm is proposed. The implementation complexity of the proposed algorithms is discussed in Section 9.4. In Section 9.5, we introduce the methodology for designing the FBMC-OQAM systems in the presence of both CD and PN effects. Finally, Section 9.5 concludes the chapter.

9.1 System model

In order to focus on the CD and PN effects, only one polarization is considered. Ideal time and frequency synchronization is assumed. The transmission model is exactly the same as the one presented in Section 8.1.

9.2 Chromatic dispersion compensation

The CD compensation method used in this chapter is a multi-tap equalizer, which coefficients are computed using the frequency sampling method, as detailed in Section 2.1.5.2 [41, 42]. The main advantage of this equalizer is its relatively low complexity of implementation and its flexibility as the number of taps can be chosen at each subcarrier depending on the quantity of CD. We assume that the CD is perfectly known at the receiver.

To focus on the performance of the multi-tap equalizer to deal with CD, additive noise and PN are first not considered. Fig. 9.1 shows the MSE of the received symbols at each subcarrier using the multi-

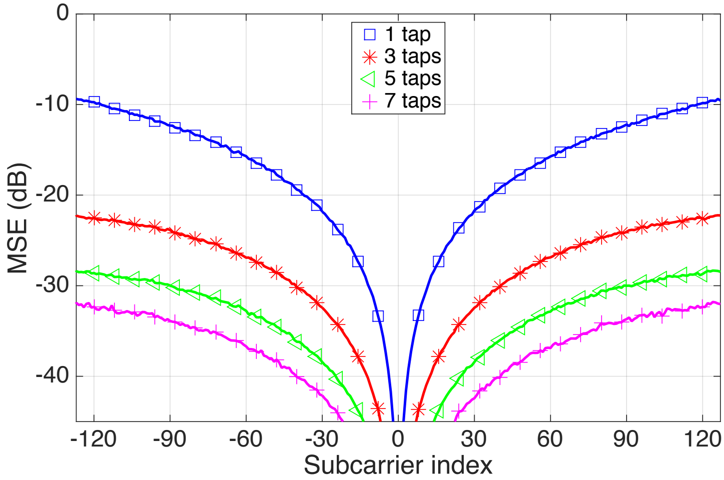

Figure 9.1 MSE of the received symbols at each subcarrier index after a $L = 1000$ km optical fiber transmission, in the absence of PN and AWGN. Normalized chromatic dispersion, $DL = 1.7 \times 10^4$ ps/nm.

tap equalizer with a varying number of taps after a 1000 km optical fiber transmission. The dispersion coefficient of SSMF D used in the simulations is 17 ps/nm/km and the sampling rate $1/T_s$ is 60 GHz. The number of subcarriers is set to 256. The MSE exhibits the highest values on the edges of the frequency band since the phase variations of the channel are increasing with the absolute value of frequency. As it would be expected, the MSE reduces when the number of taps of the multi-tap equalizer is increased.

Fig. 9.2 presents the average MSE as a function of the number of subcarriers for a 200 km and a 1000 km optical fiber transmission in the absence of additive noise and PN. In this figure, the performance of the equalizers with single-tap and 7 taps are plotted. As the number of subcarriers increases, the MSE is reduced since the subcarrier width is reduced and the frequency response of the channel can be considered to be flatter at the subcarrier level. For example, in order to achieve a MSE of -28 dB, if we use the single-tap tap equalizer and 128 subcarriers, the propagation length cannot exceed 200 km. However, using the 7 taps

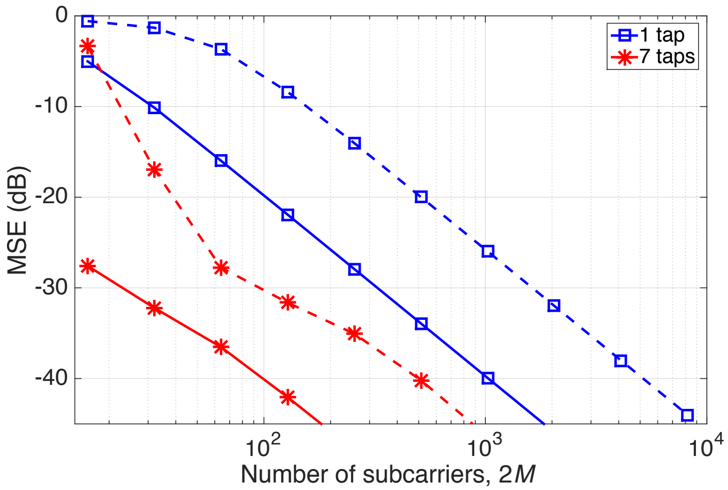

Figure 9.2 MSE versus number of subcarriers, in the absence of PN and AWGN. Solid lines: 200 km ($DL = 3.4 \times 10^3$ ps/nm), dashed lines: 1000 km ($DL = 1.7 \times 10^4$ ps/nm).

equalizer, a 1000 km fiber transmission may achieve the same MSE by using only 64 subcarriers.

9.3 Phase noise compensation

If the CD is assumed to be perfectly compensated after the AFB, we can assume that the derivations performed in Chapter 7 are holding. Under several assumptions, we found in Section 7.2.1 that the ML phase noise estimator was the solution of the following problem (particularized to the case of no estimation of the intrinsic interference $u^{(1)}_{m,l} = 0$)

$$\begin{aligned}\hat{\epsilon}_l^{\mathrm{ML}} &= \arg\max_{\epsilon} L(\epsilon) \\ L(\epsilon) &= -\frac{\sigma_u^2}{2} \sum_{m=0}^{2M-1} \Re\{\tilde{z}_{m,l} e^{-\jmath\epsilon}\} \left(\Re\{\tilde{z}_{m,l} e^{-\jmath\epsilon}\} - 2d_{m,l}\right) \\ &\quad + \frac{N_0}{2} \sum_{m=0}^{2M-1} \Re\left\{\tilde{z}_{m,l}\left(d_{m,l}\right) e^{-\jmath\epsilon}\right\},\end{aligned}$$

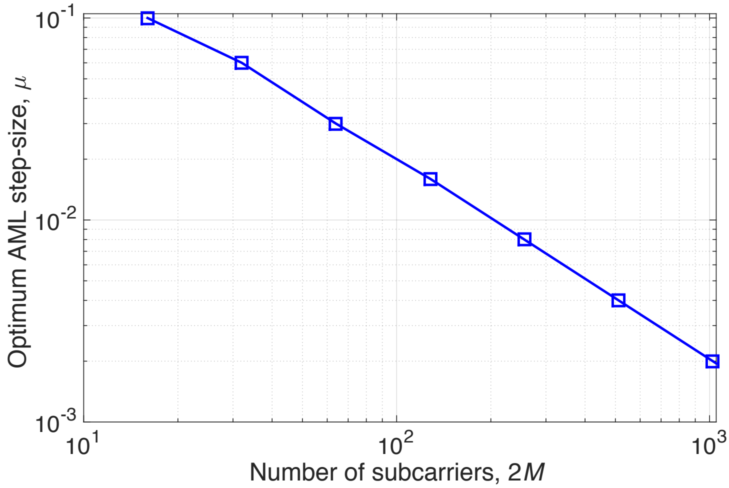

Figure 9.3 Optimum AML step-size versus number of subcarriers.

where we recall that symbols $\tilde{z}_{m,l}$ are the AFB outputs $z_{m,l}$ rotated by the previous PN estimate $\hat{\phi}_l$ and where symbols $d_{m,l}$ are primarily detected using direct detection on symbols $\tilde{z}_{m,l}$. This optimization problem is not trivial to solve. In Section 7.2.1, to avoid performing multiple phase trials as in [86], we proposed to use a linearization of the complex exponential $e^{-\jmath\epsilon}$ using the fact that the PN is assumed to slowly vary, *i.e.*, $\epsilon_l \approx 0$. Another possibility that is explored here is to use a gradient ascent approach. The derivative of the maximization criterion can be computed as

$$\frac{dL}{d\epsilon} = \sum_{m=0}^{2M-1} \left(\tilde{z}^I_{m,l}\cos\epsilon - \tilde{z}^R_{m,l}\sin\epsilon\right) \\ \left(\left(\sigma_u^2 + \frac{N_0}{2}\right) d_{m,l} - \sigma_u^2 \left(\tilde{z}^R_{m,l}\cos\epsilon + \tilde{z}^I_{m,l}\sin\epsilon\right)\right).$$

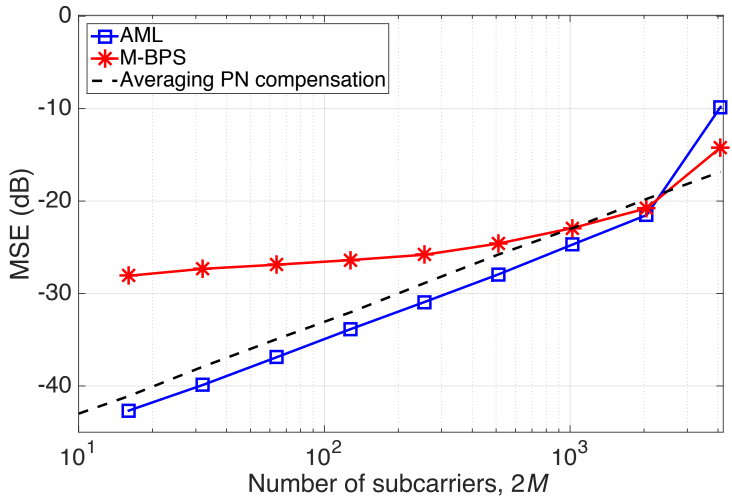

Figure 9.4 MSE versus number of subcarriers using different PN compensation. Averaging PN compensation is carried out with the assumption of knowing PN.

Assuming that we are in a low noise scenario ($\sigma_u^2 >> N_0$), the AML PN estimator is obtained as

$$\hat{\phi}_{l+1} = \hat{\phi}_l + \mu \sum_{m=0}^{2M-1} \left(\tilde{z}_{m,l}^I \cos\hat{\epsilon}_l - \tilde{z}_{m,l}^R \sin\hat{\epsilon}_l\right) \left(d_{m,l} - \tilde{z}_{m,l}^R \cos\hat{\epsilon}_l - \tilde{z}_{m,l}^I \sin\hat{\epsilon}_l\right),$$

where $\hat{\epsilon}_l$ was defined in Section 7.2.1 as $\hat{\epsilon}_l = \hat{\phi}_l - \hat{\phi}_{l-1}$ and μ is a step-size parameter controlling the rate of convergence, which needs to be optimized in order to achieve the best performance. To study the impact of the step-size on the PN compensation, the CD and AWGN are first neglected. Fig. 9.3 presents the optimum AML step-size as a function of the number of subcarriers. The optimum value is selected corresponding to the minimum MSE when varying the step-size. For the simulations, a combined laser linewidth $\Delta\nu$ of 400 kHz is considered and the sampling rate $1/T_s$ is set to 60 GHz.

Fig. 9.4 shows the MSE as a function of the number of subcarriers using the proposed AML algorithm or the M-BPS algorithm. The "average PN compensation" is also plotted as a reference. It is obtained, assuming that the PN is perfectly known, by computing the average of the PN on the duration of each FBMC symbol and compensating with this average value. It can be observed that the MSE of every method increases as a function of the number of subcarriers. This comes from the fact that the system becomes more sensitive to PN and the assumption that the PN is constant within one symbol transmission becomes less and less accurate. The performance of AML becomes worse than that of BPS for a large number of subcarriers or high normalized linewidth. As it was the case in Chapter 7, the proposed estimators are more sensitive to high PN because of the initial decision on the symbols based on the previous phase estimate, which is not the case of the M-BPS algorithm. At the same time, as shown in [137] and in Chapter 7, the M-BPS performance performs worse than AML for a low number of subcarriers, since there are not enough samples to average out the additive noise. Somewhat surprisingly, the AML shows better MSE than the compensation based on the true PN average, implying that the optimum value for the PN compensation of one FBMC symbol is not obtained by averaging the PN.

Fig. 9.5 presents the MSEs of the estimated PN using different PN compensation methods versus the SNR with the considered 400 kHz laser linewidth and $2M = 256$. The AML shows a better MSE compared to the M-BPS, especially at low SNR, which is consistent with the results in Fig. 9.4. Also, the modified Cramer-Rao lower bound (MCRLB) [144] is plotted as a benchmark.

9.4 Implementation complexity

In Table 9.1, we evaluate the complexity of the different compensation algorithms in terms of real multiplications. The number of multipli-

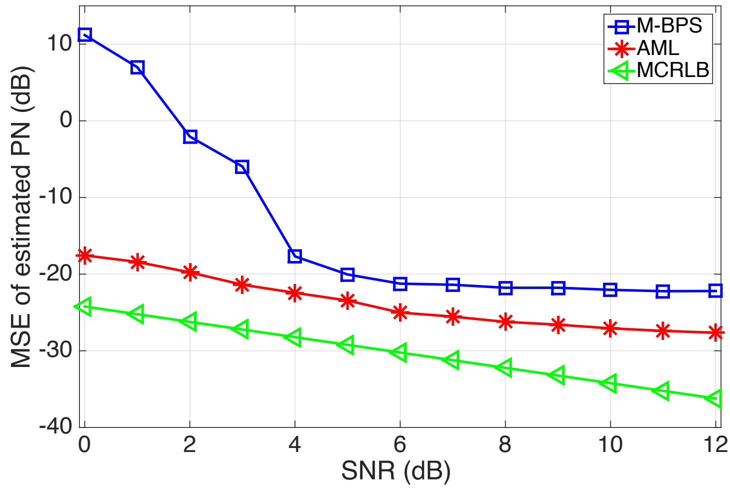

Figure 9.5 MSE of the estimated PN versus SNR. Laser linewidth is set to $\Delta\nu = 400$ kHz and $2M = 256$ giving $\Delta\nu T = 1.7 \times 10^{-3}$.

Table 9.1 Complexity of the algorithms in terms of real multiplications and decisions. N_{taps} is the number of taps and B is the number of phase tests.

	Real multiplications	Decisions
Multi-tap equ.	$8MN_{\text{taps}}$	
M-BPS	$4MB$	$2MB$
AML	$18M$	$2M$

cations required by the multi-tap FS equalizer is proportional to N_{taps}. Regarding the PN compensation, the AML reduces significantly the complexity compared to the M-BPS, as the number of phase tests B of M-BPS is generally at least equal to 16 [137]. Note that the AML algorithm approximately has the same complexity as the MAP estimator derived in Chapter 7.

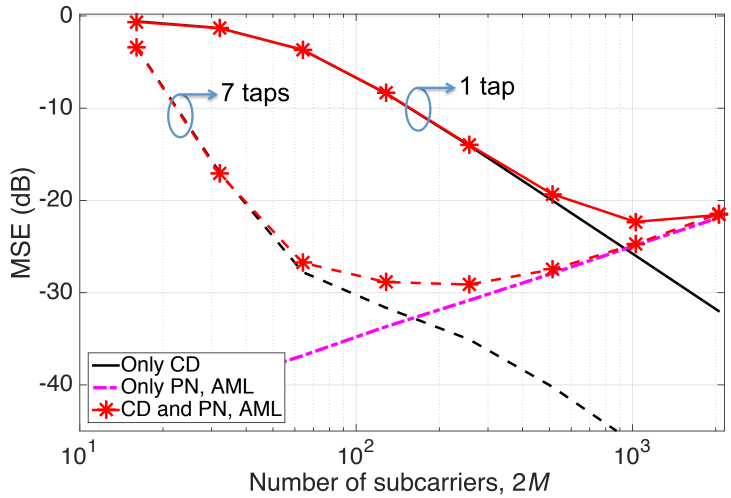

Figure 9.6 Trade-off between the CD and PN compensation, 1000 km fiber and 400 kHz linewidth. Black solid lines: single-tap equalizer; Black dashed lines: 7 taps equalizer.

9.5 System design and discussion

The performance of a 60 GBaud FBMC-OQAM system based on 4- and 16-OQAM modulations is assessed in this section in the presence of both CD and PN for a 1000 km transmission distance and a laser linewidth of 400 kHz. The number of subcarriers is considered here as a key design parameter as it directly fixes the SE in unsynchronized WDM systems using a small guard band. This number is varied in order to find the best trade-off between the CD and PN compensation. Even though the transmission distance and laser linewidth are fixed in the simulations, the system design methodology still applies for different values of CD and PN. We assume that the CFO is pre-compensated before the data detection can take place.

Fig. 9.6 shows the trade-off between the CD and PN compensation in terms of MSE when varying the number of subcarriers. Note that no AWGN is added in the simulations in order to focus on the CD and PN impacts. The performance achieved when only one of the two effects is activated is assessed as a benchmark. Regarding the CD compensation, the performance of single-tap equalizer (black solid lines) is compared to that of the 7-tap equalizer (black dashed lines). Regarding the PN compensation, only the performance of the AML algorithm is illustrated as it has been shown to outperform the M-BPS algorithm for the considered laser linewidth (Fig. 9.4). At the receiver, the CD compensation using different numbers of equalizer taps and the PN compensation using the AML algorithm are investigated. For a low number of subcarriers, it can be seen that the single-tap equalizer fails to recover the symbols and leads to a high MSE. For a high number of subcarriers, the performance of CD compensation is better, resulting in the reduction of MSE. As $2M$ is further increased, the PN compensation becomes less efficient resulting in an increase of the MSE. It is observed that there is an optimum compromise between CD and PN compensation regarding the number of subcarriers. Note that the exact value of the optimum number $2M$ varies depending on either the number of equalizer taps or the optical link parameters, *i.e.*, optical fiber length, laser linewidth. More specifically, with the considered link configuration, the optimum number of subcarriers is 1024 when using a single-tap equalizer and 256 when using a 7 taps equalizer.

In the next analysis, we investigate the performance of the optical link using the optimum number of subcarriers with 4- and 16-OQAM modulations. Fig. 9.7 shows the BER of 4- and 16-OQAM signals as a function of the SNR using AML and M-BPS algorithms. Note that we define the SNR as the ratio between the optical signal power at the receiver input and the optical noise power over the 60 GHz system bandwidth. When $2M = 256$ and a 7 tap equalizer is considered, no noticeable SNR penalty is observed for 4-OQAM signals while a 0.9 dB SNR penalty at the 10^{-3} BER is reported for 16-OQAM signals. If we now consider the single-tap equalizer, the optimum $2M$ value is 1024 (see in Fig. 8) and we can see in Fig. 8 that the BER is worse for both 4- and 16-OQAM modulations. More particularly, the 4-OQAM mod-

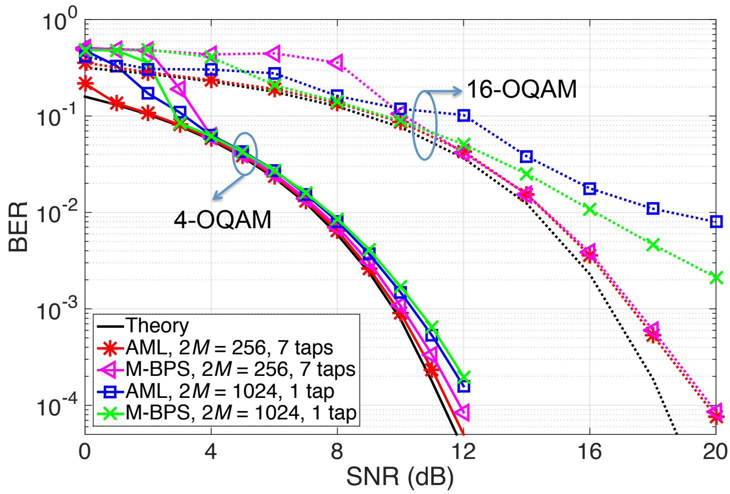

Figure 9.7 BER versus SNR after 1000 km transmission ($DL = 1.7 \times 10^4$ ps/nm) with the combined laser linewidth of $\Delta\nu = 400$ kHz ($\Delta\nu T = 1.7 \times 10^{-3}$). Theory curves are achieved with only AWGN. Solid lines: 4-OQAM modulations; dotted lines: 16-OQAM modulations.

ulation exhibits a 0.6 dB SNR penalty at the BER of 10^{-3}, whereas the 16-OQAM modulation cannot reach the 10^{-3} BER level regardless of the PN compensation algorithms. Note that, in the best design parameters set (corresponding to the lowest MSE) where the $2M = 256$ and 7 taps equalizer are used, the AML algorithm slightly outperforms the M-BPS algorithm with about 0.1 dB less SNR penalty at a BER of 10^{-3}, while the complexity of AML is lower than that of M-BPS.

In order to confirm the effectiveness of the proposed PN compensation in the laser linewidth range [10 kHz, 500 kHz] of commercial sources, we evaluate the SNR penalty to achieve a bit error rate (BER) of 10^{-3} (corresponding to the hard FEC limit) as a function of laser linewidth (Fig. 9.8). The SNRs when considering only AWGN and no transmission to achieve a BER of 10^{-3} for 4- and 16-OQAM signals are 9.8 dB and 16.7 dB, respectively, and these values are used as the benchmarks for the SNR penalty calculation. To this evaluation, the 7 taps equalizer is used to compensate for the CD after 1000 km transmission

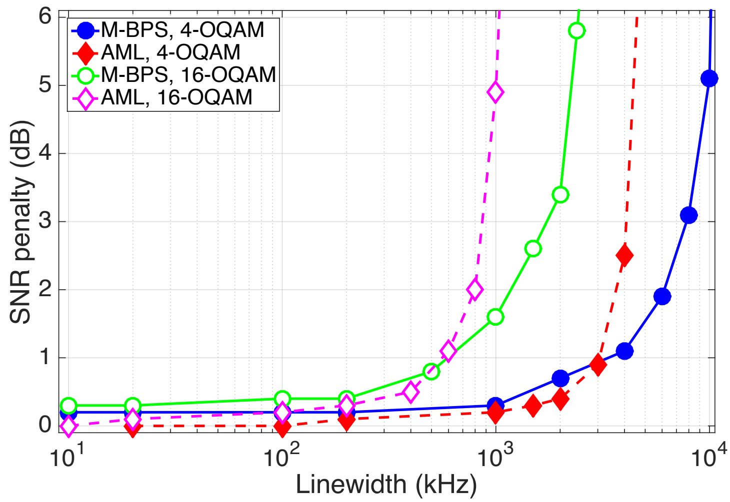

Figure 9.8 SNR penalty at a BER of 10^{-3} versus laser linewidth after 1000 km transmission. 7-tap equalizer is used. Number of subcarriers: $2M = 256$.

and $2M = 256$. The performance of AML algorithm is compared to that of M-BPS algorithm for 4- and 16-OQAM modulations. It can be seen that the AML can provide a smaller SNR penalty than the M-BPS for systems working with laser linewidths smaller than 2 MHz and 400 kHz for corresponding 4- and 16-OQAM modulations. Considering a 1-dB SNR penalty, the tolerated linewidths of AML and M-BPS are about 3 MHz and 600 kHz for 4- and 16-OQAM modulations, respectively.

A similar investigation is carried out by varying the fiber length. More specifically, we investigate the SNR penalty at a 10^{-3} BER as a function of the fiber length for 4- and 16-QAM modulations using different number of taps of the equalizer (Fig. 9.9 with $2M = 256$ and 400 kHz laser linewidth). Only AML algorithm is applied to compensate for the PN. For a 1 dB SNR penalty, the maximum reachable distances using the single-tap equalizer are 400 km and 150 km for the 4- and 16-OQAM modulations, respectively. When the 7 taps equalizer is applied, the maximum transmission distances increase to 3200 km and 1000 km for the 4- and 16-OQAM modulations, respectively. Such results confirm the

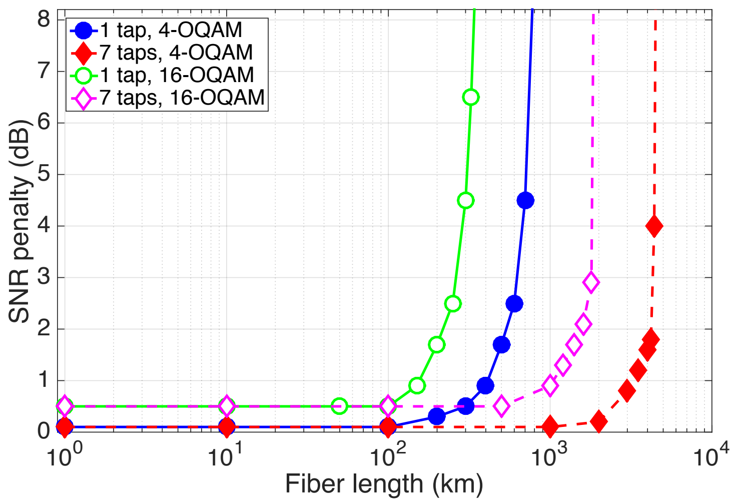

Figure 9.9 SNR penalty versus fiber length at the 10^{-3} BER for 4- and 16-OQAM signals with laser linewidth $\Delta\nu = 400kHz$ and $2M = 256$ ($\Delta\nu T = 1.7 \times 10^{-3}$).

effectiveness of the proposed algorithms for CD and PN compensation. The results shown in Figs. 9.8 and 9.9 imply that, for a fixed complexity, there is a limitation in terms of linewidth and fiber length that can be handled by the system, whatever the choice of the number of subcarriers is. The only way to improve the system performance is to go towards higher complexity receivers. It is also worthwhile to note that this is also typically the point where the performance of AML starts to degrade. However, for all practical scenarios where the impact of CD and PN is mixed, AML will be better than M-BPS.

Even though the parameters of the considered systems are suitable to the terrestrial communication links, the system design rule can easily be extended to other communication links such as submarine links.

9.6 Conclusion

We have investigated the joint CD and PN impact in optical FBMC-OQAM systems. To deal with such impairments, compensation in the frequency domain has been preferred due to its efficiency and simplicity. The first one is the multi-tap equalizer for the CD compensation and the second one is the AML algorithm for the PN compensation. The methods have been numerically validated with 4- and 16-OQAM modulations, confirming their effectiveness. We further discuss a methodology for the design of long haul FBMC-OQAM transmission systems in order to find the best trade-off between the performance of CD and PN compensation, and the complexity. It has been shown that the number of subcarriers is a critical parameter in the optimization of the system design. This investigation can be extended to different values of the fiber length and laser linewidth, providing an efficient way for system design.

Part III

Experimental study

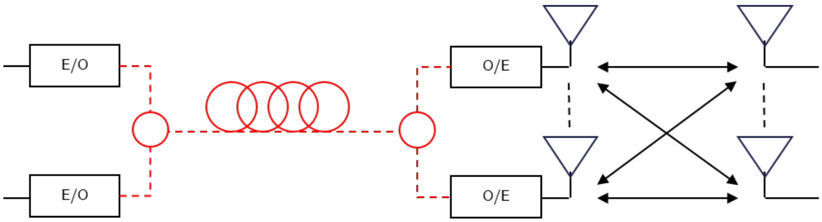

INTRODUCTION

Part III summarizes the experimental studies that were performed during the thesis. Only one contribution is included in this thesis. The others contributions to come are detailed in Section 11.2. **Chapter 10** reports on the experimental validation of a 2x2 MIMO FBMC-OQAM signal over a seamless fiber–wireless in the W-band. This work led to the following contribution:

- F. Rottenberg, P. T. Dat, T.-H. Nguyen, A. Kanno, F. Horlin, J. Louveaux, and N. Yamamoto, "2x2 MIMO FBMC-OQAM Signal Transmission over a Seamless Fiber–Wireless System in W-band," *IEEE Photonics Journal*, 2018, accepted and in press

CHAPTER 10

MIMO RADIO-OVER-FIBER SYSTEMS IN THE MILIMETER WAVE BAND

In this chapter, we first design a frame structure which is compliant with the FBMC-OQAM modulation and allows for efficient synchronization and channel estimation. The frame structure is scalable with the number of antennas and is capable of handling asynchronous UL user transmission. The proposed transceiver design is then experimentally validated in a 2x2 MIMO seamless fiber–wireless system in the W-band in both DL and UL directions. The MIMO seamless fiber-wireless system is realized using WDM intermediate frequency-over-fiber (IFoF) systems with an electrical signal up-conversion to the W-band at the RAU. At the receiver, envelope detectors are used for the signal down-conversion. The proposed system is different from previous works in [101, 102] where the authors used a multicore fiber to multiplex the streams on the optical fiber instead of WDM and where the wireless link was in the 2-GHz band instead of the W-band. Moreover, using a larger bandwidth, we achieve a data rate of up to 18 Gb/s compared to the rates of 4.42 Gb/s and 11.04 Gb/s demonstrated in [101] and [102] respectively.

In addition, we demonstrate that time domain channel estimation algorithm can provide high performance gain with respect to conventional approaches in the frequency domain. We also observed that the transmitted signals are affected by the random phase variations of local oscillators used for the signal up-conversion to the W-band at the RAU, even when the local oscillator (LO)s are synchronized by 10-MHz output and input ports. This happens when multiple LO signal sources, which are necessary for a scalable and large-scale MIMO fiber-wireless systems, are used for the signal up-conversion at RAUs, and envelope detections are used for signal down-conversion at the RRH. To compensate for the PN effects, we adopt the blind PN estimator devised in [133]. The proposed frame structure does not require the periodic transmission of pilot symbols so that the system achieves a maximal spectral efficiency. To the best of the authors knowledge, it is the first time that a MIMO FBMC-OQAM seamless fiber-wireless system in the W-band is experimentally investigated in both DL and UL directions.

The rest of this chapter is structured as follows. Section 10.1 presents a general transceiver design for MIMO FBMC-OQAM systems. Section 10.2 presents the experimental setup for MIMO signal transmission in both DL and UL directions, used to validate the proposed transceiver design. Section 10.3 provides the experimental results. Finally, Section 10.4 concludes the chapter.

10.1 Transceiver design for MIMO FBMC-OQAM systems

We consider a general MIMO FBMC-OQAM system as introduced in Section 2.1, holding both for UL and DL directions. The set of active subcarriers is denoted by $\mathcal{M}$. The number of transmitted streams is equal to S and we assume S transmit and receive antennas ($N_T = N_R = S$).

10.1.1 Preamble structure

The preamble structure is shown in Fig. 10.1 in the particular case $S = 2$. It is made of the $6 + 2S$ first OQAM symbols $\mathbf{d}_{m,l}$, which corresponds

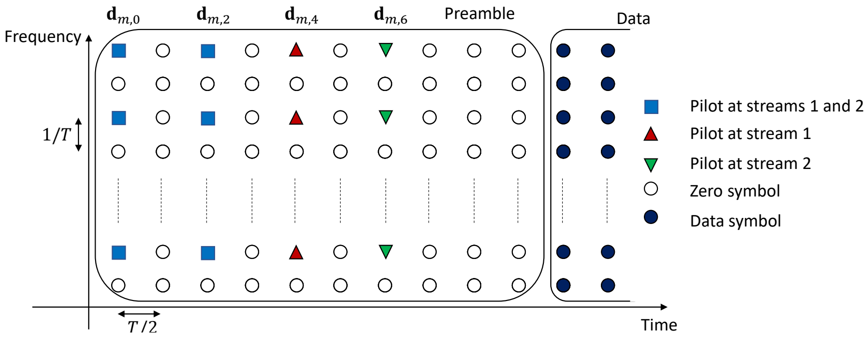

Figure 10.1 Preamble structure for $S = 2$.

to a duration of $(6 + 2S)T/2 = 3T + ST$. The preamble is constructed in order to avoid the influence of the intrinsic interference. Therefore, the 1st, 3-rd, ... $(3 + 2S)$-th odd OQAM symbols are only zeros, *i.e.*, $\mathbf{d}_{m,1} = \mathbf{d}_{m,3} = ... = \mathbf{d}_{m,3+2S} = \mathbf{0}\ \forall m$. Further, only even subcarriers are filled with pilots while the symbols on odd subcarriers are all zeros. Finally, to avoid influence from the data tones, an additional guard time of two OQAM symbols is added, *i.e.*, $\mathbf{d}_{m,4+2S} = \mathbf{d}_{m,5+2S} = \mathbf{0}\ \forall m$.

The even subcarriers of the 0-th OQAM symbol $\mathbf{d}_{m,0}$ are modulated with pseudo-randomly generated ± 1, which prevents from increasing the peak-to-average power ratio of the preamble as would be the case for interference approximation methods [33]. For synchronization purposes, the 2-nd OQAM symbol is a repetition of the first symbol, giving

$$\mathbf{d}_{m,0} = \mathbf{d}_{m,2} = \begin{cases} \begin{pmatrix} \pm 1 \\ \pm 1 \end{pmatrix} & \text{if } m \text{ is even and } m \in \mathcal{M} \\ \mathbf{0} & \text{if } m \text{ is odd or } m \notin \mathcal{M} \end{cases}.$$

For estimation purposes, the $(2 + 2s)$-th symbol is only used to estimate the s-th stream with $s = 1, 2, ..., S$. Hence, at the $(2 + 2s)$-th symbol, no pilots are transmitted on the $S-1$ streams different from s, leading to

$$\mathbf{d}_{m,2+2s} = \begin{cases} \pm 1\mathbf{e}_s & \text{if } m \text{ is even and } m \in \mathcal{M} \\ \mathbf{0} & \text{if } m \text{ is odd or } m \notin \mathcal{M} \end{cases},$$

where $\mathbf{e}_s$ is an all zero vector with a single one at the s-th row. To simplify the notations in the following, we will denote by $\mathcal{M}_p$ the set of pilot subcarriers, *i.e.*, all even subcarriers that belong to $\mathcal{M}$.

10.1.2 Synchronization

The synchronization algorithm utilizes the repetitive pattern of the 0-th and the 2-nd symbols. It can be seen as a straightforward extension of the work in [146] to the MIMO case. The algorithms work in the frequency domain, which makes the algorithms very flexible. Thanks to high spectral containment of the prototype filter, it allows for instance not to take into account some parts of the spectrum in the presence of interferers or handling asynchronous users.

The first step of the algorithm is to detect the start of the frame. This can be done by maximizing the following detection metric computed based on the AFB outputs of the two receiving antennas,

$$\xi[l] = \frac{2\left|\sum_{m\in\mathcal{M}_p} \mathbf{z}_{m,l+2}^H \mathbf{z}_{m,l}\right|}{\sum_{m\in\mathcal{M}_p} \left(\|\mathbf{z}_{m,l}\|^2 + \|\mathbf{z}_{m,l+2}\|^2\right)}.$$

Once the beginning of the frame l is detected, a first coarse CFO can be estimated by

$$\epsilon_{\text{CFO}} = \frac{1}{2\pi T} \angle \sum_{m\in\mathcal{M}_p} \mathbf{z}_{m,0}^H \mathbf{z}_{m,2}, \tag{10.1}$$

where the 0-th OQAM symbol corresponds to the first demodulated symbol of the frame. Based on the coarse CFO estimate, the CFO can be corrected in the time domain before performing a second AFB demodulation. The CFO is then re-estimated using (10.1) again. The STO is then estimated as

$$\tau_{\text{STO}} = \frac{T}{4\pi} \angle \sum_{i=\{1,2\}} \sum_{l=\{0,2\}} \sum_{\{m,m+2\} \in \mathcal{M}_p} \frac{z^{(i)*}_{m+2,l} z^{(i)}_{m,l}}{z^{(i)}_{m+2,l} z^{(i)}_{m,l}}.$$

The rest of the frame is demodulated using the refined CFO and STO estimates.

10.1.3 Channel estimation

The channel estimation relies on the transmission of the $(2+2s)$-th OQAM symbols ($s = 1, 2, ..., S$). Let us define the three following matrices

$$\begin{aligned}
\mathbf{Z}_m &= \begin{pmatrix} \mathbf{z}_{m,4} & \mathbf{z}_{m,6} & \dots & \mathbf{z}_{m,2+2S} \end{pmatrix} \in \mathbb{C}^{S \times S} \\
\mathbf{W}_m &= \begin{pmatrix} \mathbf{w}_{m,4} & \mathbf{w}_{m,6} & \dots & \mathbf{w}_{m,2+2S} \end{pmatrix} \in \mathbb{C}^{S \times S} \\
\mathbf{D}_m &= \begin{pmatrix} \mathbf{d}_{m,4} & \mathbf{d}_{m,6} & \dots & \mathbf{d}_{m,2+2S} \end{pmatrix} \in \mathbb{C}^{S \times S}.
\end{aligned}$$

Using the fact that, at the pilot positions, the intrinsic interference can be neglected thanks to the neighboring guard symbols ($\mathbf{u}_{m,l} \approx \mathbf{0}$) and assuming that the phase ϕ_l has not changed too much from the 4th to the $(2+2S)$-th symbol, we can write

$$\mathbf{Z}_m = \mathbf{H}_m \mathbf{D}_m + \mathbf{W}_m,$$

and the least squares estimate of $\mathbf{H}_m$ at the pilot positions is simply given by $\hat{\mathbf{H}}_m = \mathbf{Z}_m \mathbf{D}_m^{-1}$. This operation is very simple since $\mathbf{D}_m$ is diagonal. Note that, in theory, $\mathbf{D}_m$ is not required to be diagonal, meaning that multiple streams could be sending a pilot at the same time-frequency ressource. Other interesting designs use unitary matrices or Fourier matrices.

Still, the channel frequency response is only known at the pilot positions and the response at the non-pilot subcarriers should be interpolated. A straightforward interpolation can be done in the frequency domain by estimating the response at the non pilot subcarriers by an average of the response at the two neighboring pilot subcarriers. Another interpolation method can be conducted in the time domain. This method mainly assumes that the channel impulse response has an *a priori* known finite length L and use it to average the noise effect [147]. The specific time domain method used here is detailed in [82]. In the experiments, we will compare the frequency and time domain methods.

10.1.4 Phase tracking

The demodulated symbols can be affected by a phase rotation, which needs to be compensated for in order to avoid a phase drift. To track the phase ϕ_l, we use the MAP phase estimator derived in Chapter 7, which was straightforwardly extended to the MIMO case by combining not only all subcarriers but also the different streams of symbols. The algorithm proposed in Chapter 7 has a low complexity and is decision directed, which has the advantage of not requiring the insertion of pilots in the data frame and thus not decreasing the spectral efficiency.

10.2 Experimental setup

The transceiver design proposed in Section 10.1 is experimentally validated in a 2x2 MIMO FBMC-OQAM signal over a seamless fiber–wireless in the W-band.

The DL experimental setup is shown in Fig. 10.2(a). The 2x2 MIMO FBMC signals are generated offline in Matlab, upconverted to 5 GHz and downloaded to two synchronized arbitrary waveform generator (AWG)s. At the central station (CS), two optical signals with a frequency difference of 50 GHz from two different laser diode (LD)s are modulated independently by the generated FBMC signals at Mach-Zehnder

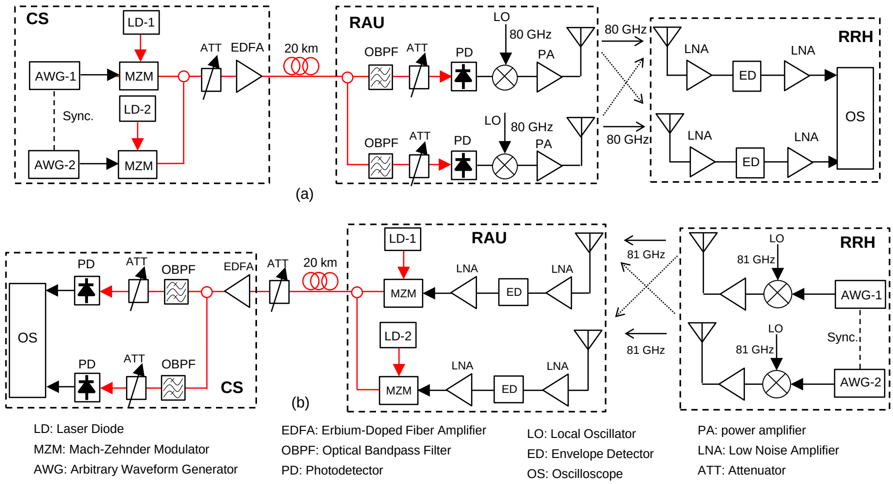

Figure 10.2 Experimental setup.

modulator (MZM)s. The modulated optical signals are combined by an optical coupler (OC) and inputted into an attenuator (ATT) to adjust the transmit power. The signals are then amplified by an optical amplifier (EDFA) and transmitted to a RAU via a 20-km SSMF. The received optical signals are separated into two branches by a 3-dB OC. At each branch, the optical signals are filtered by optical bandpass filters (OBPFs) to recover the transmitted modulated optical signals. After being converted to electrical domain by photodetector (PD)s, the recovered signals at the intermediate frequency are up-converted to 80 GHz using electronic balanced mixers and LOs. In our experiment, for the sake of simplicity, the LO signals are generated by synthesizers and frequency up-converters at the RAU. However, to simplify the RAU, these LO signals can be delivered remotely from the CS using photonic technologies for generating and transmitting the LO signals [100]. The up-converted signals in the W-band are amplified by power amplifier (PA)s before being emitted into free space by two 23-dBi horn antennas. After being transmitted over a 1-m free-space link, the signals are received by another two horn antennas at the RRH. The received signals are amplified by low-noise amplifier (LNA)s in the W-band, and down-converted to the original signals by envelope detectors (EDs). The recovered signals are then amplified by LNAs in the microwave band and connected to a real-time oscilloscope (OS). Finally, the signals are sent to a personal computer and demodulated offline in Matlab.

The UL experimental setup is shown in Fig. 10.2(b). Similar to the DL direction, 2x2 MIMO FBMC signals are generated offline in Matlab, upconverted to 4.3 GHz and downloaded to two AWGs. All parameters of the signals are the same as in the downlink direction. The generated FBMC signals are up-converted to the W-band (81 GHz) using two electrical balanced mixers and LO sources. The up-converted signals are amplified by PAs before being transmitted into free space by horn antennas. The signals are transmitted over the same 1-m free-space link as in the DL, and received by two horn antennas at the RAU. The signals are then amplified by LNAs before being coupled into two EDs for down-converting to the originally transmitted FBMC signals. The signals are then amplified by LNAs in the microwave band before modulating optical signals from two different LDs at two MZMs for conversion to optical signals. The modulated optical signals are combined by a 3-dB OC and transmitted to the CS by a 20-km SMF as in the DL. At the CS, the optical signals are amplified by an EDFA and separated into two branches by a 3-dB OC. The optical signal in each branch is then inputted to an OBPF to recover the transmitted optical signals. The received optical signals are converted to the original 2x2 MIMO FBMC signals by two PDs. Finally, the recovered signals are connected to the real-time OS and demodulated offline in Matlab.

In the experiment, to demonstrate a scalable system that can be applied for the signal transmission over a large-scale MIMO fiber-wireless system, we use a WDM IFoF system for optical links. Different electrical LO signal sources are also used for the signal up-conversion at the RAU. One should note that this system demonstration meets the general assumptions that were made in Section 10.1 on the channel variations in

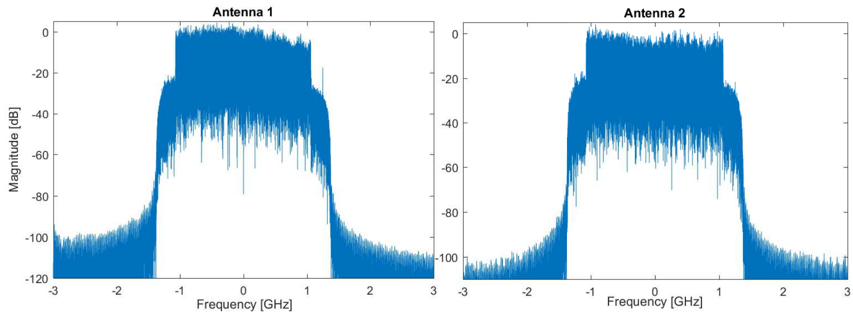

Figure 10.3 Downlink received baseband spectrum of received signals at antennas 1 and 2, $1/T_s = 2500$ MBd.

the time and frequency domains. Indeed, the link is relatively static and does not change fast over time, except for relatively slow changes due to PN. In our system, the two electrical LOs used for signal up-conversion to W-band are synchronized. However, there is still some difference in the phases of the oscillators, resulting in the presence of phase noise. Further, since the optical link is made of a few tens of kilometers and the system bandwidth is of the order of the GHz, the dispersion effect of the fiber remains quite limited. Furthermore, the millimeter-wave link is mainly composed of line-of-sight components and does not suffer much from multipath fading, resulting in slow variations of the channel in frequency, as will be further demonstrated in the next section.

10.3 Experimental results

This section aims at demonstrating and evaluating the performance of the 2x2 MIMO FBMC-OQAM fiber–wireless system using the proposed transceiver design. The number of subcarriers is fixed to 512, if not stated otherwise. Out of all subcarriers, 5% on each edge of the spectrum are left inactive. The prototype filter is the Phydyas pulse [6] with overlapping factor $\kappa = 4$. The constellation is a 16-QAM. Five values of the Baud rate are considered for the system, *i.e.*, $1/T_s = 500$ MBd, $1/T_s = 1000$ MBd, $1/T_s = 1600$ MBd, $1/T_s = 2000$ MBd and $1/T_s = 2500$

MBd. The total bit rate can then be computed as

$$\mathrm{R} = \overbrace{2}^{\text{Number of streams}} \times \underbrace{4}_{\text{16-QAM}} \overbrace{\lfloor 0.9M \rfloor}^{\text{Active subcarriers}} \underbrace{\frac{1}{MT_s}}_{\text{Inverse of symbol period}} \quad \text{[bps]}.$$

In numbers, this gives 3.6, 7.2, 11.6, 14.4 and 18 Gb/s for the 500, 1000, 1600, 2000 and 2500 MBd systems respectively. The downlink received baseband spectrum of received signals at antennas 1 and 2 are shown in Fig. 10.3. The polarization of the transmit and receive antennas can be chosen to be the same or different between each stream, to avoid inter-antenna interference. The MSE, expressed in dB, is used as the main figure of merit and is defined as

$$\mathrm{MSE} = \mathbb{E}\|\hat{\mathbf{d}}_{m,l} - \mathbf{d}_{m,l}\|^2 \quad \text{[dB]},$$

where the expectation is taken over all symbols transmitted in time and frequency.

10.3.1 Synchronization

In Fig. 10.4, the magnitudes of the received baseband signals for the two streams are plotted after downconversion to baseband. The AWGs were generating the same frame periodically. The preamble section of the frame can be clearly identified. The detection metric detailed previously using the signals of the two receiving antennas leads to a sharp peak to jointly estimate the start of the frame. Note that the two smaller following peaks are due to the following pilot symbols aimed at channel estimation, as was shown in the preamble structure in Fig. 10.1.

Fig. 10.5 plots the MSE in DL and UL directions by switching on or off the CFO correction. As can be seen, the performance is similar and hence, we see that the system is not sensitive to CFO. This makes sense since the receiver is non coherent and that the electrical oscillators at

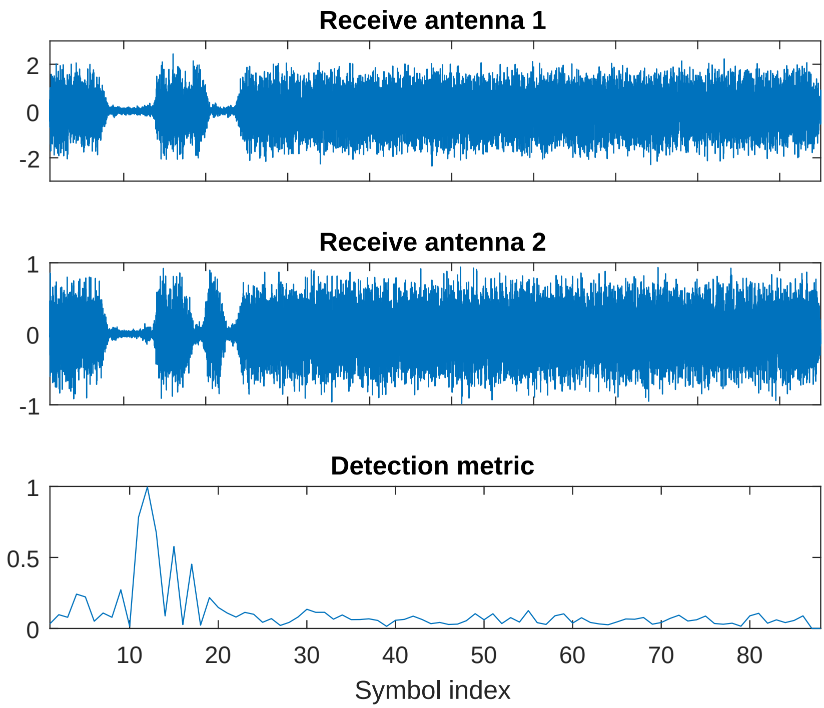

Figure 10.4 Baseband received signals and detection metric for antennas with different polarization in downlink and $1/T_s = 1000$ MBd.

the RAU are synchronized, as explained in Section 10.2. Therefore, the system does not require the CFO correction algorithm, which simplifies the receiver implementation.

10.3.2 Channel estimation

In Fig. 10.6, the MSE of the uplink system is plotted for the two channel estimation interpolation methods and for two different Baud rates. The horizontal axis of Fig. 10.6 corresponds to the channel impulse response length L, which needs to be fixed for the time domain interpolation method. The MSE reaches a minimum for a particular value of L. Indeed, for too small values, missing taps of the channel are not estimated while for too large values, more taps than the actual channel length are

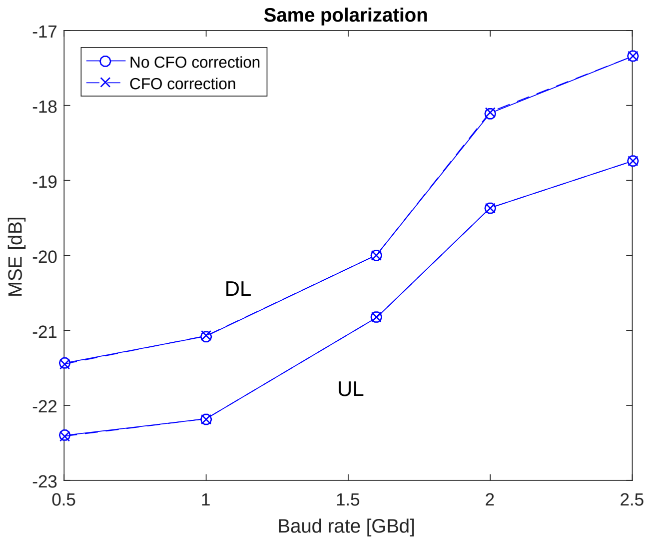

Figure 10.5 The system performance with and without using CFO compensation.

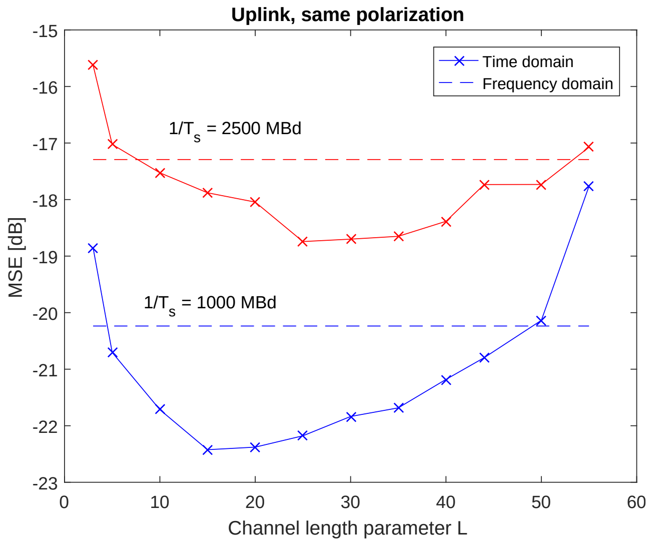

Figure 10.6 Time domain versus frequency domain channel estimation and $1/T_s = 1000$ MBd.

estimated, resulting in a larger sensitivity to noise. One can note that the minimum value of the MSE for the 2500 MBd system corresponds

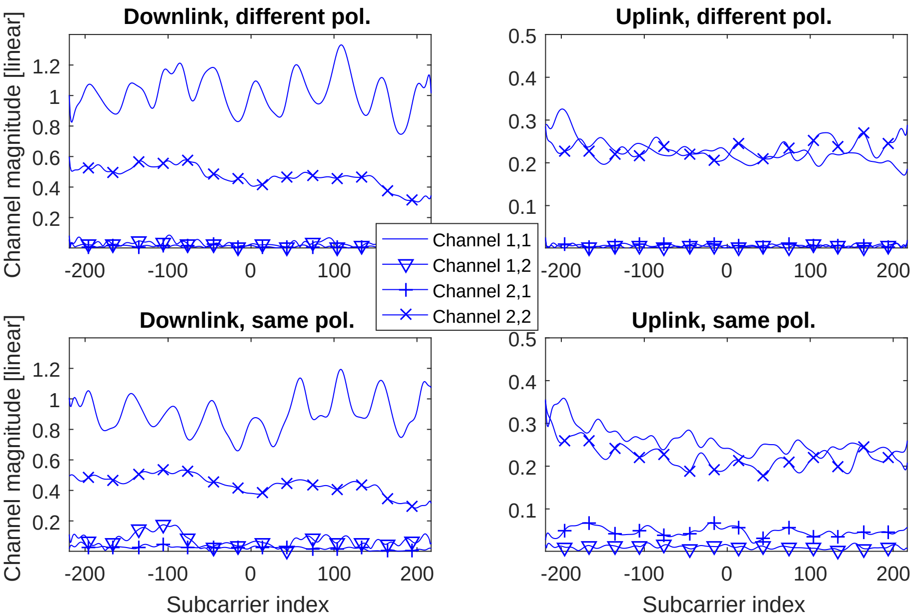

Figure 10.7 Channel frequency response between each pair of transmitted and received streams and $1/T_s = 1000$ MBd.

to an approximately 2.5 times larger value of L than for the 1000 MBd. This makes sense since the sampling frequency $1/T_s$ is 2.5 higher. On the other hand, the frequency domain method does not depend on any parameter. For most values of L, the time domain method is more performant than the frequency domain method. The gain comes from the averaging of the noise. Indeed, all pilot subcarriers outputs are combined to jointly estimate the time domain coefficients. In the following simulations, the time domain interpolation method was used with the parameter L fixed to the value of 25.

Fig. 10.7 plots the channel frequency response evaluated at each active subcarrier and for each pair of streams. As can be seen in the upper subfigures, when the polarization of the antennas is different for each stream, there is almost no inter-stream interference while it is stronger for the same polarization. An interesting observation is to see

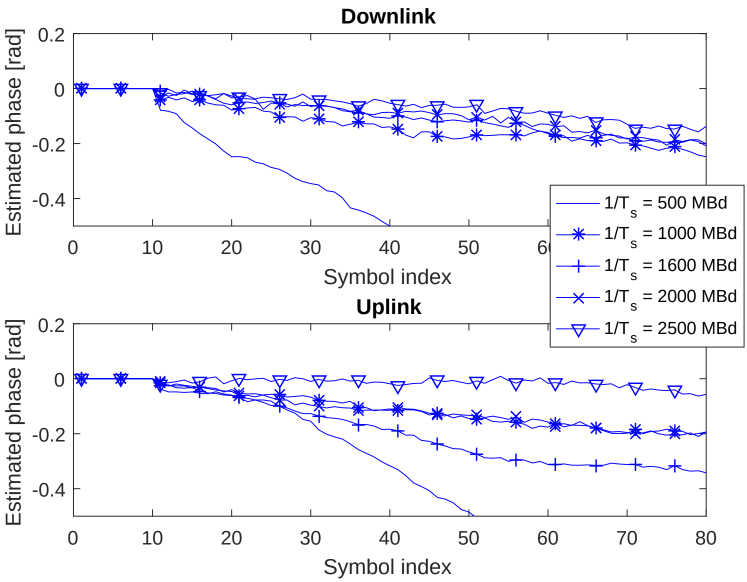

Figure 10.8 Evolution of the estimated phase as a function of time (same polarization).

that one interfering channel is almost null. This can be explained by the position of the antennas and their quite directive pattern.

10.3.3 Phase tracking

In our system, even though EDs are used for the signal down-conversion at the RRHs, some phase noise is observed in the received signals. This is due to the fact that when the antennas are placed closed to each other, the LO signal component, which is much larger than the mixed sideband signals, from one transmit antenna will leak to the other receive antenna and vice versa. As a result, the LO signal components of the input signal to the EDs at RRHs are the sum of the corresponding LO signal from the transmit antenna and the leaked LO signal from the other transmit antenna. Because the frequency of the LOs are same, the LO signals will be added up and the phase of the LO signal component to each ED

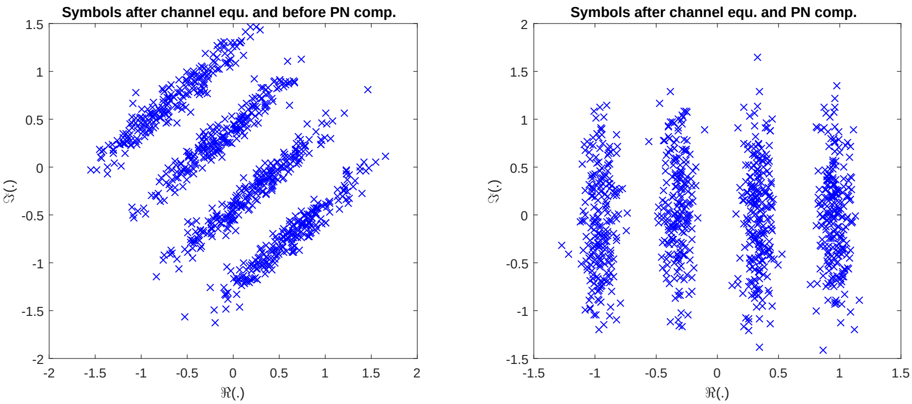

Figure 10.9 Constellation plot of the demodulated symbols at one multicarrier symbol after channel equalization and before/after PN compensation for same antenna polarization, DL and $1/T_s = 500$ MBd.

is the summed phases from different LOs. This explains why the PN compensation is still needed in our system. We should note that, when one common LO signal is used for the MIMO signal up-conversion to many antennas, the observed PN drift might not exist. However, for a large-scale MIMO system, the use of multiple LO signal sources are necessary due to the limited output power from one single LO signal generator.

Fig. 10.8 shows the estimated phase as a function of the symbol in time for different system Baud rates. In Fig. 10.9, the constellation of the demodulated symbols $\mathbf{z}_{m,l}$ is plotted after channel equalization and before/after PN compensation. Note that, in the FBMC-OQAM modulation, the QAM symbols are mapped to PAM purely real symbols. After demodulation, if the channel and PN are perfectly compensated for, we should retrieve the purely real transmitted symbols impacted by purely imaginary intrinsic interference, *i.e.*, $\mathbf{d}_{m,l} + \jmath \mathbf{u}_{m,l}$. Clearly, Fig. 10.8 and 10.9 show that a phase drift is present and it induces a rotation of the symbols before the real conversion. This phase rotation needs to be compensated for to avoid leakage of the intrinsic interference on the purely real transmitted symbol. Furthermore, we can see in the right

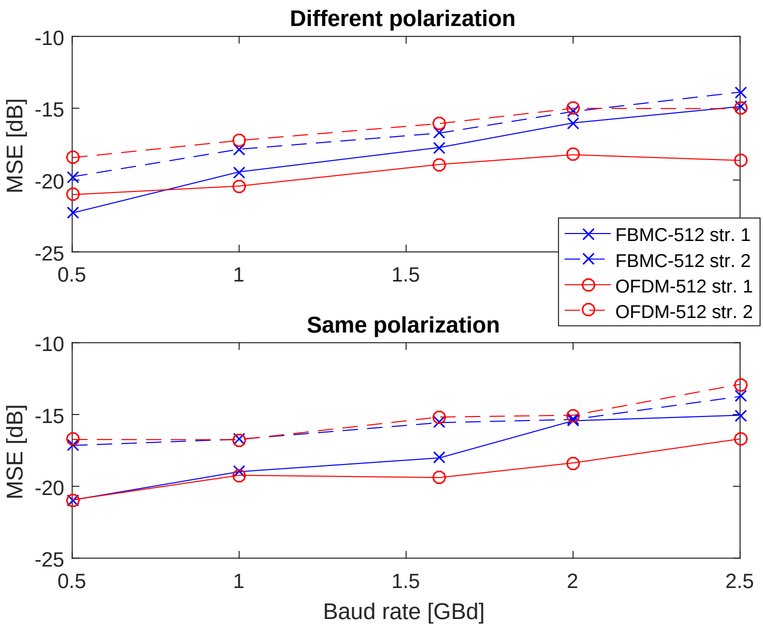

Figure 10.10 Downlink MSE of each stream as a function of the system rate for FBMC and OFDM modulations and 512 subcarriers.

figure that the PN compensation algorithm succeeds in correcting the phase drift so that the purely imaginary intrinsic interference will be completely removed after real conversion.

10.3.4 Comparison with OFDM

Fig. 10.10 plots the downlink MSE of each stream as a function of the system Baud rate for FBMC and OFDM modulations and 512 subcarriers. For the OFDM modulation, a similar frame structure was considered with a preamble designed for synchronization and channel estimation. The cyclic prefix was fixed to one fourth of the symbol period. This implies that the FBMC throughput is 25% higher than the OFDM one, as shown in Table 10.1. As one can see, the two modulations perform similarly in terms of MSE. The performance slightly degrades as the Baud rate increases. As could be expected from Fig. 10.7, stream 1 has

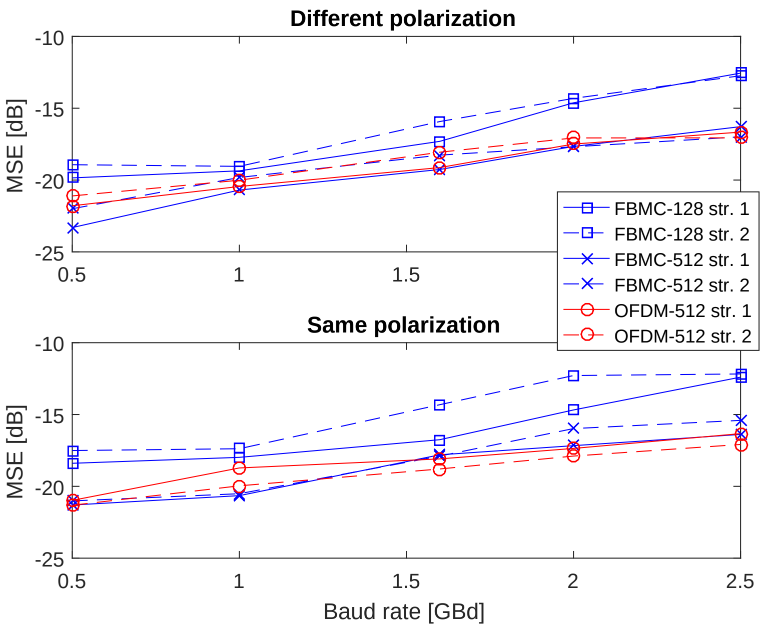

Figure 10.11 Uplink MSE of each stream as a function of the system rate for FBMC and OFDM modulations and 512/128 subcarriers.

Baud rate $1/T_s$	FBMC-OQAM bit rate	CP-OFDM bit rate
500 MBd	3.6 Gb/s	2.9 Gb/s
1000 MBd	7.2 Gb/s	5.8 Gb/s
1600 MBd	11.6 Gb/s	9.2 Gb/s
2000 MBd	14.4 Gb/s	11.5 Gb/s
2500 MBd	18 Gb/s	14.4 Gb/s

Table 10.1 Throughput comparison between FBMC-OQAM and CP-OFDM systems.

a relatively better performance since its channel frequency response is stronger.

Fig. 10.11 plots the corresponding figure as Fig. 10.10 in the uplink with the additional performance of a FBMC system having 128 subcarriers. OFDM and FBMC again perform similarly for 512 subcarriers. The FBMC performance is degraded for the lower number of subcarriers 128. This can be explained by the fact that the channel becomes relatively more selective in frequency. In this case, the channel estimation and equalization algorithms become less efficient. From this observation, an optimal number of subcarriers should be chosen to optimize the system performance.

10.4 Conclusion

In this chapter, we proposed a general framework for MIMO FBMC-OQAM transmission systems, including the description of algorithms for mitigation of the channel impairments. The proposed system is scalable in the number of transmitted streams and flexible as multiple asynchronous users can be accommodated. The transceiver chain is experimentally validated in a 2x2 MIMO seamless fiber–wireless system in the W-band. The system uses a high spectral efficiency WDM IFoF for MIMO signal transmission in the optical links, and an electrical up-conversion at the RAU. Satisfactory performance is confirmed for a data rate of up to 18 Gb/s in both DL and UL directions. We also observed that even though a simple intensity modulation and direct detection method is used, there is some phase drift in the received signals when multiple LO signal sources are used. This is due to the leakage of the local oscillators and the difference in the phase variations of the LOs. Our proposed system can be very useful for high spectral efficiency seamless fiber-wireless mobile fronthaul system and/or for transmission of large-scale MIMO mobile signals in the high frequency bands over a fiber optic fronthaul system.

CHAPTER 11

CONCLUSIONS

This chapter first summarizes the main contributions of this thesis and secondly enumerates perspectives for future works.

11.1 Summary

The contributions of this thesis are organized in three parts. **Part I** addresses channel equalization in MIMO FBMC-OQAM wireless systems. The different works presented in Part I rely on a Taylor approximation of the channel variations in the frequency and/or time domains. Part I is composed of four contributions.

Chapter 3 investigates the design of optimized single-tap equalizers and pre-equalizers for a MU-MIMO FBMC-OQAM scenario under highly frequency selective channel. The proposed single-tap equalization structure has a very low implementation complexity. The optimized (pre-)equalizers minimize the MSE of the symbol estimates under either a ZF criterion or a MMSE criterion. It is shown that, as soon as the BS has more antennas than the number of users, the optimized (pre)-equalizers can use those extra degrees of freedom to compensate for the distortion induced by channel frequency selectivity. In the asymptotically high SNR regime, the first order approximation of the distortion can be completely removed if the BS has at least twice as many antennas as the number of users.

Chapter 4 studies the performance of an FBMC-OQAM uplink massive MIMO system in terms of the MSE of the decoded symbols. Three types of single-tap equalizers are considered, namely, a ZF, a LMMSE and a MF. Using random matrix theory, the MSE is asymptotically characterized as the number of BS antennas N and the number of users K grow large, while keeping a finite ratio N/K. The obtained expressions allow to draw many conclusions. First, the MSE becomes uniform across the frequency band as a result of the channel hardening effect. Secondly, it is shown that a good synchronization of the users is crucial in a massive MIMO scenario. Finally, if the users are well synchronized, the different terms that compose the MSE, such as noise, IUI, ICI and ISI become negligible for large values of the ratio N/K.

Chapter 5 studies the effect of both time and frequency selectivity of the channel on a PTP MIMO FBMC-OQAM system. A parallel equalization structure that can compensate for the doubly dispersive nature of the channel is proposed and a theoretical approximation of the remaining distortion after equalization is given.

In **Chapter 6**, a very simple PTP MIMO equalization structure is proposed for doubly selective channels based on a simple single-tap per-subcarrier equalizer. This receiver exploits the degrees of freedom offered by the extra antennas at the receiver to compensate for the distortion induced by the time and frequency selectivity of the channel. Chapter 6 can be seen as an extension of Chapter 3 to doubly selective channels.

The compensation of PN and CD in FBMC-OQAM optical fiber systems is addressed in **Part II**, composed of three main contributions.

Chapter 7 addresses PN estimation and compensation. Two new estimators are proposed, namely, an ML estimator and a MAP estimator. Simulation results demonstrate that the proposed estimators outperform state of the art solutions in the low SNR regime and for a small number of subcarriers, with a reduced implementation complexity.

Chapter 8 investigates the performance of advanced CD compensation methods. We show that several equalization structures, initially proposed for wireless FBMC-OQAM systems, can also be applied to optical FBMC-OQAM systems to compensate efficiently for the CD effect. The different algorithms are compared in terms of performance and complexity of implementation.

Chapter 9 investigates the joint compensation of CD and PN in FBMC-OQAM optical fiber systems. The PN and CD compensation algorithms are designed to work in the frequency domain, which allows for a simple and efficient implementation. We further discuss a methodology for the design of long haul FBMC-OQAM transmission systems in order to find the best trade-off between CD and PN compensation, and the complexity.

Part III summarizes the experimental studies that were performed during the thesis. Only one contribution is included in this thesis. The others contributions to come are detailed in Section 11.2. In **Chapter 10**, a general framework for MIMO FBMC-OQAM transmission systems is first proposed. The proposed system is experimentally validated in a 2x2 MIMO FBMC-OQAM system over a seamless fiber–wireless link in the W-band for the first time. Satisfactory performance is confirmed for a data rate of up to 18 Gb/s in both downlink and uplink directions.

11.2 Perspectives

The asymptotic approach initially proposed in [53] is an efficient and powerful tool to model highly time and/or frequency selective channels in FBMC-OQAM systems. As we showed in **Part I**, the approach can be generalized and applied to various scenarios. Still, there remain many perspectives to be explored. We draw here below some of them:

- **Chapter 3** considered the optimization of single-tap pre-equalizers in the DL and single-tap equalizers in the UL. The optimization was made easier by assuming that the users are equipped with one single antenna and are not able to cooperate. In other words, the optimization is performed only at one side of the link, which makes the problem quadratic in matrices $\mathbf{A}_m$ or $\mathbf{B}_m$. A very interesting extension is to investigate the joint design of pre-equalizing and equalizing matrices at transmit and receive sides respectively, assuming full coordination. In other words, one should optimize the MSE formula in (3.1) with respect to matrices $\mathbf{A}_m$ and $\mathbf{B}_m$. This problem is not quadratic anymore and much more challenging to solve.

- **Chapter 4** only considered the massive MIMO performance in the UL. The DL performance is more complex to study due to the dependence of the asymptotic MSE formula (3.1) in the derivative of the pre-equalizer $\mathbf{A}_m^{(1)}$, modeling the fact that the performance at subcarrier m also depends on the pre-equalizers at neighboring subcarriers. Still, through simulations, we found out that the performance in UL and DL is similar even though we could not mathematically prove it. Furthermore, we did not consider the effect of pilot contamination, which is one of the main limitations in such systems. This also needs to be further investigated. Moreover, we restricted the analysis to frequency selective channels. We are convinced that the observed self-equalization effect can be extended to doubly selective channels. In that case, it would mean that increasing the ratio N/K would be beneficial to cancel the distortion coming from both types of selectivity.

- **Chapter 5** proposed a parallel equalization structure at the receiver side. A similar approach could be implemented at the transmitter side, in order to implement a pre-equalizer robust to time and frequency selectivity, as was done in [55] for the frequency selective case only. Moreover, in general, the equalizer should not be constrained to invert the channel and more general designs such as MMSE receivers are possible.

- **Part I** focused on the channel equalization task, assuming that the channel was perfectly known, which is a common assumption. In practice, channel estimation algorithms should be designed taking into account the effect of the intrinsic interference. This is particularly challenging in the presence of high channel time and frequency selectivity. One perspective is to use the asymptotic approach to improve the channel estimation performance in the case of highly selective channels. The authors in [77] already extended the auxiliary pilot scheme for the case of strongly frequency selective channels. We are now investigating the extension to doubly selective channels.

- The asymptotic approach considered in **Part I** was only applied to FBMC-OQAM systems. We could investigate if the same approach can be applied to other types of waveforms such as CP-OFDM, filtered OFDM, generalized frequency division multiplexing...

- The various Taylor approximations made in **Part I** allowed for an intuitive and efficient analysis of the linear impairments of the channel, namely, time and frequency selectivity. An extension would be to consider the same type of approximations to model non-linear distortion coming for instance from clipping, PA's, PD's...

The research on the application of the FBMC-OQAM modulation to optical fiber communications has only started recently. The different works detailed in **Part II** need more investigation in several directions:

- One main assumption in **Part II** was that the PN was assumed to be constant over one symbol transmission duration. As we showed, this has a direct limitation on the number of subcarriers that can be used in the system. Hence, the use of more complex CD algorithms should be considered. An alternative is to no longer assume that the PN is constant over one symbol duration, which would allow to use a larger number of subcarriers (or lasers with larger linewidth). Then, more advanced PN compensation algorithms should be designed.

This can be done with the parallel equalization structure proposed in Chapter 5 as PN can be seen as a special case of time selectivity. Another possibility is to compensate for the PN in the time domain before the AFB. However, these solutions will require to design new PN tracking methods.

- Only the PN and CD impairments were considered in **Part II**. However, other major impairments such as polarization mode dispersion and non linear effects need more investigation.

The results shown in **Part III** are only the first that we formalized. We are now preparing the following experiments:

- A long-haul optical fiber testbed is currently under construction at the *Université libre de Bruxelles*. We expect to experimentally validate the theoretical studies performed in **Part II**.

- One of the advantages of the experimental setup in **Chapter 10** is its simplicity, relying on direct detection. Direct detection allows for simple baseband conversion of the received signal, which suffers from low PN. However, direct detection imposes limitations on the bandwidth of the transmitted signal. An alternative is to use coherent detection at the receiver. This allows for communication with much larger bandwidth. However, the required laser at the receiver may induce large PN, which may require more advanced compensation methods. Experiments are under preparation at the *National Institute of Information and Communications Technology* to investigate the effect of PN on RoF systems, relying on coherent detection.

- The visible light communication (VLC) systems rely on the light to support wireless data transmission [148]. The approach has been considered as a promising solution for indoor communications. The FBMC-OQAM modulation has already been investigated for VLC [149, 150]. During my stay at the *National Institute of Information and*

Communications Technology, we performed measurements on such setups. The originality of the work is the use of an organic light emitting diode (OLED) rather than a conventional light emitting diode (LED). An OLED has a better performance in terms of luminous and power efficiency [151]. It is now being commercialized from companies such as LG and Philips. However, one limitation of an OLED is its narrower modulation bandwidth. To deal with this, we used the combination of a pre-emphasis circuit and per-subcarrier bit allocation. We are now discussing about new experiments to corroborate our results.

List of publications

Book chapter:

- M. Haardt, Y. Cheng, **F. Rottenberg**, J. Louveaux, E. Kofidis, "FBMC Distributed and Cooperative Systems," in *Orthogonal Waveforms and Filter Banks for Future Communication Systems*, Elsevier Ltd. 2017.

Articles published in peer-reviewed journals (6):

- **F. Rottenberg**, X. Mestre, F. Horlin and J. Louveaux, "Single-Tap Precoders and Decoders for Multi-User MIMO FBMC-OQAM under Strong Channel Frequency Selectivity," *IEEE Transactions on Signal Processing*, 2017, vol. 65, no. 3, pp. 587-600.

- T.-H. Nguyen, **F. Rottenberg**, S.-P. Gorza, F. Horlin and J. Louveaux, "Efficient Chromatic Dispersion Compensation and Carrier Phase Tracking for Optical Fiber FBMC/OQAM Systems," *IEEE/OSA Journal of Lightwave Technology*, 2017, vol. 35, no. 14, pp. 2909-2916.

- **F. Rottenberg**, X. Mestre, D. Petrov, F. Horlin and J. Louveaux, "Parallel Equalization Structure for MIMO FBMC-OQAM Systems under Strong Time and Frequency Selectivity," *IEEE Transactions on Signal Processing*, 2017, vol. 65, no. 17, pp. 4454-4467.

- **F. Rottenberg**, T.-H. Nguyen, S.-P. Gorza, F. Horlin and J. Louveaux, "Advanced Chromatic Dispersion Compensation in Optical Fiber FBMC-OQAM Systems," *IEEE Photonics Journal*, 2017, vol. 9, no. 6, pp. 1–10.

- **F. Rottenberg**, X. Mestre, F. Horlin and J. Louveaux, "Performance Analysis of Linear Receivers for Uplink Massive MIMO FBMC-OQAM Systems," *IEEE Transactions on Signal Processing*, 2018, vol. 66, no. 3, pp. 830–842.

- **F. Rottenberg**, P. T. Dat, T.-H. Nguyen, A. Kanno, F. Horlin, J. Louveaux and N. Yamamoto, "2x2 MIMO FBMC-OQAM Signal Transmission over a Seamless Fiber–Wireless System in W-band," *IEEE Photonics Journal*, 2018, accepted and in press.

Articles published in peer-reviewed conference proceedings (10):

- **F. Rottenberg** and J. Louveaux, "Dominant eigenmode transmission in MIMO FBMC for frequency selective channels." In *Joint WIC/IEEE Symposium on Information Theory and Signal Processing in the Benelux*, 2014, Eindhoven.

- M. Navaux, **F. Rottenberg** and J. Louveaux, "Phase synchronisation for FBMC/OQAM fiber-optic transmissions." In *Joint WIC/IEEE Symposium on Information Theory and Signal Processing in the Benelux*, 2015, Bruxelles.

- **F. Rottenberg**, K. Degraux, L. Jacques and J. Louveaux, "Pilots allocation for sparse channel estimation in multicarrier systems." In *Joint WIC/IEEE Symposium on Information Theory and Signal Processing in the Benelux*, 2015, Bruxelles.

- **F. Rottenberg**, Y. Medjahdi, E. Kofidis and J. Louveaux, "Preamble-based channel estimation in asynchronous FBMC-OQAM distributed MIMO systems." In *IEEE 12th International Symposium on Wireless Communications Systems (ISWCS)*, 2015, Bruxelles.

- **F. Rottenberg**, X. Mestre and J. Louveaux, "Optimal zero forcing precoder and decoder design for multi-user MIMO FBMC under strong channel selectivity." In *The 41st IEEE International Conference on Acoustics, Speech and Signal Processing (ICASSP)*, 2016, Shanghai.

- **F. Rottenberg**, F. Horlin, E. Kofidis and J. Louveaux, "Generalized optimal pilot allocation for channel estimation in multicarrier systems." In *IEEE 17th International Workshop on Signal Processing Advances in Wireless Communications (SPAWC)*, 2016, Edinburgh.
- X. Mestre, **F. Rottenberg**, M. Navarro, "Linear receivers for massive MIMO FBMC/OQAM under strong channel frequency selectivity." In *IEEE Workshop on Statistical Signal Processing (SSP)*, 2016, Palma de Mallorca.
- **F. Rottenberg**, X. Mestre, F. Horlin and J. Louveaux, "Single-tap equalizer for MIMO FBMC systems under doubly selective channels." In *The 42st IEEE International Conference on Acoustics, Speech and Signal Processing (ICASSP)*, 2017, New Orleans.
- T.-H. Nguyen, **F. Rottenberg**, S.-P. Gorza, F. Horlin and J. Louveaux, "Extended Kalman filter for carrier phase recovery in optical filter bank multicarrier offset QAM systems." In *Optical Fiber Communication Conference (OFC)*, 2017, Los Angeles.
- **F. Rottenberg**, T.-H. Nguyen, S.-P. Gorza, J. Louveaux and F. Horlin, "ML and MAP phase noise estimators for optical fiber FBMC-OQAM systems." In *IEEE International Conference on Communications (ICC)*, 2017, Paris.

References

[1] M. Shafi, A. F. Molisch, P. J. Smith, T. Haustein, P. Zhu, P. De Silva, F. Tufvesson, A. Benjebbour, and G. Wunder, "5G: A Tutorial Overview of Standards, Trials, Challenges, Deployment, and Practice," *IEEE Journal on Selected Areas in Communications*, vol. 35, no. 6, pp. 1201–1221, 2017.

[2] J. G. Andrews, S. Buzzi, W. Choi, S. V. Hanly, A. Lozano, A. C. K. Soong, and J. C. Zhang, "What Will 5G Be?," *IEEE Journal on Selected Areas in Communications*, vol. 32, pp. 1065–1082, June 2014.

[3] Q. Wu, G. Y. Li, W. Chen, D. W. K. Ng, and R. Schober, "An overview of sustainable green 5G networks," *IEEE Wireless Communications*, vol. 24, no. 4, pp. 72–80, 2017.

[4] F. Boccardi, R. W. Heath, A. Lozano, T. L. Marzetta, and P. Popovski, "Five disruptive technology directions for 5G," *IEEE Communications Magazine*, vol. 52, pp. 74–80, February 2014.

[5] Y. G. Li and G. L. Stüber, *Orthogonal Frequency Division Multiplexing for Wireless Communications*. Springer Science & Business Media, 2006.

[6] M. G. Bellanger, "Specification and design of a prototype filter for filter bank based multicarrier transmission," in *IEEE International Conference on Acoustics, Speech, and Signal Processing*, vol. 4, pp. 2417–2420, IEEE, 2001.

[7] B. Farhang-Boroujeny, "OFDM versus filter bank multicarrier," *IEEE Signal Processing Magazine*, vol. 28, pp. 92 – 112, May 2011.

[8] M. Bellanger, D. Le Ruyet, D. Roviras, M. Terré, J. Nossek, L. Baltar, Q. Bai, D. Waldhauser, M. Renfors, T. Ihalainen, *et al.*, "FBMC physical layer: a primer," *PHYDYAS, January*, 2010.

[9] A. Aminjavaheri, A. Farhang, A. RezazadehReyhani, and B. Farhang-Boroujeny, "Impact of timing and frequency offsets on multicarrier waveform candidates for 5G," in *2015 IEEE Signal Processing and Signal Processing Education Workshop (SP/SPE)*, pp. 178–183, Aug 2015.

[10] F. Rottenberg, Y. Medjahdi, E. Kofidis, and J. Louveaux, "Preamble-based channel estimation in asynchronous FBMC-OQAM distributed MIMO systems," in *2015 IEEE International Symposium on Wireless Communication Systems (ISWCS)*, pp. 566–570, Aug 2015.

[11] A. I. Pérez-Neira, M. Caus, R. Zakaria, D. L. Ruyet, E. Kofidis, M. Haardt, X. Mestre, and Y. Cheng, "MIMO Signal Processing in Offset-QAM Based Filter Bank Multicarrier Systems," *IEEE Trans. Signal Process.*, vol. 64, pp. 5733–5762, Nov 2016.

[12] M. Renfors, T. Ihalainen, and T. H. Stitz, "A block-Alamouti scheme for filter bank based multicarrier transmission," in *2010 European Wireless Conference (EW)*, pp. 1031–1037, April 2010.

[13] R. Zakaria and D. L. Ruyet, "On interference cancellation in Alamouti coding scheme for filter bank based multicarrier systems," in *ISWCS 2013; The Tenth International Symposium on Wireless Communication Systems*, pp. 1–5, Aug 2013.

[14] M. Bellanger, "Efficiency of Filter Bank Multicarrier Techniques in Burst Radio Transmission," in *2010 IEEE Global Telecommunications Conference GLOBECOM 2010*, pp. 1–4, Dec 2010.

[15] J. Yli-Kaakinen and M. Renfors, "Optimized burst truncation in fast-convolution filter bank based waveform generation," in *2015 IEEE 16th International Workshop on Signal Processing Advances in Wireless Communications (SPAWC)*, pp. 71–75, June 2015.

[16] M. J. Abdoli, M. Jia, and J. Ma, "Weighted circularly convolved filtering in OFDM/OQAM," in *2013 IEEE 24th Annual International Symposium on Personal, Indoor, and Mobile Radio Communications (PIMRC)*, pp. 657–661, Sept 2013.

[17] R. Balian, "Un principe d'incertitude fort en théorie du signal ou en mécanique quantique," *Compt. Rend. Acad. Sci. Ser. II*, vol. 292, pp. 1357–1362, 1981.

[18] F. Low, "Complete sets of wave packets," in *A Passion for Physics – Essay in Honor of Geoffrey Chew*, p. 17–22, Jun. 1985.

[19] P. Siohan and M. Renfors, "Orthogonal Communication Waveforms," in *Orthogonal Waveforms and Filter Banks for Future Communication Systems*, Elsevier Ltd., 2017.

[20] A. Sahin, I. Guvenc, and H. Arslan, "A Survey on Multicarrier Communications: Prototype Filters, Lattice Structures, and Implementation Aspects," *IEEE Communications Surveys Tutorials*, vol. 16, pp. 1312–1338, Third 2014.

[21] G. Cherubini, E. Eleftheriou, and S. Olcer, "Filtered multitone modulation for VDSL," in *Global Telecommunications Conference, 1999. GLOBECOM '99*, vol. 2, pp. 1139–1144 vol.2, 1999.

[22] G. Fettweis, M. Krondorf, and S. Bittner, "GFDM - Generalized Frequency Division Multiplexing," in *VTC Spring 2009 - IEEE 69th Vehicular Technology Conference*, pp. 1–4, April 2009.

[23] N. Michailow, M. Matthé, I. S. Gaspar, A. N. Caldevilla, L. L. Mendes, A. Festag, and G. Fettweis, "Generalized Frequency Division Multiplexing for 5th Generation Cellular Networks," *IEEE Transactions on Communications*, vol. 62, pp. 3045–3061, Sept 2014.

[24] R. Datta, N. Michailow, M. Lentmaier, and G. Fettweis, "GFDM Interference Cancellation for Flexible Cognitive Radio PHY Design," in *2012 IEEE Vehicular Technology Conference (VTC Fall)*, pp. 1–5, Sept 2012.

[25] V. Vakilian, T. Wild, F. Schaich, S. ten Brink, and J. F. Frigon, "Universal-filtered multi-carrier technique for wireless systems beyond LTE," in *2013 IEEE Globecom Workshops (GC Wkshps)*, pp. 223–228, Dec 2013.

[26] J. Li, E. Bala, and R. Yang, "Resource block filtered-OFDM for future spectrally agile and power efficient systems," *Physical Communication*, vol. 11, pp. 36–55, 2014.

[27] J. Abdoli, M. Jia, and J. Ma, "Filtered OFDM: A new waveform for future wireless systems," in *2015 IEEE 16th International Workshop on Signal Processing Advances in Wireless Communications (SPAWC)*, pp. 66–70, June 2015.

[28] R. Chang, "High-speed multichannel data transmission with bandlimited orthogonal signals," *Bell Sys. Tech. J*, vol. 45, no. 10, pp. 1775–1796, 1966.

[29] B. Saltzberg, "Performance of an Efficient Parallel Data Transmission System," *IEEE Transactions on Communication Technology*, vol. 15, pp. 805–811, December 1967.

[30] P. Siohan, C. Siclet, and N. Lacaille, "Analysis and design of OFDM/OQAM systems based on filterbank theory," *IEEE Transactions on Signal Processing*, vol. 50, pp. 1170–1183, May 2002.

[31] W. Kozek and A. F. Molisch, "Nonorthogonal pulseshapes for multicarrier communications in doubly dispersive channels," *IEEE Journal on Selected Areas in Communications*, vol. 16, pp. 1579–1589, Oct 1998.

[32] J. P. Javaudin, D. Lacroix, and A. Rouxel, "Pilot-aided channel estimation for OFDM/OQAM," in *The 57th IEEE Semiannual Vehicular Technology Conference, 2003.*, vol. 3, pp. 1581–1585 vol.3, April 2003.

[33] E. Kofidis, D. Katselis, A. Rontogiannis, and S. Theodoridis, "Preamble-based channel estimation in OFDM/OQAM systems: A review," *Signal Process.*, vol. 93, pp. 2038–2054, July 2013.

[34] Viholainen, A. et al., "Prototype filter and structure optimization," tech. rep., ICT-211887 PHYDYAS, January 2009.

[35] J. Yli-Kaakinen, P. Siohan, and M. Renfors, "FBMC Design and Implementation," in *Orthogonal Waveforms and Filter Banks for Future Communication Systems*, Elsevier Ltd., 2017.

[36] M. Renfors, J. Yli-Kaakinen, and F. J. Harris, "Analysis and Design of Efficient and Flexible Fast-Convolution Based Multirate Filter Banks," *IEEE Trans. Signal Process.*, vol. 62, pp. 3768–3783, Aug 2014.

[37] J. Yli-Kaakinen and M. Renfors, "Optimized reconfigurable fast convolution based transmultiplexers for flexible radio access," *IEEE Transactions on Circuits and Systems II: Express Briefs*, vol. PP, no. 99, pp. 1–1, 2017.

[38] M. Bellanger, "FS-FBMC: An alternative scheme for filter bank based multicarrier transmission," in *2012 5th International Symposium on Communications, Control and Signal Processing*, pp. 1–4, May 2012.

[39] D. Mattera, M. Tanda, and M. Bellanger, "Frequency-spreading implementation of OFDM/OQAM systems," in *2012 International Symposium on Wireless Communication Systems (ISWCS)*, pp. 176–180, Aug 2012.

[40] C. Lélé, J.-P. Javaudin, R. Legouable, A. Skrzypczak, and P. Siohan, "Channel estimation methods for preamble-based OFDM/OQAM modulations," *Transactions on Emerging Telecommunications Technologies*, vol. 19, no. 7, pp. 741–750, 2008.

[41] Louveaux, J. et al., "Equalization and demodulation in the receiver (single antenna)," tech. rep., ICT-211887 PHYDYAS, July 2008.

[42] T. Ihalainen, T. H. Stitz, M. Rinne, and M. Renfors, "Channel equalization in filter bank based multicarrier modulation for wireless communications," *EURASIP Journal on Applied Signal Processing*, vol. 2007, no. 1, pp. 140–140, 2007.

[43] D. Waldhauser, L. Baltar, and J. Nossek, "MMSE subcarrier equalization for filter bank based multicarrier systems," in *IEEE 9th Workshop on Signal Processing Advances in Wireless Communications, 2008. SPAWC 2008*, pp. 525–529, IEEE, 2008.

[44] T. Ihalainen, A. Ikhlef, J. Louveaux, and M. Renfors, "Channel equalization for multi-antenna FBMC/OQAM receivers," *IEEE Trans. Veh. Technol.*, vol. 60, no. 5, pp. 2070–2085, 2011.

[45] A. Ikhlef and J. Louveaux, "An enhanced MMSE per subchannel equalizer for highly frequency selective channels for FBMC/OQAM systems," in *IEEE 10th Workshop on Signal Processing Advances in Wireless Communications, 2009. SPAWC'09*, pp. 186–190, IEEE, 2009.

[46] L. G. Baltar, D. S. Waldhauser, and J. A. Nossek, "MMSE subchannel decision feedback equalization for filter bank based multicarrier systems," in *2009 IEEE International Symposium on Circuits and Systems*, pp. 2802–2805, May 2009.

[47] M. Caus, A. Pérez-Neira, *et al.*, "Transmitter-receiver designs for highly frequency selective channels in MIMO FBMC systems," *IEEE Trans. Signal Process.*, vol. 60, no. 12, pp. 6519–6532, 2012.

[48] M. Caus and A. I. Pérez-Neira, "Multi-stream transmission for highly frequency selective channels in mimo-fbmc/oqam systems," *IEEE Transactions on Signal Processing*, vol. 62, pp. 786–796, Feb 2014.

[49] M. Caus, A. I. Perez-Neira, and M. Moretti, "SDMA for FBMC with block diagonalization," in *2013 IEEE 14th Workshop on Signal Processing Advances in Wireless Communications (SPAWC)*, pp. 709–713, June 2013.

[50] Y. Cheng, P. Li, and M. Haardt, "Coordinated beamforming for the multi-user MIMO downlink using FBMC/OQAM," in *Communications, Control and Signal Processing (ISCCSP), 2014 6th International Symposium on*, pp. 465–469, May 2014.

[51] Y. Cheng, L. G. Baltar, M. Haardt, and J. A. Nossek, "Precoder and equalizer design for multi-user MIMO FBMC/OQAM with highly frequency selective channels," in *2015 IEEE International Conference on Acoustics, Speech and Signal Processing (ICASSP)*, pp. 2429–2433, April 2015.

[52] O. D. Candido, S. A. Cheema, L. G. Baltar, M. Haardt, and J. A. Nossek, "Downlink Precoder and Equalizer Designs for Multi-User MIMO FBMC/OQAM," in *WSA 2016; 20th International ITG Workshop on Smart Antennas*, pp. 1–8, March 2016.

[53] X. Mestre, M. Majoral, and S. Pfletschinger, "An Asymptotic Approach to Parallel Equalization of Filter Bank Based Multicarrier Signals," *IEEE Trans. Signal Process.*, vol. 61, pp. 3592–3606, July 2013.

[54] X. Mestre and D. Gregoratti, "A parallel processing approach to filterbank multicarrier MIMO transmission under strong frequency selectivity," in *2014 IEEE International Conference on Acoustics, Speech and Signal Processing (ICASSP)*, pp. 8078–8082, IEEE, 2014.

[55] X. Mestre and D. Gregoratti, "Parallelized Structures for MIMO FBMC Under Strong Channel Frequency Selectivity," *IEEE Transactions on Signal Processing*, vol. 64, pp. 1200–1215, March 2016.

[56] T. Xu, G. Jacobsen, S. Popov, J. Li, E. Vanin, K. Wang, A. T. Friberg, and Y. Zhang, "Chromatic dispersion compensation in coherent transmission system using digital filters," *Optics express*, vol. 18, no. 15, pp. 16243–16257, 2010.

[57] J. Rodríguez-Piñeiro, M. Lerch, T. Domínguez-Bolaño, J. A. García-Naya, S. Caban, and L. Castedo, "Experimental assessment of 5G-candidate modulation schemes at extreme speeds," in *2016 IEEE Sensor Array and Multichannel Signal Processing Workshop (SAM)*, pp. 1–5, July 2016.

[58] J. Rodríguez-Piñeiro, T. Domínguez-Bolaño, P. Suárez-Casal, J. García-Naya, and L. Castedo, "Affordable Evaluation of 5G Modulation Schemes in High Speed Train Scenarios," in *WSA*

2016; 20th International ITG Workshop on Smart Antennas, pp. 1–8, March 2016.

[59] J. Bazzi, K. Kusume, P. Weitkemper, K. Saito, A. Benjebbour, and Y. Kishiyama, "Performance of multi-carrier waveforms in vehicle-to-vehicle communications," in *Vehicular Networking Conference (VNC), 2015 IEEE*, pp. 9–16, Dec 2015.

[60] E. Kofidis and A. Rontogiannis, "Adaptive BLAST decision-feedback equalizer for MIMO-FBMC/OQAM systems," in *21st Annual IEEE International Symposium on Personal, Indoor and Mobile Radio Communications*, pp. 841–846, Sept 2010.

[61] C. Mavrokefalidis, A. Rontogiannis, E. Kofidis, A. Beikos, and S. Theodoridis, "Efficient adaptive equalization of doubly dispersive channels in MIMO-FBMC/OQAM systems," in *2014 11th International Symposium on Wireless Communications Systems (ISWCS)*, pp. 308–312, Aug 2014.

[62] L. Marijanović, S. Schwarz, and M. Rupp, "MMSE equalization for FBMC transmission over doubly-selective channels," in *2016 International Symposium on Wireless Communication Systems (ISWCS)*, pp. 170–174, Sept 2016.

[63] L. Zhang, P. Xiao, A. Zafar, A. ul Quddus, and R. Tafazolli, "FBMC System: an insight into doubly dispersive channel impact," *IEEE Trans. Veh. Technol.*, vol. PP, no. 99, pp. 1–1, 2016.

[64] G. Taubock, F. Hlawatsch, D. Eiwen, and H. Rauhut, "Compressive Estimation of Doubly Selective Channels in Multicarrier Systems: Leakage Effects and Sparsity-Enhancing Processing," *IEEE Journal of Selected Topics in Signal Processing*, vol. 4, pp. 255–271, April 2010.

[65] M. Fuhrwerk, J. Peissig, and M. Schellmann, "Channel adaptive pulse shaping for OQAM-OFDM systems," in *2014 22nd European Signal Processing Conference (EUSIPCO)*, pp. 181–185, Sept 2014.

[66] A. Şahin, I. Güvenç, and H. Arslan, "A comparative study of FBMC prototype filters in doubly dispersive channels," in *2012 IEEE Globecom Workshops*, pp. 197–203, Dec 2012.

[67] E. Kofidis, L. G. Baltar, X. Mestre, F. Bader, and V. Savaux, "FBMC Channel Estimation Techniques," in *Orthogonal Waveforms and Filter Banks for Future Communication Systems*, Elsevier Ltd., 2017.

[68] E. Kofidis, "Channel estimation in filter bank-based multicarrier systems: Challenges and solutions," in *2014 6th International Symposium on Communications, Control and Signal Processing (ISCCSP)*, pp. 453–456, May 2014.

[69] D. Katselis, E. Kofidis, A. Rontogiannis, and S. Theodoridis, "Preamble-Based Channel Estimation for CP-OFDM and OFDM/OQAM Systems: A Comparative Study," *IEEE Transactions on Signal Processing*, vol. 58, pp. 2911–2916, May 2010.

[70] V. Savaux, F. Bader, and Y. Louët, "A Joint MMSE Channel and Noise Variance Estimation for OFDM/OQAM Modulation," *IEEE Transactions on Communications*, vol. 63, pp. 4254–4266, Nov 2015.

[71] E. Kofidis, "Preamble-based Estimation of Highly Frequency Selective Channels in MIMO-FBMC/OQAM Systems," in *Proceedings of European Wireless 2015; 21th European Wireless Conference*, pp. 1–6, May 2015.

[72] E. Kofidis, "Preamble-Based Estimation of Highly Frequency Selective Channels in FBMC/OQAM Systems," *IEEE Transactions on Signal Processing*, vol. 65, pp. 1855–1868, April 2017.

[73] E. Kofidis and D. Katselis, "Preamble-based channel estimation in MIMO-OFDM/OQAM systems," in *2011 IEEE International Conference on Signal and Image Processing Applications (ICSIPA)*, pp. 579–584, Nov 2011.

[74] T. Stitz, T. Ihalainen, A. Viholainen, and M. Renfors, "Pilot-based synchronization and equalization in filter bank multicarrier communications," *EURASIP Journal on Advances in Signal Processing*, vol. 2010, p. 741429, Feb 2010.

[75] C. Lele, R. Legouable, and P. Siohan, "Channel estimation with scattered pilots in OFDM/OQAM," in *2008 IEEE 9th Workshop on Signal Processing Advances in Wireless Communications*, pp. 286–290, July 2008.

[76] W. Cui, D. Qu, T. Jiang, and B. Farhang-Boroujeny, "Coded Auxiliary Pilots for Channel Estimation in FBMC-OQAM Systems," *IEEE Transactions on Vehicular Technology*, vol. 65, pp. 2936–2946, May 2016.

[77] X. Mestre and E. Kofidis, "Pilot-based channel estimation for FBMC/OQAM systems under strong frequency selectivity," in

2016 IEEE International Conference on Acoustics, Speech and Signal Processing (ICASSP), pp. 3696–3700, March 2016.

[78] J. P. Javaudin and Y. Jiang, "Channel estimation for iterative MIMO OFDM/OQAM transceivers," in *2008 14th European Wireless Conference*, pp. 1–6, June 2008.

[79] J. P. Javaudin and Y. Jiang, "Channel estimation in MIMO OFDM/OQAM," in *2008 IEEE 9th Workshop on Signal Processing Advances in Wireless Communications*, pp. 266–270, July 2008.

[80] F. Bader and M. Shaat, "Pilot Pattern Adaptation and Channel Estimation in MIMO WiMAX-like FBMC System," in *2010 6th International Conference on Wireless and Mobile Communications*, pp. 111–116, Sept 2010.

[81] F. Rottenberg, K. Degraux, L. Jacques, and J. Louveaux, "Pilots allocation for sparse channel estimation in multicarrier systems," in *Joint WIC/IEEE Symposium on Information Theory and Signal Processing in the Benelux*, May 2015.

[82] F. Rottenberg, F. Horlin, E. Kofidis, and J. Louveaux, "Generalized optimal pilot allocation for channel estimation in multicarrier systems," in *2016 IEEE 17th International Workshop on Signal Processing Advances in Wireless Communications (SPAWC)*, pp. 1–5, July 2016.

[83] A. Paulraj, R. Nabar, and D. Gore, *Introduction to Space-Time Wireless Communications*. Cambridge university press, 2003.

[84] "Universal Mobile Telecommunications System (UMTS); Deployment aspects (3GPP TR 25.943 version 13.0.0 Release 13)," tech. rep., ETSI, 2016.

[85] H. Tang, M. Xiang, S. Fu, M. Tang, P. Shum, and D. Liu, "Feed-forward carrier phase recovery for offset-QAM Nyquist WDM transmission," *Opt. Express*, vol. 23, pp. 6215–6227, Mar. 2015.

[86] T.-H. Nguyen, S.-P. Gorza, J. Louveaux, and F. Horlin, "Low-complexity blind phase search for filter bank multicarrier Offset-QAM optical fiber systems," in *Advanced Photonics 2016 (IPR, NOMA, Sensors, Networks, SPPCom, SOF)*, p. SpW2G.2, Optical Society of America, 2016.

[87] J. Fickers, A. Ghazisaeidi, M. Salsi, G. Charlet, P. Emplit, and F. Horlin, "Multicarrier Offset-QAM for Long-Haul Coherent Optical Communications," *Journal of Lightwave Technology*, vol. 32, pp. 4671–4678, Dec. 2014.

[88] F. Horlin, J. Fickers, P. Emplit, A. Bourdoux, and J. Louveaux, "Dual-polarization OFDM-OQAM for communications over optical fibers with coherent detection," *Opt. Express*, vol. 21, no. 5, pp. 6409–6421, 2013.

[89] Z. Li, T. Jiang, H. Li, X. Zhang, C. Li, C. Li, R. Hu, M. Luo, X. Zhang, X. Xiao, *et al.*, "Experimental demonstration of 110-Gb/s unsynchronized band-multiplexed superchannel coherent optical OFDM/OQAM system," *Optics express*, vol. 21, no. 19, pp. 21924–21931, 2013.

[90] M. Born and E. Wolf, *Principles of optics: electromagnetic theory of propagation, interference and diffraction of light*. Elsevier, 2013.

[91] S. J. Savory, "Digital filters for coherent optical receivers," *Opt. Express*, vol. 16, pp. 804–817, Jan 2008.

[92] E. Ip and J. M. Kahn, "Feedforward Carrier Recovery for Coherent Optical Communications," *Journal of Lightwave Technology*, vol. 25, pp. 2675–2692, Sept 2007.

[93] X. Pang, A. Caballero, A. Dogadaev, V. Arlunno, R. Borkowski, J. S. Pedersen, L. Deng, F. Karinou, F. Roubeau, D. Zibar, X. Yu, and I. T. Monroy, "100 Gbit/s hybrid optical fiber-wireless link in the W-band (75–110 GHz)," *Opt. Express*, vol. 19, pp. 24944–24949, Dec 2011.

[94] X. Li, J. Yu, and J. Xiao, "Demonstration of Ultra-Capacity Wireless Signal Delivery at W-Band," *Journal of Lightwave Technology*, vol. 34, pp. 180–187, Jan 2016.

[95] P. T. Dat, A. Kanno, N. Yamamoto, and T. Kawanishi, "Full-Duplex Transmission of LTE-A Carrier Aggregation Signal Over a Bidirectional Seamless Fiber-Millimeter-Wave System," *Journal of Lightwave Technology*, vol. 34, pp. 691–700, Jan 2016.

[96] S. E. Alavi, I. S. Amiri, M. Khalily, N. Fisal, A. S. M. Supa'at, H. Ahmad, and S. M. Idrus, "W-Band OFDM for Radio-over-Fiber Direct-Detection Link Enabled by Frequency Nonupling Optical Up-Conversion," *IEEE Photonics Journal*, vol. 6, pp. 1–7, Dec 2014.

[97] L. Deng, X. Pang, Y. Zhao, M. B. Othman, J. B. Jensen, D. Zibar, X. Yu, D. Liu, and I. T. Monroy, "2x2 MIMO-OFDM Gigabit fiber-wireless access system based on polarization division multiplexed WDM-PON," *Opt. Express*, vol. 20, pp. 4369–4375, Feb 2012.

[98] M. Xu, J. Zhang, F. Lu, J. Wang, L. Cheng, H. J. Cho, M. I. Khalil, D. Guidotti, and G. K. Chang, "FBMC in Next-Generation Mobile Fronthaul Networks With Centralized Pre-Equalization," *IEEE Photonics Technology Letters*, vol. 28, pp. 1912–1915, Sept 2016.

[99] J. Zhang, M. Xu, J. Wang, F. Lu, L. Cheng, H. Cho, K. Ying, J. Yu, and G. K. Chang, "Full-Duplex Quasi-Gapless Carrier Aggregation Using FBMC in Centralized Radio-Over-Fiber Heterogeneous Networks," *Journal of Lightwave Technology*, vol. 35, pp. 989–996, Feb 2017.

[100] P. T. Dat, A. Kanno, N. Yamamoto, and T. Kawanishi, "Simultaneous transmission of multi-RATs and mobile fronthaul in the MMW bands over an IFoF system," in *2017 Optical Fiber Communications Conference and Exhibition (OFC)*, pp. 1–3, March 2017.

[101] J. He, B. Li, L. Deng, M. Tang, L. Gan, S. Fu, P. P. Shum, and D. Liu, "Experimental investigation of inter-core crosstalk tolerance of MIMO-OFDM/OQAM radio over multicore fiber system," *Opt. Express*, vol. 24, pp. 13418–13428, Jun 2016.

[102] C. Liu, L. Deng, J. He, D. Li, S. Fu, M. Tang, M. Cheng, and D. Liu, "Experimental demonstration of high spectral efficient 4×4 MIMO SCMA-OFDM/OQAM radio over multi-core fiber system," *Opt. Express*, vol. 25, pp. 18431–18441, Jul 2017.

[103] F. Rottenberg, X. Mestre, and J. Louveaux, "Optimal zero forcing precoder and decoder design for multi-user MIMO FBMC under strong channel selectivity," in *2016 IEEE International Conference on Acoustics, Speech and Signal Processing (ICASSP)*, pp. 3541–3545, March 2016.

[104] F. Rottenberg, X. Mestre, F. Horlin, and J. Louveaux, "Single-Tap Precoders and Decoders for Multiuser MIMO FBMC-OQAM Under Strong Channel Frequency Selectivity," *IEEE Transactions on Signal Processing*, vol. 65, pp. 587–600, Feb 2017.

[105] X. Mestre, F. Rottenberg, and M. Navarro, "Linear receivers for massive MIMO FBMC/OQAM under strong channel frequency selectivity," in *2016 IEEE Statistical Signal Processing Workshop (SSP)*, pp. 1–5, June 2016.

[106] F. Rottenberg, X. Mestre, F. Horlin, and J. Louveaux, "Performance Analysis of Linear Receivers for Uplink Massive MIMO FBMC-OQAM Systems," *IEEE Transactions on Signal Processing*, vol. 66, pp. 830–842, Feb 2018.

[107] F. Rottenberg, X. Mestre, D. Petrov, F. Horlin, and J. Louveaux, "Parallel Equalization Structure for MIMO FBMC-OQAM Systems Under Strong Time and Frequency Selectivity," *IEEE Transactions on Signal Processing*, vol. 65, pp. 4454–4467, Sept 2017.

[108] F. Rottenberg, X. Mestre, F. Horlin, and J. Louveaux, "Single-tap equalizer for MIMO FBMC systems under doubly selective channels," in *2017 IEEE International Conference on Acoustics, Speech and Signal Processing (ICASSP)*, pp. 3784–3788, March 2017.

[109] E. G. Larsson, O. Edfors, F. Tufvesson, and T. L. Marzetta, "Massive MIMO for next generation wireless systems," *IEEE Communications Magazine*, vol. 52, pp. 186–195, February 2014.

[110] F. Rusek, D. Persson, B. K. Lau, E. G. Larsson, T. L. Marzetta, O. Edfors, and F. Tufvesson, "Scaling Up MIMO: Opportunities and Challenges with Very Large Arrays," *IEEE Signal Processing Magazine*, vol. 30, pp. 40–60, Jan 2013.

[111] J. Hoydis, S. ten Brink, and M. Debbah, "Massive MIMO in the UL/DL of cellular networks: How many antennas do we need?," *IEEE Journal on Selected Areas in Communications*, vol. 31, pp. 160–171, Feb. 2013.

[112] A. Farhang, N. Marchetti, L. E. Doyle, and B. Farhang-Boroujeny, "Filter Bank Multicarrier for Massive MIMO," in *2014 IEEE 80th Vehicular Technology Conference (VTC2014-Fall)*, pp. 1–7, Sept 2014.

[113] A. Aminjavaheri, A. Farhang, N. Marchetti, L. E. Doyle, and B. Farhang-Boroujeny, "Frequency spreading equalization in multicarrier massive MIMO," in *2015 IEEE International Conference on Communication Workshop (ICCW)*, pp. 1292–1297, June 2015.

[114] A. Aminjavaheri, A. Farhang, L. E. Doyle, and B. Farhang-Boroujeny, "Prototype filter design for FBMC in massive MIMO channels," *CoRR*, vol. abs/1610.06273, 2016.

[115] A. Aminjavaheri, A. Farhang, and B. Farhang-Boroujeny, "Filter Bank Multicarrier in Massive MIMO: Analysis and Channel Equalization," *CoRR*, vol. abs/1706.09744, 2017.

[116] S. L. Loyka, "Channel capacity of MIMO architecture using the exponential correlation matrix," *IEEE Commun. Lett.*, vol. 5, pp. 369–371, Sept. 2001.

[117] V. Girko, *Theory of Random Determinants*. The Netherlands: Kluwer Academic Publishers, 1990.

[118] A. Boutet de Monvel, A. Khorunzhy, and V. Vasilchuk, "Limiting eigenvalue distribution of random matrices with correlated entries," *Markov Processes and Related Fields*, vol. 2, no. 2, pp. 607–636, 1996.

[119] W. Hachem, O. Khorunzhiy, P. Loubaton, J. Najim, and L. Pastur, "A new approach for mutual information analysis of large dimensional multi-antenna channels," *IEEE Transactions on Information Theory*, vol. 54, pp. 3987–4004, Sep. 2008.

[120] R. Couillet and W. Hachem, "Analysis of the limiting spectral measure of large random matrices of the separable covariance type," *Random Matrices: Theory and Applications*, vol. 3, no. 4, 2014.

[121] D. Paul and J. Silverstein, "No eigenvalues outside the support of limiting empirical spectral distribution of a separable covariance matrix," *Journal of Multivariate Analysis*, vol. 100, no. 1, pp. 37–57, 2009.

[122] W. Hachem, P. Loubaton, and J. Najim, "Deterministic equivalents for certain functionals of large random matrices," *The Annals of Applied Probability*, vol. 17, no. 3, pp. 875–930, 2007.

[123] L. Pastur and M.Shcherbina, *Eigenvalue Distribution of Large Random Matrices*, vol. 171 of *Mathematical Surveys and Monographs*. American Mathematical Society, 2011.

[124] F. Rubio, X. Mestre, and W. Hachem, "A CLT on the SNR of diagonally loaded MVDR filters," *IEEE Transactions on Signal Processing*, vol. 60, pp. 4178– 4195, Aug. 2012.

[125] Z. Bai and J. Silverstein, "No eigenvalues outside the support of the limiting spectral distribution of large dimensional sample covariance matrices," *Annals of probability*, vol. 26, pp. 316–345, 1998.

[126] D. Petrov, A. Oborina, L. Giupponi, and T. H. Stitz, "Link performance model for filter bank based multicarrier systems," *EURASIP Journal on Advances in Signal Processing*, vol. 2014, no. 1, p. 1, 2014.

[127] D. Petrov, B. Herman, T. Hämäläinen, and S. Melnikz, "On the system level performance of cellular FBMC-based wideband PMR

network," in *2015 International Symposium on Wireless Communication Systems (ISWCS)*, pp. 521–525, Aug 2015.

[128] D. Petrov, T. Hämäläinen, and S. Melnik, "Asymptotic Presentation of Intrinsic Interference for FBMC/OQAM Signals in Quasi-Static Channels," in *European Wireless 2016; 22th European Wireless Conference*, pp. 1–6, May 2016.

[129] P. Bello, "Characterization of randomly time-variant linear channels," *IEEE Trans. Commun.*, vol. 11, no. 4, pp. 360–393, 1963.

[130] P. Duhamel and M. Vetterli, "Fast Fourier transforms: a tutorial review and a state of the art," *Signal Proces.*, vol. 19, no. 4, pp. 259–299, 1990.

[131] M. Fuhrwerk, J. Peissig, and M. Schellmann, "Performance comparison of CP-OFDM and OQAM-OFDM systems based on LTE parameters," in *2014 IEEE 10th International Conference on Wireless and Mobile Computing, Networking and Communications (WiMob)*, pp. 604–610, Oct 2014.

[132] M. Fuhrwerk, S. Moghaddamnia, and J. Peissig, "Scattered Pilot-Based Channel Estimation for Channel Adaptive FBMC-OQAM Systems," *IEEE Trans. Wireless Commun.*, vol. 16, pp. 1687–1702, March 2017.

[133] F. Rottenberg, T. H. Nguyen, S. P. Gorza, F. Horlin, and J. Louveaux, "ML and MAP phase noise estimators for optical fiber FBMC-OQAM systems," in *2017 IEEE International Conference on Communications (ICC)*, pp. 1–6, May 2017.

[134] F. Rottenberg, T.-H. Nguyen, S.-P. Gorza, F. Horlin, and J. Louveaux, "Advanced Chromatic Dispersion Compensation in Optical Fiber FBMC-OQAM Systems," *IEEE Photonics Journal*, vol. 9, pp. 1–10, Dec 2017.

[135] T.-H. Nguyen, F. Rottenberg, S. P. Gorza, J. Louveaux, and F. Horlin, "Efficient Chromatic Dispersion Compensation and Carrier Phase Tracking for Optical Fiber FBMC/OQAM Systems," *IEEE/OSA Journal of Lightwave Technology*, vol. 35, pp. 2909–2916, July 2017.

[136] J. Lu, S. Fu, H. Tang, M. Xiang, M. Tang, and D. Liu, "Vertical blind phase search for low-complexity carrier phase recovery of offset-QAM Nyquist WDM transmission," *Optics Communications*, vol. 382, pp. 212–218, 2017.

[137] T. H. Nguyen, J. Louveaux, S. P. Gorza, and F. Horlin, "Simple feedforward carrier phase estimation for optical FBMC/OQAM systems," *IEEE Photon. Technol. Lett.*, vol. 28, pp. 2823–2826, Dec 2016.

[138] S. Randel, A. Sierra, X. Liu, S. Chandrasekhar, and P. Winzer, "Study of Multicarrier Offset-QAM for Spectrally Efficient Coherent Optical Communications," in *37th European Conference and Exposition on Optical Communications*, p. Th.11.A.1, Optical Society of America, 2011.

[139] J. Zhao and P. D. Townsend, "Dispersion tolerance enhancement using an improved offset-QAM OFDM scheme," *Opt. Express*, vol. 23, pp. 17638–17652, Jun 2015.

[140] Y. Yu, P. D. Townsend, and J. Zhao, "Equalization of Dispersion-Induced Crosstalk in Optical Offset-QAM OFDM Systems," *IEEE Photon. Technol. Lett.*, vol. 28, pp. 782–785, April 2016.

[141] X. Liu and F. Buchali, "Intra-symbol frequency-domain averaging based channel estimation for coherent optical OFDM," *Opt. Express*, vol. 16, pp. 21944–21957, Dec 2008.

[142] R. J. Essiambre, G. Kramer, P. J. Winzer, G. J. Foschini, and B. Goebel, "Capacity Limits of Optical Fiber Networks," *Journal of Lightwave Technology*, vol. 28, pp. 662–701, Feb 2010.

[143] T. Mizuochi, "Recent progress in forward error correction and its interplay with transmission impairments," *IEEE Journal of Selected Topics in Quantum Electronics*, vol. 12, pp. 544–554, July 2006.

[144] A. N. D'Andrea, U. Mengali, and R. Reggiannini, "The modified Cramer-Rao bound and its application to synchronization problems," *IEEE Transactions on Communications*, vol. 42, pp. 1391–1399, Feb 1994.

[145] F. Rottenberg, P. T. Dat, T.-H. Nguyen, A. Kanno, F. Horlin, J. Louveaux, and N. Yamamoto, "2x2 MIMO FBMC-OQAM Signal Transmission over a Seamless Fiber–Wireless System in W-band," *IEEE Photonics Journal*, 2018, accepted and in press.

[146] C. Thein, M. Schellmann, and J. Peissig, "Analysis of frequency domain frame detection and synchronization in oqam-ofdm systems," *EURASIP Journal on Advances in Signal Processing*, vol. 2014, p. 83, Jun 2014.

[147] M. K. Ozdemir and H. Arslan, “Channel estimation for wireless OFDM systems,” *IEEE Communications Surveys Tutorials*, vol. 9, pp. 18–48, Second 2007.

[148] S. Dimitrov and H. Haas, *Principles of LED Light Communications: Towards Networked Li-Fi*. Cambridge University Press, 2015.

[149] X. Hong, J. Zhang, L. Liu, and S. He, “Multi-user asynchronous full-duplex visible light communication using cp-free OFDM/OQAM-SCM,” in *2015 IEEE Summer Topicals Meeting Series (SUM)*, pp. 51–52, July 2015.

[150] B. Lin, X. Tang, Z. Ghassemlooy, X. Fang, C. Lin, Y. Li, and S. Zhang, “Experimental Demonstration of OFDM/OQAM Transmission for Visible Light Communications,” *IEEE Photonics Journal*, vol. 8, pp. 1–10, Oct 2016.

[151] S. Rajbhandari, J. J. D. McKendry, J. Herrnsdorf, H. Chun, G. Faulkner, H. Haas, I. M. Watson, D. O’Brien, and M. D. Dawson, “A review of gallium nitride LEDs for multi-gigabit-per-second visible light data communications,” *Semiconductor Science and Technology*, vol. 32, no. 2, p. 023001, 2017.